Damping, satellites and multiple excitations in oxides and nanostructures: efficient theoretical and numerical approaches towards a dynamical many-body theory

Lorenzo Sponza

▶ **To cite this version:**

Lorenzo Sponza. Damping, satellites and multiple excitations in oxides and nanostructures: efficient theoretical and numerical approaches towards a dynamical many-body theory. Materials Science [cond-mat.mtrl-sci]. Ecole Polytechnique (EDX), 2013. English. NNT : . tel-01883527

HAL Id: tel-01883527
https://hal.science/tel-01883527

Submitted on 15 Oct 2018

HAL is a multi-disciplinary open access archive for the deposit and dissemination of scientific research documents, whether they are published or not. The documents may come from teaching and research institutions in France or abroad, or from public or private research centers.

L'archive ouverte pluridisciplinaire **HAL**, est destinée au dépôt et à la diffusion de documents scientifiques de niveau recherche, publiés ou non, émanant des établissements d'enseignement et de recherche français ou étrangers, des laboratoires publics ou privés.

Thèse présentée pour obtenir le grade de

DOCTEUR DE L'ÉCOLE POLYTECHNIQUE

par

LORENZO SPONZA

Damping, satellites and multiple excitations in oxides and nanostructures: efficient theoretical and numerical approaches towards a dynamical many-body theory

---

Thèse soutenue le 30 Octobre 2013

Silke	BIERMANN	Président
Angel	RUBIO	Rapporteur
Valerio	OLEVANO	Rapporteur
Odile	STÉPHAN	Examinatrice
Mark	VAN SCHILFGAARDE	Examinateur
Christine	GIORGETTI	Co-directrice
Lucia	REINING	Directrice

Table of Contents

Chapter 1

Introduction

This thesis is about dynamical correlation between electrons effects in light absorption. This study is conducted in the framework of theoretical *ab-initio* spectroscopy. I present here the analysis of real materials spectra as well as the development of new technical and theoretical approaches.

When light is absorbed by a material, its energy gives rise to a big variety of different phenomena and is converted into excitations of the system, e.g., the creation of electron-hole pairs, the excitations of collective vibrations (electrons and nuclei), or the emission of particles. Each excitation may be the result of the direct absorption of light, or may be induced by other excitations occurring in the system.

One strong point of theoretical spectroscopy is that it allows to select which physics to include in the theory, to neglect at will some process or to focus specifically on others. *Ab initio* spectroscopy therefore constitutes an indispensable tool to interpret experimental data and to predict the behaviour of a system. Simple models, accounting only for few phenomena, lead to simple interpretations, but are most often expected to give only qualitative trends. Usually a better quantitative agreement comes with much more complicated models which account for the physics of many processes taking place at the same time.

Dynamical effects describe the coupling between different excitations of the system and are therefore a clear manifestation of the many-body nature of the electronic processes. They are included in nowadays theoretical approaches only to a limited extent. In the absorption spectrum, dynamical effects are responsible for the reduction of the spectral weight of some structures, for the renormalization of energies, but also they may create new features at higher energy which in many cases constitute a challenge for state-of-the-art theories. Moreover they are potentially important for technological applications, hence a quantitative theory to explain and predict their properties is more and more needed.

One example is the multiple exciton generation (MEG), where the absorption of a single high-energy photon is converted into the creation of multiple electron-hole pairs (excitons). Its possible applications are in the photovoltaic technology since the full exploitation of this effect could ensure high currents even at low intensity. This process can be correctly described only by including a dynamical coupling at the level of the electron-hole interaction.

In the present work I try to analyse successes and flaws of present theories, and I propose some steps towards more efficient and precise calculations based on methodological and theoretical advances.

1.1 An introduction to spectroscopy

The general framework of a spectroscopic experiment is depicted in Fig. 1.1. It is composed by a source, a scatterer and an analyser. A perturbing (or external) field created by the source interacts with the scatterer (for us an N-electron system). By effect of the interaction, the field exchanges energy with the system, which consequently undergoes some excitations. After the interaction, the outgoing field contains information on the exchanged quantities. It is eventually analysed to get this information out and to reconstruct and characterise the spectrum of the possible excitations of the system.

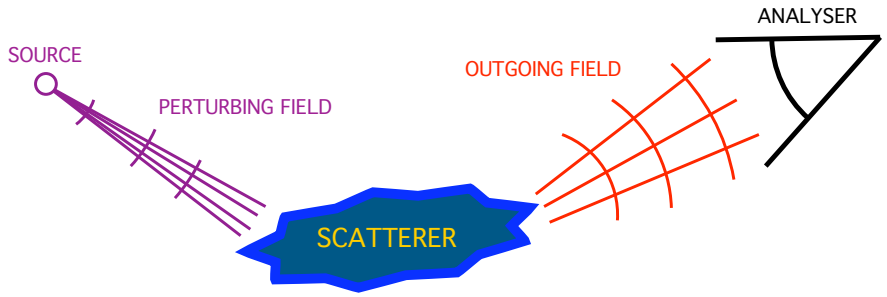

Figure 1.1: The perturbing field produced by the source impinges onto the scatterer (the system). The outgoing field is measured and analysed.

The perturbing field is typically a beam of photons, electrons, neutrons or other particles the sample can interact with. It must be characterised to some extent by the knowledge of the source itself or by measuring some parameters of the field before the interaction with the sample. For instance in photoemission spectroscopy or absorption experiments, the perturbing field is a light radiation that can be characterised by its energy, polarization, intensity and its angle of incidence. In electron energy loss spectroscopy, fast electrons pass through a thin sample. The electron beam can be parametrised by the average kinetic energy of the electrons.

On the other side of this scheme, far from the interaction point, the analyser measures the field after the interaction with the sample . Typically it records the number of particles at given energy and momentum, or the intensity of the outgoing field. Losses of energy and modifications of the momentum are related to the exchanged quantities between the system and the perturbing field, which gives insight into the excitations of the system.

How do we describe what happens in between?

Describing the system: independent particles and effective fields

The true N-electron system is completely characterised by its N-particle wave function $\Psi(\mathbf{r}_1, \mathbf{r}_2, \ldots, \mathbf{r}_N, t)$, eigenfunction of the N-particle Hamiltonian $H(t)$ which depends on time in presence of a time-dependent perturbation. The external field excites the system from an initial state Ψ^i to a final state Ψ^f. But already for few electrons, the knowledge of the exact electronic wave function is out of reach, and different schemes have to be employed to try an interpretation of the process.

In an independent-particle (IP) picture, each electron interacts only with the external field. In this framework each electron behaves as if it were alone in the external field, the description of its properties being completely independent of the presence of other electrons. Correspondingly, the spectrum of the excitations of the whole system is just the weighted

sum over all possible excitations of the electrons, as depicted schematically in Fig. 1.2. In formulae the spectrum $S(\omega)$, function of the frequency of the incoming field ω, is computed according to the Fermi's golden rule

$$S(\omega) \propto \sum_{if} |M_{if}|^2 \delta(E_f - E_i - \omega) \,, \tag{1.1}$$

where $|M_{if}|^2$ is the energy-independent probability for one electron to be excited from the initial state $|i\rangle$ of energy E_i to the final state $|f\rangle$ of energy E_f, and the delta-function ensures energy conservation.

But of course electrons are not blind to each other. Mutual interactions between them always take place in the form of the Coulomb potential, and the Pauli exclusion principle. Some of these ingredients can be included quite straightforwardly into an effective IP picture, and the Pauli exclusion principle can be accounted for at the level of occupation numbers for single particle states. A way to include mutual interactions without losing the advantages of the IP picture is to introduce some effective (mean) field. The effective field accounts implicitly for the sum of the external field and the field resulting from interaction with all other electrons. In this picture each particle is still blind to the others, but every change of its own state modifies the effective field which modifies back the particle state, in a game of reciprocal (selfconsistent) modifications.

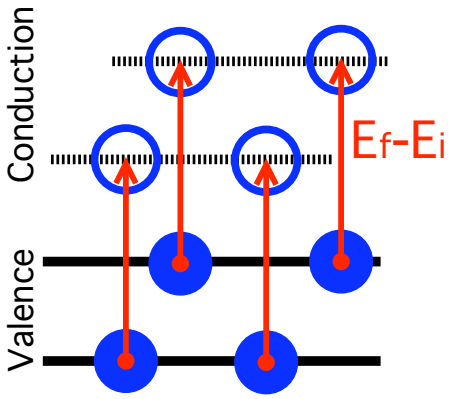

Figure 1.2: Pictorial representation of the sum over states (1.1) in the case of absorption. All electronic transitions of energy $E_f - E_i = \omega$, contribute to the spectrum. ω is the photon energy.

The theories presented in the first chapters can all be read in this view. In some cases (Chapters 3 and 4) we will call our independent electrons "Kohn-Sham" electrons, and what will play the role of the effective field will be composed by the Hartree and the exchange-correlation potential. In other cases (Chapter 5) our independent particles will be called "quasiparticles" and the effective field will be composed of the Hartree potential and the self-energy. Of course the real scheme of these theories is much more refined than the sketch outlined above, but the time is not yet right to go through the differences: the next chapters will be devoted to that. At this stage I am interested only in clarifying the origin of the effective field.

1.2 Many-body interactions and dynamical effects

Let us divide the N-electron system into two subsystems: the one electron $\mathbf{e}_s$, and all the rest $\mathbf{e}_m$. Knowing the Hamiltonian H of the system, the properties of the system are determined by the eigenvalue problem

$$\begin{pmatrix} S & C_1 \\ C_2 & M \end{pmatrix} \cdot \begin{pmatrix} \mathbf{e}_s \\ \mathbf{e}_m \end{pmatrix} = \omega \begin{pmatrix} \mathbf{e}_s \\ \mathbf{e}_m \end{pmatrix} \quad \text{with} \quad H = \begin{pmatrix} S & C_1 \\ C_2 & M \end{pmatrix}$$

The block S is the Hamiltonian of a single electron; at an IP level, the description of the process would reduce to $H = S$. The block M describes the rest of the system, and the two

coupling terms C_1 and C_2 describe the interactions between the electron of interest and all the other electrons.

If now one solves the eigenvalue equation for the one-electron space only, one gets

$$\left[S + C_1(\omega - M)^{-1}C_2\right]\mathbf{e}_s = \left[S + V_{\text{eff}}(\omega)\right]\mathbf{e}_s = \omega\mathbf{e}_s$$

which is still an eigenvalue equation written in the one-electron space only. To the purely independent-electron Hamiltonian S the dynamical term $V_{\text{eff}}(\omega) = C_1(\omega - M)^{-1}C_2$ is added which is nothing but an effective field which accounts for all mutual interactions of the system. The folding of all the other electrons into an effective field allows, on one hand, to solve the problem in the one-electron space, on the other hand, it spawns an extra dynamical effective field.

What is the meaning of this dynamical dependence?

Dynamical potential and coupling between excitations

Everyday life tells us that in mutual interactions, the energy of one part strongly determines the reaction of the other part. In descending from the metro, if you ask "excuse me" and you move slowly, people will (hopefully) let you through without complaining; on the contrary, if you start running all of the sudden, it is unlikely that they will react in the same way.

In a similar way, let an electron be excited at an energy E_s. The rest of the system reacts to this excitation in a way that, in general, depends on the energy of the excitation: the other electrons change their state in response to the earliest excitation. This response is dynamical and it may involve other one-particle excitations, collective excitations or more complicated scattering events. Each of these processes to happen requires a transfer of a certain energy E_m from the first excitation to the rest of the system. The original excitation is therefore coupled to the other excitations of the system.

That is the origin of the energy dependence of $V_{\text{eff}}(\omega)$: it describes the transfer of energy from the one-electron space to the rest of the system and, of course, vice-versa.

If now one imagines a system with an instantaneous reaction, the effect of the coupling to the system can be expressed as a simple renormalization of the energy needed to excite an electron. The effective potential becomes then energy-independent and all the de-excitation channels are closed. As a consequence, excitations are decoupled and have an infinite lifetime becoming stationary states of $H = S + V_{\text{eff}}$.

1.3 Dynamical effects in real systems

I will now go more into detail in describing some dynamical effect in experimental and theoretical spectra. I will focus mostly on two spectroscopic techniques to which I will often refer in the rest of this work: photoemission and absorption.

1.3.1 Photoemission and plasmon satellites

In photoemission spectroscopy (PES), the probing field is a radiation of given frequency ω_{ph}[1], impinging on the sample from a direction well characterised by the geometry of the

[1]Other parameters of the radiation field, such as the intensity or the polarization, may characterise the beam as well, but they are not relevant quantities for our scopes.

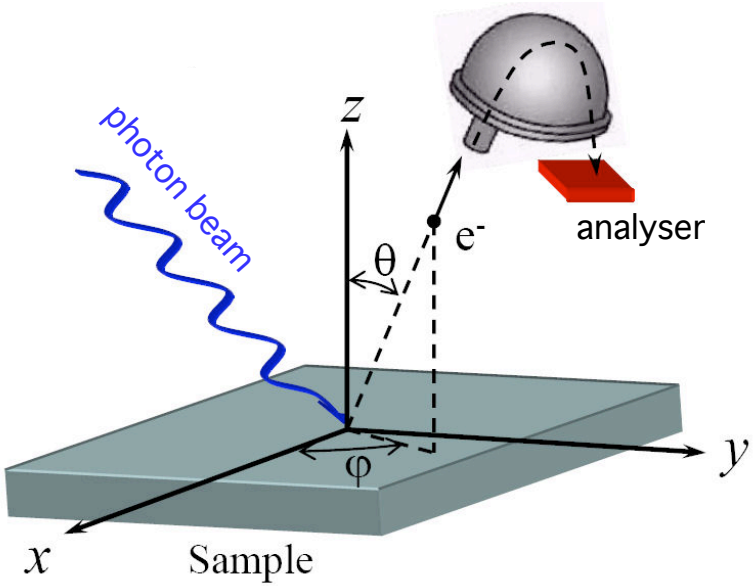

Figure 1.3: Schematic experimental set up of a PES experiment: a light beam of energy $\omega_{\rm ph}$ impinges on the sample. The photoemitted electron is collected by the analyser which measures its kinetic energy $E_k = k^2/2$. From the geometrical configuration (angles φ and θ), the direction of the wave vector $\mathbf{k}$ can be reconstructed (ARPES). Image taken from [1].

experimental set up. The measured outgoing field is composed by electrons (photo)emitted from the sample. They are usually described as time-inverted scattering states [2] of kinetic energy E_k propagating towards the analyser where their energy (and in angular-resolved PES (ARPES) their momentum $\mathbf{k}$) is (are) recorded. A schematic representation is found in Fig. 1.3.

What is measured is the removal energy spectrum, that is the energy needed to extract one electron from the system. Information about the removal energy spectrum of the system is given by

$$E_b(\mathbf{k}) = \omega_{\rm ph} - E_k(\mathbf{k}) - \Phi$$

where E_b is the binding energy of the electron and Φ is the work-function (essentially arising from surface effects).

A simple description of photoemission is offered by the so called three step model [3]. In this model the process is divided into the actual single-electron excitation due to the light field, the drift of the excited electrons up to the surface, and finally the emission from the surface to the analyser. More refined quantum-mechanical models (see e.g. [4]) have been also developed depicting the entire process at once (one-step model).

A common approximation made in describing photoemission processes is the sudden approximation (see e.g. [2]), where the second point of the three step model is neglected, or in different words, the electron does not perturb the system during its propagation and does not interact with the hole it left. Hence the picture becomes that of the instantaneous creation of a hole inside the material.

The system passes from its N-particle ground state $|N, 0; 0\rangle$ to the state $|N-1, m; \mathbf{k}\rangle$ corresponding to a fully-interacting (infinite sum of Slater determinants) state of N-1 electrons in the system plus plus the photoemitted electron of wave vector $\mathbf{k}$. When the sudden approximation is assumed, the many-body state $|N-1, m; \mathbf{k}\rangle \approx |N-1, m\rangle|\mathbf{k}\rangle$ is factorised in the photoemitted electron $|\mathbf{k}\rangle$ and the rest $|N-1, m\rangle$. The problem is then solved only

for the electrons of the system, disregarding the emitted particle. In this approximation, the photocurrent of the emitted electrons $\mathcal{J}_{\mathbf{k}}(\omega)$ assumes the form

$$\mathcal{J}_{\mathbf{k}}(\omega) = \sum_i |\Delta_{\mathbf{k},i}|^2 \mathcal{A}_{ii}(E_{\mathbf{k}} - \omega) \tag{1.2}$$

with $\Delta_{\mathbf{k},i}$ matrix elements and the spectral weight $\mathcal{A}_{ii}(\omega) = \langle i|\mathcal{A}(\mathbf{r},\mathbf{r}',\omega)|i\rangle$ projected onto the single-particle basis set $|i\rangle$. The quantity $\mathcal{A}_{ii}(\omega)$ reads

$$\mathcal{A}_{ii}(\omega) = \sum_m f_{im} f_{im}^* \delta(\omega - E_m) \tag{1.3}$$

with $f_{im} = \langle N,0|\hat{c}_i^\dagger|N-1,m\rangle$ the probability amplitude for the N-electron system to be excited to the m-th state of the the (N-1)-electron system. Note that, although its similarity with (1.1), in this expression states $|N,0\rangle$ and $|N-1,m\rangle$ are fully interacting many-body states.

In an independent-particle picture, each many-body state is represented by one single Slater determinant. The creation of a hole in the state $|i\rangle$, that is the exclusion of the state $|i\rangle$, in the construction of the determinant, does not change the other single-particle states. The state $\hat{c}_i|N,0\rangle = |N-1,i\rangle$ is constructed with the N lowest energy states with the exception of the state $|i\rangle$. Therefore only one state $|N-1,m\rangle$ is accessible, namely the one for which $m = i$. Correspondingly $f_{im}^{IP} = f_i \delta_{im}$ and the spectral function $\mathcal{A}_{ii}(\omega)$ reduces to a delta-function at energy

$$E_i^{IP} = E_0^{N\,IP} - E_i^{N-1\,IP}$$

If one allows electrons to interact, then the IP delta-peak broadens and loses part of its spectral weight, becoming what is called a quasiparticle peak. Even though the energy of the peak is shifted with respect to the IP peak, one can often establish a one-to-one correspondence between the two. The broadening of the quasiparticle peak is inversely proportional to the lifetime of the excitation (and indeed it is infinite in the independent-particle picture). The weight lost by the peak because of the broadening is moved to extra structures appearing at higher binding energies: the satellites which have no equivalent in the IP picture. A comparison between the independent-particle and an interacting spectral-function is given in Fig. 1.4.

Let us give a qualitative example: let us imagine that the creation of the hole in the state $|i\rangle$ is coupled with a bosonic excitation (for example a plasmon) of energy $\tilde{\omega}$. The probability amplitude $f_{im} \neq 0$ for several states labelled $m = i_0, i_1, i_2, ...$ each corresponding to a different (N-1)-electron state with a hole in $|i\rangle$. At a first level of approximation, these states can be described as corresponding to the creation of the hole alone $|N-1,i_0\rangle$, the creation of the hole plus the excitation of one boson $|N-1,i_1\rangle$, plus two bosons $|N-1,i_2\rangle$, and so on. The spectral function $\mathcal{A}_{ii}(\omega)$ has peaks at energies

$$\begin{aligned} E_0^N - E_{i_0}^{N-1} &= E_{i_0} \\ E_0^N - E_{i_1}^{N-1} &= E_{i_1} \approx E_{i_0} - \tilde{\omega} \\ E_0^N - E_{i_2}^{N-1} &= E_{i_2} \approx E_{i_0} - 2\tilde{\omega} \end{aligned}$$

and so on.

This is exactly what is observed, for example, in bulk Si [5]. In Fig. 1.5 I report the integrated spectral function $\mathcal{A}(\omega) = \sum_i \mathcal{A}_{ii}(\omega)$ of the photoemission spectrum from the

valence bands of Si at photon energy $\omega_{\rm ph} = 800$ eV. The first peaks, with a binding energy between 0 and -12 eV, correspond to three quasiparticle peaks (E_{i_0}, E_{j_0} and E_{k_0}). Beyond them, other structures are visible at integer multiples of the plasmon frequency $\tilde{\omega} \sim 16$ eV: the first group of satellites are approximately at energies $E_{i_0} - \tilde{\omega}$,$E_{j_0} - \tilde{\omega}$, $E_{k_0} - \tilde{\omega}$ and similarly for farther satellites. Their presence is a clear sign of the coupling between different excitations of the system, that is of the dynamical effects in the photoemission process.

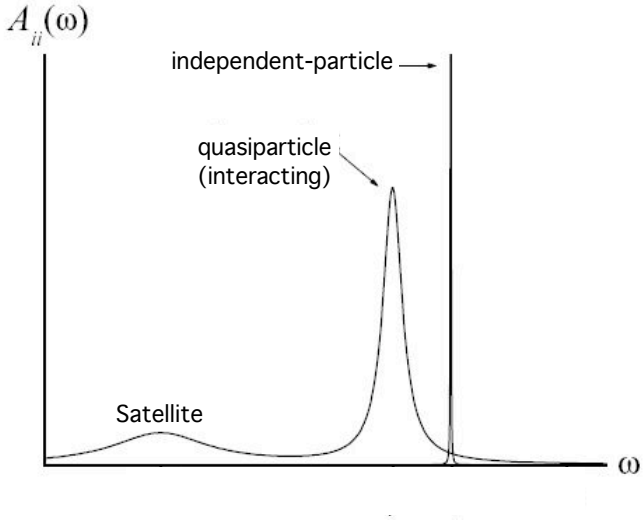

Figure 1.4: In the independent-particle picture the spectral function $\mathcal{A}_{ii}(\omega)$ is a delta-function. When the interaction between electrons is included, the peak is shifted (quasiparticle peak) and broadened. Correspondingly satellite structures arise at higher energy. Image taken from [1].

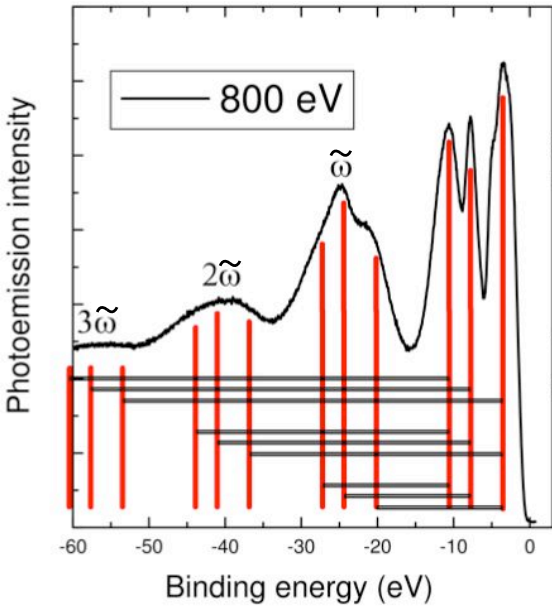

Figure 1.5: Valence band photoemission spectrum of Si measured at $\omega_{\rm ph} = 800$ eV. Satellites are observed distances $n\tilde{\omega}$ from the quasiparticle peaks. Here $n = 1, 2, 3$ and $\tilde{\omega} \sim 16$ eV is the plasmon energy. Image kindly given by M. Guzzo [5] and F. Sirotti [6].

1.3.2 Light absorption and multiple exciton generation

A basic set up of an absorption experiment is quite simple: from one side of the sample, the source irradiates a target of thickness d and from the other side, in axis with the beam, an analyser (such as a photodiode) measures the intensity of the transmitted field. Knowing the intensity $I_0(\omega)$ of the radiation before the sample, and the transmitted intensity $I(\omega)$, the extinction coefficient

$$\kappa(\omega) = \frac{c}{2d\omega} \log\left[\frac{I_0(\omega)}{I(d,\omega)}\right] \quad \text{with } c \text{ speed of light in vacuum} \tag{1.4}$$

can be measured. Structures of $\kappa(\omega)$ individuate energies where light is absorbed to excite the system.

In an independent particle picture, light absorption takes the form of Fermi's golden rule (1.1) where the initial state $|i\rangle = |v, \mathbf{k}\rangle$ is in the valence band with energy $E_i = E_v(\mathbf{k})$, and the final conduction state $|f\rangle = |c, \mathbf{k} + \mathbf{q}\rangle$ has energy $E_f = E_c(\mathbf{k} + \mathbf{q})$. $\mathbf{q}$ is the momentum transferred from the radiation field to the sample ($\mathbf{q} \approx 0$ in optical absorption). In this

picture each peak of the spectrum can be directly related with the band structure of the material (cfr. section 6.4.2 and subsequent).

But the real scenario is much more complicated: a more correct interpretation of the process implies the simultaneous creation of an electron and a hole. Each of the two particles may be described separately, as discussed in the case of photoemission (broad quasiparticle peak, plasmon satellites), but in addition the two particles (of different charge) attract each other. They form a neutral state: the *e-h* pair called also exciton. The exciton interacts as a whole with the other electrons of the system; its energy E_{exc} can be transferred to other excitations.

For example let us imagine an exciton coupled with a boson reservoir (e.g. other excitons) which need an energy E_λ to be excited. The possible spectrum of the creation of the excitonic state could be

$$\begin{aligned} E_{\text{exc}} \quad & \text{if no additional exciton is created, or} \\ E_{\text{exc}} + E_\lambda \quad & \text{if one additional exciton is created, or} \\ E_{\text{exc}} + 2E_\lambda \quad & \text{if two additional excitons are created,...} \end{aligned}$$

and so on, similarly to what seen in the photoemission case. Similarly we can imagine that a photon of high energy ω'_{ph} is absorbed by an exciton of energy E_{vc}. Successively the high energy exciton may decay transferring part of its energy to the boson reservoir hence exciting one or more bosons of energy E_λ. Therefore the same photon ω'_{ph} may give rise to different final states of energy

$$\begin{aligned} E_{vc} \quad & \text{one high energy exciton state, or} \\ (E_{vc} - E_\lambda) + E_\lambda \quad & \text{one energetic exciton and one boson, or} \\ (E_{vc} - 2E_\lambda) + 2E_\lambda \quad & \text{one exciton and two bosons,...} \end{aligned}$$

This scheme depicts what happens in the multiple exciton generation process, where the boson reservoir is composed by other excitons.

In Chapter 5 a more appropriate formalism is introduced and in Chapter 10 these concepts are developed on a more rigorous way constituting the theoretical developments of this work.

1.4 Multiple exciton generation and solar energy production

What is described qualitatively at the end of the last section is the fact that the dynamical coupling between electron-hole excitations may give rise to multiple excitation processes. Of this kind is the multiple exciton generation (MEG).

The main process leading to MEG in real materials is the so called impact ionization [7], which can be schematically described in two steps depicted in Fig. 1.6. A first step is the creation of one single exciton $|vc\rangle$ of energy $E_{vc}^{(1)}$ due to the absorption of a high energy photon. At a second step, scattering events take place between the "hot" exciton and the other particles of the system. Consequently, a part $E_{v'c'}$ of its energy can be transferred to the system with a resulting creation of another exciton of energy $E_{v'c'}$, while the first one is now left with energy $E_{vc}^{(2)} = E_{vc}^{(1)} - E_{v'c'}$. For this process to happen, the earliest exciton energy must be at least $E_{vc}^{(1)} > 2E_{\text{gap}}$ with E_{gap} the optical gap

of the system, but the phenomenon starts usually to be appreciable at higher photon energies [8, 9]. If the energy $E_{vc}^{(1)}$ is high enough, impact ionization can occur many times.

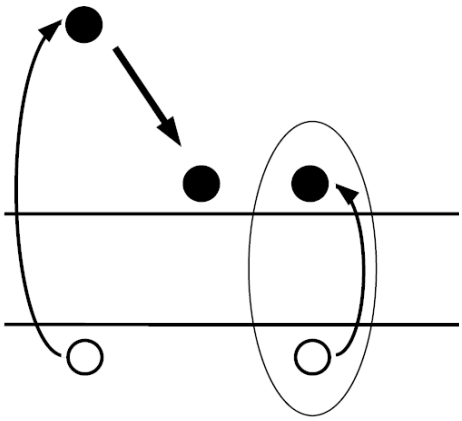

Figure 1.6: Pictorial representation of the impact ionization process: first a high-energy exciton is created, successively it looses part of its energy to create an additional e-h pair.

This process is not the only way for an exciton to decay: the exciton may transfer energy to other excitations, like phonons, and, most important, e-h hole recombination may be favoured. However in confined system and especially in nanostructured materials (see e.g. [9–11]) the exciton generation may involve a charge transfer process, i.e. the electron and the hole of the e-h pair are localised in different regions of the material, for instance in two neighbouring nanoparticles. This charge separation actually hinders the direct recombination of the e-h pair, and other channels of de-excitation, such as MEG, become more probable.

These two ingredients (the charge separation and the enhancement of MEG rate) make nanostructured materials excellent candidates for the production of efficient solar cells. The ideal HOMO-LUMO gap of a solar device should be in the range 1-1.6 eV, in order to absorb light where the solar spectrum attains its maximum intensity. MEG is believed to improve significantly the solar conversion efficiency [7, 10, 12] because it may ensure a higher charge carrier production rate, even in low intensity regions of the solar emission spectrum.

Theoretical works devoted to the prediction of the lifetime [10], exciton generation rates [13], conversion efficiencies [7] carrier multiplication rates or the free carrier density have been carried on, but no quantitative prediction of the full absorption spectrum in presence of MEG has been given. As explained in this introduction, the correct description of MEG passes through the correct description of dynamical effects in the e-h interaction.

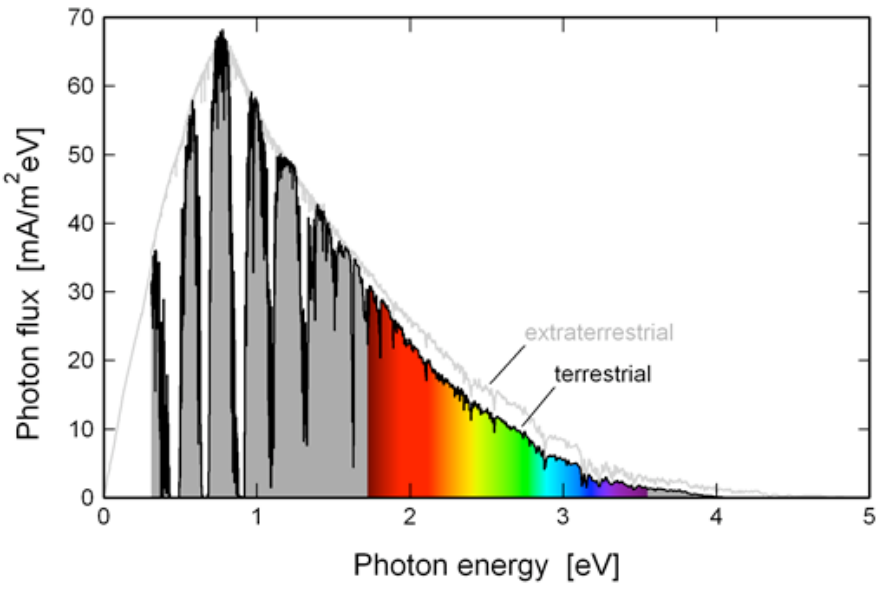

Figure 1.7: Solar emission spectrum. Image taken from [14].

In this thesis I show the performances and limitations of today's state-of-the-art calculations of optical spectra taking the example of $SrTiO_3$ (Chapter 6), I discuss dynamical effects in electronic spectra of carbon nanostructures (Chapters 7 and 8), I introduce methodological developments for a more efficient and precise description of these effects (Chapter 9) and I develop a new theoretical approach to the *ab-initio* description of dynamical effects in absorption spectra, and hence, amongst other phenomena, to the prediction of MEG.

Part I

Ab initio theoretical spectroscopy

Chapter 2

Dielectric theory and theoretical spectroscopy

This chapter is devoted to the connection between the microscopic description of the dielectric properties of a material and their macroscopic description in terms of measurable fields.

Starting from Maxwell's equation in matter, and assuming a linear response of the material, I will introduce the microscopic dielectric tensor which connects the external field to the total field.

In order to link the microscopic description with a macroscopic picture, the macroscopic average of microscopic components of a field is then defined rigorously on a periodic lattice. This will lead me to the definition of the macroscopic dielectric function which I will eventually link to the microscopic dielectric function through equation (2.19)*.*

Once the micro-macro connection in the context of dielectric theory is established, I will give a general presentation of electron energy loss spectroscopy and absorption spectroscopy, with particular emphasis on what is measured in experiments and its link to the dielectric properties of the matter.

2.1 An introduction to dielectric theory

2.1.1 The microscopic dielectric constant

The microscopic Maxwell's equations in presence of matter read, in the Fourier space,

$$\mathbf{k} \times \mathbf{E}(\mathbf{k},\omega) = \frac{\omega}{c}\mathbf{B}(\mathbf{k},\omega) \tag{2.1}$$

$$\mathbf{k} \times \mathbf{H}(\mathbf{k},\omega) = -i\frac{4\pi}{c}\mathbf{J}_{\text{ext}}(\mathbf{k},\omega) - \frac{\omega}{c}\mathbf{D}(\mathbf{k},\omega) \tag{2.2}$$

$$\mathbf{k} \cdot \mathbf{D}(\mathbf{k},\omega) = -i4\pi\rho_{\text{ext}}(\mathbf{k},\omega) \tag{2.3}$$

$$\mathbf{k} \cdot \mathbf{B}(\mathbf{k},\omega) = 0 \tag{2.4}$$

where c is the speed of light and the dielectric displacement $\mathbf{D}$ and the magnetization field $\mathbf{H}$ are defined by their constitutive relations

$$\mathbf{D}(\mathbf{k},\omega) := \mathbf{E}(\mathbf{k},\omega) + 4\pi\mathbf{P}(\mathbf{k},\omega) \qquad \text{and} \qquad \mathbf{H}(\mathbf{k},\omega) := \mathbf{B}(\mathbf{k},\omega) - 4\pi\mathbf{M}(\mathbf{k},\omega)\ . \tag{2.5}$$

In writing the two equations (2.5) a distinction is made between the induced fields ($\mathbf{P}$ and $\mathbf{M}$), the external fields ($\mathbf{D}$ and $\mathbf{H}$) and the total fields inside the material ($\mathbf{E}$ and $\mathbf{B}$).

The polarization field, expressed as a functional $\mathbf{P}[\mathbf{E}]$ of the total field, is self-consistently related to $\mathbf{E}$.

For low intensities of the total field $\mathbf{E}$, a linear response can be assumed, consequently the electric displacement reads

$$\mathbf{D}(\mathbf{k},\omega) = \int \overleftrightarrow{\epsilon}(\mathbf{k},\mathbf{k}',\omega)\mathbf{E}(\mathbf{k}',\omega)d\mathbf{k}' \tag{2.6}$$

which defines the microscopic dielectric tensor $\overleftrightarrow{\epsilon}(\mathbf{k},\mathbf{k}',\omega)$.

2.1.2 Longitudinal-longitudinal framework

The equations above are expressed in a Cartesian system of reference. However, in order to reduce the complexity of the problem, it is convenient to leave such a system of reference in favour of a longitudinal-transverse reference.

Be $\mathbf{A}(\mathbf{k})$ a (vectorial) quantity depending on $\mathbf{k}$ ($k = |\mathbf{k}|$), and be $\hat{\mathbf{k}} = \mathbf{k}/k$ the unitary vector (versor) pointing in the direction of $\mathbf{k}$, then the vector $\mathbf{A}$ can be decomposed into a longitudinal part $\mathbf{A}^L(\mathbf{k}) := \hat{\mathbf{k}}[\hat{\mathbf{k}} \cdot \mathbf{A}(\mathbf{k})]$ and a transverse part $\mathbf{A}^T(\mathbf{k}) := \mathbf{A}(\mathbf{k}) - \hat{\mathbf{k}}A^L(\mathbf{k})$, where $A^L = |\mathbf{A}^L|$.

Decomposing $\mathbf{D}$ and $\mathbf{E}$ on this system of reference, equation (2.6) reads

$$\mathbf{D}^\nu(\mathbf{k},\omega) = \sum_{\mu=L,T} \int \tilde{\epsilon}^{\nu\mu}(\mathbf{k},\mathbf{k}',\omega)\mathbf{E}^\mu(\mathbf{k}',\omega)d\mathbf{k}' \quad \text{with} \quad \nu = L \text{ or } T \tag{2.7}$$

where the dielectric tensor written in this system of reference $\tilde{\epsilon}$ is a matrix of components[2]

$$\tilde{\epsilon}(\mathbf{k},\mathbf{k}',\omega) = \begin{pmatrix} \tilde{\epsilon}^{LL}(\mathbf{k},\mathbf{k}',\omega) & \tilde{\epsilon}^{LT}(\mathbf{k},\mathbf{k}',\omega) \\ \tilde{\epsilon}^{TL}(\mathbf{k},\mathbf{k}',\omega) & \tilde{\epsilon}^{TT}(\mathbf{k},\mathbf{k}',\omega) \end{pmatrix} .$$

In particular, if one focuses on the longitudinal-longitudinal framework, only scalar quantities are involved and the expressions are simplified. The electric field in general is given by the scalar potential V_{tot} and by the vector potential $\mathbf{A}$ according to

$$\mathbf{E}(\mathbf{k},\omega) = i\omega\mathbf{A}(\mathbf{k},\omega) - i\mathbf{k}V_{\text{tot}}(\mathbf{k},\omega) .$$

Setting the vector potential to zero[3], only the longitudinal component $-i\mathbf{k}V_{\text{tot}}(\mathbf{k},\omega)$ is left and $\mathbf{E}(\mathbf{k}) = \mathbf{E}^L(\mathbf{k}) = -i\mathbf{k}V_{\text{tot}}(\mathbf{k})$. The longitudinal component of $\mathbf{D}(\mathbf{k})$ is then obtained from expression (2.7):

$$\mathbf{D}^L(\mathbf{k},\omega) = \int \tilde{\epsilon}^{LL}(\mathbf{k},\mathbf{k}',\omega)\mathbf{E}^L(\mathbf{k}',\omega)d\mathbf{k}'. \tag{2.8}$$

[2]Note that taking the Cartesian axis z along $\mathbf{k}$, longitudinal components are all parallel to z. Correspondingly $\tilde{\epsilon}^{LL}$ is scalar. Transverse components, on the other hand, lay on the xy plane, so $\tilde{\epsilon}^{LT}$ and $\tilde{\epsilon}^{TL}$ are a row and a column vectors of 2 components and $\tilde{\epsilon}^{TT}$ is a 2×2 matrix.

[3]In the LT reference system the electric field decomposes

$$\mathbf{E}^L(\mathbf{k},\omega) = i\omega\hat{\mathbf{k}}\left[\hat{\mathbf{k}} \cdot \mathbf{A}(\mathbf{k},\omega)\right] - i\mathbf{k}V_{\text{tot}}(\mathbf{k},\omega) \quad \text{and} \quad \mathbf{E}^T = \left[i\omega\hat{\mathbf{k}} \times \mathbf{A}\right]^T$$

from which one sees that $\mathbf{A} = 0$ gives a purely longitudinal electric field.

One can now introduce an external potential V_{ext} such that $\mathbf{D}(\mathbf{k},\omega) = -i\mathbf{k}V_{\text{ext}}(\mathbf{k},\omega)$; by defining $\epsilon(\mathbf{k},\mathbf{k}',\omega) = \frac{k'}{k}\tilde{\epsilon}^{LL}(\mathbf{k},\mathbf{k}',\omega)$, equation (2.8) becomes a scalar equation linking the two potentials

$$V_{\text{ext}}(\mathbf{k},\omega) = \int \epsilon(\mathbf{k},\mathbf{k}',\omega)V_{\text{tot}}(\mathbf{k}',\omega)d\mathbf{k}' \ . \tag{2.9}$$

The last equation (2.9) is one of the crucial passages of this chapter: the longitudinal-longitudinal dielectric function $\epsilon(\mathbf{k},\mathbf{k}',\omega)$ is here defined as the ratio between the external and the total potentials. This quantity can be computed from *ab-initio* techniques which will be explained more in detail in Chapters 4 and 5. The interest of this chapter is bridging the gap between the microscopic description of the dielectric properties of a material and the macroscopic potentials measured in real experiments. The main result of the microscopic description of matter is equation (2.9).

Let us now tackle the macroscopic framework.

2.1.3 Macroscopic average of microscopic quantities

The physics we want to describe is that of a sample perturbed by an external field which is controlled and characterised up to a certain extent by the experimentalist. The electrons of the sample react to the perturbation establishing an induced field inside the material which adds to the perturbation. In formulae,

$$\mathbf{E}_{\text{tot}} = \mathbf{E}_{\text{ext}} + \mathbf{E}_{\text{ind}} \ . \tag{2.10}$$

The external field $\mathbf{E}_{\text{ext}}$ is what the observer uses to probe the system. Therefore it varies on a macroscopic scale. On the other hand, the induced field reacts to very microscopic variations and $\mathbf{E}_{\text{ind}}$ is consequently and intrinsically a microscopic field. The same is valid for the measured (total) field $\mathbf{E}_{\text{tot}}$, because it contains the induced field, even though only macroscopic components of $\mathbf{E}_{\text{tot}}$ are actually measured.

If the Fourier component of a field (let us take $\mathbf{E}_{\text{tot}}(\mathbf{k})$) is such that $2\pi/k \gg a$ where a is a typical length of the atomic structure (such as the cell parameter or an (average) nearest neighbour distance), then the component $\mathbf{E}_{\text{tot}}(\mathbf{k})$ is said to be macroscopic, otherwise it is microscopic. With these definitions we can now give a more rigorous definition of what is a macroscopic average of the microscopic components.

Macroscopic average in periodic systems

Since I will always treat periodic systems throughout the next chapters, I will give a definition of macroscopic average in such systems. Moreover I will split a generic wave vector $\mathbf{k} = \mathbf{q}+\mathbf{G}$ into a long-wavelength component $\mathbf{q}$, continuously varying inside the first Brillouin zone, and short-wavelength component $\mathbf{G}$. Accordingly the compact notation $A(\mathbf{k}) = A_{\mathbf{G}}(\mathbf{q})$ will be introduced .

Let us take the generic scalar potential $A(\mathbf{r},\omega)$ which varies rapidly inside a cell volume, and let us define $\mathbf{R}$ as the position in space of the center of the cell, then the macroscopic average of A is

$$A_M(\mathbf{R},\omega) = \langle A(\mathbf{r},\omega)\rangle_{\mathbf{R}} = \frac{1}{\mathcal{V}_{\text{cell}}}\int_{\mathcal{V}(\mathbf{R})} A(\mathbf{r},\omega)d\mathbf{r} \tag{2.11}$$

where $\mathcal{V}_{\text{cell}}$ is the volume of the unitary cell and the integral is performed inside the unitary cell centred in $\mathbf{R}$. At a microscopic scale, $\mathbf{R}$ is a discrete variable, but at a macroscopic scale it varies continuously.

Let us now pass to the reciprocal space:

$$A(\mathbf{r},\omega) = \frac{1}{(2\pi)^3}\sum_{\mathbf{G}}\int A_{\mathbf{G}}(\mathbf{q},\omega)e^{i(\mathbf{q}+\mathbf{G})\cdot\mathbf{r}}d\mathbf{q} = \frac{1}{(2\pi)^3}\int A(\mathbf{q},\omega;\mathbf{r})e^{i\mathbf{q}\cdot\mathbf{r}}d\mathbf{q}$$

where the function

$$A(\mathbf{q},\omega;\mathbf{r}) = \sum_{\mathbf{G}} A_{\mathbf{G}}(\mathbf{q},\omega)e^{i\mathbf{G}\cdot\mathbf{r}} \ . \tag{2.12}$$

is the sum of all microscopic components, each of which has at least the period of the cell.

The macroscopic average in Fourier space is then defined analogously to (2.11)

$$A_M(\mathbf{q},\omega) = \langle A_M(\mathbf{q},\omega;\mathbf{r})\rangle_{\mathbf{R}} = \frac{1}{\mathcal{V}_{\text{cell}}}\int_{\mathcal{V}(\mathbf{R})} A(\mathbf{q},\omega;\mathbf{r})d\mathbf{r} \ . \tag{2.13}$$

Remembering the definition (2.12) and exploiting the periodicity in real space of $A(\mathbf{q},\omega;\mathbf{r})$, expression (2.14) eventually reduces to

$$A_M(\mathbf{q},\omega) = A_0(\mathbf{q},\omega) \tag{2.14}$$

since only the integral of the $\mathbf{G}=0$ component does not vanish.

2.1.4 Micro-macro connection

We have now all the ingredients to establish the link between dielectric properties at a microscopic scale and at a macroscopic scale.

I rewrite the microscopic relation (2.9) in the case of a periodic system

$$V_{\text{ext}}^{\mathbf{G}}(\mathbf{q},\omega) = \sum_{\mathbf{G}'}\epsilon_{\mathbf{G}\mathbf{G}'}(\mathbf{q},\omega)V_{\text{tot}}^{\mathbf{G}'}(\mathbf{q},\omega) \ . \tag{2.15}$$

In the context of spectroscopy, the external field is purely macroscopic, hence the last equation reads

$$V_{\text{ext}}^{0}(\mathbf{q},\omega) = \sum_{\mathbf{G}'}\epsilon_{0\mathbf{G}'}(\mathbf{q},\omega)V_{\text{tot}}^{\mathbf{G}'}(\mathbf{q},\omega) \ . \tag{2.16}$$

Then one defines the macroscopic dielectric function $\epsilon_M(\omega)$ as the scalar function satisfying the relation

$$V_{\text{ext}}^{0}(\mathbf{q},\omega) = \epsilon_M(\mathbf{q},\omega)V_{\text{tot}}^{0}(\mathbf{q},\omega) \ . \tag{2.17}$$

Note that this is the definition of the macroscopic dielectric function.

The micro-macro connection is accomplished when $\epsilon_M(\omega)$ is written in terms of $\epsilon_{\mathbf{G}\mathbf{G}'}(\mathbf{q},\omega)$. One might try to consider only the $\mathbf{G}'=0$ component in (2.16), but in this way all microscopic components of $V_{\text{tot}}^{\mathbf{G}'}(\mathbf{q},\omega)$ are neglected (neglect of local fields, cfr. Chapter 4.5.3). Instead, one can account for all $\mathbf{G}'$ by inverting (2.16):

$$V_{\text{tot}}^{0}(\mathbf{q},\omega) = \epsilon_{00}^{-1}(\mathbf{q},\omega)V_{\text{ext}}^{0}(\mathbf{q},\omega) \ . \tag{2.18}$$

and consequently

$$\epsilon_M(\mathbf{q},\omega) = \frac{1}{\epsilon_{00}^{-1}(\mathbf{q},\omega)} \tag{2.19}$$

2.1.5 Why longitudinal framework?

For some kind of spectroscopic techniques, as electron energy loss spectroscopy (EELS), the perturbation and the response are indeed longitudinal and the use of the LL framework is completely justified at any wave vector $\mathbf{q}$.

Instead, in the case of light absorption, the perturbation is a transverse field. The transverse case though is much more difficult to treat. At the present date, few reliable calculations of optical spectra have been done in this framework.

However, if the transferred momentum is negligible ($\mathbf{q} \approx 0$, optical transitions), then transverse and longitudinal parts can be related one to the other. In this limit, and in the case of cubic symmetry (isotropic materials), the transverse and the longitudinal part coincide. For lower-symmetry crystals, one can still compute the transverse-transverse components from a longitudinal-longitudinal component, but some care must be paid on the direction along which the limit $\mathbf{q} \to 0$ is taken.

2.2 Connection with some spectroscopic technique: EELS and absorption

2.2.1 Angle-resolved electron energy loss spectroscopy

The electron energy loss spectroscopy (EELS) consists in impinging on the sample with a beam of electrons. The source (e.g., a transmission electron microscope) irradiates a beam of fast, but still non-relativistic, electrons (kinetic energy ~ 100 keV) onto a thin sample. If sufficiently broad, the electron beam can be modelled by a single plane wave of wave vector $\mathbf{k}$ and energy $E = k^2/2$.

Because of the high kinetic energy of the electrons of the beam, exchange effects between the electrons of the system and the perturbing field can be neglected. The interaction is therefore approximated with the classical Hartree interaction between the electron density ρ_{int} of the system and that of the electron beam ρ_{ext}. The Hartree potential felt by the electrons of the system at the point $\mathbf{r}$ is

$$V_H(\mathbf{r}) = \int \frac{\rho_{\text{ext}}(\mathbf{r}')}{|\mathbf{r} - \mathbf{r}'|} d\mathbf{r}' \ .$$

Far from the sample an analyser collects the outgoing electrons within a solid angle $d\Omega$. The exit kinetic energy $E_{k'} = k'^2/2$ of the scattered electrons is also measured within a precision dE. The set up allow then for a measurement of the exchanged momentum $(\mathbf{q} + \mathbf{G}) = \mathbf{k} - \mathbf{k}'$ and exchanged energy $\omega = E_k - E_{k'}$, $\mathbf{G}$ being a reciprocal space vector assuring crystal momentum conservation.

From these elements one can compute the inelastic differential cross section (see e.g. [15, 16]), $\frac{\partial^2\sigma}{\partial\Omega\partial\omega}$ defined as the probability for an electron of initial wave vector $\mathbf{k}$ to be scattered into a state of wave vector $\mathbf{k}'$ within a solid angle $d\Omega$ losing an energy $\omega \pm dE/2$

$$\frac{\partial^2\sigma}{\partial\Omega\partial\omega} = \frac{k'}{k} \left[\frac{1}{4\pi} v(\mathbf{q} + \mathbf{G})\right]^2 S_{\mathbf{G}}(\mathbf{q}, \omega) \ ,$$

where $v(\mathbf{q}+\mathbf{G}) = 4\pi/|\mathbf{q}+\mathbf{G}|^2$ is the Coulomb potential and $S_{\mathbf{G}}(\mathbf{q}, \omega)$ is the dynamical structure factor. It describes the properties of the sample and it does not depend on the electron beam nor on the interaction potential between the scatterer and the incident electrons.

The dynamic structure factor $S_{\mathbf{G}}(\mathbf{q},\omega)$ can be generalised [17] to the matrix

$$S_{\mathbf{G}\mathbf{G}'}(\mathbf{q},\omega) = \frac{1}{2\pi}\int e^{i\omega\tau}\langle 0|\hat{n}(\mathbf{q}+\mathbf{G},\tau)\hat{n}^{+}(\mathbf{q}+\mathbf{G}',0)|0\rangle d\tau$$

which is a density-density correlation function, with $\hat{n}$ density operator in the Heisemberg picture. The dynamical structure factor is the diagonal $S_{\mathbf{G}}(\mathbf{q},\omega) = S_{\mathbf{G}\mathbf{G}}(\mathbf{q},\omega)$.

Through a generalization of the fluctuation-dissipation theorem [16, 18] it is finally possible to link S to the inverse dielectric function ϵ^{-1} according to

$$S_{\mathbf{G}\mathbf{G}'}(\mathbf{q},\omega) = -\frac{|\mathbf{q}+\mathbf{G}|^2}{4\pi^2}\Im[\epsilon^{-1}_{\mathbf{G}\mathbf{G}'}(\mathbf{q},\omega)]$$

which leads to a differential cross section

$$\frac{\partial^2\sigma}{\partial\Omega\partial\omega} = -\frac{k'}{k}\frac{1}{16\pi^3}v(\mathbf{q}+\mathbf{G})\Im[\epsilon^{-1}_{\mathbf{G}\mathbf{G}}(\mathbf{q},\omega)]\ . \tag{2.20}$$

The latter equation contains the important result of this small revision of the EEL spectroscopy: the differential cross section gives access to the diagonal elements of the inverse (longitudinal-longitudinal) microscopic dielectric function.

For an exhaustive introduction on EELS we refer the reader to [19].

2.2.2 Light absorption

The propagation of the electromagnetic radiation inside a material is completely described by the refractive index $\mathbf{n}$, a vector with complex entries, related to the dielectric properties through Fresnel's equation.

In the case of an isotropic material (e.g. cubic crystal), Fresnel's equation reduces to a scalar equation[4] which is solved by the complex refractive index $n(\omega)$

$$\sqrt{\epsilon_M(\omega)} = n(\omega) = \nu(\omega) + i\kappa(\omega) \tag{2.21}$$

After travelling a distance z inside an absorbing isotropic medium, the intensity $I(z,\omega)$ of a monochromatic wave

$$\mathbf{E}(z,t) = \mathbf{E}(n,\omega)e^{-i\omega(t-\frac{\nu}{c}z)}e^{-\frac{\omega}{c}\kappa z}$$

is damped to

$$I(z,\omega) = |\mathbf{E}(z,t)|^2 = I_0(\omega)e^{-2\frac{\omega}{c}\kappa(\omega)z}$$

where $I_0(\omega) = |\mathbf{E}(\omega)|^2$ is the intensity of the radiation at $z = 0$ (for instance at the sharp surface of the sample) and c is the speed of light in vacuum.

If d is the travelled distance, the imaginary part of the refractive index is measured according to formula (1.4). $\nu(\omega)$ and $\kappa(\omega)$ are connected by the Kramers-Kronig relations

$$\nu(\omega) = 1 + \frac{2}{\pi}\mathcal{P}\int_0^\infty \frac{\kappa(\omega')}{\omega'-\omega}d\omega' \quad \text{and} \quad \kappa(\omega) = -\frac{2}{\pi}\mathcal{P}\int_0^\infty \frac{\nu(\omega')-1}{\omega'-\omega}d\omega' \tag{2.22}$$

[4]For non isotropic materials, Fresnel's equation is a polynomial equation of the fourth order in each Cartesian component of $\mathbf{n}(\omega)$. The relation linking $\mathbf{n}(\omega)$ to the dielectric tensor is therefore much more complicated.

where $\mathcal{P}$ denotes the Cauchy principal value. Through the Kramers-Kronig relations, one can measure only one of the two optical functions over a wide range of energies and reconstruct the second. The full refractive index $n(\omega)$ is then obtained and so is the macroscopic dielectric function $\epsilon_M(\mathbf{q},\omega)|_{\mathbf{q}=0}$ at vanishing $\mathbf{q}$ (optical absorption).

So the measure of κ gives access to the imaginary part of ϵ_M, or, because of (2.19),

$$Abs(\omega) = \lim_{\mathbf{q}\to 0} \Im[\epsilon_M(\mathbf{q},\omega)] = \lim_{\mathbf{q}\to 0} \Im\left[\frac{1}{\epsilon_{00}^{-1}(\mathbf{q},\omega)}\right] . \tag{2.23}$$

2.3 Summary

In this Chapter three important results have been obtained. They will be used throughout the entire work, it is therefore worthwhile to summarise them here.

- From microscopic Maxwell's equation in matter, the microscopic dielectric tensor has been defined. Working in a purely longitudinal framework, the definition of the dielectric function
$$V_{\text{ext}}^{\mathbf{G}}(\mathbf{q},\omega) = \sum_{\mathbf{G}'} \epsilon_{\mathbf{G}\mathbf{G}'}(\mathbf{q},\omega) V_{\text{tot}}^{\mathbf{G}'}(\mathbf{q},\omega) \tag{2.15}$$
has been given.

- Once I have introduced the concept of macroscopic average over microscopic components, the definition of the macroscopic dielectric function has been introduced:
$$V_{\text{ext}}^{0}(\mathbf{q},\omega) = \epsilon_M(\mathbf{q},\omega) V_{\text{tot}}^{0}(\mathbf{q},\omega) . \tag{2.17}$$

- The connection between microscopic and macroscopic dielectric properties is finally found accounting for all microscopic components of $V_{\text{tot}}^{\mathbf{G}}(\mathbf{q},\omega)$ (local fields).
$$\epsilon_M(\mathbf{q},\omega) = \frac{1}{\epsilon_{00}^{-1}(\mathbf{q},\omega)} . \tag{2.19}$$

Moreover two spectroscopic techniques have been briefly introduced. They give direct access to the dielectric properties. The main relations (neglecting prefactors) are

$$EELS(\mathbf{q},\omega) = -\Im\left[\epsilon_{\mathbf{G}\mathbf{G}}^{-1}(\mathbf{q},\omega)\right] \left(= -\Im\left[\frac{1}{\epsilon_M(\mathbf{q},\omega)}\right] \text{ if } \mathbf{G}=0\right) \tag{2.24}$$

$$Abs(\omega) = \lim_{\mathbf{q}\to 0} \Im\left[\frac{1}{\epsilon_{00}^{-1}(\mathbf{q},\omega)}\right] = \lim_{\mathbf{q}\to 0} \Im\left[\epsilon_M(\mathbf{q},\omega)\right] \tag{2.25}$$

Chapter 3

Density-Functional Theory

In this chapter I will briefly revise Density-Functional Theory. It was introduced in the mid sixties by Hohemberg, Kohn and Sham [20, 21], and is one of the most fruitful theories in electronic structure calculations.

I will touch on its conceptual justification, explaining its fundamental theorems and highlighting their implications. Then I will focus on the Kohn-Sham system, which maps the interacting many body problem onto a non-interacting N-particle problem which has the same electron density as the real system.

To this aim, a non-interacting Hamiltonian is defined via the introduction of an effective potential that has to be approximated. I will present one of the most widely used approximations, the Local Density Approximation (LDA), which will be employed in all calculations presented in this thesis.

Finally I will show that a physical interpretation of electronic properties based on the Kohn-Sham system, together with the prediction of quantities else than the ground state density, is often reasonable, although not rigorously justified. The independent-particle picture of the Kohn-Sham system rarely gives quantitatively accurate results for excited states, and one has to go beyond DFT.

3.1 Solving the many-body problem

The problem of predicting all the properties of a non-relativistic N-electron system in presence of a static background[5] is equivalent to that of solving the Schrödinger equation $\hat{H}\Psi_k = E_k\Psi_k$ with the Hamiltonian

$$\hat{H} = -\frac{1}{2}\sum_{i=1}^{N}\nabla_i^2 + \sum_{i=1}^{N} V_{\mathrm{bgr}}(\mathbf{r}_i, \{\tilde{\mathbf{r}}\}) + \frac{1}{2}\sum_{i\neq j}\frac{1}{|\mathbf{r}_i - \mathbf{r}_j|}\,. \tag{3.1}$$

The Hamiltonian of the N-electron system is the sum of the kinetic energy $\frac{1}{2}\nabla_i^2$ of each electron, the background potential $V_{\mathrm{bgr}}(\mathbf{r}_i, \{\tilde{\mathbf{r}}\})$ characterised by a set of parameters $\{\tilde{\mathbf{r}}\}$ (typically the position of nuclei) and of the Coulomb interaction $v(\mathbf{r}_i, \mathbf{r}_j) = \frac{1}{|\mathbf{r}_i - \mathbf{r}_j|}$ between

[5] In assuming the background field to be static, I intrinsically assume the Born-Oppenheimer approximation. Atoms are kept fixed so that the electronic problem is decoupled from the nuclear problem.

all electrons excluding the self-interacting term ($i \neq j$)[6]. Note that the shape of the mutual interaction v and the kinetic term are always the same in whatever system, so the characteristics of the system are given only by the background V_{bgr}.

Solving the Schrödinger equation with (3.1) is a desperate task, but fortunately it is not compulsory. Indeed the knowledge of the N-body wave function $\Psi(\mathbf{r}_1, ..., \mathbf{r}_N)$ gives access to all possible properties of the N-particle system, which is not what one is usually looking for. In all practical situations one wants to predict the expectation value of some observable, e.g. the total energy, or to estimate some other property, such as the direct gap. The wave function of the system carries too much information with respect to real needs. Therefore one is interested in recasting the N-particle problem in a much simpler form in order to access only the observables of interest.

Reducing the complexity of the problem in order to compute only the properties of interest is the underlying philosophy of Density-Functional Theories, which are the subject of this chapter and the next one.

3.2 Foundations of Density-Functional Theory

With the works of Hohenberg and Kohn [20] and Kohn and Sham [21] in the mid sixties one of the most fruitful theories in electronic structure calculations was born:, the Density-Functional Theory (DFT). Its theoretical foundations stem from two theorems that identify the electronic density as the basic quantity for solving the many-body problem. The attention is then moved from a 3N-variable quantity $\Psi(\mathbf{r}_1, ..., \mathbf{r}_N)$ to the 3-variable quantity $\rho(\mathbf{r})$.

I will state the theorems and give a physical intuition of what they mean, but I will not prove them. For more details about the two theorems mostly all books on modern electronic theory treat DFT in a complete way. I will refer in particular to R. M. Martin's textbook *Electronic Structure: Basic Theory and Practical Methods* [22].

Theorem 1: *For any system of interacting particles in a background potential $V_{bgr}(\mathbf{r}, \{\tilde{\mathbf{r}}\})$, the potential $V_{bgr}(\mathbf{r}, \{\tilde{\mathbf{r}}\})$ is determined uniquely, except for a constant, by the ground state particle density $\rho_{gr}(\mathbf{r}, \{\tilde{\mathbf{r}}\})$.*

This theorem proves the bijective relation between the potential V_{bgr} and the ground state density ρ_{gr}. This theorem states that the whole Hamiltonian can be in principle determined by the knowledge of the ground state density ρ_{gr} because the kinetic and the electron-electron terms are universal in the sense that they do not depend on the specific system (or that is the same, on the set of parameters $\{\tilde{\mathbf{r}}\}$).

Theorem 2 : *A functional for the energy $E[\rho]$ in terms of the density $\rho(\mathbf{r})$ can be defined, valid for any background potential $V_{bgr}(\mathbf{r}, \{\tilde{\mathbf{r}}\})$. For any particular $V_{bgr}(\mathbf{r}, \{\tilde{\mathbf{r}}'\})$, the exact ground state energy of the system is the global minimum value of this functional, and the density $\rho_{gr}(\mathbf{r}, \{\tilde{\mathbf{r}}'\})$ that minimizes the functional is the exact ground state density.*

[6]The notation V_{bgr} is not standard. Usually people speak of "external field" in this context, as done by the book [22] I will refer to. Actually the term "external field" will be introduced in next chapter to designate a time-dependent perturbation. To prevent confusion, I prefer the notion of background field.

This theorem completes the previous one by offering a way to find $\rho_{\rm gr}(\mathbf{r})$. Indeed by minimising the energy functional $E[\rho]$ the ground state density is found as the density for which the functional attains its global minimum E_0. Unfortunately the energy functional $E[\rho]$ is in general unknown and one has to rely on approximations.

3.2.1 The energy functional

With the two Hohenberg and Kohn theorems, the passage from the wave function Ψ to the density is accomplished. They prove that all properties of the system can be expressed as proper functionals of the density $\rho(\mathbf{r})$, and in particular the total energy of the system is a functional of the form

$$E[\rho](\{\tilde{\mathbf{r}}\}) = \langle\Psi[\rho]|\hat{H}[\rho]|\Psi[\rho]\rangle = \int V_{\rm bgr}(\mathbf{r},\{\tilde{\mathbf{r}}\})\rho(\mathbf{r})d\mathbf{r} + F[\rho] \tag{3.2}$$

where $F = T[\rho] + W[\rho]$ is an unknown functional. It has the property of being universal, in the sense that it does not depend on the characteristics of the system (that is on the external parameters $\{\tilde{\mathbf{r}}\}$). It is composed by a the kinetic term $T[\rho] = -\langle\frac{1}{2}\sum_i \nabla_i^2\rangle$ and by an interaction term $W[\rho] = \langle\frac{1}{2}\sum_{ij}|\mathbf{r}_i - \mathbf{r}_j|^{-1}\rangle$. Both $T[\rho]$ and $W[\rho]$ are not known and they have to be approximated.

The Thomas-Fermi-Dirac functional

The homogeneous electron gas (HEG), is completely characterised by its density $\rho^{\rm HEG}$ which is constant in the whole space. Therefore the energy functional $F^{\rm HEG}[\rho] = F^{\rm HEG}(\rho)$. The functional $W[\rho] = E_H[\rho] + E_{\rm x}[\rho] + E_{\rm c}[\rho]$ can be separated into a Hartree (classical) term, a Fock (exchange) term and a correlation term. Except for the correlation term, both the exchange and the Hartree components can be expressed as analytic functions of the density ρ, and similarly for the kinetic term.

This property of the HEG has been used in the past to try a first approximation of equation (3.2) well before the theorems of Hohenberg and Kohn. The Thomas-Fermi-Dirac (TFD) approximation [23–25] assumes the energy density of the real system to be locally the same as that of the HEG:

$$\begin{aligned} F^{TFD}[\rho] &= \int \rho(\mathbf{r}) f^{\rm HEG}(\rho(\mathbf{r}))d\mathbf{r} \\ &= \frac{3}{10}(3\pi^2)^{\frac{2}{3}}\int \rho^{\frac{5}{3}}(\mathbf{r})d\mathbf{r} + \frac{1}{2}\int\frac{\rho(\mathbf{r})\rho(\mathbf{r}')}{|\mathbf{r}-\mathbf{r}'|}d\mathbf{r}d\mathbf{r}' - \frac{3}{4}\left(\frac{3}{\pi}\right)^{\frac{1}{3}}\int\rho^{\frac{4}{3}}(\mathbf{r})d\mathbf{r}\,. \end{aligned} \tag{3.3}$$

The first and the third terms are the local-density approximation of the kinetic term $T[\rho]$, and the exchange term respectively, the second is the exact Hartree contribution. Correlation terms are still missing ($E_c[\rho] \approx 0$).

What poses a problem in this approximation is the kinetic term. Indeed through the virial theorem it can be shown [26] that T is of the same order of magnitude as the total energy of the system. The TFD approximation has the merit to demonstrate the big advantage of working with functionals of the density, but the assumptions used to model the kinetic term are too crude. Better approximations are therefore needed to be used in practical calculations.

A different approach to the minimization of the energy $E[\rho]$ has been proposed in 1965 by the work of Kohn and Sham [21].

3.3 The Kohn-Sham system and the exchange-correlation potential

The Kohn-Sham scheme relies on an auxiliary independent-particle system subject to an effective potential $V_{\rm KS}[\rho](\mathbf{r})$. The KS system has the property that it has the same ground state density as the interacting system: $\rho_{\rm gr}^{\rm KS}(\mathbf{r}) \equiv \rho_{\rm gr}(\mathbf{r})$.

For both the interacting and the Kohn-Sham systems the Hohenberg and Kohn theorems are valid. As a consequence one and only one Kohn-Sham potential $V_{\rm KS}[\rho](\mathbf{r})$ is associated to each interacting system $V_{\rm bgr}(\mathbf{r}, \{\tilde{\mathbf{r}}\})$. A bijective relation $V_{\rm bgr}(\mathbf{r}, \{\tilde{\mathbf{r}}\}) \leftrightarrow V_{\rm KS}[\rho](\mathbf{r})$ is then established. The price of working with an independent-particle system is paid by introducing the unknown potential

$$V_{\rm KS}[\rho](\mathbf{r}, \{\tilde{\mathbf{r}}\}) = V_{\rm bgr}(\mathbf{r}, \{\tilde{\mathbf{r}}\}) + V_H[\rho](\mathbf{r}) + V_{\rm xc}[\rho](\mathbf{r})\,, \tag{3.4}$$

where the external and the Hartree potentials are the same as those of the real system and where the extra exchange-correlation potential $V_{\rm xc}[\rho](\mathbf{r})$ is the unknown part.

In defining the exchange-correlation energy as

$$E_{\rm xc}[\rho] := F[\rho] - E_H[\rho] - T^{\rm KS}[\rho] = \big(T[\rho] - T^{\rm KS}[\rho]\big) + \big(W[\rho] - E_H[\rho]\big)\ , \tag{3.5}$$

the exchange-correlation potential is defined as

$$V_{\rm xc}[\rho](\mathbf{r}) := \frac{\delta E_{\rm xc}[\rho]}{\delta \rho(\mathbf{r})}\ . \tag{3.6}$$

The exchange-correlation energy $E_{\rm xc}$ can be split into two terms, the first $\big(T[\rho] - T^{\rm KS}[\rho]\big)$ accounts for the difference between the kinetic energies of the real system and the independent-particle one, the second $(W[\rho] - E_H[\rho])$ includes the non-Hartree components of the particle-particle interaction $W[\rho]$.

3.3.1 The Local Density Approximation

The KS scheme shifts the problem of approximating the functional $F[\rho]$ to that of approximating the exchange-correlation energy $E_{\rm xc}[\rho]$. Since the contribution of $E_{\rm xc}$ to the total energy is smaller than that of $F[\rho]$, errors in the approximation have less severe consequences.

The simplest and oldest approximation, and by far one of the most used, is the Local Density Approximation [21] or LDA. Under the assumption of LDA there is the idea that the exchange-correlation energy per particle at the point $\mathbf{r}$ is equal to the exchange-correlation energy density of a homogeneous-electron gas of density $\rho(\mathbf{r})$, namely

$$\varepsilon_{\rm xc}^{\rm LDA}[\rho](\mathbf{r}) := \varepsilon_{\rm xc}^{\rm HEG}(\rho(\mathbf{r}))\,. \tag{3.7}$$

This leads to the LDA exchange correlation energy $E_{\rm xc}^{\rm LDA} = \int \rho(\mathbf{r}) \varepsilon_{\rm xc}^{\rm HEG}(\rho(\mathbf{r})) d\mathbf{r}$.

The energy density $\varepsilon_{\rm xc}^{\rm HEG}(\rho)$ is known exactly for the high density limit and it can be computed accurately for all homogeneous densities ρ via Quantum Monte Carlo methods [27].

At the moment of its formulation, this approximation was supposed to be valid for slowly varying densities and for near-electron gas systems, such as alkali metals. Actually this approximation happens to give accurate results well beyond these limits and it is still one of most broadly used approximations.

All the DFT calculations of this thesis are performed within the LDA.

3.3.2 Kohn-Sham eigenvalues and eigenfunctions

Another great advantage of the KS scheme resides in the minimization procedure itself, which is much easier in the independent-particle framework than in the interacting system. In fact the problem of minimizing the KS total energy $E^{\mathrm{KS}}[\rho]$ can be decoupled in N independent equations, thanks to the introduction of the non-interacting orbitals ϕ_i. The minimization of $E^{KS}[\rho]$ is rephrased in the constrained search of a stationary point through the Lagrange multipliers method.

The total energy $E^{\mathrm{KS}}[\rho]$ can be written using orbitals. In fact, from the density

$$\rho(\mathbf{r}) = \sum_{i=1}^{N} \phi_i^*(\mathbf{r})\phi_i(\mathbf{r}) \quad \text{with} \quad \int \rho(\mathbf{r})d\mathbf{r} - N = 0 \ ,$$

the expectation value of the energy is obtained

$$E^{\mathrm{KS}}[\rho] = -\frac{1}{2}\sum_{i}^{N} \int \phi_i^*(\mathbf{r})\nabla^2\phi_i(\mathbf{r}) + \int \rho(\mathbf{r})V_{\mathrm{bgr}}(\mathbf{r},\{\tilde{\mathbf{r}}\})d\mathbf{r} + E_H[\rho] + E_{xc}[\rho] \ . \tag{3.8}$$

The constrained search of the stationary point of E^{KS} leads to N equations of the form

$$\frac{\delta}{\delta\phi_j^*(\mathbf{r})}\left[E^{KS} - \sum_i \varepsilon_i \left(\int \phi_j^*(\mathbf{r})\phi_i(\mathbf{r})d\mathbf{r} - \delta_{ij}\right)\right] = 0 \quad \text{for} \quad j = 1, ..., N \tag{3.9}$$

where the Lagrange multipliers ε_i account for the orthonormality constraint $\int \phi_j^*(\mathbf{r})\phi_i(\mathbf{r})d\mathbf{r} = \delta_{ij}$.

By inserting expression (3.8) into (3.9) one gets N independent Schrödinger-like equations of the kind

$$\left[-\frac{1}{2}\nabla^2 + V_{\mathrm{bgr}}(\mathbf{r},\{\tilde{\mathbf{r}}\}) + V_H[\rho](\mathbf{r}) + V_{\mathrm{xc}}[\rho](\mathbf{r})\right]\phi_i(\mathbf{r}) = \varepsilon_i\phi_i(\mathbf{r}) \tag{3.10}$$

called Kohn-Sham equations. Consequently the Lagrange multipliers ε_i can be interpreted as the energies of the KS states. The Hartree potential and V_{xc} depends explicitly on the density, so the solution of (3.10) must be found self-consistently.

By the use of Lagrange multipliers method, the problem of minimizing the KS energy is mapped into a fixed-point problem that can be solved for instance by an iterative diagonalization of the KS equations. In practice an initial guess $\{\phi_i^{(0)}\}_i$ is done for the KS states, the density $\rho^{(0)}$ is then computed and correspondingly the Hartree and the exchange-correlation potentials are constructed. Successively the N equations (3.10) are solved getting to a new set of KS states $\{\phi_i^{(1)}\}_i$ and energies $\{\varepsilon_i^{(1)}\}_i$. A new density $\rho^{(1)}$ is then computed and the cycle is repeated until some self-consistent criterion is met[7]. Once self-consistency is reached, the output density $\rho^{(\infty)}$ corresponds to the ground state density $\rho_{\mathrm{gr}}(\mathbf{r})$ of the material.

Together with the density, structural properties are usually well reproduced such as the bulk modulus, the stress tensor or the atomic rearrangement in the case of phase transitions.

The KS eigenvalues ε_i and eigenfunctions $\phi_i(\mathbf{r})$ are by-products of the minimization scheme. In principle they have no physical meaning: they belong to an effective non-interacting system which has the only scope of reproducing the exact density. Koopmans'

[7]Most often mixing of old and new results improves the stability of the algorithm.

theorems are not satisfied by the KS system so, in principle, the KS energies $\{\varepsilon_i\}_i$ can not be interpreted as ionization energies, except for the highest occupied eigenvalue [28]. For the same reason differences of KS states do not give correct excitation energies, except in the one electron limit.

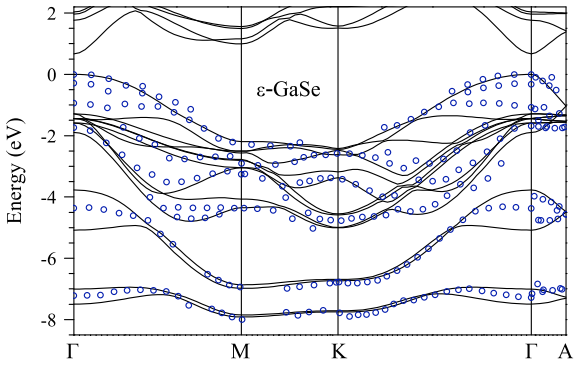

Figure 3.1: LDA band structure (solid line) and experimental photoemission data (dots) of GaSe. Image taken from Ref. [29].

Nevertheless, it often turns out that for the occupied states KS energies do not differ too much from the removal energies (measured e.g., in photoemission experiments), as exemplified in Fig. 3.1. This can be traced back to the fact that the KS potential yields the correct density and is designed to reproduce the highest occupied state correctly. If the other states do not differ too much in character, they will be reasonably described by the same potential.

For this reason the KS system is often seen as something more than a mere mathematical tool. KS wave functions and energies are often used to describe and predict properties of real systems in terms of independent particles. This interpretation can be useful and can give some insight into the electronic properties. Nevertheless attention must be paid to the fact that the KS system is supposed to have nothing in common with the real system but the electron density. This is especially true when discussing excited state properties as optical spectra, electronic gap and ionization energies.

3.4 Excited states with DFT

To investigate optical absorption, the simplest approximation is to consider the process as the sum over all possible single-particle transitions. One electron is excited from the occupied state $|v\mathbf{k}\rangle$ of energy $\varepsilon_v(\mathbf{k})$ to the conduction state $|c\mathbf{k}+\mathbf{q}\rangle$ of energy $\varepsilon_c(\mathbf{k}+\mathbf{q})$ where $\mathbf{q}$ is the small transferred momentum in the dipole approximation. The other electrons instead are supposed to be independent, so no electronic relaxation of the system is included. In this picture Fermi's golden rule for optical transitions ($\mathbf{q} \to 0$) gives

$$\Im[\epsilon_M(\omega)] \propto \lim_{\mathbf{q}\to 0} \sum_{v,c} \int v(\mathbf{q}) \left|\langle v, \mathbf{k}|e^{-i\mathbf{q}\cdot\mathbf{r}}|c, \mathbf{k}+\mathbf{q}\rangle\right|^2 \delta(\varepsilon_c(\mathbf{k}+\mathbf{q}) - \varepsilon_v(\mathbf{k}) - \omega) d\mathbf{k} \qquad (3.11)$$

where $v(\mathbf{q}) = 4\pi/q^2$ is the Coulomb interaction in Fourier space, the delta-function ensures energy conservation in the transition and where single particle states can be the KS wave functions and energies.

In the case $\mathbf{q} \to 0$, one can develop $\langle v, \mathbf{k}|e^{-i\mathbf{q}\cdot\mathbf{r}}|c, \mathbf{k}+\mathbf{q}\rangle$ in $\mathbf{k}\cdot\mathbf{p}$-theory (see Appendix E of [30]), getting

$$\langle v, \mathbf{k}|e^{-i\mathbf{q}\cdot\mathbf{r}}|c, \mathbf{k}+\mathbf{q}\rangle \approx -i\mathbf{q}\frac{\langle v, \mathbf{k}|\nabla|c, \mathbf{k}\rangle}{\varepsilon_c(\mathbf{k}) - \varepsilon_v(\mathbf{k})} .$$

Inserting the expression above into (3.11) and assuming the dipole matrix elements $\langle v, \mathbf{k}|\nabla|c, \mathbf{k}\rangle$ constant, one gets

$$\Im[\epsilon_M(\omega)] \propto \frac{1}{\omega^2}\text{JDOS}(\omega + \varepsilon_l) \tag{3.12}$$

where the energy conservation has been exploited. This expression can be easily computed with DFT.

For example, if one considers the absorption from a deep core state l, with no-dispersing (flat) energy $\varepsilon_l(\mathbf{k}) = \varepsilon_l$, then the JDOS($\omega$) becomes a shifted DOS($\omega$) of conduction states and the absorption spectrum (3.12) is proportional to the density of the empty states

$$\Im[\epsilon_M(\omega)] \propto \frac{1}{\omega^2}\text{DOS}(\omega) \text{ of conduction states .} \tag{3.13}$$

Even though a series of rough approximation have been used in this derivation, actually in some cases this formula turns out to give qualitatively good results. In Fig. 3.2 I show the density of states of the conduction bands I computed for bulk graphite (blue) and graphene (black) in LDA. In the top panel the computed DOS is reported; in the bottom panel, valence X-ray absorption spectra are reported for the same materials with the same color-code. As it can be seen, the qualitative trend is indeed well reproduced: The two $\pi*$ peaks are in a ratio that is comparable with experimental data and the slope after the peak (at $\sim$ 286 eV) is qualitatively well reproduced[8].

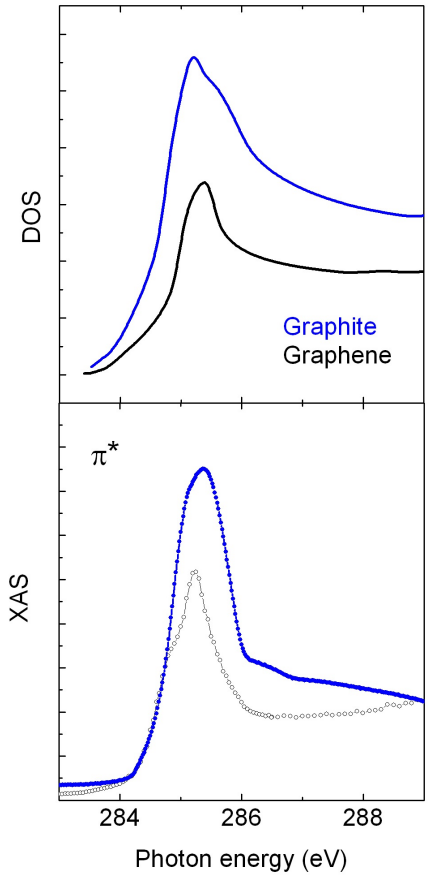

Figure 3.2: DOS (top panel) and X-ray absorption spectroscopy (XAS, bottom panel) of graphite and graphene.

3.5 Summary

In this chapter I presented the main aspects of density functional theory. This theory allows for very efficient calculations, especially in the Kohn-Sham framework, because it reduces the complexity of the N-body problem to the evaluation of the ground state density $\rho(\mathbf{r})$, which is function of only one variable in space. This simplification is paid by the introduction of the unknown exchange-correlation potential for which many approximations have been developed.

In principle the Kohn-Sham system only gives the correct ground state density, and no physical meaning should be given in principle to its eigenfunctions and eigenvalues, especially when excited states are concerned. As a matter of fact, the Kohn-Sham system often turns out to be a good starting point even for the calculation of some excited-state properties such as light absorption spectra, photoemission spectra, electron removal energies (band structure), activation energy of some process and so on.

For a more rigorous description of excited states one needs a time-dependent theory.

[8]Data reported in Fig. 3.2 have been measured in the beam line TEMPO [6] at the Soleil synchrotron light source; I performed the theoretical calculations within a wider project on carbon-based nanostructures which will be the subject of Chapters 7, 8 and 9. See also Appendix D.

Chapter 4

Neutral excitations in Time-Dependent DFT

A theory of the excited states must include time-dependent phenomena as the promotion of electrons and relaxation processes. The dependence on time is mapped through the Fourier transform into a dependence on energy. A complete theory of absorption must account for energy-dependent processes. In this chapter the extension of DFT to time-domain is presented.

After an introduction, I will present the foundations of the theory: the principal theorems of Runge and Gross [31] are discussed. I will underline the main differences with the static DFT and I will point out what are the active research topics in this field.

Subsequently I will concentrate on linear response theory, especially in the framework of periodic systems. I will go through the path from the microscopic polarizability to the macroscopic dielectric tensor and finally to absorption spectroscopy and Electron Energy Loss spectroscopy. A particular attention will be given to approximations and assumptions used later on throughout this work.

4.1 Spectroscopy and evolution in time

Spectroscopy consists in measuring the response of a sample to some time-dependent external potential. Before a time t_0 the system is in the state Ψ^0, that we assume for clarity to be its ground-state Ψ^{gs}, although it is not mandatory. At time t_0 a time-dependent perturbation $V_{\text{ext}}(\mathbf{r}, t)$ is switched on. Transfers of energy and momentum occur between the external potential and the system whose properties start evolving in time. This reaction to the perturbation gives rise, as a consequence, to an induced potential inside the system.

The changes of energy and momentum of the total potential V_{tot}, sum of both the external potential and the induced one, are the object of spectroscopic measurements. From these data, the response function of the system can be obtained.

Theoretical spectroscopy fills the gap between the (measured) response of the system and its microscopic properties. With the help of theoretical spectroscopy one can reconstruct the path that goes from the measured modifications of the total potential to the electronic properties of the system.

In the previous chapter I stressed how the lack of Koopmans' theorems for the KS system prevents the interpretation of KS eigenvalues as electron addition and removal energies and

hence that differences between KS eigenvalues are not excitation energies of the system. If one wants to discuss spectroscopic data on a rigorous theoretical basis, an extension of DFT to the time-dependent domain is mandatory.

4.1.1 The time-dependent many-body problem

The time-dependent Hamiltonian reads

$$\hat{H}(t) = \hat{T} + \hat{V}_{\text{bgr}}(\mathbf{r}, \{\tilde{\mathbf{r}}\}) + \hat{W} + \hat{V}_{\text{ext}}(\mathbf{r}, t) \ , \tag{4.1}$$

where the kinetic $\hat{T}$ and the mutual interacting term $\hat{W}$ and the ionic potential $\hat{V}_{\text{bgr}}$ are the same as in the time-independent problem (3.1)[9]. The external field $\hat{V}_{\text{ext}}$ depends explicitly on time (e.g. a light pulse)[10].

The corresponding time-dependent Schrödinger equation is a differential equation of the kind

$$\hat{H}(t)\Psi(\mathbf{r}_1, ..., \mathbf{r}_N, t) = i\hbar\frac{\partial}{\partial t}\Psi(\mathbf{r}_1, ..., \mathbf{r}_N, t)$$

with initial state at t_0.

$$\Psi(\mathbf{r}_1, ..., \mathbf{r}_N, t_0) = \Psi^0(\mathbf{r}_1, ..., \mathbf{r}_N) \ .$$

Note that $\Psi^0(\mathbf{r}_1, ..., \mathbf{r}_N)$ can be any state, not only the ground-state.

4.2 The foundations of TDDFT

Attempts to generalise the DFT to time domain date back to the late seventies with the works of Ando [32, 33], Peukert [34] and Zangwill-Soven [35, 36] who introduced a time-dependent KS system just assuming the extension to time domain to be possible. A more rigorous approach to time-dependent DFT came some years later and it was given by E. Runge and E. K. U. Gross in a work dated 1984 [31]. This paper set the foundations of modern TDDFT.

It is beyond the scope of this introductory overview to give and demonstrate the four theorems presented in their work. I will therefore discuss the main results, tracing a parallel with the HK and KS theorems of DFT, and underlining the most important differences and implications.

4.2.1 Functionals of the TD-density

The first Runge-Gross (RG) theorem states that

Theorem : *For every single-particle potential $V_{ext}(\mathbf{r}, t)$, which can be expanded into a Taylor series with respect to the time coordinate around $t = t_0$, a map $G_{\Psi^0} : V_{ext}(\mathbf{r}, t) \rightarrow \rho[\Psi^0](\mathbf{r}, t)$ is defined by solving the time-dependent Schrödinger equation with a fixed*

[9] In principle, because of the presence of the external field, the ions can start moving, so a general form of the ionic potential should be $\hat{V}_{\text{bgr}}(\mathbf{r}, \{\tilde{\mathbf{r}}(t)\}$. However, in this work I will assume the Born-Oppenheimer approximation also in the presence of a time-dependent perturbation, i.e. I will neglect electron-phonon coupling.

[10] Most of the time other authors include V_{bgr} in V_{ext}.

initial state $\Psi^0(\mathbf{r}_1, ..., \mathbf{r}_N) = \Psi(\mathbf{r}_1, ..., \mathbf{r}_N, t_0)$ *and calculating the corresponding densities* $\rho(\mathbf{r}, t)$*. This map can be inverted up to an additive merely time-dependant function in the potential.*

This theorem demonstrates that for any time-dependent external potential $V_{\text{ext}}(\mathbf{r}, t)$ and for any initial condition Ψ^0, a bijective relation between the time-dependent density $\rho(\mathbf{r}, t)$ and the external potential can be established. As a consequence, any observable $O(t)$ of the system can be expressed as a functional $O[\rho, \Psi^0](t)$ of the time-dependent density **and** the initial-state Ψ^0.

Note the important difference with respect to the first HK theorem where there is no initial-state dependence. In TDDFT, the knowledge of the density itself is not sufficient to invert the map $G_{\Psi^0} : V_{\text{ext}}(\mathbf{r}, t) \to \rho[\Psi^0](\mathbf{r}, t)$. This is related to the memory of the system. Investigations on this initial-state dependence are quite recent; see e.g., works of N. T. Maitra and K. Burke [37, 38].

A necessary hypothesis of the first RG theorem is V_{ext} to be analytic in time. The analyticity in time of V_{ext} is another recent subject of investigation. The problem started to be explored only recently, e.g. by N. T. Maitra and co-workers [39].

The second HK theorem of DFT states that the total energy is a (universal) functional of the density and that it attains its minimum at the ground-state density. When extended to time domain, a variational minimum principle can not be found. Instead, one looks for the stationary points of the action integral

$$A := \int_{t_0}^{t} \langle \Psi(\mathbf{r}_1, ..., \mathbf{r}_N, \tau) | i\frac{\partial}{\partial \tau} - \hat{H}(\tau) | \Psi(\mathbf{r}_1, ..., \mathbf{r}_N, \tau) \rangle d\tau \ . \tag{4.2}$$

Theorem : *The action integral A can be represented as a functional of the density* $A[\rho]$*. If the potential* $V_{ext}(\mathbf{r}, t)$ *is chosen such that no additive time-dependent function can be split, the total action can be written as* $A[\rho] = B[\rho] - \int_{t_0}^{t} \int \rho(\mathbf{r}, \tau) V_{ext}(\mathbf{r}, \tau) d\mathbf{r} d\tau$ *where* $B[\rho]$ *is a universal function of the density in the sense that the same dependence on* $\rho(\mathbf{r}, t)$ *holds for all external potentials* $V_{ext}(\mathbf{r}, t)$*.* $A[\rho]$ *has a stationary point at the exact density of the system, i.e. the exact density can be computed from the Euler equation* $\delta A[\rho]/\delta\rho(\mathbf{r}, \tau) = 0$*.*

4.2.2 A time-dependent Kohn-Sham system

Stationary points of the action integral (4.2) correspond to the density of the real system. Nevertheless this prescription to find the real density is not directly useful for application; the last RG theorem generalises to time-domain the concept of the KS system giving a way to interpret excited state properties in terms of the evolution of independent-particles.

Theorem : *The exact time-dependent density of the system can be computed from* $\rho(\mathbf{r}, t) = \sum_{i=1}^{N} \phi_i^*(\mathbf{r}, t)\phi_i(\mathbf{r}, t)$ *where the single-particle orbitals* $\phi_i(\mathbf{r}, t)$ *fulfil the time-dependent Schrödinger-like equation*

$$\left(i\frac{\partial}{\partial t} + \frac{1}{2}\nabla^2 \right) \phi_i(\mathbf{r}, t) = \left[V_{bgr}(\mathbf{r}, \{\tilde{\mathbf{r}}\}) + V_{\mathit{eff}}[\rho](\mathbf{r}, t) \right] \phi_i(\mathbf{r}, t)$$

with an effective one-particle potential given by

$$V_{\mathit{eff}}[\rho](\mathbf{r}, t) = V_{ext}(\mathbf{r}, t) + V_H[\rho](\mathbf{r}, t) + \frac{\delta A_{xc}[\rho]}{\delta\rho(\mathbf{r}, t)} \ . \tag{4.3}$$

The three potentials appearing in the equation above are the external potential, the Hartree potential and the time-dependent exchange-correlation potential $V_{\rm xc}(\mathbf{r},t) := \delta A_{\rm xc}[\rho]/\delta\rho(\mathbf{r},t)$.

4.3 Linear response to a perturbation

We now go back to the spectroscopy experiments: before and at time t_0 the system is at rest in its ground state: $\Psi^0 = \Psi^{\rm gr}$. and at time t_0 a perturbation $V_{\rm ext}(\mathbf{r},t) = \theta(t-t_0)\delta V_{\rm ext}(\mathbf{r},t)$ is turned on. Correspondingly the system starts evolving in time.

The value of a generic observable $O(\mathbf{r},t)$ of the system can be expanded in orders of the perturbation $\delta V_{\rm ext}$

$$\begin{aligned} O(\mathbf{r},t) &= O(\mathbf{r},t_0) + \delta O(\mathbf{r},t) + ... \\ &= O(\mathbf{r},t_0) + \int\int_{t_0}^{t} \chi^{\rm O}(\mathbf{r},\mathbf{r}',t-t')\delta V_{\rm ext}(\mathbf{r}',t')dt'd\mathbf{r}' + ... \ . \end{aligned} \tag{4.4}$$

In the expression above I introduced the susceptibility, also called response function, $\chi^O(\mathbf{r},\mathbf{r}',t-t')$, defined as the functional derivative of the observable O with respect to the variation of the field, namely

$$\chi^O(\mathbf{r},\mathbf{r}',t-t') := \left.\frac{\delta O(\mathbf{r},t)}{\delta V_{\rm ext}(\mathbf{r}',t')}\right|_{V_{\rm ext}=0} .$$

The susceptibility is the linear coefficient of the first order term in equation (4.4) and it is independent of the external field. Note that the susceptibility depends on the time-difference because the functional derivative is taken at vanishing perturbation.

When first order terms dominate the response, then one is the linear regime and the susceptibility carries all information needed to describe the linear response of the system.

4.3.1 The density-density response function

In the framework of TDDFT the central observable is the density $\rho(\mathbf{r},t)$. The correspondent susceptibility is the density-density response function

$$\chi(\mathbf{r},\mathbf{r}',t-t') = \left.\frac{\delta\rho(\mathbf{r},t)}{\delta V_{\rm ext}(\mathbf{r}',t')}\right|_{V_{\rm ext}=0} . \tag{4.5}$$

In the same way, one can define the response function of the TD-KS system, related to the same density ρ of the real system and evolving under the action of the effective potential $V_{\rm eff}$ of equation (4.3). The independent-particle response function (often called IP-polarizability) then reads

$$\chi^{KS}(\mathbf{r},\mathbf{r}',t-t') = \frac{\delta\rho(\mathbf{r},t)}{\delta V_{\rm eff}(\mathbf{r}',t')} \tag{4.6}$$

This expression is of great importance because this quantity can be calculated within first order perturbation theory [40] through a sum over states (cfr. equation (4.10)).

Since the density of the TD-KS system coincides with the real density, one can establish a relation between χ and χ^{KS} using expressions (4.5) and (4.6). By means of the chain rule

and remembering definition (4.3), a Dyson equation linking the IP-polarizability and the full density-density response function can be derived[11]

$$\begin{aligned}\chi(\mathbf{r},\mathbf{r}',t-t') &= \frac{\delta\rho(\mathbf{r},t)}{\delta V_{\text{eff}}(\mathbf{r}'',t'')}\frac{\delta V_{\text{eff}}(\mathbf{r}'',t'')}{\delta V_{\text{ext}}(\mathbf{r}',t')} \\ &= \chi^{KS}(\mathbf{r},\mathbf{r}',t-t') + \chi^{KS}(\mathbf{r},\mathbf{r}'',t-t'')K(\mathbf{r}'',\mathbf{r}''',t'',t''')\chi(\mathbf{r}''',\mathbf{r}',t'''-t') \,,\end{aligned} \tag{4.7}$$

where integration is done over repeated indexes. The integrand

$$K(\mathbf{r},\mathbf{r}',t,t') := \frac{\delta(t-t')}{|\mathbf{r}-\mathbf{r}'|} + f_{\text{xc}}(\mathbf{r},\mathbf{r}',t,t') \quad \text{with} \quad f_{\text{xc}}(\mathbf{r},\mathbf{r}',t,t') := \frac{\delta V_{\text{xc}}(\mathbf{r},t)}{\delta\rho(\mathbf{r}',t')} \tag{4.8}$$

contains a static Coulomb contribution $v(\mathbf{r},\mathbf{r}') = 1/|\mathbf{r}-\mathbf{r}'|$, and a dynamical exchange-correlation kernel.

Response function and Dyson equation in periodic systems

In this work I will focus on solid state properties and on periodic supercells for the simulation of finite systems.

Because of the translational symmetry characterising these systems, it is more convenient to work in reciprocal space by Fourier transforming real space quantities. because the decomposition into plane waves takes intrinsically into account the translational symmetry of these systems. Any function $F(\mathbf{r})$ can be expanded in plane waves of wave vector $\mathbf{k}$ according to

$$F(\mathbf{r}) = \frac{1}{(2\pi)^3}\int F(\mathbf{k})e^{-i\mathbf{k}\cdot\mathbf{r}}d\mathbf{k} = \frac{1}{(2\pi)^3}\sum_{\mathbf{G}} e^{-i\mathbf{G}\cdot\mathbf{r}}\int F_{\mathbf{G}}(\mathbf{q})e^{-i\mathbf{q}\cdot\mathbf{r}}d\mathbf{q} \,, \tag{4.9}$$

where the wave vector $\mathbf{k} = \mathbf{q}+\mathbf{G}$ has been split into a continuous long-wavelength component $\mathbf{q}$ laying inside the first Brillouin zone, and a reciprocal lattice vector $\mathbf{G}$. Correspondingly the Fourier transform $F(\mathbf{k})$ is written as a vector $F_{\mathbf{G}}(\mathbf{q})$ where each $\mathbf{G}$-component is a function of the continuous variable $\mathbf{q}$.

In this framework the IP-polarizability can be written in the spectral representation (cfr. Adler [40]) as a matrix[12] in $\mathbf{G}$ and $\mathbf{G}'$

$$\chi^{KS}_{\mathbf{G}\mathbf{G}'}(\mathbf{q},\omega) = \frac{1}{\mathcal{V}}\sum_{ij\mathbf{k}}(f_{i\mathbf{k}} - f_{j\mathbf{k}+\mathbf{q}})\frac{\tilde{\rho}_{ij\mathbf{k}}(\mathbf{q}+\mathbf{G})\tilde{\rho}^*_{ij\mathbf{k}}(\mathbf{q}+\mathbf{G}')}{\omega - (\varepsilon_j(\mathbf{k}+\mathbf{q}) - \varepsilon_i(\mathbf{k})) + i\eta} \tag{4.10}$$

where f are the occupation numbers, the oscillator strengths $\tilde{\rho}$ are defined

$$\tilde{\rho}_{ij\mathbf{k}}(\mathbf{q}+\mathbf{G}) := \int \phi_{i\mathbf{k}}(\mathbf{r})\phi^*_{j\mathbf{k}+\mathbf{q}}(\mathbf{r})e^{-i(\mathbf{q}+\mathbf{G})\cdot\mathbf{r}}d\mathbf{r} \,, \tag{4.11}$$

[11] The response function χ is a causal function, that is $\chi(t-t') = 0$ for $t < t'$ in (4.5). Actually, using (4.3) and (4.8) the resulting $\chi(t-t')$ is symmetric. This contradiction has been solved by R. van Leeuwen defining a new action functional on the Keldysh contour [41].

[12] In principle from the generic function $F(\mathbf{r},\mathbf{r}')$ one gets a matrix $F_{\mathbf{G}\mathbf{G}'}(\mathbf{q},\mathbf{q}')$, but for a periodic function $F(\mathbf{r},\mathbf{r}') = F(\mathbf{r}+\mathbf{P},\mathbf{r}'+\mathbf{P})$ with $\mathbf{P} = n_1\mathbf{a}_1 + n_2\mathbf{a}_2 + n_3\mathbf{a}_3$ linear combination of the unitary vectors $\mathbf{a}_j$ with integer coefficients, the crystal momentum conservation imposes $\mathbf{q}+\mathbf{G} = \mathbf{k}-\mathbf{k}'$, so the elements of the $F_{\mathbf{G}\mathbf{G}'}$ depend only on $\mathbf{q}$.

$\varepsilon_m(\mathbf{k})$ are the KS energies, the normalization constant $\mathcal{V}$ is the crystal volume[13], and η is a positive infinitesimal quantity needed to Fourier transform from time to frequency.

In a similar way the Dyson equation (4.7) reads

$$\chi_{\mathbf{G}\mathbf{G}'}(\mathbf{q},\omega) = \chi^{KS}_{\mathbf{G}\mathbf{G}'}(\mathbf{q},\omega) + \chi^{KS}_{\mathbf{G}\mathbf{G}''}(\mathbf{q},\omega) K_{\mathbf{G}''\mathbf{G}'''}(\mathbf{q},\omega) \chi_{\mathbf{G}''',\mathbf{G}'}(\mathbf{q},\omega) \tag{4.12}$$

where repeated indexes are summed over, and

$$K_{\mathbf{G}\mathbf{G}'}(\mathbf{q},\omega) = \delta_{\mathbf{G}\mathbf{G}'} \frac{4\pi}{|\mathbf{q}+\mathbf{G}|^2} + f_{\text{xc}}^{\mathbf{G}\mathbf{G}'}(\mathbf{q},\omega) \; .$$

Neglecting the spin, in insulators and semiconductors the occupation numbers f_j are strictly 2 or 0; this allows for some simplification in the sum over states (4.10). In particular one can consider only IP-transitions from an occupied state v to an unoccupied c. For each (v,c) couple, two terms contribute:

$$\chi^{KS}(\omega) = \frac{2}{\mathcal{V}} \sum_{vc} \left\{ \frac{\tilde{\rho}_{vc}\tilde{\rho}^*_{vc}}{\omega - (\varepsilon_c - \varepsilon_v) + i\eta} - \frac{\tilde{\rho}_{cv}\tilde{\rho}^*_{cv}}{\omega + (\varepsilon_c - \varepsilon_v) + i\eta} \right\} \tag{4.13}$$

where the dependence in $\mathbf{q}$, $\mathbf{G}$ and $\mathbf{G}'$ has been omitted for simplicity.

For each IP-transition $v \to c$ the IP-polarizability has two poles: the resonant excitation at $\omega = (\varepsilon_c - \varepsilon_v)$ on the real positive axis and the antriresonant excitation at the negative energy $\omega = -(\varepsilon_c - \varepsilon_v)$.

4.4 From the susceptibility to the spectra

In this work, linear response TDDFT has been used mainly to compute absorption and EEL spectra. Both are computed from the macroscopic dielectric function $\epsilon_M(\mathbf{q},\omega)$, which is the measured observable. The two spectra are obtained according to

$$\text{Abs}(\omega) = \Im\left[\epsilon_M(\omega)\right] \quad \text{and} \quad \text{EELS}(\mathbf{q}+\mathbf{G},\omega) = -\Im\left[\frac{1}{\epsilon^{-1}_{\mathbf{G}\mathbf{G}}(\mathbf{q},\omega)}\right] \; , \tag{4.14}$$

where $\mathbf{q}$ and ω are the momentum and energy transferred from the perturbing field to the system.

In the case of periodic (cubic) systems the relation between the macroscopic dielectric function and the microscopic susceptibility χ is found in the works by Adler [40], and Wiser [42] and is the important relation (2.19).

In equation (2.15) the total potential V_{tot} and the external potential V_{ext} are defined as classical potentials. Therefore $V_{\text{tot}} = V_H + V_{\text{ext}}$. By inverting (2.15), the microscopic inverse dielectric function is given by

$$\epsilon^{-1}(\mathbf{r},\mathbf{r}',t,t') = \frac{\delta V_{\text{tot}}(\mathbf{r},t)}{\delta V_{\text{ext}}(\mathbf{r}',t')} = \frac{\delta V_{\text{ext}}(\mathbf{r},t)}{\delta V_{\text{ext}}(\mathbf{r}',t')} + \int \frac{\delta V_H(\mathbf{r},t)}{\delta \rho(\mathbf{r}'',t'')} \frac{\delta \rho(\mathbf{r}'',t'')}{\delta V_{\text{ext}}(\mathbf{r}',t')} d\mathbf{r}'' dt'' \; . \tag{4.15}$$

[13] In practical calculations the Brillouin zone is sampled with $N_{\mathbf{k}}$ points arranged on a mesh. In this case the crystal volume (in principle infinite) writes $\mathcal{V} = \mathcal{V}_{\text{cell}} N_{\mathbf{k}} = (2\pi)^3 N_{\mathbf{k}} / \mathcal{V}_{\text{BZ}}$ with $\mathcal{V}_{\text{cell}}$ and $\mathcal{V}_{\text{BZ}}$ volumes of the real unitary cell and of the first Brillouin zone respectively.

where derivative with respect to V_{ext} are taken at vanishing external potential. Making use of (4.5), one obtains the following expression

$$\epsilon^{-1}(\mathbf{r},\mathbf{r}',t-t') = \delta(\mathbf{r}-\mathbf{r}')\delta(t-t') + \int\int v(\mathbf{r}-\mathbf{r}'')\delta(t-t'')\chi(\mathbf{r}'',\mathbf{r}',t''-t')d\mathbf{r}''dt''$$

which links the dielectric properties of the material to the polarizability χ. In reciprocal space the above equation reads

$$\epsilon^{-1}_{\mathbf{G}\mathbf{G}'}(\mathbf{q},\omega) := \delta_{\mathbf{G}\mathbf{G}'} + \sum_{\mathbf{G}''} v_{\mathbf{G}\mathbf{G}''}(\mathbf{q})\chi_{\mathbf{G}''\mathbf{G}'}(\mathbf{q},\omega)\ . \tag{4.16}$$

where the Coulomb interaction $v_{\mathbf{G}\mathbf{G}'}(\mathbf{q}) = \delta_{\mathbf{G}\mathbf{G}'}4\pi/|\mathbf{q}+\mathbf{G}|^2$.

In the last expression (4.16) (test-particle expression) exchange-correlation processes between the electrons of the system and the external field are omitted.

In the case of absorption spectra, this is not an approximation since the electrons of the system can not exchange with the photons of the external field; on the other hand, in the case of EELS this may be an approximation. In ordinary EEL spectroscopy, the impinging electrons have a kinetic energy high enough to be distinguished from the electrons of the system, hence no exchange effect can take place. Hence the external field can be approximated with a classical field. When low energy electrons are involved, then exchange-correlation effects can not be neglected and an exchange-correlation kernel f_{xc} must be added to the coulomb interaction in equation (4.16) (test-electron expression).

4.5 Practical calculations and approximations

The procedure followed in this work to compute absorption spectra and EEL spectra is summarised in four steps.

1. A static DFT calculation is performed using the LDA for the exchange-correlation potential V_{xc}. The corresponding KS system is characterised by eigenvalues $\varepsilon_m(\mathbf{k})$ and eigenfunctions $\phi_{m\mathbf{k}}(\mathbf{r})$ computed on a mesh of k-points sampling the Brillouin Zone.

2. With the KS eigenfunctions and eigenvalues[14], the IP-polarizability is computed according to equation (4.10). At this step, one has to stop the sum at a cutoff value (cutoff band) and similarly one has to cutoff the dimension of the matrix $\chi^{KS}_{\mathbf{G}\mathbf{G}'}$.

3. The full susceptibility χ is then computed through the inversion of the Dyson equation (4.12). At this stage the exchange-correlation kernel f_{xc} must be approximated[15]. Convergence on the parameters used has to be checked.

4. The inverse dielectric matrix ϵ^{-1} is finally computed via expression (4.16) and the macroscopic dielectric function ϵ_M is obtained (equation (2.19)).

[14]KS eigenfunctions will be used in all cases. Instead, quasiparticle energies are used most often in the place of KS eigenvalues (see Chapter 5).

[15] Actually in the case of RPA, the Dyson equation is not inverted, but other techniques are used. See below at Chapter 4.5.2.

The most demanding step of the calculation is the second, where the IP-polarizability is computed as a sum over states. Alternative methods exist that avoid the direct calculation of χ^{KS} [43], but they are not efficient when, besides spectra, the full matrix $\chi_{\mathbf{GG'}}$ is needed (e.g. in GW calculations), as it is the case in this thesis.

4.5.1 Tamm-Dancoff Approximation

Resonant and antiresonant components of the polarizability are reported in equation (4.13). The inversion of the Dyson equation mixes the two components, so that the polarizability has mixed contributions. In some cases, and especially when computing absorption spectra of systems with a considerable gap, the antiresonant terms can be neglected, that is the

$$\text{Tamm-Dancoff approximation:} \quad \chi^{KS} \equiv \chi^{KS}_R \ . \tag{4.17}$$

The Tamm-Dancoff approximation consists in computing the IP-polarizability (4.13) summing over resonant excitations only.

When computing EEL spectra or absorption from small band-gap systems, the validity of this approximation has to be checked.

4.5.2 Exchange-correlation kernels

the exchange-correlation kernel is given formally by

$$f_{\text{xc}}^{\mathbf{GG'}}(\mathbf{q},\omega) = \chi^{KS\,-1}_{\mathbf{GG'}}(\mathbf{q},\omega) - \chi^{-1}_{\mathbf{GG'}}(\mathbf{q},\omega) - 4\pi\frac{\delta_{\mathbf{GG'}}}{|\mathbf{q}+\mathbf{G}|^2} \ ,$$

but of course χ is not known, so in real calculations the exchange-correlation kernel f_{xc} must be approximated. In this section I present four approximations used in this work.

Random Phase Approximation (RPA)

The simplest approximation is to neglect f_{xc}:

$$f_{\text{xc}}^{\text{RPA}}(\mathbf{q},\omega) = 0 \tag{4.18}$$

This approximation is called Random Phase Approximation.

In the RPA it is not necessary to solve the Dyson equation (4.12), in fact equations (4.12) and (4.16) can be combined to give directly (see footnote 15)

$$\epsilon_{\mathbf{GG'}}(\mathbf{q},\omega) = \delta_{\mathbf{GG'}} - v_{\mathbf{GG'}}(\mathbf{q})\chi^{KS}_{\mathbf{GG'}}(\mathbf{q},\omega) \ . \tag{4.19}$$

By inverting the last matrix, and making use of (2.19), one can compute ϵ_M.

In RPA one assumes that the electrons of the system interact as classical charge densities, that is via the Hartree potential. Instead exchange-correlation effects such as quasiparticle corrections to the KS energies and electron-hole interaction are neglected. For metals or confined small molecules this approximation gives often reasonably good results, but in insulators the RPA is usually a too strong approximation and other kernels must be used.

Adiabatic Local Density Approximation (ALDA)

An improvement over the RPA is the Adiabatic Local Density Approximation

$$f_{\rm xc}^{\rm ALDA}(\mathbf{r},\mathbf{r}',t-t') = \delta(t-t')\delta(\mathbf{r}-\mathbf{r}')\frac{dV_{\rm xc}^{\rm LDA}(\mathbf{r},\rho(\mathbf{r},t))}{d\rho(\mathbf{r}',t)} \tag{4.20}$$

obtained by inserting into equation (4.8) the LDA potential (3.7) computed at the instantaneous density.

This approximation performs quite well in small molecules and confined systems. However, as it is local in space and time, it does not catch non-local effects important in solids and can not describe dynamical effects such as double excitations in molecules or satellites.

Long Range Corrected (LRC)

In the long range limit $\mathbf{q}+\mathbf{G}\to 0$ the Coulomb interaction diverges, whereas the polarizabilities χ and χ^{KS} vanish as $|\mathbf{q}|^2$. The Long Range Corrected kernel [44, 45]

$$f_{\rm xc}^{LRC}(\mathbf{q},\mathbf{G},\mathbf{G}',\omega) = -\alpha\frac{\delta_{\mathbf{G}\mathbf{G}'}}{|\mathbf{q}+\mathbf{G}|^2} \tag{4.21}$$

corrects the long range component by subtracting a function that has the same spatial dependence as the Coulomb interaction, hence $\chi^{KS}f_{\rm xc}$ is finite, contrary to LDA where $f_{\rm xc}(\mathbf{q}\to 0)$ is constant, so that its effect is zero if finite $\mathbf{G}$ components are negligible.

The constant α is material dependent. For a wide class of semiconductors and insulators it can be fixed following the linear prescription

$$\alpha = 4.615\epsilon_\infty^{-1} - 0.213 \tag{4.22}$$

where ϵ_∞^{-1} is the dielectric constant computed e.g. in RPA or taken from experiment.

This kernel has been derived from Many-Body Perturbation Theory (MBPT) that will be presented in the next Chapter. It is meant to include to some extent the electron-hole interaction and indeed when applied to calculations of semiconductors, it is able to reproduce continuum exciton effects that are missed by (local) ALDA or RPA kernels.

On the other hand, other exchange-correlation effects such as quasiparticle corrections to the gap must be included at the level of the IP-polarizability, by substituting quasiparticle energies ε_m^{QP} in the denominator of equation (4.10) and by assuming that $\phi_m^{QP}\approx\phi_m^{KS}$ [16].

Finally, an extension to frequency domain has been included [46] in the form $f_{\rm xc} = -(\alpha+\beta\omega^2)/|\mathbf{q}+\mathbf{G}|^2$.

Bootstrap kernel (BS)

The last approximation I will discuss here, is the recently developed Bootstrap Kernel [47, 48] which is defined by the empirical relation

$$f_{\rm xc}^{\rm BS}(\mathbf{q},\mathbf{G},\mathbf{G}') = \frac{\epsilon^{-1}_{\mathbf{G}\mathbf{G}'}(\mathbf{q},\omega=0)}{\chi^{KS}_{\mathbf{0}\mathbf{0}}(\mathbf{q},\omega=0)} \tag{4.23}$$

with the prescription that it should be computed self-consistently together with equations (4.12) and (4.16).

[16] See Chapter 5 for a discussion on quasiparticle energies and the electron-hole interaction.

Because $1/\chi^{KS}$ diverges as $|\mathbf{q}|^{-2}$, also the BS kernel has the correct singularity in the long-range limit, giving continuum exciton effects in good agreement with MBPT calculations. It is similar to the LRC, but it has the advantage that the linear relation to determine the constant α is replaced by a more sophisticated materials-dependent prescription, so it is valid also for those materials for which the linear relation (4.22) fails. Moreover it has an enhanced dependence on $\mathbf{G}$ and $\mathbf{G}'$.

Any how, for materials where LRC gives good results, LRC-spectra are almost identical to BS-spectra. Bound excitons instead can only be accessed by the Bootstrap kernel unless one modifies (4.22).

As in the case of the LRC kernel, quasiparticle corrections to the KS energies must be added "by hand" in the IP-polarizability.

Other developments, not used in this thesis include kernels derived from the homogeneous electron gas [49] or empirical modifications of the Bootstrap [50].

4.5.3 The Local Field Effects

Looking back at (2.19), one may wonder why it is necessary to solve a matrix equation (4.16) if at the end only one element is used. Indeed it is useful to define an alternative response function $\bar{\chi}$ such that

$$\epsilon_M(\omega) := \lim_{\mathbf{q}\to 0} [1 - v_{\mathbf{0}}(\mathbf{q})\bar{\chi}_{\mathbf{00}}(\mathbf{q},\omega)] \tag{4.24}$$

In this way the two spectra read respectively

$$\mathrm{Abs}(\omega) = \Im\left[\epsilon_M(\omega)\right] = -\lim_{\mathbf{q}\to 0} v_{\mathbf{0}}(\mathbf{q})\Im\left[\bar{\chi}_{\mathbf{00}}(\mathbf{q},\omega)\right] \tag{4.25}$$

$$\mathrm{EELS}(\mathbf{q},\omega) = -\Im\left[\epsilon^{-1}_{\mathbf{00}}(\mathbf{q},\omega)\right] = -v_{\mathbf{0}}(\mathbf{q})\Im\left[\chi_{\mathbf{00}}(\mathbf{q},\omega)\right] \tag{4.26}$$

The difference between $\bar{\chi}$ and χ is the only difference between the absorption and the EEL spectrum at vanishing momentum transfer.

From the definitions (4.24) and (2.19) one gets immediately that

$$\bar{\chi}_{\mathbf{00}} = \chi_{\mathbf{00}}/(1 + v_{\mathbf{0}}\chi_{\mathbf{00}}) \quad \text{thus} \quad \chi_{\mathbf{00}} = \bar{\chi}_{\mathbf{00}} + \bar{\chi}_{\mathbf{00}}v_{\mathbf{0}}\chi_{\mathbf{00}}\ . \tag{4.27}$$

This equation shows that $\bar{\chi}$ is essentially a screened polarizability, so not sensible to long-range effects.

Let us split the Coulomb interaction in equation (4.7) into two parts

$$v_{\mathbf{G}}(\mathbf{q}) = \bar{v}_{\mathbf{G}}(\mathbf{q}) + v_{\mathbf{0}}(\mathbf{q})\delta_{\mathbf{G0}} \qquad \text{with} \qquad \bar{v}_{\mathbf{G}}(\mathbf{q}) := \begin{cases} 0 & \text{if } \mathbf{G} = 0 \\ 4\pi|\mathbf{q}+\mathbf{G}|^{-2} & \text{if } \mathbf{G} \neq 0 \end{cases} \tag{4.28}$$

where we put in evidence a long-range part $v_{\mathbf{0}}$ and a short-range $\bar{v}$. Then the Dyson equation splits accordingly into two equations

$$\begin{aligned} \bar{\chi}_{\mathbf{GG}'} &= \chi^{KS}_{\mathbf{GG}'} + \chi^{KS}_{\mathbf{GG}''}[\bar{v}_{\mathbf{G}''}\delta_{\mathbf{G}''\mathbf{G}'''} + f_{\mathrm{xc}}^{\mathbf{G}''\mathbf{G}'''}]\bar{\chi}_{\mathbf{G}'''\mathbf{G}'} \\ \chi_{\mathbf{GG}'} &= \bar{\chi}_{\mathbf{GG}'} + \bar{\chi}_{\mathbf{G0}}v_{\mathbf{0}}\chi_{\mathbf{0G}'}\ . \end{aligned}$$

The first equation is essentially a a Dyson equation for $\bar{\chi}$. Note that the second equation gives (4.27) in the case $(\mathbf{G},\mathbf{G}') = (\mathbf{0},\mathbf{0})$.

This tells us that for optical absorption only short-range components of the Coulomb interaction are relevant, whereas EEL spectra are sensible to the potential also at long

distances. Indeed it is the long range Coulomb interaction that gives rise to the plasmons measured in EELS. $\bar{v}$ carries the fast-varying components of the Coulomb interaction which account for local inhomogeneities of the polarizability (the local field). Local field effects are taken into account by the inversion of the Dyson equation, or the inversion of equation (4.19) in the case of RPA calculations. They may be important whenever localised electrons (d and f orbitals) are present, when polarizable states are concerned or for large momentum transfer $\mathbf{q}$, where shorter distances are probed.

Note also that neglecting LFE in the RPA gives $\bar{\chi} = \chi^{KS}$. Consequently the absorption spectrum computed with (4.25) reduces to

$$\text{NLF + RPA absorption spectrum : } \text{Abs}(\omega) = -\lim_{\mathbf{q}\to 0} v_{\mathbf{0}}(\mathbf{q}) \Im[\chi^{KS}_{\mathbf{00}}(\mathbf{q},\omega)] \tag{4.29}$$

and no matrix inversion is needed any more.

4.5.4 Spectra of isolated systems

In isolated systems excitations are determined only by short range interactions. For what stated in the previous section, we expect absorption spectra and EELS (at vanishing momentum) to be equal. Indeed for isolated systems simulated in a supercell, the volume of the unit cell $\mathcal{V}_{\text{cell}} \to \infty$. Since the IP-polarizability is proportional to $1/\mathcal{V}_{\text{cell}}$ (cfr. expression (4.10) and footnote 13 at page 34), the susceptibility $\chi_{\mathbf{00}} \to 0$. From equations (4.27) and $v_{\mathbf{0}} = 4\pi/|\mathbf{q}|^2$, one obtains the relation between the macroscopic averages

$$v_{\mathbf{00}}\bar{\chi}_{\mathbf{00}} = \frac{\chi_{\mathbf{00}} v_{\mathbf{00}}}{1 + v_{\mathbf{00}}\chi_{\mathbf{00}}} \approx v_{\mathbf{00}}\chi_{\mathbf{00}} \quad \text{for } \mathcal{V}_{\text{cell}} \to \infty \,. \tag{4.30}$$

This demonstrates that in isolated systems $\Im[\epsilon_M] \approx -\Im[1/\epsilon_M]$, that is absorption spectrum $\approx$ EEL spectrum.

The same relation holds also for very weakly polarizable systems, where $v_{\mathbf{00}}\chi_{\mathbf{00}} \ll 1$, for instance for core levels.

4.6 Summary

In this chapter I introduced the Time-Dependent Density Functional Theory (TDDFT) which generalises the approach of DFT to account for time-dependent processes. This allows for the correct description of the inverse dielectric function which is closely related to measurable quantities in spectroscopic experiments such as EELS (cfr. (2.24)) and absorption (cfr. (2.25)).

The relation between the KS polarizability χ^{KS} and the macroscopic dielectric function ϵ_M has been traced assuming a linear response. It passes through the calculation of polarizability χ, obtained from χ^{KS} via a Dyson equation (4.12), and of the inverse dielectric function ϵ^{-1}, derived in (4.16).

Some approximations for the exchange-correlation kernel f_{xc} have been also presented and briefly discussed. They will be used later on in the theoretical spectra presented in this work.

The difference between EEL and absorption spectra has been pointed out by splitting the Coulomb interaction $v_{\mathbf{G}}(\mathbf{q})$ into a with the local fields $\bar{v}$, defined in (4.28), and the

long range component $v_0(\mathbf{q})$. The second term, which diverges for $\mathbf{q} \to 0$, enters in the EEL spectra, whereas it does not in absorption spectra. For an isolated object, the long-range components of the Coulomb interaction vanish, so one expect the EEL spectrum and the absorption spectrum to coincide, as demonstrated by the relation (4.30). This relation constitutes a criterion to state whether a system is isolated or not.

Chapter 5

Many Body Perturbation Theory

If in density functional theories, the key variable is the density, in many-body perturbation theory (MBPT) this role is played by the Green's function G. In the framework of MBPT, the spectrum of the one-particle excitations of the system (spectral function) finds a natural formulation. It is given by the poles of the one-particle Green's function. In fact, by definition they are the one electron addition and removal energies, which makes the spectral function closely related to the spectra measured in photoemission and inverse photoemission spectroscopy.

In the first section, the principal concepts useful for the description of one-particle excitations are introduced: from the definition of the one-particle Green's function G, the derivation of the Dyson equation through the Schwinger functional-derivative method, to the introduction of self-energy Σ. Then I will introduce Hedin's pentagon together with the GW approximation for the self-energy which will be discussed in detail, with a special attention for different schemes (perturbative, self-consistent) or implementations (plasmon-pole models, contour deformation). I will conclude the one-particle excitation part with a final highlight on dynamical effects.

In MBPT also two-particle processes can be described. In the second section of this chapter, I will define the two-particle correlation function L, which can be expressed through a Dyson equation called Bethe-Salpeter equation (BSE) containing a 4-point kernel Ξ. I will present the typical approximations used for the kernel with a special emphasis on the static approximation usually assumed. I will also outline one possible way to overcome the static approximation to the BSE. I will finally conclude the section with an overview of dynamical effects in BSE.

5.1 Charged excitations with MBPT

In the second quantization formalism, the many-body Hamiltonian (3.1) reads

$$\begin{aligned}\hat{H} = &-\frac{1}{2}\sum_{\sigma}\int \psi^{\dagger}(\mathbf{r},\sigma)\nabla^2\psi(\mathbf{r},\sigma)d\mathbf{r}+\\ &+\sum_{\sigma}\int \psi^{\dagger}(\mathbf{r},\sigma)V_{\text{bgr}}(\mathbf{r},\{\tilde{\mathbf{r}}\})\psi(\mathbf{r},\sigma)d\mathbf{r}+\\ &+\frac{1}{2}\sum_{\sigma,\sigma'}\int \psi^{\dagger}(\mathbf{r},\sigma)\psi^{\dagger}(\mathbf{r}',\sigma')v(\mathbf{r},\mathbf{r}')\psi(\mathbf{r},\sigma)\psi(\mathbf{r}',\sigma')d\mathbf{r}d\mathbf{r}' \qquad (5.1)\end{aligned}$$

where the introduction of creation and annihilation field operators $\psi^\dagger$ and ψ allow the number of particles to vary. Calling $|N\rangle$ the ground-state of an N interacting particle system, we can associate to the Hamiltonian (5.1) the time-ordered Green's function $G(\mathbf{r}_1, \mathbf{r}_2, t_1, t_2, \sigma_1, \sigma_2)$ at zero temperature, defined

$$G(1,2) = i\theta(t_2 - t_1)\langle N|\psi^\dagger(2)\psi(1)|N\rangle - i\theta(t_1 - t_2)\langle N|\psi(1)\psi^\dagger(2)|N\rangle \tag{5.2}$$

where the notation $n = (\mathbf{r}_n, t_n, \sigma_n)$ is introduced to label space, time and spin variables in a more compact way. This definition corresponds to the expectation value of injecting ($t_1 > t_2$) an electron of spin σ_2 into the N particle system at time t_2 and in point $\mathbf{r}_2$ and of extracting an electron with spin σ_1 at time t_1 and point $\mathbf{r}_1$, and similarly for the hole in inverse time-order. It is therefore the one-particle correlation function of the system.

It can be shown that the average value of any single-particle operator $\hat{O}$ can be expressed as

$$\langle N|\hat{O}(1,2)|N\rangle = -i\int O(1,2)G(2,1)d1d2,$$

which includes e.g., density matrix, kinetic energy and spectral functions[17]. This property highlights an intrinsic advantage of the Green's function formalism if compared with DFT, in fact in DFT all observables can be expressed as a functional of the density, but the functional is unknown and must be approximated. In the Green's function approach, the single-particle observables have a known formulation in terms of G.

Another advantage of this approach is the fact that Koopmans' theorems are satisfied by the Green's function. One can rewrite the expectation value (5.2) making use of a complete basis of the N+1 and the N-1 systems (cfr. equation (1.3))

$$\begin{aligned} G(1,2) = &+i\theta(t_2 - t_1)\sum_m \langle N|\psi^\dagger(2)|N-1,m\rangle\langle N-1,m|\psi(1)|N\rangle + \\ &- i\theta(t_1 - t_2)\sum_m \langle N|\psi(1)|N+1,m\rangle\langle N+1,m|\psi^\dagger(2)|N\rangle \end{aligned}$$

where $|N+1,m\rangle$ is the m-th state of the (N+1)-particle system and similar for the N-1. The first term is called hole Green's function: the action of the annihilation and creation fields is projected onto an (N-1)-particle system, so it is expressed in terms of the creation of a hole (extraction of an electron). The second term is called electron Green's function since it has been projected onto a (N+1)-particle system, hence it is described in terms of electron injections.

Taking the Fourier transform of the expression above, one gets the Lehmann representation [52] of the Green's function

$$G(\mathbf{r}_1, \sigma_1, \mathbf{r}_2, \sigma_2, \omega) = \sum_m \frac{f_m(\mathbf{r}_1, \sigma_1) f_m^*(\mathbf{r}_2, \sigma_2)}{\omega - E_m + i\eta\,\mathrm{sign}(E_m - \mu)} \tag{5.3}$$

with the Lehmann amplitudes defined

$$f_m(\mathbf{r}, \sigma) := \begin{cases} \langle N|\psi(\mathbf{r},\sigma)|N+1,m\rangle \text{ and } E_m = E_m^{N+1} - E_0^N & \text{for} \quad E_m > \mu \\ \langle N-1,m|\psi(\mathbf{r},\sigma)|N\rangle \text{ and } E_m = E_0^N - E_m^{N-1} & \text{for} \quad E_m < \mu\ . \end{cases}$$

[17] Also the total energy can be expressed with G [51], although it is actually a two-particle operator.

The excitation energies E_m are by construction the addition $(E_m^{N+1} - E_0^N)$ and removal $(E_0^N - E_m^{N-1})$ energies of one particle in the fully interacting system. So Koopman's theorems are satisfied by construction.

The term $i\eta\,\mathrm{sign}(E_m - \mu)$ with $\eta \to 0^+$ is introduced in the denominator to ensure convergence of the Fourier transform between time and frequency. It changes sign passing the chemical potential μ thus discriminating between electrons and holes. This change of sign is related to the different domains of analyticity of the hole and the electron Green's functions.

The Green's function can also be written in the spectral representation

$$G(\mathbf{r}_1, \sigma_1, \mathbf{r}_2, \sigma_2, \omega) = \int_{-\infty}^{+\infty} \frac{\mathcal{A}(\mathbf{r}_1, \sigma_1, \mathbf{r}_2, \sigma_2, \omega')}{\omega - \omega' + i\eta\,\mathrm{sign}(\omega' - \mu)} d\omega' \,, \tag{5.4}$$

where the spectral function

$$\mathcal{A}(\mathbf{r}, \sigma, \mathbf{r}', \sigma', \omega) = \sum_m f_m(\mathbf{r}, \sigma) f_m^*(\mathbf{r}', \sigma') \delta(\omega - E_m) = \frac{1}{\pi} |\Im[G(\mathbf{r}, \sigma, \mathbf{r}', \sigma', \omega)]| \tag{5.5}$$

can be proven to be a real quantity for a stationary Hamiltonian without magnetic fields. The second equation comes from Sokhatsky-Weierstrass theorem

$$\lim_{\eta \to 0^+} \int \frac{a(x)}{x \pm i\eta} dx = \mp i\pi \int a(x)\delta(x) dx + \mathcal{P} \int \frac{a(x)}{x} dx$$

with $\mathcal{P}$ denoting the Cauchy principal value of the integral.

The definition (5.5) shows that the spectral function is a series of delta peaks on the real axis. For finite systems (clusters and molecules), peaks are generally well separated and the sum runs indeed over a series of discrete excited states, giving rise to separated peaks in the spectral function. They correspond to well separated poles of G arranged along the real axis. In the thermodynamic limit of infinite systems, the excited states become closer and closer ad eventually the spectral function becomes an integral over infinitely close delta-functions, which corresponds to a branch cut of G along the real axis.

It is evident that the hole and electron contributions are closely related to the photoemission (electron extraction) and inverse photoemission spectroscopies (electron addition). It is important to note that m may differ from 0, that means that the creation of a hole (electron extraction) can either promote the system to its (N-1)-ground state ($m = 0$) or to any other excited (N-1)-particle state $m \neq 0$. And similarly for the creation of the electron (electron addition).

5.1.1 The equations of motion of the Green's function

In this section I will follow the review article of G. Strinati [53] to introduce the equation of motion of the single-particle Green's function. Note, however, that the definition given in this work of the self-energy differs from that given in the referred article, as specified in footnote 18 at page 45.

Hierarchical equation

The very definition (5.2) of the Green's function, or its Lehmann representation (5.3) in practice are of no help in computing the Green's function of an N-particle system. This

because in general the many-body eigenstates $|N\rangle$, $N-1\rangle$ and$|N+1\rangle$ are not known. However using the time-evolution of an operator in the Heisenberg picture, the equation of motion of the Green's function can be written

$$\left[i\frac{\partial}{\partial t_1} - H_0(\mathbf{r}_1)\right] G(1,2) + i\int v(\mathbf{r}_1,\mathbf{r}_3) G_2(1,2,3,3^+) d3 = \delta(1,2) \tag{5.6}$$

where $H_0(\mathbf{r}_1) = -\frac{1}{2}\nabla_1^2 + V_{\text{bgr}}(\mathbf{r}_1)$ is the non-interacting Hamiltonian, $v(\mathbf{r}_1,\mathbf{r}_2)$ is the Coulomb potential and $G_2(1,2,3,4)$ is the two-particle Green's function which describes the addition and removal of two particles. The notation $3^+ = (\mathbf{r}_3, \sigma_3, t_3 + \lambda)$ with $\lambda \to 0^+$ real number.

The equation above is the first of a set of hierarchical equations where the equation of motion of the j-particle Green's function is expressed in terms of the (j+1)-particle Green's function (in this sense $G \equiv G_1$). The two-particle Green's function G_2 can be computed only through the G_3 and so on, until the knowledge of the N-particle G_N is required. Hence the complexity of the problem is not reduced, and some strategy must be adopted to close the equation for G.

Differential equation

The idea is to hide the 2-particle and higher order interactions contained in the G_2 via the introduction of an external field U. The formal tool to do so is offered by Schwinger's equation [54]:

$$\left.\frac{\delta G(1,2)}{\delta U(3,4)}\right|_{U=0} = G(1,2)G(3,4) - G_2(1,2,3,4) = iL(1,2,3,4) \tag{5.7}$$

where the fictitious field $U(1,2)$, introduced as a perturbation ($U \to 0$), mimics the polarisation induced in the system. Schwinger's equation (5.7) tells us that the difference between the propagation of a non-interacting (GG) pair and an interacting (G_2) pair is equal to the variation $\delta G/\delta U$. L is a two-particle (or 4-point) correlation function. The equation (5.7) holds also at non-vanishing U, therefore the field U must also be added to the single-particle Hamiltonian for the derivation to be consistent.

If one inserts (5.7) into (5.6) and makes use of $-iG(1,1^+) = \rho(\mathbf{r}_1, t_1, \sigma_1)$, the integro-differential functional equation

$$\left[i\frac{\partial}{\partial t_1} - H_0(\mathbf{r}_1) - U(1) - V_H(\mathbf{r}_1)\right] G(1,2) = \delta(1,2) + i\int d3 v(\mathbf{r}_1,\mathbf{r}_3)\frac{\delta G(1,2)}{\delta U(3)} \tag{5.8}$$

is obtained.

The solution of this equation has been recently the subject of the works of G. Lani [55] and M. Guzzo [5] and it will be addressed also in this thesis in the theoretical development chapters. Since this chapter is an introduction to state-of-the-art methods and theories, I will follow here the usual way to solve the equation of motion which relies on the concept of self-energy.

The Dyson equation and the self-energy

To overcome the problem of solving such a complicated differential equation, the concept of self-energy is introduced[18]

$$\Sigma(1,2) := iv(\mathbf{r}_1,\mathbf{r}_3)\frac{\delta G(1,4)}{\delta U(3)}G^{-1}(4,2)d3d4 \tag{5.9}$$

which inserted into (5.8) leads to the Dyson equation [56, 57] for the Green's function[19]

$$\left[i\frac{\partial}{\partial t_1} - H_0(\mathbf{r}_1) - U(1) - V_H(\mathbf{r}_1)\right]G(1,2) - \int \Sigma(1,3)G(3,2)d3 = \delta(1,2)\ . \tag{5.10}$$

By defining the Hartree Hamiltonian $H_H(1) := H_0(\mathbf{r}_1) + U(1) + V_H(\mathbf{r}_1)$, then the Hartree and the fully-interacting Green's functions G_H and G are formally defined as the resolvent of the following many-body operators

$$G_H^{-1}(1,2) := \delta(1,2)\left[i\frac{\partial}{\partial t_1} - H_H(1)\right] \qquad \text{and} \tag{5.11}$$

$$G^{-1}(1,2) := i\delta(1,2)\frac{\partial}{\partial t_1} - H(1,2) = G_H^{-1}(1,2) - \Sigma(1,2) \tag{5.12}$$

having defined the effective Hamiltonian $H(1,2) := H_H(1)\delta(1,2) + \Sigma(1,2)$.

The Dyson equation offers a clear physical interpretation of the Green's function: in fact it can be rewritten as an infinite sum

$$\begin{aligned} G(1,2) = G_H(1,2) &+ \int G_H(1,3)\Sigma(3,4)G_H(4,2)d3d4 + \\ &+ \int G_H(1,3)\Sigma(3,4)G_H(4,5)\Sigma(5,6)G_H(6,2)d3d4d5d6 + \dots\ . \end{aligned}$$

This way of writing puts in evidence the self-consistent relation determining G, that is the essence of the Dyson equation. In propagating inside the system, the undressed particle G_H induces a polarisation which in turns determines a change in its propagation, which induces a new polarisation and so on... The fully interacting G is the self-consistent solution of the Dyson equation and it is the limit of the infinite sum reported above.

The physical meaning of the self-energy $\Sigma[G]$ is finally clear. It plays the role of an effective field describing the response of the entire system to the propagation of a particle (hole or electron). It is determined by, and it determines, the solution of the equation in a self-consistent way. Its role is thus very similar to that played by V_{xc} in the KS scheme. Let us go deeper in this analogy.

[18] In the referenced article [53] the self-energy is defined $\Sigma = \Sigma_H + \Sigma_{\text{xc}}$ where Σ_{xc} corresponds to the self-energy of this work (5.9) and $\Sigma_H = V_H$ is the Hartree contribution.

[19] Here we keep $U \neq 0$. Normally when one works with Σ, $U \to 0$, but we will need U later on. Hence all quantities are functionals of U.

5.1.2 The quasi-particle equation

The poles of G appearing in the Lehmann representation (5.3) are real and discrete excitation energies. Correspondingly the spectral function (5.5) is a set of delta functions $\delta(E_m - \omega)$. The excitations in finite systems (molecules, clusters) are discrete and well separated in energy, so the poles of the spectral functions are delta-functions separated by finite energy differences. To study infinite systems, the thermodynamic limit is taken, hence the spectrum of possible excitations constitutes a continuum, and accordingly the poles of G get closer and closer. By consequence G is no longer defined in the whole positive real axis.

One great advantage of the KS theory is the possibility to work in an independent-particle framework. In infinite systems though, the occurrence of a continuum of excitations, complicates the interpretation in terms of independent excitations. Instead of describing the bare particles interacting via the bare Coulomb interaction v, one prefers to handle dressed particles, or quasiparticles, that are bare particles together with the screening cloud surrounding them. Quasiparticles are still fermions, but with a lower (renormalised) charge. As a consequence quasiparticles interact via the screened Coulomb interaction $W = \epsilon^{-1}v$.

In the limit $U = 0$, the effective Hamiltonian introduced in (5.12) depends only on time differences, hence on only one frequency. With an analytical continuation in the complex plane ($\omega \to z$), the now non-hermitian operator $H(z)$ can be diagonalised for each z by solving the left and right equations

$$\begin{aligned} [H_0(\mathbf{r}_1) + V_H(\mathbf{r}_1)]\,\Phi_j(\mathbf{r}_1, z) + \int \Sigma(\mathbf{r}_1, \mathbf{r}_2, z)\Phi_j(\mathbf{r}_2, z)d\mathbf{r}_2 &= E_j(z)\Phi_j(\mathbf{r}_1, z) \qquad (5.13)\\ \bar{\Phi}_j(\mathbf{r}_1, z)\,[H_0(\mathbf{r}_1) + V_H(\mathbf{r}_1)] + \int \bar{\Phi}_j(\mathbf{r}_2, z)\Sigma(\mathbf{r}_2, \mathbf{r}_1, z)d\mathbf{r}_2 &= E_j^*(z)\bar{\Phi}_j(\mathbf{r}_1, z)\ . \end{aligned}$$

Correspondingly $G(z)$ (analytic continuation of $G(\omega)$) is the resolvent of $H(z)$ hence it can be written in terms of its eigenvectors and eigenvalues

$$G(\mathbf{r}_1, \mathbf{r}_2, z) = \sum_j \frac{\bar{\Phi}_j(\mathbf{r}_1, z)\Phi_j(\mathbf{r}_2, z)}{z - E_j(z)}\ . \qquad (5.14)$$

Note how this expression differs from the Lehmann representation (5.3) in the dependence on z of both the eigenfunctions and the eigenvalues.

One can consider that main contributions to $G(z)$ come from the poles of (5.14), which are found for those complex energies E_j^{QP} obeying $E_j^{QP} - E_j(E_j^{QP}) = 0$. These are found by solving the quasiparticle equation

$$[H_0(\mathbf{r}_1) + V_H(\mathbf{r}_1)]\,\phi_j^{QP}(\mathbf{r}_1) + \int \Sigma(\mathbf{r}_1, \mathbf{r}_2, E_j^{QP})\phi_j^{QP}(\mathbf{r}_2)d\mathbf{r}_2 = E_j^{QP}\phi_j^{QP}(\mathbf{r}_1) \qquad (5.15)$$

which is nothing else than the re-writing of (5.13) in $z = E_j^{QP}$, with the definition of the quasiparticle wave functions $\phi_j^{QP}(\mathbf{r}) = \Phi_j(\mathbf{r}, E_j^{QP})$. The Lehmann representation of the Green's function is therefore

$$G(\mathbf{r}_1, \mathbf{r}_2, \omega) = \sum_j Z_j \frac{\phi_j^{QP}(\mathbf{r}_1)\phi_j^{QP\,*}(\mathbf{r}_2)}{\omega - E_j^{QP}} \quad \text{with} \quad Z_j = \left[1 - \left.\frac{dE_j(z)}{dz}\right|_{z=E_j^{QP}}\right]^{-1}\ , \qquad (5.16)$$

where Z_i are renormalization factors coming from an expansion of $E_j(z)$ around the pole E_j^{QP}. A pictorial illustration of the idea laying beneath the quasiparticle representation and the Lehmann representation is depicted in Fig. 5.1.

It is useful to compare (5.15) with (3.10)

$$[H_0(\mathbf{r}_1) + V_H(\mathbf{r}_1)]\,\phi_j^{KS}(\mathbf{r}_1) + V_{\rm xc}(\mathbf{r}_1)\phi_j^{KS}(\mathbf{r}_1) = \varepsilon_j \phi_j^{KS}(\mathbf{r}_1) \tag{5.17}$$

$$[H_0(\mathbf{r}_1) + V_H(\mathbf{r}_1)]\,\phi_j^{QP}(\mathbf{r}_1) + \int \Sigma(\mathbf{r}_1, \mathbf{r}_2, E_j^{QP})\phi_j^{QP}(\mathbf{r}_2)d\mathbf{r}_2 = E_j^{QP}\phi_j^{QP}(\mathbf{r}_1)\ . \tag{5.18}$$

Now that an effective single-particle-like picture has been introduced also in the Green's function formalism, the similar role played by Σ and $V_{\rm xc}$ is much more evident. Despite the much higher complexity of the self-energy operator, the Dyson equation offers a systematic way to expand it and approximate it, whereas approximations for $V_{\rm xc}[\rho]$ are much more difficult to devise. The expansion of Σ in terms of the screened Coulomb potential W and one particular approximation are the subject of next section.

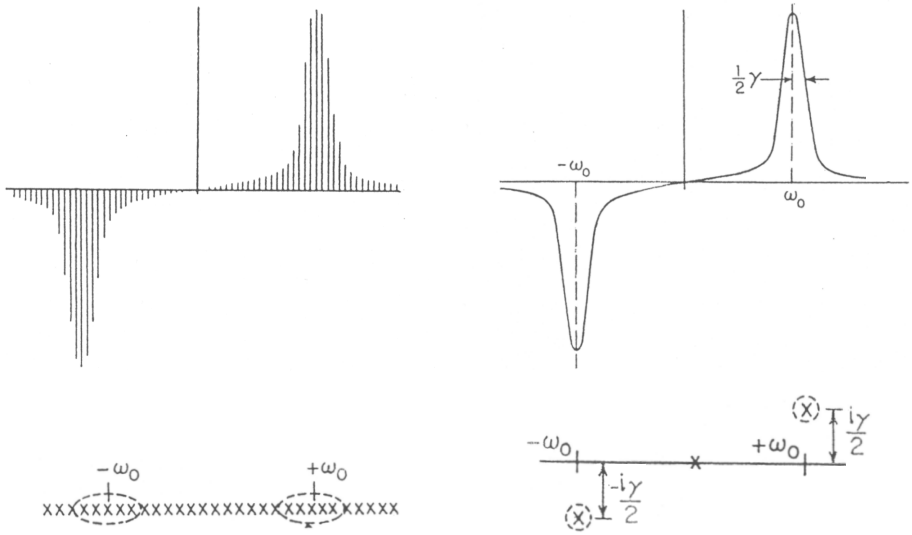

Figure 5.1: Pictorial representation of the difference between the Lehmann representation (on the left) and the quasiparticle representation (on the right). In the thermodynamic limit, an infinite number of delta-like poles on the real axis (noted as crosses) forming a continuum can be represented as separated poles with a non vanishing imaginary part. Image taken from [1].

5.1.3 Hedin's equations and the GW approximation

In small systems as atoms and molecules, the main effect beyond the Hartree interaction is the exchange, exactly described by the Hartree-Fock operator. In the language of Green's functions, the Hartree-Fock operator corresponds to a self-energy $\Sigma = iGv$ where v is the bare Coulomb interaction. In extended systems the bare exchange is not a good approximation and an expansion of Σ in powers of the bare Coulomb interaction is ill-defined.

Lars Hedin has stressed the fact that in extended systems the main effect beyond Hartree-Fock is the screening of the charged particles (holes and electrons). This effect of the dynamical correlation damps the long-range contribution of v. Following this intuition and inspired by preceding works, e.g. [58], he proposed [59] an expansion of Σ in powers of the

screened interaction $W = \epsilon^{-1}v$, presenting a closed set of five equations

$$G(1,2) = G_H(1,2) + \int G_H(1,3)\Sigma(3,4)G(4,2)d3d4 \tag{5.19}$$

$$\Sigma(1,2) = i\int G(1,3)W(4,1)\Gamma(3,2,4)d3d4 \tag{5.20}$$

$$W(1,2) = v(1,2) + \int v(1,3)\tilde{P}(3,4)W(4,2)d3d4 \tag{5.21}$$

$$\tilde{P}(1,2) = -i\int G(1,3)G(4,1)\Gamma(3,4,2)d3d4 \tag{5.22}$$

$$\Gamma(1,2,3) = \delta(1,3)\delta(1,2) + \\ + \int \frac{\delta\Sigma(1,2)}{\delta G(4,5)}G(4,6)G(7,5)\Gamma(6,7,3)d4d5d6d7 \tag{5.23}$$

where the first equation is the Dyson equation (5.10), the second defines the self-energy, the third is a Dyson equation for the screened Coulomb interaction W in terms of the irreducible polarizability $\tilde{P}(1,2) := \delta\rho(1)/\delta V_{\rm tot}(2)$ and the last is the Dyson equation for the irreducible vertex function $\Gamma(1,2,3) = -\delta G^{-1}(1,2)/\delta V_{\rm tot}(3)$. The potential $V_{\rm tot} = U + V_H$ is the sum of all classical potentials acting on the system.

These five equations can be derived directly from (5.6) and (5.7) taking $U = 0$ at the end of the calculation. They form Hedin's pentagon reported schematically also in Fig. 5.2. In principle they must be solved self-consistently.

The vertex Γ defined

$$\Gamma(123) := -\frac{\delta G^{-1}(1,2)}{\delta V_{\rm tot}(3)} \tag{5.24}$$

contains electron-hole and particle-particle interactions. It is found in the description of the irreducible polarizability $\tilde{P}$ (5.22) and in the definition of Σ (5.20). It is itself defined by a Dyson equation (5.23).

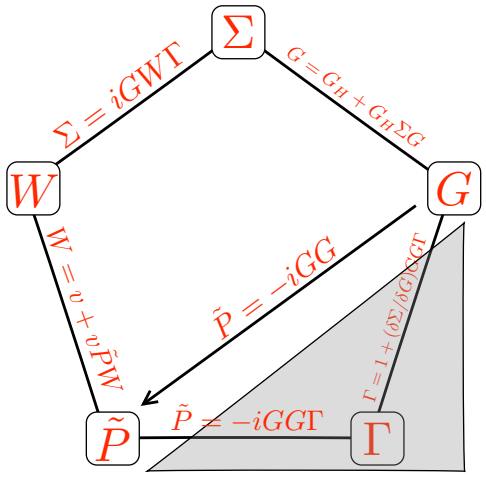

Figure 5.2: Hedin's pentagon. The GW approximation (see text below) skips the calculation of the vertex Γ (shaded area). Correspondingly the $\tilde{P} = -iGG$ is a shortcut for the GW circle.

In the expression of the irreducible polarizability $\tilde{P} = -iGG\Gamma$ one recognizes the independent propagation of the electron and the hole (the group GG) and the interaction between the two caused by the vertex Γ. In a similar way, the self-energy is described by the propagation of a particle (G) which interacts with the rest of the system ($W\Gamma$). Using the definition of the irreducible polarizability and the chain rule, the reducible polarizability $P = \delta\rho/\delta U$ can be obtained as solution of a Dyson equation

$$P(1,2) = \frac{\delta\rho(1)}{\delta U(2)} = \tilde{P}(1,2) + \tilde{P}(1,3)v(3,4)P(4,2) = \tilde{P}(1,3)\epsilon^{-1}(3,2)\ . \tag{5.25}$$

The first equality is the time-ordered analogous[20] of equation (4.7); in deriving the last equation, the definition $\epsilon^{-1} = \delta V_{\rm tot}/\delta U$ has been used.

[20]There is another difference beyond the fact that $\tilde{P}$ is time ordered and χ^{KS} is retarded. In equation (4.7) I make explicit reference to the KS system, where exchange-correlation effects are inserted in the potential and in $f_{\rm xc}$. Instead, in the equation above, $V_{\rm tot}$ is classical. A true retarded analogous of (5.25) would be $\chi = \tilde{\chi} + \tilde{\chi}v\chi$ with $\tilde{\chi} = \delta\rho/\delta V_{\rm tot}$ irreducible susceptibility for which χ^{KS} is sometimes a good approximation.

GW approximation

In practice, iterating Hedin's pentagon until full self-consistency is impossible. The most demanding quantity to compute is the 3-point vertex Γ. An approximation suggested by Hedin [59] is to take the 0-th order of the vertex at every cycle of the pentagon, that is

$$\Gamma(1,2,3) \approx \delta(1,3)\delta(1,2) \; . \tag{5.26}$$

This approximation defines therefore a shorter self-consistent circle, drawn in Fig. 5.2 as the non-shaded arrows.

Neglecting the vertex correction leads to a polarizability

$$\tilde{P}(1,2) \approx -iG(1,2)G(2,1) \; . \tag{5.27}$$

In this approximation, both the electron and the hole fully interact with the system (they are dressed G)[21], but they are mutually independent (no e-h interaction).

The approximation (5.26) is known as GW approximation (GWA) because of the resulting shape of the self-energy which reads

$$\Sigma(1,2) \approx iG(1,2)W(2,1) \; . \tag{5.28}$$

The GW self-energy is a product in time (and space), so its Fourier transform is the convolution

$$\Sigma(\mathbf{r},\mathbf{r}',\omega) = \frac{i}{2\pi}\int e^{-i\delta\omega'} G(\mathbf{r},\mathbf{r}',\omega-\omega')v(\mathbf{r}',\mathbf{r})d\omega' + \tag{5.29}$$

$$+ \; \frac{i}{2\pi}\int e^{-i\delta\omega'} G(\mathbf{r},\mathbf{r}',\omega-\omega')W_p(\mathbf{r}',\mathbf{r},\omega')d\omega' \; . \tag{5.30}$$

where $W = v + v\chi v = v + W_p$ has been divided into a static (bare Coulomb) component and a dynamic part and $\delta \to 0^+$ is needed to ensure convergence of the Fourier transform. The first term gives the exchange self-energy $\Sigma_{\rm x} = iGv$, whereas the dynamical contributions define the correlation part of the self-energy $\Sigma_{\rm c} = iGW_p$.

Most practical implementations of the Green's function approach for real systems rely on the GWA. In the next section I will present how it is used in practice, together with some of its limitations and strong points.

5.1.4 GW in practice

Even avoiding the calculation of the vertex Γ, reaching self-consistency in the GW equations is far from obvious: only recently it has been possible to perform calculations of fully self-consistent GW, but only on small systems and still some short-cut is needed to make the calculations computationally feasible [60].

Although approximated self-consistent approaches have been proposed and employed in the past (CohSex, QPscGW and Hedin's [2]), much more diffused are the "one shot GW" or G_0W_0 methods, which are based on a single iteration of the GW cycle starting from an appropriate Green's function G_0.

[21] If the Green's function appearing in this expression are G_H, that would be the RPA or time-dependent Hartree approximation in the Green's function formalism.

a) The first GW iteration: the G_0W_0 scheme

In the G_0W_0 scheme only the first iteration of the GW circle of Fig. 5.2 is done. One starts from the wave functions ϕ^0 and energies ε^0 obtained in an independent-particle picture (typically in the KS scheme), and makes use of equation (5.16) to construct an initial guess G_0. With the same states and energies, also the screening ϵ^{-1} and the screened Coulomb interaction W_0 are computed, most often within the RPA. The G_0W_0 self-energy is then obtained following equation (5.28), and the Dyson equation is solved, getting an interacting Green's function $G^{G_0W_0}$ including dynamical correlation effects.

By far, the most widely used application of the G_0W_0 method is the computation of the real part of the quasiparticle energies in order to get reliable single-particle excitation energies such as the extraction energies, or the HOMO-LUMO gap. Looking back to equations (5.17) and (5.18), one can compute quasiparticle energies from KS energies treating the difference $\Sigma - V_{\text{xc}}$ as a perturbation to the KS Hamiltonian. In first order perturbation theory, the correction energy $\Delta E_i = E_i^{QP} - \varepsilon_i^{KS}$ to the state i is

$$\Delta E_i = \Sigma_i(E_i^{QP}) - V_i^{\text{xc}} = \int \phi_i^*(\mathbf{r}) \left[\Sigma(\mathbf{r}, \mathbf{r}', E_i^{QP}) - V_i^{\text{xc}}(\mathbf{r})\delta(\mathbf{r}, \mathbf{r}')\right] \phi_i(\mathbf{r}')d\mathbf{r}d\mathbf{r}'$$

where the states ϕ_i are the KS states[22].

In principle, to solve the equation above, one should know the full function $\Sigma(\omega)$. Otherwise, and in the majority of cases, a linear approximation for the self-energy is made, leading to the expression

$$E_i^{QP} - \varepsilon_i^{KS} = \mathcal{Z}_i \left[\Sigma_i(\varepsilon_i^{KS}) - V_i^{\text{xc}}\right] \quad \text{with} \quad \mathcal{Z}_i := \frac{1}{1 - \left(\partial\Sigma_i(\omega)/\partial\omega\right)_{\omega=\varepsilon_i^{KS}}} \,. \tag{5.31}$$

The performance of this method to compute the band structure of some real materials can be appreciated in Fig. 5.3 where the LDA starting point is marked with red squares (note the systematic underestimation) and the G_0W_0 gap energies are reported as blue dots (image taken from [61]). The renormalization factor $\mathcal{Z}$ accounts for the redistribution of the spectral weight from the quasiparticle peak to other structures called satellites. This is due to the dynamical structure of the self-energy, and is a signature of the coupling between the hole (electron) and other neutral excitations of the system. Static approximations (such as HF, CohSex or QPscGW) give $\mathcal{Z} = 1$: no satellite is predicted and the quasiparticle peak is indeed a delta-function at the energy E_i^{QP}.

Renormalization moves spectral weight to satellites. The equations above do not contain information about structures beyond the quasiparticle peaks, except their intensity (the spectral weight is indeed conserved). To investigate the full spectrum of single-particle excitations one has to look at the spectral function $\mathcal{A}_i(\omega)$, introduced in equation (5.5) and here expressed in a single-state basis as function of the self-energy (cfr. also expression (1.3))

$$\mathcal{A}_i(\omega) = \frac{1}{\pi} \frac{|\Im[\Sigma_i(\omega)]|}{\left(\omega - E_i^H - \Re[\Sigma_i(\omega)]\right)^2 + \Im[\Sigma_i(\omega)]^2} = \frac{1}{\pi} \frac{|\mathcal{I}_i(\omega)|}{\mathcal{R}_i(\omega)^2 + \mathcal{I}_i(\omega)^2} \,. \tag{5.32}$$

The imaginary part $\mathcal{I}(\omega) = \Im[\Sigma(\omega)]$ and the shifted real part $\mathcal{R}(\omega) = \omega - E^H - \Re[\Sigma]$ have been introduced to simplify future discussions. For an example refer to Fig. 5.4, reporting

[22]The assumption $\phi^{KS} \approx \phi^{QP}$ is often a good approximation, but in some cases a different zero-order Hamiltonian must be chosen, for instance the CohSex (see below).

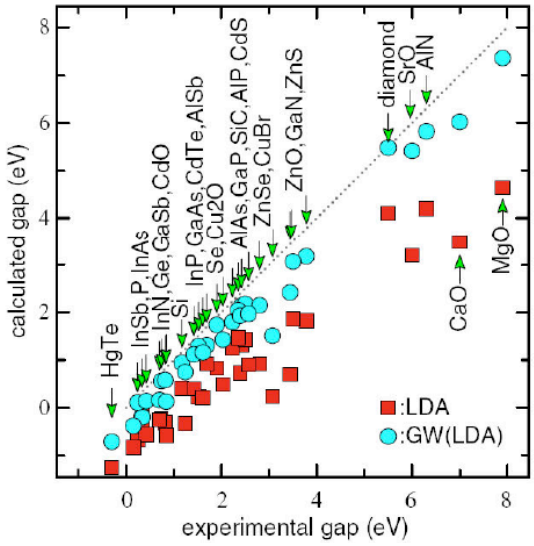

Figure 5.3: G_0W_0 and LDA HOMO-LUMO gaps for selected materials versus their experimental values. LDA systematically underestimates the gap, whereas G_0W_0 calculations show a better agreement, but still dependent on the starting LDA calculation. Image taken from [61].

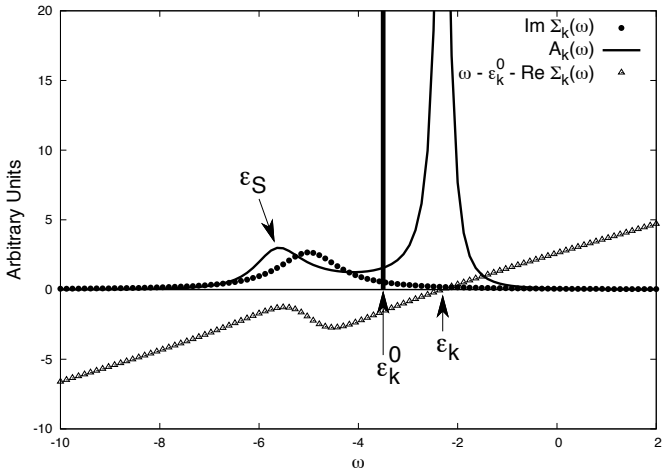

Figure 5.4: The function $\mathcal{A}_k(\omega)$ of a static self-energy is a delta-peak at energy ε_k^0 (here Hartree energy). In the case of a dynamical Σ, the spectral function $\mathcal{A}_k(\omega)$ (balck solid) is a broadened peak at ε_k with a satellite at energy ε_S given by the interplay of function $\mathcal{I}_k(\omega)$ (peaked at the plasmon resonance) and $\mathcal{R}_k(\omega)$.

a comparison between $\mathcal{A}_k(\omega)$ computed with a static self-energy (thick line) and with a dynamical self-energy (thin solid line). The functions $\mathcal{R}$ and $\mathcal{I}$ are also reported with triangles and dots.

This kind of calculation is more cumbersome than the previous one because Σ is needed at all energies.

b) Different self-consistent schemes

The general framework of a self consistent scheme starts from an initial guess G^0 (0-th order input), and the successive calculation of a new Green's function G^1, that passes through the calculation of W, Σ and the inversion of an appropriate Dyson equation. The output G^1 is the output of the first iteration which is used as input for the second and so on until the condition $G^n = G^{n+1}$ is met and convergence achieved[23].

A full self-consistent scheme seems to be crucial for total energy calculations [62, 63], but calculations performed on the homogeneous electron gas [64] indicate that spectral features would not be reproduced correctly. Structures of $\mathcal{A}$ are degraded at each iteration of the Dyson equation, because of the neglect of the vertex Γ in the self-energy and in W and the resulting underestimation of the screening. It has indeed been demonstrated that self-consistency and vertex correction have opposite sign [65–67], so the neglect of only one of the two may lead to severe errors. Following this argument, partial self-consistency is preferable.

[23]The self-consistency condition input=output is checked on specific quantities, such as quasiparticle energies, or eigenfunctions. Moreover the iteration scheme can be more complicated than this: the input of one cycle can be "mixed" with a previous input to stabilise the iterative algorithm. I will not enter in detail of convergence criteria or iterative methods, my aim being that of presenting an overview on state-of-the-art techniques.

In particular a scheme leading to good results in the homogeneous electron gas [68] seems to be an update of only the poles of G and not of W, that constitutes an energy-only GW_0 self-consistent approach.

Let us go now through the state-of-the-art partial self-consistent schemes applied to real materials. Original results obtained with the latter two will be presented in Chapter 8.

Coulomb hole plus screened exchange (CohSex) : A first static and Hermitian approximation of the GW self-energy has been introduced by Hedin in [59]. The exchange and correlation part of the self-energy are approximated according to

$$\begin{aligned}\Sigma^{\text{CohSex}}(\mathbf{r},\mathbf{r}') &= \Sigma^{\text{Sex}}(\mathbf{r},\mathbf{r}') + \Sigma^{\text{Coh}}(\mathbf{r},\mathbf{r}') \\ \Sigma^{\text{Sex}}(\mathbf{r},\mathbf{r}') &= -\sum_{i}^{\text{occ.}} \phi_i(\mathbf{r}) W(\mathbf{r},\mathbf{r}',\omega=0)\phi_i^*(\mathbf{r}') \\ \Sigma^{\text{Coh}}(\mathbf{r},\mathbf{r}') &= \frac{1}{2}\delta(\mathbf{r}-\mathbf{r}')W_p(\mathbf{r},\mathbf{r}',\omega=0)\end{aligned} \tag{5.33}$$

where one recognises a screened exchange term in Σ^{Sex}, and the creation of a charged particle polarizing the system (Coulomb hole) in Σ^{Coh}.

When it was introduced, this approximation was not meant to be used specifically for self-consistent calculations, but given the properties of the CohSex self-energy, this scheme can actually be employed in an iterative scheme. Often self-consistent CohSex is the method of choice when KS is found to be a poor starting points for G_0W_0 calculations [69].

Quasiparticle self-consitent GW (QPscGW) : The scheme proposed by Faleev and coworkers in [61, 70] relies on a different static approximation for the self-energy. The $(n+1)$-th step of the QPscGW self-energy reads

$$\Sigma_{ij}^{\text{QPGW}} = \frac{1}{2}\Re\left[\langle i_n|\Sigma(\varepsilon_i^n) + \Sigma(\varepsilon_j^n)|j_n\rangle\right] \tag{5.34}$$

where the Σ is the true GW self-energy, therefore diagonal elements of Σ^{QPGW} are exact in the GW scheme. The Hamiltonian resulting from this self energy is hermitian and static, thus it can be diagonalised. New states $|i_{n+1}\rangle = \phi_i^{n+1}(\mathbf{r})$ and energies ε_i^{n+1} are then obtained. The computed energy gap versus the experimental gap of some materials is reported in Fig. 5.5.

In many cases, the KS states can be considered a good approximation to any n-th order states (that is $\phi_i^n = \phi_i^{KS}$ for all n), consequently only energies are updated. Moreover, in this case the self-energy becomes diagonal on the DFT basis and only diagonal elements of (5.34) are needed.

Hedin's approximation to self-consistency (see Ref. [2]): The approximation described here does not rely on a self-consistent scheme. Indeed it is a one-shot GW calculation made from a wisely chosen G^{Δ}.

When employing the energy-only self-consistent scheme in G, the difference between the n-th step Green's function and G^{∞} is only on the position of the poles. At the self-consistent condition, input and output coincide: $G^{n-1} = G^n$.

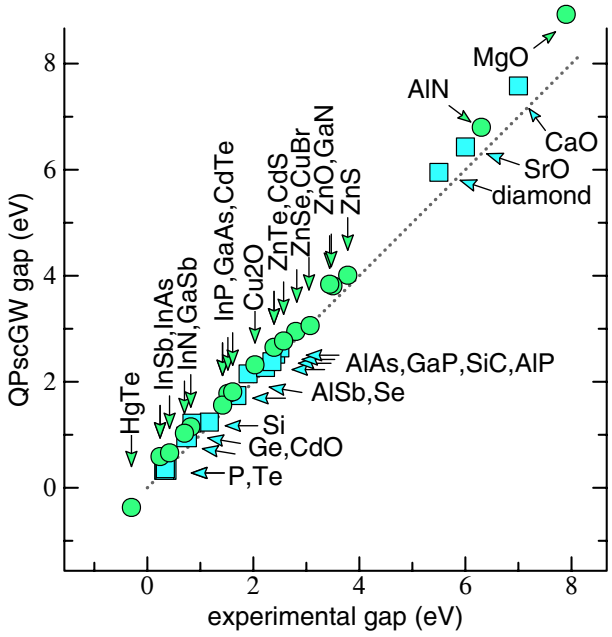

Figure 5.5: QPscGW energy gap versus their experimental values. Circles are relative to zinc-blende compounds with direct Γ-Γ gap, while squares are other kind of compounds. The agreement with experimental gap is much higher with respect to G_0W_0 calculations (see Fig. 5.3). A systematic small overestimation is observed. Image taken from [61].

The input Green's function is the generic G^Δ defined according to

$$G^\Delta(\mathbf{r},\mathbf{r}',\omega) = \sum_i \frac{\phi_i(\mathbf{r})\phi_i^*(\mathbf{r}')}{\omega - \varepsilon_i^{KS} - \Delta \pm i\eta}$$

where the $\pm$ sign depends whether the state i is empty $(-)$ or occupied $(+)$. The energy shift Δ, not specified for the moment, allows for a generic position of the poles of G^Δ, but note that it does not depend on the state i, so the poles of G are rigidly shifted. States $\phi_i(\mathbf{r})$ are KS eigenstates[24].

When computing $G_0W_0$with this generic Green's function the resulting self-energy Σ^Δ is such that

$$\Sigma^\Delta(\mathbf{r},\mathbf{r}',\omega) = \Sigma^0(\mathbf{r},\mathbf{r}',\omega-\Delta)\ , \tag{5.35}$$

as it is clear from equations (5.29) and (5.30), where $\Sigma^0 = \Sigma^{\Delta=0}$ corresponds to the $\Sigma^{G_0W_0}$ computed on top of a KS calculation. The generic spectral function of G^Δ can be computed according to equation (5.32)

$$\mathcal{A}_i^\Delta(\omega) = \frac{1}{\pi}\frac{|\Im[\Sigma_i^0(\omega-\Delta)]|}{\left(\omega - \varepsilon_i^{KS} + V_i^{\rm xc} - \Re[\Sigma_i^0(\omega-\Delta)]\right)^2 + \Im[\Sigma_i^0(\omega-\Delta)]^2} \tag{5.36}$$

where $\Sigma_i = \langle i|\Sigma|i\rangle$. Still, as long as the shift Δ in not fixed, the relation above is general.

[24]The derivation is not limited to the use of KS states and energies, and any single-particle scheme (such as Hartree Fock or CohSex) can be employed instead. In its original formulation [2] the Hartree eigenvalues are used.

The new energies E_i computed with Σ^Δ and the initial energies read respectively

$$\text{OUTPUT} : E_i = \varepsilon_i^{KS} - V_i^{\text{xc}} + \langle i|\Sigma^\Delta(E_i)|i\rangle \quad ; \quad \text{INPUT} : \varepsilon_i^{KS} + \Delta \, .$$

The energy shift Δ is then fixed by requiring the self-consistency condition at the Fermi level, i.e. $E_F^{\text{in}} = E_F^{\text{out}}$. This condition leads to two equations:

$$\Delta = \langle F|\Sigma^\Delta(E_F)|F\rangle - V_F^{\text{xc}} \quad \text{and} \quad E_F = \varepsilon_F^{KS} + \Delta \tag{5.37}$$

This fixes Δ, in fact using the second into the first and making use of relation (5.35), one defines

$$\Delta := \langle F|\Sigma^0(\varepsilon_F^{KS})|F\rangle - V_F^{\text{xc}} \, . \tag{5.38}$$

and the approximate self-consistent spectral function (5.36) can be computed using only quantities issued from a G_0W_0 calculation.

c) Computing the screening: approximations and techniques

The correlation self-energy is a convolution in frequency space, as depicted by (5.30). The most demanding step is the calculation of $W_p(\omega)$ at all frequencies. Two methods to perform the convolution integral are here presented, the first is an approximation based on a Plasmon pole model (PPM) for ϵ^{-1} and the second is the contour deformation method.

Plasmon pole model : Because of the integration over frequencies, one may disregard all the structures of $W_p(\omega)$, approximating the imaginary part of the screened interaction with a delta peak of appropriate weight. Each element of the inverse dielectric matrix $\epsilon^{-1}_{\mathbf{GG'}}(\mathbf{q},\omega)$ is then approximated with

$$\epsilon^{-1}_{\mathbf{GG'}}(\mathbf{q},\omega) = \delta_{\mathbf{GG'}} + \frac{\Omega^2_{\mathbf{GG'}}(\mathbf{q})}{\omega^2 - \bar{\omega}^2_{\mathbf{GG'}}(\mathbf{q})} \tag{5.39}$$

defined by two parameters: the plasmon energies $\bar{\omega}^2_{\mathbf{GG'}}(\mathbf{q})$ and their weights $\Omega^2_{\mathbf{GG'}}(\mathbf{q})$.

A fitting method is then required to fix the two parameters of the model. In the Godby-Needs scheme [71] these parameters are fitted on two calculations performed at $\omega = 0$ and $\omega = i\omega_p$, where ω_p is a real value, by preference close to the plasmon energy of the material. Other schemes have been devised exploiting e.g., sum-rules [72, 73].

This approximation is justified by the fact that for many materials the measured EELS is well described by a single peak centred at the plasmon energy (cfr. EELS of Si).

In some cases though, this approximation is not reliable because of the presence of several plasmon peaks on ϵ^{-1}. For example, kinks in the band structure of graphene have been shown to be due to low energy excitations, and they can only be described when at least two poles are used [74]. A multi-plasmon pole model may be used, or one has to perform the actual calculation of the convolution integral (5.30), for example with the contour deformation method.

Contour deformation method: To evaluate the self-energy integral on the whole real axis it is possible to exploit the residue theorem

$$\oint_C F(z)dz = 2\pi i \sum_{p\,:\,z_p \in C} \text{Res}[F(z_p)] \text{ with } z_p \text{ pole with multiplicity 1,}$$

where

$$\mathrm{Res}[F(z_p)] := \lim_{z\to z_p}(z-z_p)F(z)\ .$$

To this aim a contour C is chosen as in Fig. 5.6 and the correlation part of Σ (5.30) splits into two contributions

$$\Sigma_{\mathrm{c}}(\omega) = \frac{i}{2\pi}\int_{-i\infty}^{+i\infty} G(\omega+z)W_p(z)dz - \sum_{p\,:\,z_p}\lim_{z\to z_p} G(\omega+z)W_p(z)(z-z_p)$$

that are computed numerically by interpolating $W_p(\omega)$. To get reliable results, the interpolation requires the calculation of $\epsilon^{-1}(\omega)$ in several real (order of hundreds) and few imaginary frequencies. It is therefore much heavier than the PPM, but it gives more accurate results, especially when computing full spectral functions, and not only quasiparticle energies.

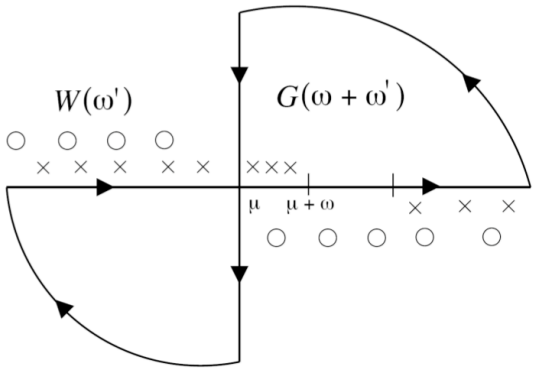

Figure 5.6: The integration path in the contour deformation method.

5.1.5 A focus on dynamical effects on the one-particle Green's function: GW and the cumulant expansion

In this section I will focus on how GW performs in describing the dynamical effects due to $\Sigma_{\mathrm{c}}(\omega)$. The dynamical self-energy broadens the quasiparticle peak, which loses intensity in favour of structures occurring at higher energy, called satellites.

We have seen (5.31) how the renormalization of the peak is usually accounted for. The renormalization factor $\mathcal{Z}_i$ indeed reduces the weight of the peak. This may give a measure of the importance of dynamical self-energy effects at the QP level. But to see satellites, one has to look at the spectral function (5.32) $\mathcal{A}_i$.

The full spectrum

In section 1.3.1, I introduced photoemission spectroscopy from an experimental point of view. I remember that the binding energy of the emitted electrons is

$$E_b = \hbar\omega - E_k - \varphi\ ,$$

that is the difference between the photon energy$\hbar\omega$, the kinetic energy E_k of the photoelectron and the work function φ of the system.

Referring to Fig. 1.5, relatively sharp peaks in the spectrum are observed in correspondence of the quasiparticle peaks, while at higher energies much broader structures are found at frequency intervals that multiples of the plasmon frequency. They are plasmon satellites[25]. As underlined in the introduction, the broadening of the quasiparticle peak with respect to an ideal (independent-particle) delta-function and the resulting creation of additional structures at higher energies are both clear signs of the dynamical correlation between the electrons of the system.

Given this experimental scenario, the question is "*How does the GWA describe the satellites?*"

The GW approximation and the plasmaron

To calculate satellites in the GWA, one has to compute the spectral function $\mathcal{A}$ according to expression (5.32)

$$\mathcal{A}(\omega) = \frac{1}{\pi}\frac{|\mathcal{I}(\omega)|}{\mathcal{R}^2(\omega) + \mathcal{I}^2(\omega)} \,, \tag{5.32-bis}$$

where the state index i has been dropped for simplicity, and the functions $\mathcal{I} = \Im[\Sigma(\omega)]$ and $\mathcal{R}(\omega) = \omega - E^H - \Re[\Sigma(\omega)]$ have the same meaning as in (5.32).

Looking at (5.32-bis), one realises that structures are found essentially when energy ω is such that:
i) either $\mathcal{R}(\omega) = 0$ and $\mathcal{I}(\omega) \approx 0$ (vanishing denominator),
ii) or $\mathcal{I}(\omega)$ has a significant peak and $\mathcal{R}(\omega)$ is not too large and does not cross the zero line.
In the first case (i), sharp peaks are observed. We speak of quasiparticle (QP) peak when the structure is in one-to-one correspondence to a peak in the non interacting spectral function, and we speak of plasmaron [75, 76] in all other cases. The second case (ii) usually gives rise to broader and less intense structures, corresponding to plasmon satellites, ascribed to the coupling of the QP with neutral collective excitations of the system. Again, other kinds of coupling can be observed when one goes beyond GW.

The concept of plasmaron has been introduced initially by L. Hedin who discovered it in the homogeneous electron gas [75]. He pointed it out as a novel quasiparticle-plasmon bound state. It is found in the spectral function $\mathcal{A}(\omega)$ at energies where the imaginary part of the self-energy $\mathcal{I}$ is small and $\mathcal{R} = 0$. So it has the same characteristics of a quasiparticle, but it is found at higher binding energy.

Later, D. C. Langreth [77] showed on a model Hamiltonian that the correct spectrum of excitations is indeed a series of satellites separated from the QP peak by multiples of the plasmon energy, which is experimentally observed in core-electron photoemission spectroscopy. Therefore the plasmaron has been first interpreted as an average of the correct solution, and eventually recognised as a spurious product of GW [76].

A complete treatment of the problem and a historical overview are beyond our scope, rather we refer the interested reader to a recent work of M. Guzzo [5] and especially to his Ph.D. thesis [78].

But other satellites are described by the spectral function: they fall in the case ii), where the numerator dominates. Since $\mathcal{I}(\omega) \propto \Im[W(\omega)]$, it has structures at energies corresponding

[25]There are also other kind of satellites, for example structures due to hole-hole bound states.

to essentially plasmon resonances. Because of the Kramers-Kronig relations between $\mathcal{I}$ and $\mathcal{R}$, when the first has a structure (let us say in ω_p), the latter oscillates and has a peak at energy $\tilde{\omega}$, usually higher than ω_p (see Fig. 5.4 for a qualitative description). As a consequence the spectral function $\mathcal{A}$ happens to have a plasmonic peak at a binding energy $E = \omega_p + \delta$ higher than the true plasmon frequency. The entity of the discrepancy δ depends on the system and may be of the order of some eV. Moreover, each plasmonic structure of $\mathcal{I}$ creates only one structure on $\mathcal{A}$, so satellite replicas are not reproduced.

We can conclude that GW is not a good approximation for the description of satellites. Main responsible is the real part of the self-energy $\Re[\Sigma(\omega)]$ which, whit its peaks, can generate unphysical peaks by crossing the zero (plasmarons), or shift plasmon satellites to too large binding energies.

The Cumulant expansion and the satellite series

The cumulant expansion

$$G_l(\tau) = i\theta(-\tau)e^{-iE_l^{QP}\tau + C_l(\tau)} \tag{5.40}$$

is an ansatz for the single-particle Green's function (here reported for the hole contribution). One assumes an exponential form for G, moreover states are assumed decoupled. The cumulant function $C_l(\tau)$ contains dynamical one-particle effects. An exponential G is obtained as exact solution of the quasi-boson Hamiltonian [77], where an electron is coupled with a boson reservoir (e.g. plasmons), but it can be derived also by an analogy with statistical concepts [79, 80] or by manipulations of the Dyson equation [81].

By expanding (6.1) in powers of C

$$G_l(\tau) \;=\; i\theta(-\tau)e^{-iE_l^{QP}\tau}\left[1 + C_l(\tau) + \frac{1}{2}C_l^2(\tau) + O(3)\right], \tag{5.41}$$

and approximating $C_l \approx \lambda_l e^{-i\omega_l\tau}$ with a plasmon pole[26], the series reads

$$\begin{aligned} G_l(\tau) &= i\theta(-\tau)e^{-iE_l^{QP}\tau}\left[1 + \lambda_l e^{-i\omega_l\tau} + \frac{\lambda_l^2}{2}e^{-i2\omega_l\tau} + O(3)\right], \\ G_l(\omega) &= Z_l\left[\frac{1}{\omega - E^{QP} - i\eta} + \frac{\lambda_l}{\omega - (E^{QP}+\omega_l) - i\eta} + \frac{\lambda_l^2}{\omega - (E^{QP}+2\omega_l) - i\eta} + O(3)\right] \end{aligned}$$

where Z_l is a renormalization factor. In the last expression we recognize a series of peaks at energies that are integer multiples of the plasmon peak. So, what was not reproduced by the GWA is indeed given by the cumulant expansion formalism.

Recently [55, 82], the exponential form of G has been derived from (5.8) by linearizing the Hartree potential with respect to the external field U and assuming decoupled states. The idea has been to abandon the Dyson equation and the concept of self-energy, in favour of the differential equations formalism. This new derivation led to a correct description of satellite structures in Si [5] and in bulk graphite [78], and allowed for prediction in undoped graphene (see [78] and Appendix D). Furthermore it is put in practice through a simple post-processing method of G_0W_0 spectra. The main interest in this recent derivation is

[26] This can be justified, e.g. by equating the first order of the expansion (5.41) with the first order of the Dyson equation (5.19) in the GW approximation for Σ. C is then expressed in terms of Σ and a plasmon pole can be used to approximate the screened Coulomb interaction.

not the exponential form itself, but it is indeed the way it is derived since it starts from a basic equation and makes use of simple approximation that can be generalised. Chapter 10 is actually devoted to the generalization of this approach to the case of two-particle phenomena (namely absorption).

5.2 Neutral excitations with MBPT

The Green's function formalism offers a natural framework also for the description of neutral excitations. As seen before, equation (5.22) gives the polarizability $\tilde{P} = -iGG\Gamma$ of the system in terms of the propagation of two particles (electron and hole) and the vertex Γ which accounts for the mutual interaction between them. Dielectric properties are strictly related to the polarizability of the system, as pointed out in the introduction. The key to access the polarizability is the 2-particle correlation function L[27] already introduced in Schwinger's equation[28] (5.7)

$$L(1,2,3,4) := -i \left.\frac{\delta G(1,2)}{\delta U(3,4)}\right|_{U=0} = iG(1,5)G(6,2) \left.\frac{\delta G^{-1}(5,6)}{\delta U(3,4)}\right|_{U=0} , \tag{5.42}$$

where integration over repeated variables is assumed. Second and third terms are related by differentiating the exact relation $\delta(1,2) = G^{-1}(1,3)G(3,2)$.

By using definitions (5.24) and (5.25) together with $\tilde{P} = -iGG$ and the chain rule, one gets the relation between the reducible polarizability (2-point function) and the 2-particle correlation function (4-point function):

$$P(1,3) = L(1,1,3,3) , \tag{5.43}$$

so the polarizability of the system can be obtained by contracting space and time variables of the 4-point function L.

It is possible to express L with a Dyson equation by combining definitions[29] (5.42), (5.11) and (5.12), with $V_H(5) = -iv(5,7)G(7,8)\delta(7,8)$ and exploiting the chain rule. The equation obtained in this way is the Bethe-Salpeter equation

$$\begin{aligned} &L(1,2,3,4) = \\ &= L^0(1,2,3,4) + L^0(1,2,5,6)\left[v(5,7)\delta(7,8)\delta(5,6) + \Xi(5,6,7,8)\right] L(7,8,3,4) \end{aligned} \tag{5.44}$$

which describes the propagation of two interacting particles inside a many-body environment in relation with the independent particles L^0 and the kernel Ξ defined as

$$L^0(1,2,3,4) := -iG(1,3)G(4,2) \qquad \text{and} \qquad \Xi(1,2,3,4) := i\frac{\delta\Sigma(1,2)}{\delta G(3,4)} . \tag{5.45}$$

Three contributions are recognised.

1) An "independent particle" contribution ($L^0 = -iGG$) , depicting the effect of the two

[27] The two particle correlation function describes the propagation of any particle pair: the electron-hole pair (exciton) as well as the electron-electron or hole-hole particle pairs. Since I am interested in neutral excitations, I will mostly refer to the two particles as electron and hole, but the following equations are general.

[28] All functional differentiations with respect to U are taken at vanishing U in the rest of this chapter, but this will be omitted from now on to simplify the notation.

[29] Note that in (5.42) one has to use the non local $U(1,2)$ instead of the local $U(1)$.

particles, propagating in the system. Each particle fully interacts with the environment (dressed G), but they are not interacting each other. Note the similarity between L^0 and the GW polarizability (5.27).
2) A term L^0vL representing the classical polarisation (Hartree) induced in the rest of the system by the particle pair.
3) The e-h direct interaction $L^0\Xi L$ which constitutes the strong point of this approach. The BSE kernel indeed includes explicitly the excitonic effect, that is the interaction between the electron and the hole. In contrast with the exchange-correlation kernel $f_{\rm xc}$ of TDDFT (4.8), systematic approximations for Ξ can be devised.

5.2.1 Approximations to the BSE

Independent Quasiparticle approximation and GW+RPA

The easiest approximation to the kernel is simply to neglect it. When $\Xi = 0$, left and right hand side of the BSE can be contracted before solving the equation, which leads to the 2-point equation

$$P(13) = P^0(13) + P^0(15)v(56)P(63) \; . \tag{5.46}$$

In the "independent particle term" $P^0(13) = -iG(13)G(31)$ each particle is represented by a fully interacting G. Dynamical self-energy effects (renormalization of the quasiparticle and resulting occurrence of satellite structures) are then accounted completely in the propagation of each particle, together with the bare e-h exchange contribution (P^0vP). What is missing is the direct particle-particle interaction. When only the quasiparticles are retained in the Gs composing P^0, that is G is written as in (5.16), then this formula has the name of Independent Quasiparticle (IQP) approximation.

In the IQP approximation, the intensity of absorption spectra is actually underestimated by ~ 30 % [83]. This is because the quasiparticle peak is renormalised by the dynamical factor $\mathcal{Z}$ introduced in (5.31), as a consequence a total renormalization $\propto \mathcal{Z}^2$ affects the weight of optical spectra leading to a strong underestimation of the structures. The profound reason of this underestimation of the spectra is related to the interplay between the dynamical self-energy and the dynamical BSE kernel.

I will come to this point later, for the moment I focus on a practical solution to this problem. In practice, it is preferable to compute an RPA spectrum as in (4.12) but substituting KS energies with quasiparticle energies, for instance computed using (5.31). Transition energies are therefore accurate, but the spectral weight is not lost because no dynamical effect on G is taken into account ($Z = 1$). I will refer to this approximation either with the name "GW+RPA" or "SO+RPA" depending whether GW or scissor operator have been used to compute quasiparticle energies.

GWA+BSE and Static screening approximation

To evaluate the kernel, one can rely on the GWA for which $\Sigma = iGW$. Disregarding the term $\delta W/\delta G$, the kernel $\Xi = i\delta\Sigma/\delta G$ can easily be computed, leading to

$$L(1234) = L^0(1234) + L^0(1256)\left[v(57)\delta(56)\delta(78) - W(56)\delta(57)\delta(68)\right]L(7834) \; . \tag{5.47}$$

This equation is still extremely difficult to solve because of the cumbersome time structure of the Kernel. In principle, $L(\mathbf{r}_{1234}, t_{1234})$ is a function of four times, that is three frequencies.

Results on the two-site Hubbard model [84] and on small molecular systems [85] have been computed, but applications to extended (infinite) systems are not feasible for the time being.

Instead, a static approximation to $W(t-t') = W\delta(t-t')$ is usually made. The time contractions $t_2 = t_1$ and $t_4 = t_3$ can then be done immediately (that is the simultaneous creation and recombination of the e-h pair). Consequently, one can Fourier transform the BSE equation,

$$\begin{aligned} &L(\mathbf{r}_{1234}, \omega) = \\ &= L^0(\mathbf{r}_{1234}, \omega) + L^0(\mathbf{r}_{1256}, \omega) \left[v(\mathbf{r}_{57})\delta(\mathbf{r}_{56})\delta(\mathbf{r}_{78}) - W(\mathbf{r}_{56})\delta(\mathbf{r}_{57})\delta(\mathbf{r}_{68}) \right] L(\mathbf{r}_{7834}, \omega) \ , \end{aligned} \quad (5.48)$$

obtaining that both L and L^0 depend only on one frequency ω.

Contrary to what happened in the IQP approximation, the equation above can not be contracted in space from the beginning, so the full 4-point (in space and spin) $L(\omega)$ has to be computed.

For the same reasons as those explained for the IQP approximation, neglecting the dynamical contributions prevents the mutual cancellation between the dynamical self-energy and the dynamical kernel contributions. Because of this, instead of an $L^0 = -iGG$, one usually uses a different IP-polarizability $L^{0'} = -iG_0G_0$ constructed according to (5.16), but using KS wavefunctions instead of QP eigenstates, and inserting the real part of the quasiparticle energies E_i^{QP} in the denominator. I will refer to this approach as GW+BSE (or SO+BSE if a rigid shift is used to approximate GW corrections).

The solution of equation (5.48) is computationally demanding. It is the solution to this equation one usually refers to when reporting Bethe-Salpeter spectra.

Many methods to solve the equation above have been developed and implemented in different flavours. In the following section I present a matrix diagonalization method implemented in the code EXC [86], that is useful to perform successive analysis of the spectra.

5.2.2 Solving the BSE in practice

BSE for optical spectra

Since I will solve BSE mainly for absorption processes, I substitute v with the local field $\bar{v}$ introduced in equation (4.28). Correspondingly the computed 2-particle correlation function is $\bar{L}$ which gives $\bar{\chi}$ once contracted. So the absorption spectrum is easily obtained as the imaginary part of

$$\epsilon_M(\omega) = 1 - \lim_{\mathbf{q}\to 0} \left[v_{\mathbf{0}}(\mathbf{q}) \int \bar{L}(\mathbf{r}_{1133}, \omega) e^{-i\mathbf{q}\cdot(\mathbf{r}_1 - \mathbf{r}_3)} d\mathbf{r}_{13} \right] \ , \quad (5.49)$$

in agreement with equation (4.25).

Static excitonic Hamiltonian

One method to solve the BSE equation is to switch to a state-representation of the operators. Taking $\phi_i(\mathbf{r})$ any single-particle state, a pair-function basis can be defined by the coupled-states $|i_1, j_2\rangle := \phi_i(\mathbf{r}_1)\phi_j^*(\mathbf{r}_2) = \Phi_{ij}(\mathbf{r}_1, \mathbf{r}_2)$. Although (i, j) is a generic couple of states, I will refer to this basis as the transition-basis even if conduction-conduction and valence-valence pairs are included. In particular, if one takes ϕ_i as the quasiparticle wave functions,

and assumes the quasiparticle approximation for G, then $L^0 = -iGG$ is diagonal on the transition-basis

$$L^{0\,ab}_{\;\;cd}(\omega) = (f_a - f_b)\frac{\delta_{ac}\delta_{db}}{\omega - (E_b - E_a) + i\eta\,\mathrm{sign}(E_b - E_a)}\ , \tag{5.50}$$

where the difference between quasiparticle energies $(E_b - E_a)$ is the $|a\rangle \to |b\rangle$ transition energy and f_i is the occupation number of the state i. The infinitesimal quantity η coming from the denominator of the Gs will have no impact on future discussion, therefore will be omitted for simplicity.

Projected on this basis, the formal solution of the BSE is given by

$$\begin{aligned}\bar{L}^{ab}_{cd}(\omega) &= \left\{\delta_{ik}\delta_{jl} - L^{0\,ij}_{\;\;mn}(\omega)K^{mn}_{kl}\right\}^{-1}_{(ab)(ef)} L^{0\,ef}_{\;\;cd}(\omega) \\ &= \left\{\delta_{ik}\delta_{jl} - L^{0\,ij}_{\;\;mn}(\omega)K^{mn}_{kl}\right\}^{-1}_{(ab)(ef)} \left\{(E_f - E_e)\delta_{ec}\delta_{fd}\right\}^{-1}_{(ef)(cd)} (f_c - f_d)\ ,\end{aligned}$$

where $K = \bar{v} - W$ is the static interaction term defined in terms of the matrix elements

$$\bar{v}^{mn}_{kl} = \langle\langle\ \bar{v}(\mathbf{r}_{13})\delta(\mathbf{r}_{12})\delta(\mathbf{r}_{34})\ \rangle\rangle = \int \phi^*_m(\mathbf{r}_1)\phi_n(\mathbf{r}_1)\bar{v}(\mathbf{r}_{13})\phi_k(\mathbf{r}_3)\phi^*_l(\mathbf{r}_3)d\mathbf{r}_{13} \quad \text{and} \tag{5.51}$$

$$W^{mk}_{nl} = \langle\langle\ W(\mathbf{r}_{12})\delta(\mathbf{r}_{13})\delta(\mathbf{r}_{42})\ \rangle\rangle = \int \phi^*_m(\mathbf{r}_1)\phi_k(\mathbf{r}_1)W(\mathbf{r}_{12})\phi_n(\mathbf{r}_2)\phi^*_l(\mathbf{r}_2)d\mathbf{r}_{12}\ . \tag{5.52}$$

N.B. The notation used to represent matrix elements is not standard. If $A(\mathbf{r}_1, \mathbf{r}_2)$ is a generic two-variable quantity, upper indexes are related to contraction with wave functions depending on the first space variable ($\mathbf{r}_1$ in the example) whereas lower indexes are referred to the second variable ($\mathbf{r}_2$). Because of the difference in the delta-functions of the BSE kernel, this notation leads to a mismatch in the order of the indexes between v and W. Consequently attention must be paid in taking $\bar{v} - W$.

Making use of the operatorial identity $[BC]^{-1} = C^{-1}B^{-1}$ in the expression above, and after some algebraic manipulation, one gets

$$\bar{L}^{ab}_{cd}(\omega) = \left\{\tilde{\mathbf{H}}^{\mathrm{exc}} - \mathbf{1}\omega\right\}^{-1}_{(ab)(cd)} (f_c - f_d) \tag{5.53}$$

with the identity matrix $\mathbf{1}^{ab}_{cd} = \delta_{ac}\delta_{db}$ and the frequency-independent excitonic Hamiltonian

$$\tilde{H}^{\mathrm{exc}}_{(ij)(mn)} := (E_j - E_i)\delta_{im}\delta_{jn} - (f_i - f_j)\left[\bar{v}^{ij}_{mn} - W^{im}_{jn}\right]\ . \tag{5.54}$$

The solution of equation (5.53) is not trivial only for eigenenergies E_λ and eigenvectors $\mathbf{A}_\lambda$ satisfying the eigenvalue equation

$$\tilde{\mathbf{H}}^{\mathrm{exc}}\mathbf{A}_\lambda = E^{\mathrm{exc}}_\lambda \mathbf{A}_\lambda \quad \text{, so that} \quad \bar{L}^{ij}_{kl} = \sum_{\lambda,\lambda'} \frac{A^{ij}_\lambda S^{-1}_{\lambda\lambda'} A^{kl}_{\lambda'}}{E^{\mathrm{exc}}_\lambda - \omega}\ . \tag{5.55}$$

In the last expression the spectral representation of $\bar{L}$ has been used. The fact that vectors $\mathbf{A}$ are not necessarily orthonormal is accounted for by the overlap matrix $S_{\lambda\lambda'} = \mathbf{A}^*_\lambda \cdot \mathbf{A}_{\lambda'}$.

Because of the differences $(f_i - f_j)$ in (5.53) and (5.54), the eigenvalue problem has to be solved only in the subspace spanned by IP-transitions, i.e. paired states of the kind[30] $|vc\rangle$.

[30]Indeed one also have paired states of the kind $|cc'\rangle$ or $|vv'\rangle$.

In this subspace, the excitonic Hamiltonian is a block matrix of the form

$$\tilde{H}^{\text{exc}}_{(vc)(v'c')} = \begin{pmatrix} H^{\text{res}}_{(vc)(v'c')} & K^{\text{coup}}_{(vc)(c'v')} \\ -K^{\text{coup}\,*}_{(vc)(c'v')} & -H^{\text{res}\,*}_{(vc)(v'c')} \end{pmatrix} , \tag{5.56}$$

with H^{res} the resonant part, $-H^{\text{res}\,*} = H^{\text{antir}}$ the antiresonant parts, and K^{coup} the coupling between resonant and antiresonant matrices.

Spectra of Si and LiF obtained with this method are reported in Fig. 5.7. In black solid lines I report the BSE spectra, in blue the RPA spectra, violet lines stand for RPA+GW (Si) or RPA+SO (LiF) calculations and red dots are for experimental data. Both systems present an excitonic peak which is well described by the BSE calculation, while other simulations do not get this structure.

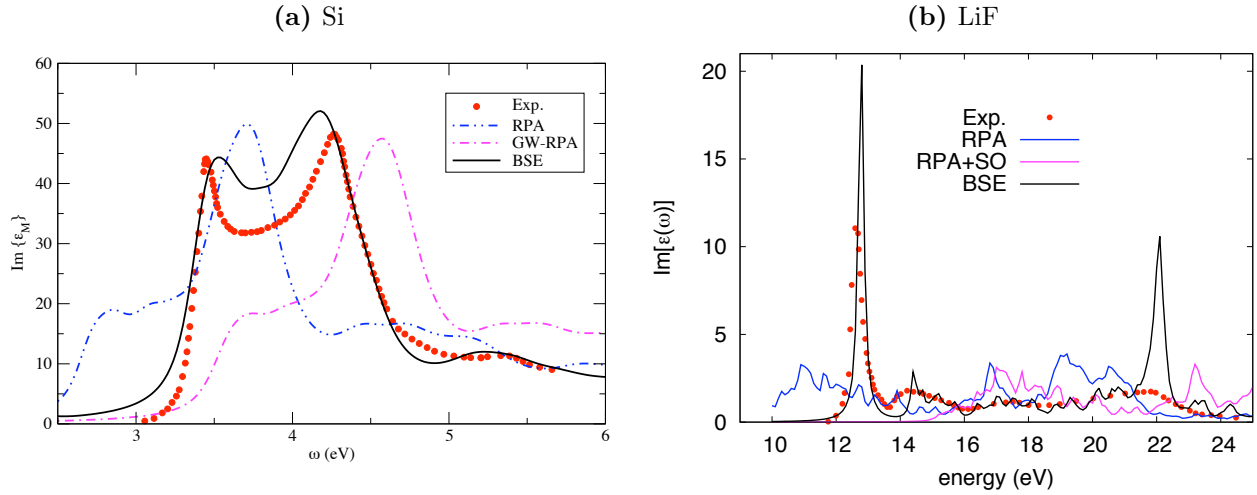

Figure 5.7: Standard BSE calculations of optical spectra of Si (5.7a) and LiF (5.7b). In Fig. 5.7a RPA+LFE (double dot-dahsed blue), RPA+GW (dot-dashed violet) and BSE calculation (solid black) are compared with experimental data (red dots). Similar color code is used for LiF in Fig. 5.7b. The excitonic peak at the onset is reproduced only by the BSE calculations. Note the strong excitonic peak in the LiF spectrum at 22 eV predicted by BSE. A similar feature will be analised in Chapter 6 in the case of $SrTiO_3$. The image of Si taken from [87].

Spectral weight analysis

The matrix element $L^{0\,vc}_{v'c'}$ has resonant and antiresonant components, exactly as in (4.13).

Antiresonant contribution and coupling terms can usually be neglected in absorption spectra (Tamm-Dancoff approximation, cfr section 4.5.1). The resonant contribution $H^{\text{res}}_{(vc)(v'c')} = (E_c - E_v)\delta_{vv'}\delta(cc') - v^{vc}_{v'c'} + W^{vv'}_{cc'}$ is in principle non hermitian because of the imaginary part of the quasiparticle energies E_j. On the contrary, $\langle\langle \bar{v} \rangle\rangle$ and $\langle\langle W \rangle\rangle$ are Hermitian matrices. Therefore if one neglects the lifetime of the excitations (that is coherent with neglecting the dynamical contributions in the kernel) then the full H^{exc} matrix becomes hermitian. Consequently eigenvalues E^{exc}_λ are real and eigenvectors $\mathbf{A}$ are orthogonal so that $\mathbf{S} = \mathbf{1}$.

Under these approximations equation (5.49) reduces to

$$\epsilon_M(\omega) = 1 - \lim_{\mathbf{q}\to 0} v_{\mathbf{0}}(\mathbf{q}) \sum_\lambda \frac{|\sum_{vc} \tilde{\rho}_{vc}(\mathbf{q}) A^{vc}_\lambda|^2}{E^{\text{exc}}_\lambda - \omega - i\eta} , \tag{5.57}$$

where the oscillator strengths $\tilde{\rho}_{vc} = \langle v|e^{-i\mathbf{q}\cdot\mathbf{r}}|c\rangle$ have been defined in (4.11).

Although computationally demanding, this approach has the advantage that the optical spectrum can be decomposed on independent-particle transitions. The excitonic wave function

$$A_\lambda(\mathbf{r},\mathbf{r}') = \sum_{vc} \phi_v(\mathbf{r}) A^{vc}_\lambda \phi^*_c(\mathbf{r}') \tag{5.58}$$

gives the conditioned probability amplitude to find a particle (e.g., the electron) in $\mathbf{r}'$ given the other (e.g., the hole) in $\mathbf{r}$.

The numerator of equation (5.57) gives the excitonic spectral weight at the energy $E^{\rm exc}_\lambda$. It can be decomposed on its independent-particle transitions as well. We introduce the $\mathcal{E}$-restricted spectral weight

$$J_{E_\lambda}(\mathbf{q},\mathcal{E}) = \sum_{(vc):E_{vc}<\mathcal{E}} \tilde{\rho}_{vc}(\mathbf{q}) A^{vc}_\lambda \quad \text{with IP-transition energy} \quad E_{vc} = E_c - E_v \ , \tag{5.59}$$

which is the spectral weight at energy E_λ obtained by summing all IP-transitions of energy $E_{vc} < \mathcal{E}$. Correspondingly the converged spectrum[31] $J^\infty_{E_\lambda}(\mathbf{q}) = \lim_{\mathcal{E}\to\infty} J_{E_\lambda}(\mathbf{q},\mathcal{E})$. Then, the cumulant function

$$f_{E_\lambda}(\mathbf{q},\omega) := \frac{|J_{E_\lambda}(\mathbf{q},\omega)|^2}{|J^\infty_{E_\lambda}(\mathbf{q})|^2} \tag{5.61}$$

tends to the value of 1. It is a useful tool to analyse the decomposition of the spectral weight in terms of the IP-transitions of given frequency. In fact it takes into account the interference between the terms $\tilde{\rho}_{vc}(\mathbf{q})A^{vc}_\lambda$ entering in J_{E_λ} because all contributions of energy $\omega < \omega'$ are included in its definition.

5.2.3 Going beyond the static screening approximation

Is it possible to solve the BSE equation in a fully dynamical description of absorption? Theories and approximations have been proposed in the past, for example Ref. [88] or [89], the latter being based on the calculation of selected diagrams in the homogeneous electron gas. To give a description of dynamical effects in light absorption, one should describe on the same footing two different aspects of the phenomenon.

On one hand the exciton is formed by two charged particles: the electron and the hole. The effects that each of them induces in propagating in the system are accounted for by the dynamical $\Sigma_c(\omega)$. Hence the renormalization of the QP peak and the occurrence of satellites is one key aspect of the dynamics of absorption.

On the other hand the exciton, as electron-hole pair with neutral charge, has a lower impact in perturbing the system with respect to the sum of its two components. The perturbation induced in the system by a propagating dipole is much more short-range than that of a monopole. This is the second aspect to account for: the *e-h* pair term has to cancel part of the self-energy contribution. The latter aspect is ascribed to the very propagation of the

[31] In terms of the $\mathcal{E}$-restricted spectral weight, equation (5.57) reads

$$\epsilon_M(\omega) = 1 - \lim_{\mathbf{q}\to 0} v_{\mathbf{0}}(\mathbf{q}) \sum_\lambda \frac{\left|J^\infty_{E_\lambda}(\mathbf{q})\right|^2}{E^{\rm exc}_\lambda - \omega - i\eta} \ . \tag{5.60}$$

exciton, it is then a mere 2-particle effect and is therefore described by the dynamical kernel $\Xi(t_{1234}) = i\delta\Sigma(12)/\delta G(34)$.

To give a coherent description of the dynamical effects in light absorption, these two aspects have to be treated on the same footing.

This delicate interplay is at the origin of many different phenomena that are not reproducible in single-particle schemes. Amongst them the renormalization of the absorption peaks [83, 90, 91] and the occurrence of extra structures due to multiple excitations [84, 85] have been investigated recently.

The interference between dynamical self-energy and BSE kernel

Some studies have been conducted about the interplay between self-energy and dynamical kernel effects [83, 90, 91], with major attention on the renormalization of the absorption peaks.

As explained when introducing the IQP approximation ($\Xi = 0$, section 5.2.1), if one neglects the kernel but still includes dynamical self-energy effects within the quasiparticle approximation, computed spectra have underestimated weight. This has been shown by R. Del Sole and R. Girlanda [83] on the prototypical case of Si. Further studies conducted by F. Bechstedt and coworkers [90] showed that indeed interference effects coming from the kernel have opposite sign and partially cancel with the self-energy contributions.

In their paper, Bechstedt, Tenelsen, Adolph and Del Sole calculated the polarizability, neglecting the Hartree contribution, and to first order in W, namely

$$L = -iGG - GGWGG \text{ with } G \text{ from the first iteration of } G = G^0 + G^0\left[\Sigma - V_{\text{xc}}\right]G$$

using a G^0 computed with KS states. The resulting polarizability L includes linear contributions from both the dynamical self-energy and the BSE kernel (in the GW approximation). Moreover G was supposed to be diagonal in the single-particle basis (later on, in chapter 10, I will refer to this approximation as the decoupling approximation on G), and L was assumed to be diagonal in the band indexes but not in the wave vector $\mathbf{k}$. It must be noticed that in solids one has to expand corrections beyond the first order in W for the transition energies to change. Instead, changes in the exciton wave function to first order are not vanishing and can have significant impact on spectra [92].

The resulting optical absorption spectrum

$$\Im[\epsilon_M(\omega)] = \sum_{vc}\sum_{\mathbf{k}} |M_{vc}(\mathbf{k})|^2 \mathcal{A}_{vc}(\mathbf{k},\omega)$$

is expressed in terms of the squares of the optical oscillators

$$M_{vc}(\mathbf{k}) = \frac{\langle c\mathbf{k}|\mathtt{v}|v\mathbf{k}\rangle}{E_c^{LDA}(\mathbf{k}) - E_v^{LDA}(\mathbf{k})} \text{ with } \mathtt{v} \text{ velocity operator,}$$

and the absorption spectral function

$$\mathcal{A}_{vc}(\mathbf{k},\omega) = [1 - \beta_{vc}(\mathbf{k})]\delta(E_c(\mathbf{k}) - E_v(\mathbf{k}) - \omega) + \text{ first satellites}$$

with the (first order) renormalization factor $\beta_{vc}(\mathbf{k})$ given by

$$\beta_{vc}(\mathbf{k}) = -\frac{1}{\pi}\sum_{\mathbf{k}'\in BZ}\Im\left[\int_0^\infty \frac{W^{cc\mathbf{k}}_{cc\mathbf{k}'}(\omega')}{|\omega' - E_c(\mathbf{k}) + E_c(\mathbf{k}')|^2} + \frac{W^{vv\mathbf{k}}_{vv\mathbf{k}'}(\omega')}{|\omega' - E_v(\mathbf{k}') + E_v(\mathbf{k})|^2} + \right.$$
$$\left. -2\Re\frac{M_{vc}(\mathbf{k}')}{M_{vc}(\mathbf{k})}\frac{W^{cc\mathbf{k}}_{vv\mathbf{k}'}(\omega')}{(\omega' - E_c(\mathbf{k}) + E_c(\mathbf{k}'))\,(\omega' - E_v(\mathbf{k}') + E_v(\mathbf{k}))}d\omega'\right] . \qquad (5.62)$$

Matrices $W^{ij\mathbf{k}}_{ml\mathbf{k}'}$ are the same[32] as in (5.52), with an explicit index for the $\mathbf{k}$ points.

The three terms appearing in formula (5.62) are exactly the terms one has to account for: the dynamical effects of the hole ($W^{vv\mathbf{k}}_{vv\mathbf{k}'}$) and the electron ($W^{cc\mathbf{k}}_{cc\mathbf{k}'}$) come from the self-energy contribution, whereas the interference term $W^{cc\mathbf{k}}_{vv\mathbf{k}'}$ with opposite sign and double weight is the interference term coming from the dynamical kernel. Given the opposite sign between the *e-h* and the single-particle contributions, partial cancellation between the three terms happen, giving a negligible renormalization of the peak, that justifies the static GW+BSE approach. This is the result found by Del Sole and Girlanda [83].

Marini and Del Sole [91] successively derived a dynamical kernel for the BSE at first and second order in W which depends only on one frequency ω. They have shown that in some metals as Cu and Ag dynamical excitonic effects together with the renormalization of quasiparticles have to be included in the calculation to get correct absorption amplitudes up to first order in W. For the case of the semiconductor Si, corrections even beyond first order are needed. They showed that the renormalization factors $\mathcal{Z}$ and the first order of the dynamical kernel have the same weight with opposite sign.

Coupling between excitations

Beside renormalization aspects, the inclusion of dynamical effects is mandatory when double or multiple excitations are of interest.

Extra poles are observed when the excitation involves the simultaneous creation of several electron-hole pairs. Of this kind are phenomena like the direct generation of several excitons by absorption of single photon or the generation of electron-hole pairs due to the decay of a high energy (hot) exciton (impact ionization process). Multiple excitations and decay processes are accounted for by the coupling between single and multiple excitations. For instance, in systems like molecules with open-shell ground state, the presence of double excitations is an experimental evidence as it is the multiple exciton generation in some nanostructures. The latter are potentially important for application in solar cells [7, 9, 10, 93].

To understand better the link between dynamical kernel and multiple excitations, let us write a generic Dyson equation

$$\tilde{L}(\omega) = L^0(\omega) + L^0(\omega)\tilde{K}(\omega)\tilde{L}(\omega)$$

defined in terms of the independent-particle polarizability L^0. L^0 has a number of poles (counting the multiplicity) equal to the number of independent 2-particle transitions. The fully interacting solution $\tilde{L}$ instead accounts for all possible excitations of the system. As a consequence it must have extra poles corresponding to multiple-excitation processes. Hence to account for multiple transitions, it is necessary for the number of poles in $\tilde{L}$ to be higher than in L^0, task that can be accomplished only by a dynamical kernel $\tilde{K}(\omega)$.

[32]Note that in the original paper, the matrix $W_{\mathbf{GG}'}$ is supposed diagonal. For our scope this detail is irrelevant.

So, the role played by $\tilde{K}(\omega)$ is that of adding poles by folding all possible multiple excitations of the system into the single-excitation space where both L^0 and $\tilde{L}$ are represented. One can imagine to divide the fully interacting space into two subspaces: one spanned by a basis of single-excitations $\mathbf{e}_s$ (for example the transition-basis introduced in section 5.2.2) and the other spanned by a basis of multiple excitations $\mathbf{e}_m$. Following the same way of reasoning as in section 1.2, one obtains

$$\left[S + C_1(\omega - M)^{-1}C_2\right]\mathbf{e}_s = \omega\mathbf{e}_s$$

where the single-multiple coupling blocks (C_1 and C_2) together with the multiple-multiple block (M) are folded into the dynamical kernel $C_1(M-\omega)^{-1}C_2$.

This is exactly the framework of BSE: it is formulated in the 2-particle space but incorporates into the dynamical kernel $\Xi(\omega) = \delta\Sigma/\delta G$ the coupling with all other possible excitations of the system.

Having this in mind, two recent works have tried to exploit the same intuition to devise TDDFT kernels derived from dynamical BSE. In [84], P. Romaniello et al. solved the dynamical BSE in a 2-site Hubbard model within the GWA for the BSE kernel. Instead of a self-consistent screened interaction, they solved the dynamical problem using a W coming from a static BSE calculation, thus including dynamical effects only to the first order. The resulting kernel of the dynamical BSE reads

$$\tilde{W}^{ab}_{cd}(\omega_\lambda) = \frac{i}{2\pi}\int W^{ab}_{cd}\left\{\frac{1}{\omega_\lambda - \omega - E_{cb} + i\eta} + \frac{1}{\omega_\lambda + \omega - E_{ad} + i\eta}\right\}d\omega \tag{5.63}$$

with $E_{ij} = E_i - E_j$ difference of quasiparticle energies and W^{ab}_{cd} coming from the static BSE calculation.

The solution they found for the dynamical BSE has four poles: two involves single-excitations, one is a singlet double excitation and the fourth unphysical pole has been ascribed to the self-screening problem of the GWA. The latter issue has been solved in a successive paper by D. Sangalli et al.[85] where a number conserving approach based on second RPA is invoked to get rid of spurious solutions. The approach led to the application to small molecules.

Inspirations from the one-particle case

Some progress in the inclusion of dynamical effects in the theory of absorption has been done. However these approaches stop at the first [84, 85, 90] or at the second [89, 91] order in W, and it is a very hard task to go beyond. Moreover most of these works focus on specific aspects of the spectrum, making use of approximations in order to neglect the aspects of no interest.

Instead, one would like to achieve a full description of the phenomenon. One would like to take into account at the same time and with the same theory both the renormalization of the spectrum and the occurrence of multiple excitations. It is desirable to sum all diagrams of the dynamical coupling between the exciton and the other excitations. Additionally, one would like this theory to be used in practice, and not only on model systems. This would most likely require an implementation exploiting available results, in the spirit of some post-processing technique, demanding minor modifications to already existing codes.

The culumant expansion of G (6.1) can be seen as an inspiring example: in its exponential form it contains all extra peaks. The derivation of the exponential G presented in the works

of G. Lani [55, 82] can be taken as a starting point to explore the dynamical effects in L. Its underlying philosophy can be adopted also in the two-particle problem, suggesting to drop the kernel Ξ of (5.45) in favour of a differential formulation. Furthermore, the post-processing method implemented and used by M. Guzzo [5, 78, 94] can inspire a way to add dynamical corrections to static BSE results.

The last chapter of this thesis is devoted to the search of such a dynamical theory of absorption. In Chapter 10, a differential equation for L is derived and solved within some approximations. In some aspects, the theoretical development presented in this thesis can be seen as an exploratory work indicating some new ideas to address this problem.

Part II

Application to real systems and analysis

Chapter 6

Optical properties of $SrTiO_3$

In this chapter I will use the theories introduced in Chapters 3, 4 and 5 at the state-of-the-art to compute the optical properties of $SrTiO_3$, a transition metal oxide displaying interesting electronic properties.

The analysis of the computed spectra is based on the comparison between the calculation of diverse properties, performed at different levels of approximation, and experimental data. Different theories and approximations give access to different aspects of the same physics which, collected together, give a clearer interpretation of the observed phenomenon. This study constitutes therefore a good example to present all tools introduced in the previous chapters.

But it is not only a "didactic" scope what aimed with this chapter. In fact this analysis also pointed out some limitation of the theories used, indicating an insufficient description of dynamical effects in this material.

A large part of the material of this Chapter has been published in Ref. [95]:
L. Sponza, V. Véniard, F. Sottile, C. Giorgetti and L. Reining, Phys. Rev. B **87**, 235102 (2013).

6.1 Preface to $SrTiO_3$

Strontium Titanate $SrTiO_3$ (STO) (pure, doped or in junctions) displays several peculiar properties which make this material widely investigated for technological applications and for theoretical understanding of basic processes. It is prototypical amongst the transition metal oxides so it has been often taken as a benchmark material to test the performances of different theories [96–98]. Of interest are its conducting [99–101], structural [102–104], and magnetic [105] properties. All these features are closely related to its electronic structure.

Optical spectra of STO measured in different range of energy and with different techniques (reflectivity [106–109], ellipsometry [109, 110], x-ray absorption spectroscopy [111] and others) have been compared early on with theoretical works, mostly calculations based on the independent-particle picture [112, 113]. More recent *ab initio* calculations include all-electron [114–118] and planewave-pseudopotential approaches [119], but to our knowledge, optical properties have always been calculated in RPA neglecting local fields, that is by means of equation (4.29).

In this chapter the optical properties of STO are computed using state-of-the-art calculations including many-body effects. These are evaluated with the TDDFT and also by solving the Bethe-Salpeter equation (5.48) within standard approximations (GWA and static W in

the e-h interaction). Special care has been taken in treating localized d electrons and the interplay between the empty d-states and the occupied O $2p$ states. Results are compared with experiments [109, 120]. The remaining discrepancies between theory and experiments are also discussed.

6.2 Geometry and Crystal field splitting

STO is a transition metal oxide, which crystallizes at room temperature in the cubic perovskite structure of the kind ABO_3, with a lattice parameter $a = 3.905$ Å [121]. Its fundamental absorption edge is around 3.2 eV at room temperature [106, 109], and the direct gap is 3.75 eV [109].

In such materials, the A-atoms (Sr) occupy the corners of a cubic lattice, the B-atom (Ti) occupies the center of the cube, and O atoms lay at the center of the faces of the cubic cell, as shown in Fig. 6.1.

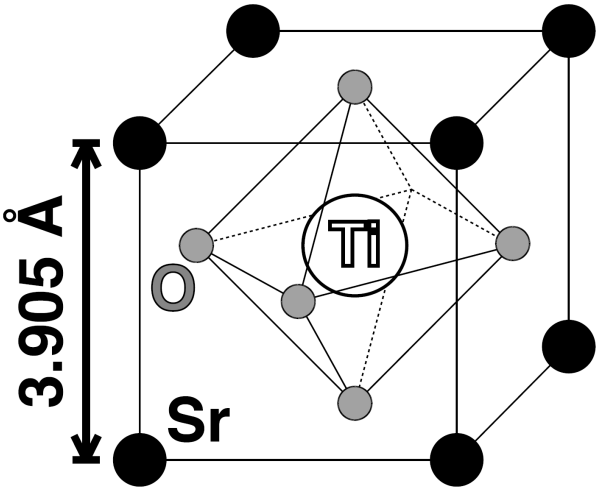

Figure 6.1: Atomic position in the cubic STO cell. Ti (empty circle) lay on the center of the cell, O atoms (grey circles) form an octahedron centred on the Ti atom. Sr atoms (black circles) sit at the corners of the cell.

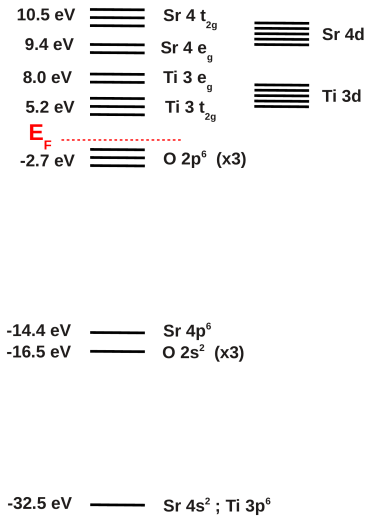

Figure 6.2: Calculated energy of electronic states in STO compared to Sr $4d$ and Ti $3d$ atomic levels. The ordering of the energy levels refers to the Γ point, the corresponding energies are average values taken from the l-DOS (see beyond).

The presence of the oxygens around the A and B ions breaks the atomic spherical symmetry, removing the five fold-degeneracy of the d levels of A and B atoms (crystal field effect). The atomic five fold-degenerate d levels split into two subgroups according to their symmetry properties. The three orbitals labelled d_{xy}, d_{yz} and d_{zx} form the t_{2g} group. The remaining two orbitals labelled d_{z^2} and $d_{x^2-y^2}$ form the e_g group. The respective energy position of the e_g and t_{2g} depends on the symmetry of the environment of the cations [122].

Since A ions are surrounded by 12 O, they are in a dodecahedral symmetry, so the three A t_{2g} orbitals are at higher energy than the two A e_g orbitals. The B ions are surrounded by six O ions, corresponding to an octahedral symmetry, with the consequence that the three t_{2g} orbitals are at lower energy than the two e_g orbitals. The energy of the different levels is in agreement with recent *ab initio* DFT calculation on electronic properties of $SrTiO_3$ [123]. There is a slight difference to the experimental assignment from ref. [109], where e_g and t_{2g}

states of Sr are reversed, but since the states are significantly hybridized and our assignment is refers to the Γ point, this is no fundamental contradiction. Since O $2p$ extend along the Cartesian axis, one should expect a strong spatial overlap between the O $2p_z$ and the Ti d_{z^2} and between the O $2p_{x,y}$ and the Ti $d_{x^2-y^2}$, giving rise to hybridizations.

6.3 DFT and GW band structure

This section is devoted to the discussion of the band structure and density of state (DOS) of the material. On-site and angular momentum projected density of states (l-DOS) will be analysed to identify the character of the first eleven conduction bands. Quasiparticle corrections to KS energies and possible approximations are also discussed.

Computational details: Groundstate properties and GW corrections to KS eigenvalues have been computed with ABINIT [124], a planewave-based software.

Semicore pseudopotentials have been used in all calculations, including 40 electrons per cell. The Ti atom participates with 12 electrons $[3s^2 + 3p^6 + 4s^2 + 3d^2]$, the Sr atom with 10 $[4s^2 + 4p^6 + 5s^2]$ and each O atom participates with 6 electrons $[2s^2 + 2p^4]$. Working with semi-core pseudopotentials is crucial because dividing an atomic shell into core and valence can lead to severe errors in the evaluation of the exchange term[33]. The pseudopotentials have been created partially in a doubly ionized configuration (for Sr and Ti). Core radii, within which the atomic pseudo-wave-functions are exact, were $r_c = 1.7$ Bohr for all components of Sr, 1.25 Bohr for Ti s and Ti p while $r_c = 1.65$ Bohr for Ti d channel and finally $r_c = 1.5$ Bohr for oxygen.

The exchange-correlation potential of the DFT calculations (band structure and density of states), has been computed in the LDA. A cutoff of 70 Ha has been used to the planewave basis set. The density of states has been calculated using a $8 \times 8 \times 8$ **k**-point grid centred in Γ (i.e. 35 **k**-points in the irreducible wedge).

GW corrections have been evaluated with the G_0W_0 method[34], with a cutoff energy of 32 Ha for the basis set, and 25 Ha for the exchange and correlation components of the self-energy. 80 bands have been included in the calculation of the self-energy, and 200 bands were used for the screening. For both screening and self-energy calculations, the same **k**-point grid as for the ground state has been used. The dimension of the screening matrix is of 2373×2373 **G** vectors (~ 25 Ha). To speed up the calculations, the Godby-Needs [71] plasmon pole approximation has been used. I have tested its validity by performing also calculations using contour deformation. When applied, the scissor operator (SO) shift is based on the results of these calculations, not on experimental results.

6.3.1 Distribution of quasiparticle corrections

The results of the LDA band structure calculations are in good agreement with experiments [106, 107, 109] and previous calculations [106, 109, 113–117, 119]. LDA predicts a direct

[33] Including semicore electrons is of fundamental importance in the computation of the GW corrections, as can be seen comparing our results with those of Kim and coworkers [96]. The reason has been demonstrated clearly by M. Rohlfing, P. Krüger and J. Pollmann in Ref. [125].

[34] Since the localized d states are empty, self-consistency on wave functions is not crucial for this material.

gap at Γ of 2.21 eV, much smaller than the experimental value of 3.75 eV [109]. This underestimation is the well known KS bandgap problem. To correct the LDA bandgap, quasiparticle corrections have been computed within the perturbative G_0W_0 approximation using formula (5.31). The resulting bandstructures (LDA and GW), aligned at the HOMO level, are reported in Fig. 8.5

As it is the case in many materials, near the Fermi energy, GW corrections open the photoemission gap, giving a GW gap at Γ of 3.76 eV in very good agreement with the experimental value of 3.75 eV.

(a) LDA and G_0W_0 band structure

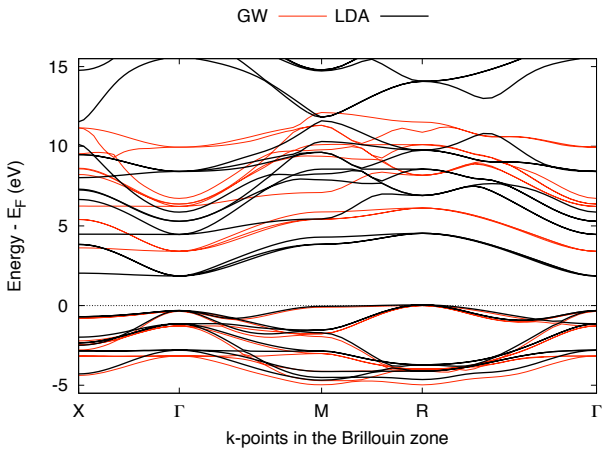

(b) Dispersion of G_0W_0 corrections

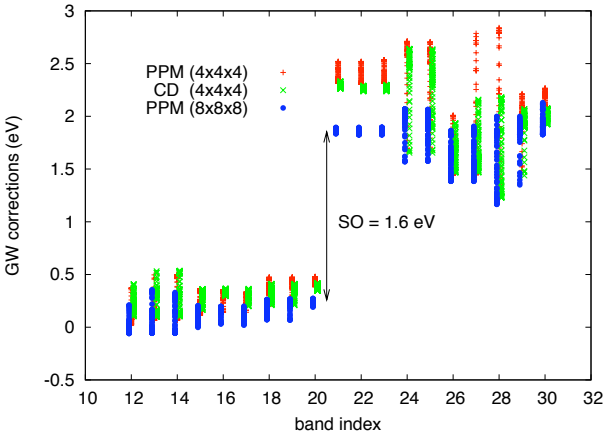

Figure 6.3: In Fig.6.3a, the GW (red) and the LDA (black) band structure along high symmetry directions are reported. In Fig. 6.3b the GW correction versus band index is reported for all 35 points of the irreducible wedge.

To investigate the effect of GW corrections beyond the gap, quasiparticle corrections versus band index are reported in Fig. 6.3b for different GW calculations. For each band index i, the corrections are evaluated for the **k**-points sampling the Brillouin zone: the resulting line of dots accounts for the deformation of the corresponding band. Small shifts in the x axis are made to ease the visualization.

If all points of a band collapse in a single spot, then G_0W_0 corrections mainly shift the bands, whereas when a dispersion is observed, it means that quasiparticle effects modify the dispersion of the band too. One can notice that for the HOMO (band 20) and the first three conduction bands (bands indexes 21, 22 and 23), a rigid shift of constitutes an excellent approximation, while for other bands one has to be more careful.

Modifications of the band shape become more important for the three deepest bands (12, 13 and 14) as well as for conduction bands starting from index 24. These bands give rise to optical transitions around 7 eV, which correspond to energies where the electron energy loss spectrum displays its first structures [109]. In such a case, the validity of the plasmon pole model (PPM) has to be checked [126].

Using a contour deformation integration (CD; green crosses), I have verified that the dispersion of the GW corrections were not due to the PPM (red crosses). Both calculations have been done on a (close to convergence) $4 \times 4 \times 4$ **k**-point grid because of the higher computational effort needed for CD calculations. The green and red group of points have very similar distribution indicating that the dispersion of the corrections is not due to the PPM approximation. In Bands 27 and 28 the two calculations differ more substantially,

but I estimate that the effect would be reduced by densifying the grid of **k**-points. The CD calculation confirms the validity of the plasmon pole model.

To evaluate correctly the GW corrections, a PPM calculation has been carried out on a $8 \times 8 \times 8$ **k**-point grid (blue dots), which leads to converged quasiparticle energies. The behaviour of the different bands is the same as for the $4 \times 4 \times 4$ grid. The mean value of the corrections differs in the PPM(888) and PPM(444) calculations by almost ~ 0.8 eV, and in particular for bands 24 and 25 the correction dispersion of the PPM(444) is twice as large as for the PPM(888).

In any case, in the reference PPM(888) calculation, the deformation of the band shape does not exceed 1 eV and the separation in energy between the bands is large enough to be able to distinguish the projected states, thus the character of the bands deduced from the LDA calculation will still be valid. On the basis of the PPM(888) results, the scissor operator, whenever used, will be set to the value of 1.6 eV.

6.3.2 State assignment

The quite small deformation of the bands due to G_0W_0 corrections justifies using alternatively G_0W_0-corrected LDA eigenvalues, or a scissor operator (SO) of 1.6 eV . On the l-DOS reported in Fig. 6.4b, the SO has been applied, while for the band plot of Fig. 6.4a, G_0W_0 energies have been used. In both cases the HOMO level has been set to 0 eV.

(a) GW band structure

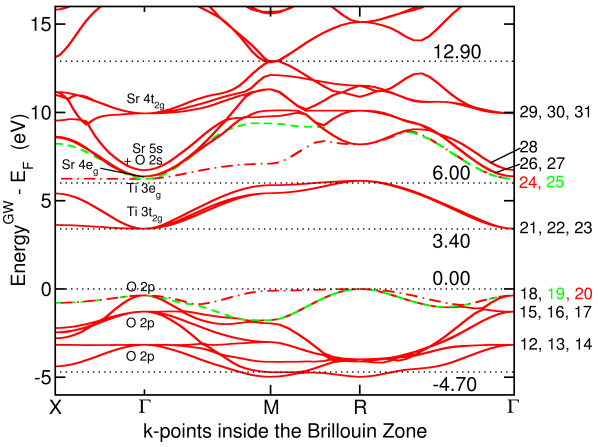

(b) Total DOS and atom-centred l-DOS for selected components

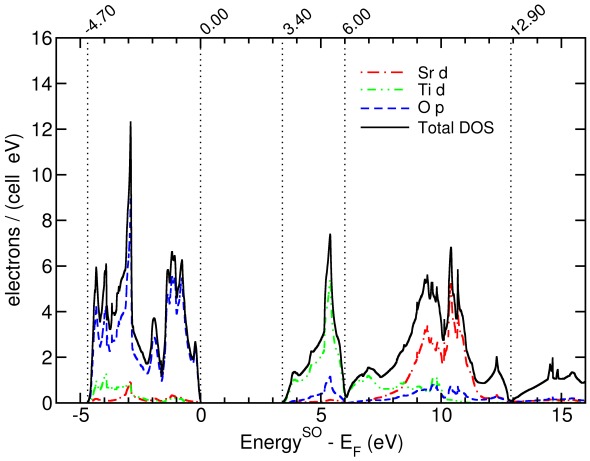

Figure 6.4: State assignment by GW band structure and SO l-DOS. Horizontal dotted lines in 6.4a and vertical dotted lines in 6.4b highlight specific groups of bands in the band plot and the corresponding structures in the l-DOS. In the band plot 6.4a, state assignment is reported at Γ (inside the plot) together with the band index (right axis). Notable bands (20 and 24 dot-dashed; 19 and 25 in green dashed) are also reported.

To calculate the on site and angular momenta-projected l-DOS, the radii of the spheres where wave functions were projected were adjusted so that the sum of partial DOS matches the total DOS. The resulting radii are equal to 3.7 Bohr for Sr, 2.3 Bohr for Ti and 2.2 Bohr for O. Fig. 6.4b shows the total quasiparticle density of states and dominant contributions to the on site-projected l-DOS for selected elements and angular momenta. Energies range

from -6 to 16 eV to include the highest valence states (band index from 12 to 20) and first 11 conduction bands.

Three main structures can be identified: a part of the valence band extending from -4.7 eV to the Fermi energy, a first peaked structure in the conduction band extending from 3.4 to 6 eV and a second broader group of structures between 6 eV and 12.9 eV. The high electronegativity of oxygen atoms drains almost all the $4s^2$ and the $3d^2$ electrons from the Ti atom and the $5s^2$ electrons from the Sr atom, filling almost completely the O $2p$ levels. Correspondingly the valence band is essentially composed by O $2p$ states, which weakly hybridise with the Ti $3e_g$ levels, as expected from the strong spatial overlap between these states. The Fermi energy lays between the O $2p$ levels and the Ti $3d$ bands.

The first group of empty states has a predominant Ti $3d$ character. Due to crystal-field symmetry, one can conclude that they are Ti $3t_{2g}$ levels, that form an almost separate band $(3.4 - 6$ eV). The second group of structures $(6 - 12.9$ eV) has a predominant d-momentum character shared between the remaining Ti $3e_g$ levels and the whole Sr $4d$ subshell, expected to be also split in e_g et t_{2g} levels.

These assignments allow for a more precise description of the band structure (Fig. 6.4a) where GW energies for valence and conduction bands are plotted in the same energy range as in Fig. 6.4b. Dotted lines delimiting energy ranges have been drawn in both figures to facilitate the identification of the three groups of bands. Referring to the bandplot, the three main groups identified in the l-DOS are recovered. The first is a group of valence bands extending from around -4.7 eV to the HOMO level and formed by nine bands labelled from 12 to 20 corresponding to O $2p$ states. At higher energies we find a first group of three conduction bands (labelled 21, 22 and 23) extending between 3.4 and 6 eV due to Ti $3t_{2g}$ and finally a wider group of bands from 6 eV to 12.9 eV composed by 8 bands (24 to 31).

The bands 24 and 25 can be assigned to e_g states of Ti with the support of the l-DOS. To identify the character of Sr states, we can use the crystal-field symmetry argument as well as the degeneracy of the bands at Γ: the bands 26 and 27 are assigned to the Sr $4e_g$ and the bands 29, 30 and 31 are assigned to Sr $4t_{2g}$.

A careful analysis of the l-DOS in this energy range shows the presence of Sr $5s$ hybridised with O $2s$ states (not shown for clarity). For this reason, band 28 is assigned to Sr $5s$ states and O $2s$ in agreement with reference [123].

Concerning the dispersion of the bands, one can note the presence of regions where some bands are flat, especially along the ΓX direction, indicating localized states. Of particular interest for the following analysis are the two topmost valence bands (labelled 19 and 20) and the lower energy Ti $3e_g$ level (band 24). One can notice that band 24 is flat along $\Gamma - X$, but it strongly disperses in other parts of the BZ indicating that the degree of localization changes along the same band.

6.3.3 Quasiparticle effects on electrons of different character

Now that bands have been assigned to electrons of different character, one can study the impact of quasiparticle corrections on the different groups.

Dispersion of the levels

In Fig. 6.5 I report GW quasiparticle correction as a function of the LDA energy of the KS state.

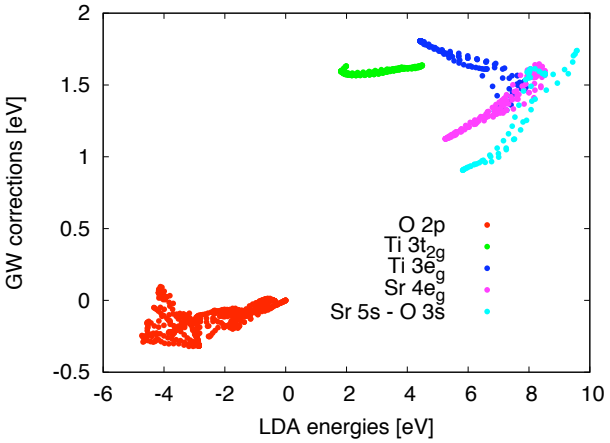

Figure 6.5: GW corrections versus LDA energies. States of different character are coloured differently: valence O p state (red dots), Ti $3t_{2g}$ states (green), Ti $3e_g$ states (blue), Sr $4e_g$ states (violet) and [Sr $5s$ + O $2s$] states (cyan).

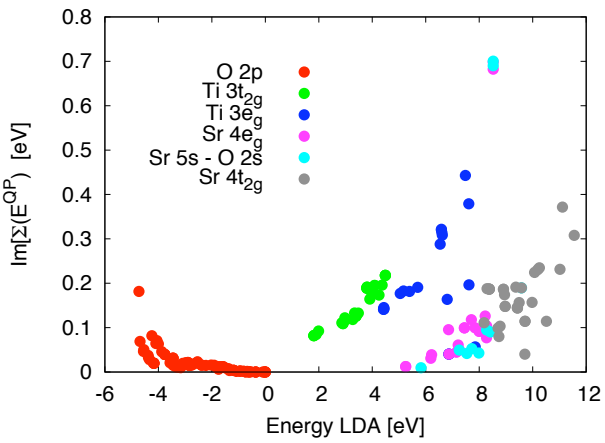

Figure 6.6: Imaginary part of $\Sigma(E^{QP})$ as a function of E^{LDA}. In STO a quadratic law $\Sigma(E^{QP}) = \kappa(E^{LDA})^2$ is observed with $\kappa_{\rm Ti}$ different from $\kappa_{\rm Sr}$.

For simple materials, as in bulk Si, quasiparticle corrections are almost constant near the gap, which justifies the use of SO, whereas a linear relation is often observed at higher energy [126]. In the case of STO, the valence bands (red dots) display a common trend with almost constant corrections, where in conduction bands different trends can be associated to different groups of electrons. The Ti $3t_{2g}$ corrections (green dots) dispose essentially as a flat line, confirming the validity of the rigid shift approximation to represent their GW corrections. An essentially linear dispersion is instead displayed by the Sr $e_{\rm g}$ levels (violet dots) that have higher corrections at higher LDA energies, similar to what happens is Si. A completely different behaviour is displayed instead by the Ti $3e_{\rm g}$ levels(blue dots), for which a linear law can still be used to represent their dispersion, but with a negative derivative: the higher the LDA energy, the lower the correction. These bands (24 and 25 in Fig. 6.4a) are quite dispersing at the LDA level, this results in more important modifications of the band shape, with lower corrections around the M and R points than in Γ.

Dynamical effects

Dynamical effects of the self-energy account for the decay of the quasiparticle due to the coupling with all the neutral excitations. Correspondingly quasiparticle peaks broaden and acquire an imaginary part proportional to the inverse of the lifetime of the excitation. The imaginary part of Σ at the quasiparticle energy has been investigated by Fleszar and Hanke [126] in bulk Si. As expected, near the Fermi level, $\Im[\Sigma(E^{QP})] \sim (E^{LDA})^2$ has a quadratic dependence on the LDA energies. In Fig. 6.6, I report $\Im[\Sigma(E^{QP})]$ versus E^{LDA} where the different groups of electrons are marked with dots. The same color code as in Fig. 6.5 has been used.

The different groups of electrons display different behaviours: in particular $\Im[\Sigma(E^{QP})]$ fits in a quadratic law $\Im[\Sigma(E^{QP})] = \kappa(E^{LDA})^2$ for both Ti $3d$ and Sr $4d$ states, but with different coefficients $\kappa_{Ti} > \kappa_{Sr}$. We can see that lifetime effects are stronger in Ti d states, and especially the two higher energy e_g bands[35]. The lifetime of electrons in Ti d states is

[35]The bottom conduction should have $\Im[\Sigma] \approx 0$ because an electron in the bottom valence needs an energy

lower which suggests a stronger coupling with other excitations of the system.

The occurrence of band-crossing may be responsible for interchanged characters of some spots between 7 an 8 eV.

6.4 Optical absorption

In this section I present the absorption spectrum of $SrTiO_3$. The section is divided in four subsections. In the first part, I will discuss the role of the LFE in the high-energy $O \rightarrow Sr$ transitions. In the second part, I will concentrate on the $0-15$ eV region where excitonic effects are important: I will present BSE calculations (in the standard GW+static W approach) together with RPA calculation on STO which will constitute the basis for a detailed study of the origin of the different structures of the spectrum and the different role played by Ti $3d$ and Sr $4d$ electrons (paragraphs **a** and **b**). My results will be compared to experimental data [109, 120]. Then I will pass to the investigation of the spectrum computed within TDDFT (with different kernels) or by solving the BSE (in the static approximation (5.48)), inside a smaller range of energies (from 0 to 15 eV). The different role played by Ti $3d$ electrons and Sr $4d$ electrons is analysed referring to the l-DOS and the band structure discussed in the previous section. This careful analysis allowed me to evidence interference effects (paragraph **c**). The third part is devoted to the role of the screened Coulomb interaction W in the e-h interaction, and the fourth part is focused on the test of different kernels to capture excitonic effects in TDDFT.

Computational details: TDDFT spectra (LRC and Bootstrap) have been computed up to 15 eV, while RPA up to 30 eV, using the DP simulation code [127]. In the calculation of $\chi^{KS}_{\mathbf{GG'}}$ summation over 31 bands was needed to converge the spectrum within 15 eV, and 50 bands to reach convergence at 30 eV. In all cases the dimension of the $\chi^{KS}_{\mathbf{GG'}}$ matrix is 33×33. 1237 plane waves have been included in the basis set. The Brillouin zone has been sampled with a shifted **k**-point grid $8 \times 8 \times 8$, counting 512 inequivalent **k**-points. In all TDDFT calculations, G_0W_0 energies have been used instead of LDA energies, except where explicitly specified.

The BSE has been solved using the EXC code [86]. Except for the spectra of figure 6.12, where the full diagonalisation of the excitonic Hamiltonian has been performed, the Haydock diagonalisation algorithm has been employed, with 150 iterations to achieve converged spectra. The number of plane waves, the range of energy, the dimension of the matrix and the **k**-points grid used are the same as for the TDDFT calculations, except where explicitly specified.

6.4.1 The role of the local field effects

The RPA spectrum with (LFE) and without (NLF) local fields is reported in Fig. 6.7 together with two experimental curves [109, 120].

Experimental data (blue and violet crosses) present major structures below 15 eV, and are essentially featureless beyond this energy. The RPA+LFE (black line) and RPA+NLF

at least twice as large as the gap to decay. Actually, the gap entering in Σ is the LDA gap, lower than the GW gap, because we did not make self-consistency in W. That could explain the non vanishing imaginary part of the bottom conduction in Fig. 6.6.

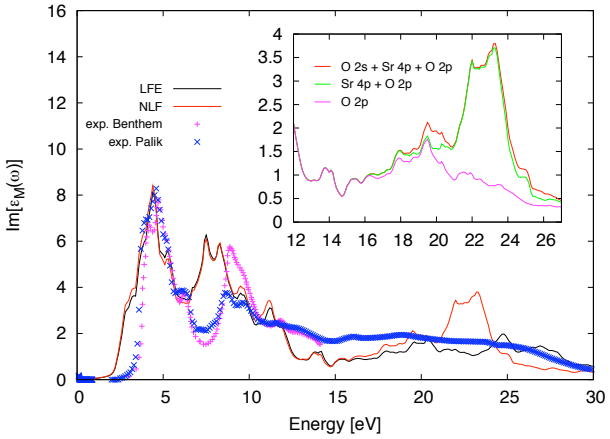

Figure 6.7: Optical spectrum of STO computed in RPA+LFE (black) and RPA+NLF (red) spectra. Experimental data from Palik [120] and from more recent measures made by Benthem et al [109] are reported with blue and violet crosses respectively. **Inset:** The peak at 23 eV is analysed by reducing the number of bands included in valence. When eliminating Sr $4p$ states, the NLF peak is completely suppressed.

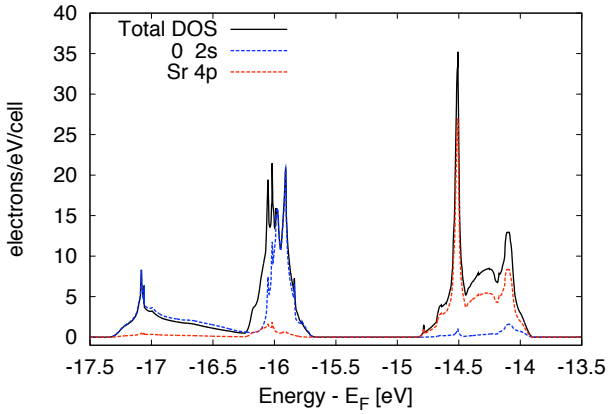

Figure 6.8: Total DOS (black solid line) and site projected l-DOS of semi-core levels O $2s$ (dashed blue) and Sr $4p$ (dashed red). Transitions from these states to the Ti and Sr d levels are compatible with the energy of the peak at $\sim$ 23 eV in the RPA+NLF calculation.

(red line) calculations reproduce these structures within the quality one can expect from RPA calculations. We will focus our attention on this range of energy later on in this chapter, however it is important to point out that within 15 eV, no significant difference can be found between RPA+LFE and RPA+NLF calculations, indicating that in this range local fields can be neglected without committing a severe error. The NLF calculation is in good agreement with previous calculations [116].

At energies around 23 eV, the neglect of local fields give rise to an absorbing structure absent in the experimental spectra. It is completely washed out when local fields are accounted for. This feature is common to other transition metal oxides structures as $BaTiO_3$ [116] and $CaTiO_3$.

Because of the peaked nature of the structure, well localised semicore states are supposed to be involved in the transition. The transition energy of 23 eV is compatible with transitions from deep energy states of O $2s$ (between -17 and -16 eV) and Sr $4p$ (between -14.7 and -14 eV) towards the Ti $3d$ bands. The total DOS and the site-projected l-DOS of these states are reported in Fig. 6.8. The first transitions (O $2s \rightarrow$ Ti $3d$) are forbidden in the dipole approximation, so the peak is due entirely to the Sr $4p$ states, as well shown in the inset of Fig. 6.7, where three NLF calculations are shown. I remember that without local fields, the spectrum reduces to the Fermi's golden rule and can therefore be interpreted in terms of single-particle transitions.

The red curve in the inset corresponds to the full NLF spectrum, including all the valence bands plus semicore states. When O $2s$ states are subtracted from the calculation (green curve) the peak is not affected, indicating that these states do not participate to the creation of the peak. It is only when the Sr $4p$ states are excluded too (violet line), that the peak completely vanishes.

When localised states are involved, as in this case, the correct description of the local inhomogeneities of the response has to be accounted for. For this reason the full matrix $\epsilon^{-1}_{\mathbf{GG'}}$

has to be computed.

6.4.2 Analysis of the transitions

Let us now look closer at the first part of the spectrum, from the absorption onset to 15 eV. The reduced range of energies requires a smaller number of bands, and BSE calculations are then feasible.

In Fig. 6.9, I report two BSE absorption spectra, computed respectively using GW corrections (black solid line) and the SO of 1.6 eV (red dashed line). The curves are compared with an GW+RPA (green dashed dotted line) and with experimental data [109, 120] (blue and violet dotted lines). Both BSE calculations have been performed in the Tamm Dancoff approximation, that is neglecting antiresonant components of L^0 as mentioned in section 5.2.2. I checked that this approximation is indeed valid within the energy range of interest.

In the experimental spectra (violet and blue lines) one can identify three notable structures: a principal wide structure between 3.5 and 5.6 eV, a step-like bump between 5.6 and 7 eV, and finally a third wider group of peaks between 8 and 11 eV.

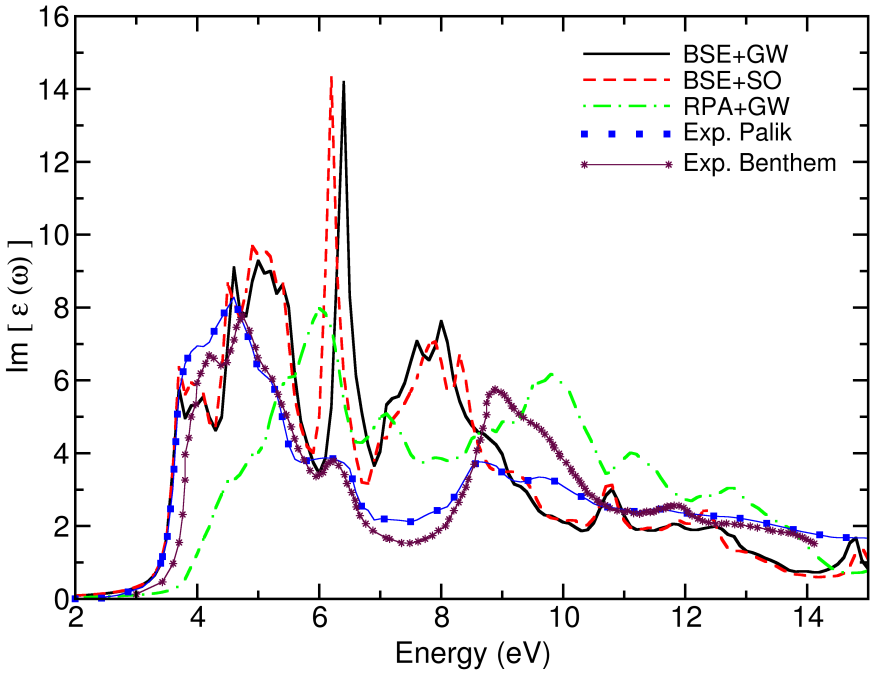

Figure 6.9: Absorption spectrum of STO: GW+BSE (black solid) and SO+BSE (red dashed), GW+RPA (green dashed-dotted) and experimental data from Palik [120] (blue dotted) and from Benthem [109] (violet crosses).

To include electron-hole interactions in the optical spectrum, the BSE has been solved. Indeed, when the electron-hole interaction is taken into account through the resolution of the BSE, all the structures are moved to lower energies indicating a strong excitonic effect. Comparing the two BSE spectra, one notices that they are very similar. In both spectra, one can identify four structures of interest: a first group extending from the onset until about 6 eV, a strong and narrow peak around 6.3 eV, a wider group extending between 7 eV and 9.5 eV and finally an isolated peak centred at 10.8 eV.

The slight differences between the two BSE spectra arise from the difference between the G_0W_0 distortion of the bands shown on Fig. 6.3b and the rigid shift approximated by the SO. The lowest energy feature comes from transitions between bands close to Fermi energy, where SO is a very good approximation. There the two BSE spectra almost coincide. Farther from the absorption edge, GW corrections slightly modify the band dispersion with the consequence of a blueshift of 0.1 eV of the strong narrow peak at 6.3 eV, and minor modifications in the other structures. In the following, GW energies will be always used, but this result indicates that SO may be used safely in more complex structures.

The comparison between RPA+GW (cfr. section 5.2.1) and BSE+GW shows that the excitonic interaction reduces the optical gap leading to a shift of ~ 0.8 eV of the peak at the onset. This is mainly an effect of the change in line shape since the corresponding exciton binding energy that one obtains by comparing the lowest energy E_λ in equation (5.57) to the direct gap, is only 0.22 eV.

The first BSE structure is on top of the experimental curve up to almost 4 eV, giving a very good description of the absorption onset. From 4 eV to 6 eV, the BSE spectrum looses some accuracy in the height of the peaks, but the position of the structure is still well reproduced. This proves that excitonic effects are very important and should not be neglected to understand the optical spectrum of $SrTiO_3$.

The second structure predicted by the BSE calculation is a sharp peak centred at 6.4 eV. It is in the range of the step-like structure in experiment extending from 5.5 and 7 eV, but the calculated intensity is strongly overestimated. Concerning the third structure, the amplitude is too strong and the energy position is centred at 8 eV for the BSE calculation while it is 9 eV for the measured spectrum. These two facts indicate a too strong excitonic effect predicted by theory.

a) Independent particle $O\ 2p \rightarrow Ti\ 3d$ and $O\ 2p \rightarrow Sr\ 4d$ transitions

In order to identify the role of different bands in the spectra, I reduced progressively the number of conduction bands included in the calculation.

Let us first analyse the RPA+GW spectrum. Since the effect of local fields is negligible in this range of energies, as shown in Fig. 6.7, the spectra reported in Fig. 6.10a have been calculated without local field effects. This allows for a direct interpretation of the structures of the spectrum in terms of vertical transitions in the GW band structure because no mixing of the IP transitions occurs (cfr. expression (4.29)).

Structure A_a is due to transitions from the valence to bands 21, 22 and 23, which have been assigned to Ti $3t_{2g}$ states. Since inclusion of higher conduction bands do not affect the A_a structure, I conclude that it is created by transition involving *only* the Ti $3t_{2g}$ states.

Structure B_a is peaked at 7.1 eV. It is created by transitions to band 24 which alone account for more than 80 % of the spectral weight, and attains full convergence including band 25. It is therefore completely ascribed to transitions to the two Ti $3e_g$ states.

It is important to note that the two Ti $3e_g$ states concur also to the formation of all the other spectral features, as expected from their density of states ranging to 11 eV. In particular C_a is for around 50 % due to these states, the remaining part coming from transitions to bands 26, 27 (Sr $4e_g$) and band 28 which has been assigned to an hybridised Sr $5s-$O $2s$ state. The inclusion of bands 29, 30 and 31 (Sr $4t_{2g}$) allows the full convergence of the spectrum.

Since B_a is of particular interest for the sharp excitonic peak, I investigated in greater

(a) Excluding conduction bands **(b)** Excluding specific transitions

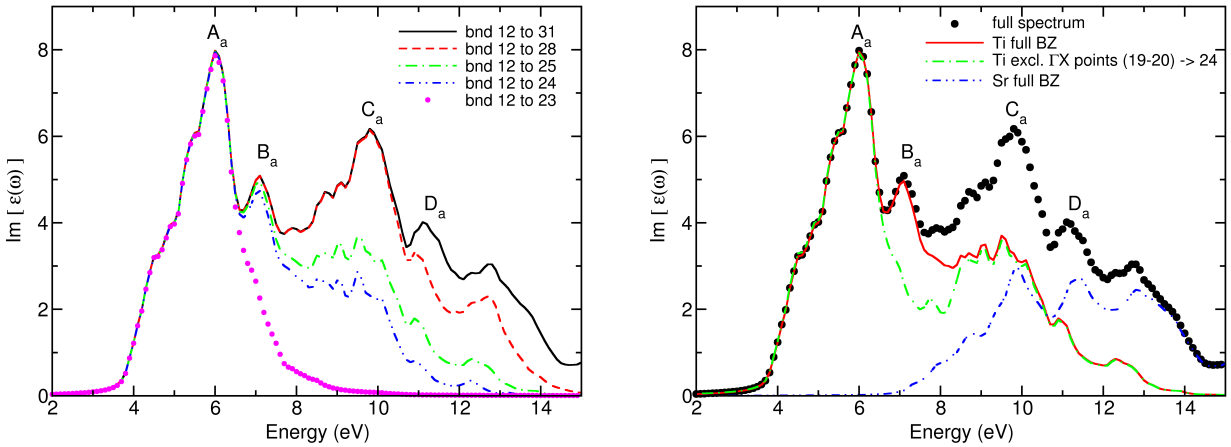

Figure 6.10: RPA+GW spectra without local fields. In Fig. 6.10a the number of conduction bands included in the calculation is up to 31 (black solid: full spectrum), up to 28 (red dashed: Ti $3d$ + Sr $4d$), up to 25 (green dashed-dotted: full Ti $3t_{2g}$ + full Ti e_g shell) up to 24 (blue dashed-double dotted: full Ti $3t_{2g}$ + lower energy Ti e_g), up to 23 (violed dots: only Ti $3t_{2g}$). Fig. 6.10b has been obtained including only Ti $3d$ states (red), only Sr $4d$ states (dashed-double dotted blue) and subtracting from the red spectrum the transitions 19→24 and 20→24 between Γ and X (green dashed-dotted).

detail the origin of the transitions in the Brillouin zone. In Fig. 6.10b I report RPA+GW spectra calculated including all Ti $3d$ states -conduction band 21 to 25 - (red solid line) and calculated excluding Ti $3d$, but including Sr $3d$ states -conduction bands 26 to 31 - (blue dashed-double dotted line). The full spectrum (black plain circles) is the sum of these two contributions. These three spectra are computed by summing transitions over all the 512 k-points sampling the Brillouin zone. The green dashed-dotted curve corresponds to a spectrum calculated including all Ti $3d$ states - conduction bands 21 to 25 - but we suppressed in the summation the transitions from valence bands 19 and 20 to conduction band 24 arising from **k**-points that falls into three cylinders enclosing the $\Gamma - X$ axes of the BZ: the B_a peak disappears. This demonstrates that this peak is mainly due to transitions from bands 19 and 20 (top valence O $2p$) to conduction bands 24 (Ti $3e_g$), for **k**-points along $\Gamma - X$. As already underlined in subsection 6.3.2, these bands are flat, corresponding to well localized states.

Peak C_a is due for about 50 % to transitions to bands 24 and 25. We checked that the valence bands involved are the 12 to 17. The remaining part involves transitions from all valence states to bands 26, 27 and 28.

To conclude, I summarise the analysis of the RPA+GW spectrum in Tab. 6.1.

Table 6.1: Transition analysis of the GW+RPA w/o LFE spectrum

peak	transitions involved
A_a	O $2p \rightarrow Ti$ $3t_{2g}$
B_a	bands 19, 20 along $\Gamma X \rightarrow$ band 24 (Ti $3e_g$)
C_a	bands from 12 to 17 $\rightarrow Ti$ $3t_{2g}$ AND O $2p \rightarrow Sr$ $4e_g$ + band 28
D_a	O $2p \rightarrow Sr$ $4t_{2g}$

b) Electron-hole interaction in $O\ 2p \rightarrow Ti\ 3d$ and $O\ 2p \rightarrow Sr\ 4d$

The same analysis as in the previous section has been performed on the BSE+GW spectrum. Parent structures have been labelled with the same letters (A, B, C and D) as in Fig. 6.10a.

(a) BSE+GW spectra

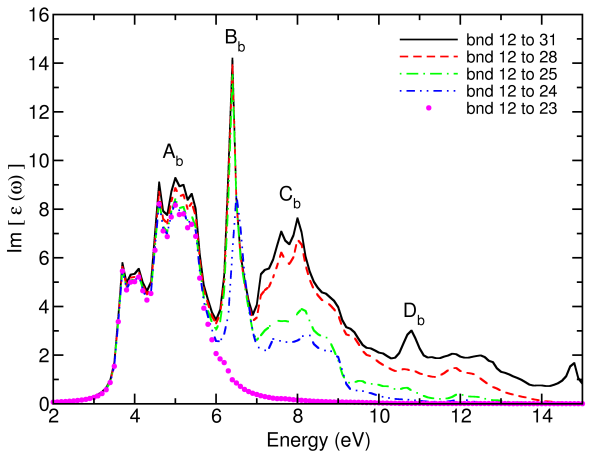

(b) Killing the excitonic peak

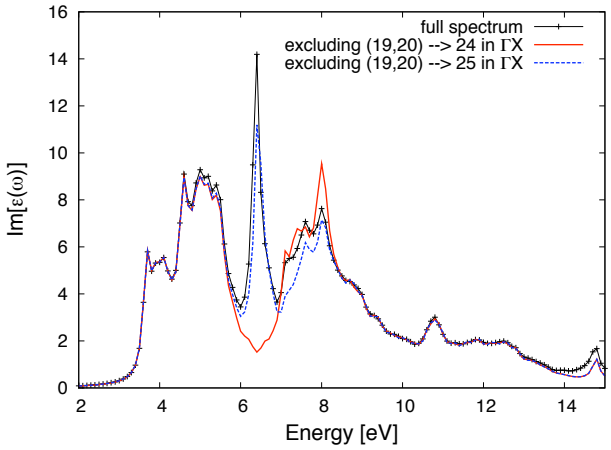

Figure 6.11: BSE+GW spectra with reduced number of bands and transitions. The color code and the method used in 6.11a is the same as in Fig. 6.10a. In 6.11b is shown that the excitonic peak at 6.4 eV is originated by transitions [19,20]→24 with **k**-points in the ΓX direction.

As in the RPA case, one can see that the group A_b is completely described by the inclusion of the bands 21, 22 and 23, corresponding to $O\ 2p \rightarrow Ti\ 3t_{2g}$ transitions.

The inclusion of bands 24 and 25 is once again responsible for the creation of the structure labelled B_b at 6.4 eV (with a shift in energy of $\sim$ 0.8 eV with respect to B_a). In the RPA case, band 24 was responsible for around 80 % of the peak intensity, and band 25 for the remaining. In the excitonic case, each band accounts for more or less half of the amplitude. The peak is very sharp and narrow.

As for the RPA calculation, bands 24 and 25 create half of the C_b peak centred at around 8 eV, the remaining part coming from the $Sr\ 4e_g$ states (bands 26 to 28). The energy difference between C_b and C_a is $\sim$ 2 eV, corresponding to a very large excitonic effect.

The structure D_b at 10.8 eV is formed essentially by $Sr\ 4t_{2g}$ states as it is determined only by bands 29, 30 and 31. The excitonic effect on D_b is much smaller.

This analysis shows that the bands 24 and 25 (constituting the $Ti\ 3e_g$ states) play a major and intriguing role in the formation of the two excitonic structures B_b and C_b. Transitions arising from these bands give on one hand the strong and narrow exciton B_b, and on the other hand contribute to the much broader exciton C_b. In section 6.3.2, I underlined that band 24 has a character that depends on its momentum **k**. Along the ΓX direction, it is flat, whereas in other regions of the BZ it is dispersing.

Since we expect the strong and narrow exciton B_b to arise from localized (non-dispersing) states, we suggest that B_b arises essentially from transitions between valence bands 19, 20 and conduction band 24 along the ΓX direction. This has been checked by suppressing in the numerator of (5.57) the IP transitions [19,20]→[24, 25] along ΓX (Fig. 6.11b). It is clear that the excitonic peak at 6.4 eV is due to the IP transitions 19→24 and 20→24 for **k**-points along ΓX.

Transitions to 24 and 25 giving rise to the C_b broad excitonic peak (and the background

that contributes to the total amplitude of B_b) come from the much more dispersing 12 to 18 valence bands, as well as from [19, 20] $\rightarrow$ 24 excluding the ΓX direction. The remaining part of the broad C_b exciton is due to transitions to Sr $4e_g$.

Even though BSE spectra can not be deconvolved in a sum over states, the peak assignment concluding the previous section is essentially confirmed here.

c) Mixing of O $\rightarrow$ Ti transitions: interference effects

The excitonic effects mix the single particle transitions T, calling for a much deeper analysis of the spectral weights $\tilde{\rho}_T A^T_\lambda$ entering equation (5.57). The coefficients $\mathbf{A}^T_\lambda$ give the weight and phase with which the various independent-particle transitions T contribute. Let us first concentrate on the weight. This is readily analysed by plotting $|\mathbf{A}^T_\lambda|^2$ as a function of the GW transition energies $\mathcal{E}_T$, for a given excitonic energy E_λ. The space of transitions is in principle continuous; therefore, the result is given as a histogram where each segment contains transitions in a range of 100 meV. Fig. 6.12 shows the result for the peak B_b, where $E_\lambda = 6.4$ eV.

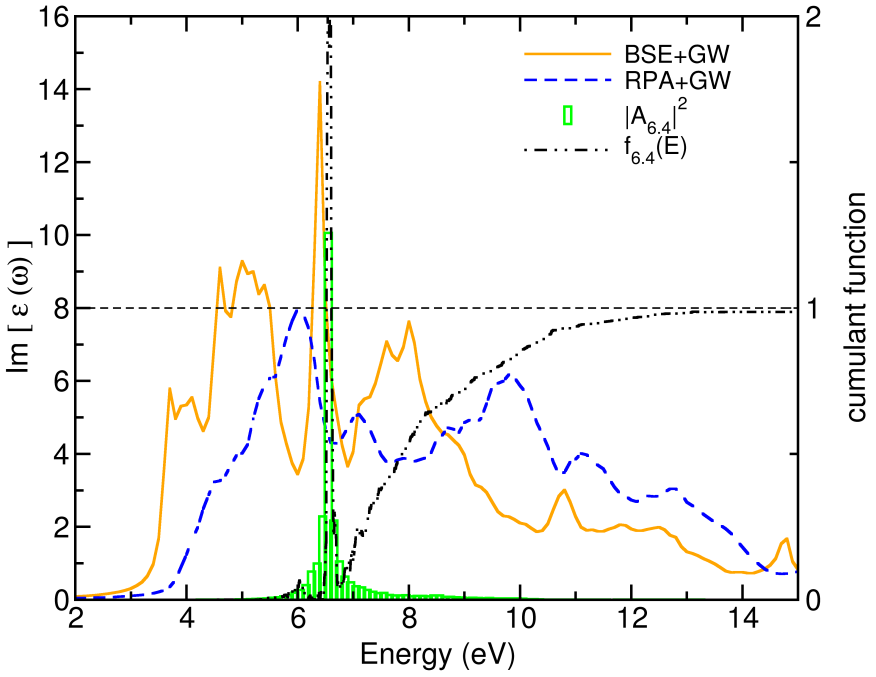

Figure 6.12: Spectral weight analysis of the exciton energy $E_\lambda = 6.4$ eV. BSE (yellow solid) and RPA+GW w/o local fields (blue dashed) are shown for comparison. The excitonic amplitude $|\mathbf{A}|^2$ (green boxes) is bigger in the range 6-7 eV, but $\mathbf{A}$ it rapidly changes sign which comports a destructive interference. The cumulant function $f_{6.4}(\omega)$ (double dotted-dashed line) starts constructing the spectrum only starting from 7 eV, where the RPA calculation displays the a small bump.

Without mixing of transitions, one would find a δ-peak. Because of the mixing instead, what it is observed is a broad distribution (green boxes), with a pronounced asymmetry extending more towards higher than towards lower energies. In order to situate the energy range, the figure also shows the BSE and RPA spectra.

From the histogram alone, it is difficult to get a quantitative idea of the role of higher energy transitions: to this end, one has to consider also the phase of the various contributions.

One way to do this is to introduce the partial spectral weight [128] defined in formula (5.61):

$$f_{E_\lambda}(E) = \frac{|J_{E_\lambda}(E)|^2}{|J^\infty_{E_\lambda}|^2}. \tag{6.1}$$

This function[36], for the peak energy $E_\lambda = 6.4$ eV, is given by the black dashed double-dotted curve in Fig. 6.12.

One distinguishes two transition energy ranges: the first region is composed by RPA transitions located between 5.5 and 6.8 eV. These are transitions involving the Ti $3t_{2g}$ states. The maximum of $|A^T_{6.4}|^2$ falls in this energy range. This, however, does not mean that these transitions dominate the final spectrum: in fact because of the phase factors, $f_{6.4}(E)$ first builds up to a sharp peak with increasing E, but this rise is followed by a steep decrease indicating a destructive interference, until the final result is almost zero around 6.8 eV. The important contribution to B_b is then given by the second energy range, extending from 6.8 eV to higher energies. It is composed by the independent GW transitions involving the Ti $3e_g$ levels. Here $f_{6.4}(E)$ exhibits a quite monotonic rise that tends to the plateau value of 1 as it should be at convergence. The cumulant function reaches the value 0.5 around 7.5 eV, that corresponds to the peak B_a in the RPA+GW spectrum. The remaining contribution essentially comes from transitions associated to peak C_a. These findings confirm our previous analysis based on figure 6.11a.

6.4.3 Localized excitations and the screening of the electron-hole pair

The previous results have been obtained using the standard approximations to the Bethe-Salpeter equation. Beside the static approximation of W, for bulk systems this includes the fact that the matrix $W_{\mathbf{GG}'}$ is taken to be diagonal in the reciprocal lattice vectors. This is exact only for homogeneous systems: the off-diagonal elements of W are determined by the off-diagonal elements of the inverse dielectric matrix. These elements are given by

$$\epsilon^{-1}_{\mathbf{GG}'}(\mathbf{q},\omega) = \frac{\partial V^{\mathrm{tot}}_{\mathbf{G}}(\mathbf{q},\omega)}{\partial V^{\mathrm{ext}}_{\mathbf{G}'}(\mathbf{q},\omega)}\ , \tag{6.2}$$

so they describe the variation of the total potential V_{tot} at a certain length scale induced by the variation of an external potential V_{ext} at a different length scale.

The effect can often be neglected in optical spectra of bulk materials, when the density is quite homogeneous or, on the contrary, for strongly localized (e.g. core) electrons which are not polarizable enough to give a sizable contribution to the induced potential. Moreover, the exciton may extend over an area that averages out the inhomogeneities of the material. However, in other systems such as clusters, one has to go beyond the diagonal approximation. In a material like $SrTiO_3$ one has to be careful, since, as we have seen above, excitations of quite different character contribute to the spectrum. In particular peak B_b is a candidate for

[36]Indeed at this energy the excitons are in the continuum, so infinitely many excitons can be found within a small interval in energy (we computed ≈ 1300 excitons between 6.2 eV and 6.4 eV). Moreover in some case they can also be degenerate. The curve shown here is actually taken from one exciton only. This has been chosen because it clearly shows the common features of all the excitons in the range, that is the interference peak and the monotonic convergence of the function f_{E_λ}. Chosing to analyse a different exciton in this range does not change the conclusions.

a more careful study, since localized states play a crucial role. Indeed, Fig. 6.13 compares the result of a standard BSE calculation using a diagonal W (same as previous figure) to the result obtained when the full matrix $W_{\mathbf{GG'}}$ is taken into account.

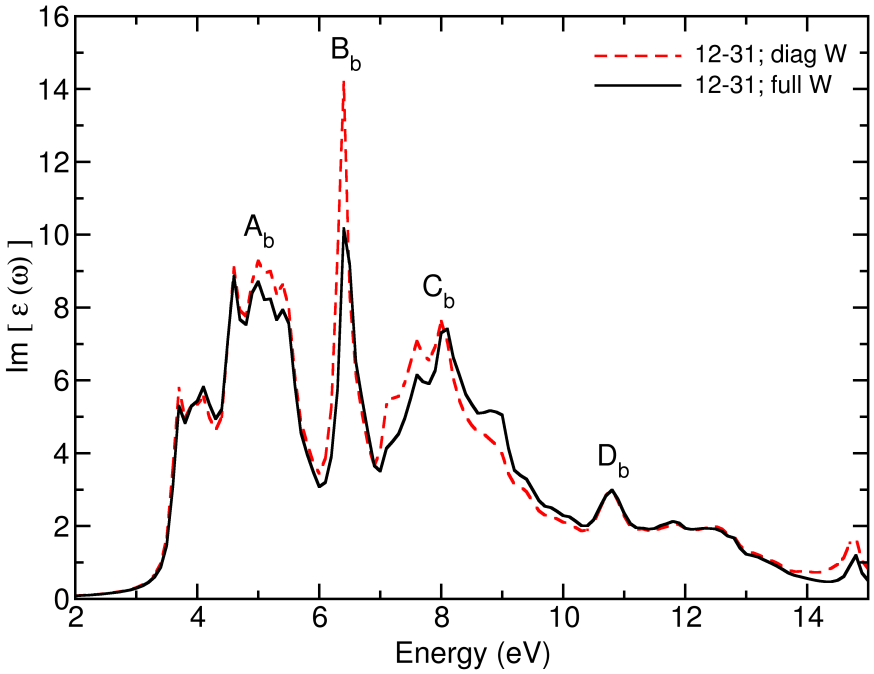

Figure 6.13: BSE+GW spectrum with diagonal (red dashed line) and full-matrix $W_{\mathbf{GG'}}$ (black line). The excitonic effects are reduced once the microscopic inhomogeneities of the response are taken into account by off-diagonal elements of $W_{\mathbf{GG'}}$.

The inclusion of the off-diagonal elements leads to minor changes on the C_b structure, while A_b and D_b are totally unaffected. Instead, the excitonic peak B_b is reduced by almost a factor of two. When the local polarizability of the electrons is correctly taken into account, there is hence significant improvement in the agreement between theory and experiment.

Nevertheless, the agreement is still not perfect, with the calculated B_b peak noticeably sharper than in experiment. One possible explanation is that this may be due to the neglect of other coupling terms in the approach used here: first, we have used the standard static screening approximation to the BSE, meaning that the one-particle Green's functions in L_0 are used in the quasiparticle approximation (expression (5.16), though setting $Z_i = 0$ for all i), and that the screening of the electron-hole interaction in W is taken at $\omega = 0$. Instead, as discussed in section 5.2.3, one should in principle use the full one-particle Green's function including the quasiparticle damping and its satellite structure, as well as the frequency-dependent W. These two kinds of dynamical effects, which contain the coupling of the primary excitation to other neutral excitations of the system, are known to cancel each other to a large extent in simple semiconductors [90]. However, this may no longer be true in a more complex material with states of different nature. The dominant effect of the dynamical contribution would be a damping of peaks. Second, we do not take into account electron-phonon coupling. The latter may be source of errors in oxide perovskite, known to have a strong electron-phonon coupling constant and so prone to host polaronic [129–131] excitations that can modify strongly the absorption spectrum.

6.4.4 Excitons via TDDFT

BSE calculations are computationally heavy, even when the SO is used instead of state-dependent GW corrections. In principle also TDDFT gives access to optical spectra, in a more efficient way. Especially for the description of continuum excitons, relatively simple kernels have been designed that allow one to perform calculations with an effort comparable to the RPA. It is therefore interesting to test various TDDFT flavours in the case of STO, where our BSE results can be considered as benchmarks, and where one would eventually like to carry out calculations for more complex structures, like interfaces, for which BSE calculations might come to their limit of feasibility.

I have performed a series of tests with two TDDFT kernels designed to include excitonic effects: the LRC [45] (see definition 4.22) and the more recent empirical Bootstrap kernel [47] (see definition (4.23)). One should not expect very good agreement at the onset, where the BSE predicts a bound exciton, but it is still interesting to investigate whether deviations lie in a tolerable range. Moreover, one may think to obtain a good description in the range of the continuum excitons, where interference effects dominate. In the spirit of searching for a simple approach, I used the SO instead of the GW corrections, as we have shown above the quality of this approximation (sections 6.3.1 and 6.4.2. The result of these calculations is reported in Fig. 6.14 where also BSE+GW, RPA+GW and the experimental spectra are shown for comparison.

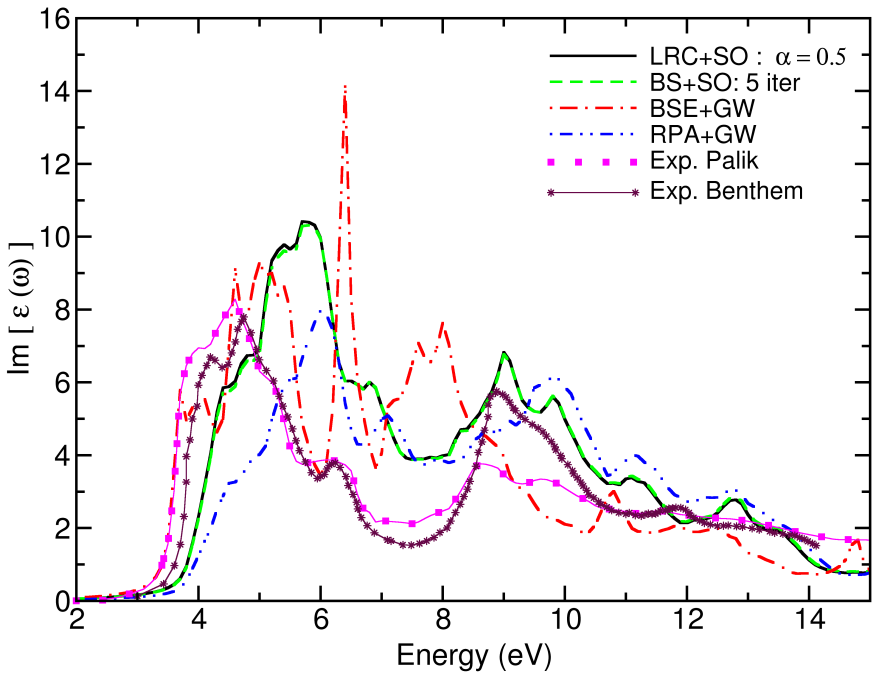

Figure 6.14: TDDFT calculations using *LRC* (black solid) and *Bootstrap* (green dashed). The experimental spectra from Palik [120] (pink connected squares) and from Benthem [109] (violet crosses) together with the BSE+GW calculation (red dash-dotted) and the RPA+GW calculation (blue dashed-double-dotted) are shown for comparison.

As can be expected in view of the similar structure of the LRC and the Bootstrap kernel, and in particular in force of their identical behaviour as $-c/|\mathbf{q}|^2$ for $\mathbf{q} \to 0$, the two approximations act in a similar way: the effect of both kernels is to transfer oscillator

strength to lower energies with respect to the RPA+SO spectrum, simulating in this way the effect of the electron-hole interaction. In the case of LRC [45] the constant c that determines the $\mathbf{q} \to 0$ divergence of the kernel is a material-dependent scalar parameter α which is determined by an established linear relation (4.22) between α and the macroscopic dielectric constant ϵ_∞^{-1}. The value $\epsilon_\infty = 6.4$ as calculated in RPA+LDA has been used, which yields $\alpha = 0.5$. The results are not very sensitive to the precise value of α. In the case of the Bootstrap kernel, the proportionality term is computed self-consistently from ϵ_∞^{-1}. Five iteration cycles have been enough to converge the parameter c. This leads to a similar value of $c = 0.478$, and therefore finally yields results that are almost undistinguishable from those of the LRC kernel.

As expected, in both cases the presence of a bound exciton at the onset cannot be well reproduced. Spectra therefore exhibit a blue-shift of the order of 1 eV. Still, about 50 % of the RPA+GW error is removed by the TDDFT calculations. Overall excitonic effects are weaker than in the BSE, also in the continuum. In particular, peak B_b remains a shoulder, though it is enhanced by the electron-hole interaction, and also the rest of the spectrum is less modified by the electron-hole interaction than in the BSE case. This leads to a puzzling situation: apart from the onset region, the agreement between the approximate TDDFT results and experiment turns out to be better than when BSE is solved.

However, this should not induce us to think that the TDDFT is superior. These kernels have been derived directly or indirectly from the BSE, and deviations have to be considered as errors. Improved results must therefore involve some error cancelling. On one hand, we have of course the simplified LRC-like form of the tested kernels. Moreover, in both cases one constant value was chosen for the proportionality constant c. However, it has been shown [46] that the constant approximation is valid only over a restricted energy range, whereas improved results over a wider range are obtained with a frequency-dependent prefactor. With the relation between parameters given by Botti and coworkers [46], one finds that c is increased by more than a factor of two around B_b, which leads to a slight red-shift of the peaks. Using this frequency dependent kernel, the discrepancy to the BSE is reduced then, but only very partially, and B_b remains a shoulder instead of a sharp peak. In other words, the simple LRC form of the kernel, even when augmented with a frequency-dependent term, cannot capture the complexity of the BSE.

It is however still interesting to note that in the high energy range the rough approximation to TDDFT leads to better agreement with experiment than the BSE: though based on error cancelling as stated above, this should not be considered as a pure coincidence. Rather, a reduced kernel can visibly simulate to some extent the reduction of the electron-hole interaction due to coupling effects that are neglected, e.g. damping due to dynamical effects.

6.5 Conclusion

In conclusion, the optical spectrum of $SrTiO_3$ shows strong excitonic effects. Hence, an independent-particle description is not sufficient to obtain good agreement with experiment. There is a bound exciton and significant shift of oscillator strength at the onset that are well described by state-of-the-art Bethe-Salpeter calculations in the framework of the GW approximation. Moreover the use of SO quasiparticle correction gives a very good description of the absorption onset. Transitions between localized electronic states dominate the

spectrum between 6 and 7 eV, leading to a sharp excitonic peak. This peak is overestimated when the spatial resolution of the screening of the localized electron-hole pair is not taken into account. Going beyond this standard approximation to Bethe-Salpeter calculations in solids, the peak is reduced, but it still remains too sharp as compared with experiment. Further structures around 8 eV also show too strong excitonic effects.

A possible explanation of the discrepancy between BSE and experiments could be the neglect of coupling to other excitations, such as phonons and/or neutral electronic excitations contained in principle in the screening of the electron, hole, and electron-hole pair. With the QP approximation to the electron and hole, and the static approximation to the electron-hole interaction, these possible excitations are lost[37]. Overall, it turns out that a quantitatively correct description of the absorption spectrum of $SrTiO_3$ requires to go beyond state-of-the-art Bethe Salpeter calculations.

TDDFT in simple long-range approximations to the exchange-correlation kernel recovers about 50 % of the RPA+GW error at the onset, and yields a better description of the higher energy part of the spectrum than the BSE. This feature should be due to error cancelling.

However, I also showed that one can obtain agreement with experiment on a level that is sufficient to analyze the various structures and explain their origin by using computationally efficient approximate approaches, including the scissor operator to replace GW corrections to the bandstructure, and TDDFT using a simple long-range kernel.

[37]Note that similar features are found also in other materials (cfr. peak at 22 eV in LiF reported in Fig. 5.7b) which also may be ascribed to the lack of coupling.

Chapter 7

Graphite allotropes

One of the main objectives of this thesis is to understand and predict absorption and EEL spectra of isolated and interacting nanostructures. In this context systems made of graphene sheets can be considered as prototype cases.

Investigation on optical [19, 132–135] and EEL spectra [19, 134, 136, 137] have been already subject of several works. Quasiparticle dispersion has also been studied [138–143], especially near the point K of the Brillouin zone, but when compared to theory, only the band structure was considered. Instead, in order to reach the full complexity of electronic excitations, it is interesting to study also spectral functions, for they are composed of a quasiparticle peak and satellites. The latter stem from long range plasmon excitations and can therefore be expected to be more sensible to neighbouring layers than the quasiparticle peaks. To our knowledge, only few results [74] are available concerning the one-particle spectral function, as measured e.g. in photoemission.

In this chapter I investigate the full one-particle excitation spectrum, with special emphasis on dynamical effects such as plasmon satellites. In this perspective I have taken part into a theoretical and experimental work which has been recently submitted [94].

Chapters 7, 8 and 9 are devoted to the study of dynamical effects in graphene and graphitic structures. In this chapter, the interaction between graphene sheets is investigated by looking at three allotropes of graphite differing only by the stacking of the graphene sheets. I report the analysis of EEL spectra for parallel and perpendicular momentum and spectral functions. The main question this chapter wants to answer to is "How sensitive are EEL spectra and the spectral functions to the geometrical details?"

7.1 Carbon allotropes

Graphite is an allotrope of Carbon. Its bulk structure is composed by 2D layers of atoms arranged on a honeycomb lattice. Atoms of each layer are strongly bound together by covalent bonding, whereas the interlayer interactions are essentially of van der Waals nature [144], and hence much weaker. For this reason graphite exfoliates easily (that let us write with pencils, as etymology indicates!). The graphene sheets can be therefore considered as building blocks of the bulk material. By changing the stacking of graphene layers, different graphitic crystals can be obtained.

(a) AA stacking

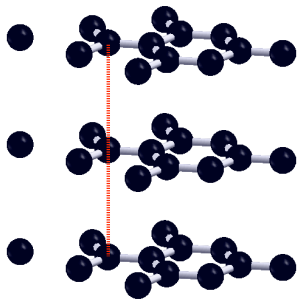

Atomic coordinates

$\mathbf{a}_1$	$\mathbf{a}_2$	$\mathbf{a}_3$
0.0	0.0	0.0
1/3	2/3	0.0

(a) ABA stacking

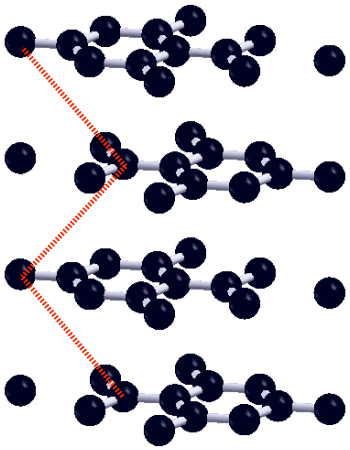

Atomic coordinates

$\mathbf{a}_1$	$\mathbf{a}_2$	$\mathbf{a}_3$
0.0	0.0	1/4
1/3	2/3	1/4
0.0	0.0	3/4
2/3	1/3	3/4

(a) ABC stacking

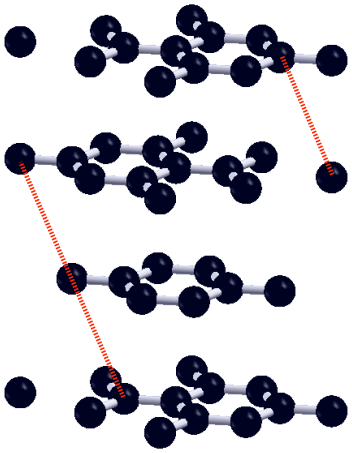

Atomic coordinates

$\mathbf{a}_1$	$\mathbf{a}_2$	$\mathbf{a}_3$
0.0	0.0	0.0
1/3	2/3	0.0
1/3	2/3	1/3
2/3	1/3	1/3
0.0	0.0	2/3
2/3	1/3	2/3

Figure 7.4: Three different stacking of graphene with the atomic coordinates for unit cell, expressed in the hcp unitary vectors.

Different stacking of graphene

The AA stacking (Fig. 7.1a) is the simplest way to pile up graphene layers: all atoms of one layer are on top of those of the layer below. Although this configuration is not found in nature, it is possible to synthesize it using high-density dc plasma in appropriate atmosphere from a diamond substrate [145]. Via transmission electron microscopy or electron diffraction [146] it is also possible to characterize the samples. The difficulty in growing this stacking comes from the repulsion between the p_z orbitals of different planes which have a big overlap for all atoms are superimposed. The measured interlayer distance d between two graphene planes is between 4.3 Å and 5 Å [146], while the theoretical equilibrium distance I computed[38] is $d \approx 3.64$ Å, close to other theoretical works [147]. This structure has two atoms per unit cell of height $L_z = d$.

In the ABA stacking (reported in Fig. 7.2a), also called hexagonal graphite, the graphene sheets are superimposed following a zig-zag pattern in such a way that each layer has the same position as two layers below, as depicted in Fig. 7.2a. So each hexagon of a sheet is centred on one atom of the layers below and above. It is the most stable form of graphite [148] and can indeed be found in nature. The hexagonal close packing (hcp) unitary cell contains four atoms arranged on two layers. It has an height $L_z = 2d_0$. The theoretical equilibrium distance between two planes presented in this work is $d_0 \approx 3.335$ Å in very good agreement with experimental data [148, 149] and other theoretical predictions [147].

The rhombohedral graphite (ABC stacking) is a metastable phase which is not found at temperatures $T > 2000$°C, and which is not observed alone but always mixed together with the ABA structure. Recently it has been possible to synthesize bulk ABC graphite [150, 151]. In the rhombohedral graphite (Fig. 7.3a), graphene layers are shifted along one direction in such a way that every three layers the same atomic disposition is found. Although the unitary cell has a rombohedral symmetry, including 6 atoms per unit cell, it is better to use a less symmetric hcp cell, to ease the comparison with other structures. The hcp cell encloses three layers and it contains 6 electrons. I computed the interlayer distance that minimizes the total energy getting $d \approx 3.36$Å, in agreement with the experimental value of ≈ 3.35Å and recent theoretical calculations [147]. The corresponding cell height $L_z = 3d = 10.08$Å. The nearest neighbour environment of the p_z orbitals is similar to that of the ABA stacking, which explains the similar value of d.

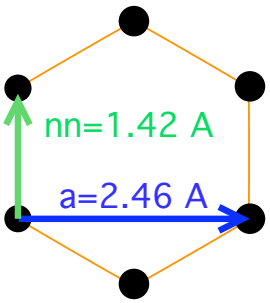

Figure 7.5: In-plane geometry of the unit cell. Carbon atoms are circles.

A fourth graphitic material is also observed. It is called turbostatic graphite, it is still made by graphene layers, but no periodicity in the stacking [152] is found.

In all the three periodic structures, the experimental value of the in-plane lattice parameter $a = 2.46$ Å has been used [149], which corresponds to a nearest neighbour distance of 1.42 Å.

[38] The bulk interlayer equilibrium distance has been computed by minimising the total energy with respect to d

7.2 Ground state properties

In this section different contributions to the total energy of the three structures are discussed and the KS band structure of the three systems are presented.

Computational Details: The k-point grid used to sample the Brillouin zone in the three systems is a $17 \times 17 \times 8$ Monkhorst-Pack grid. The total energy was converged applying a cutoff to the plane waves basis set of 31 Hartree. Troullier-Martins pseudopotentials have been used to model core electrons. The exchange-correlation potential has been approximated within LDA. All calculations have been done with the ABINIT [124] simulation code. Equilibrium interlayer distances have been computed through minimization of the total energy with respect to the cell height L_z.

Energy contributions

The ground state total energy is the sum of different contributions: kinetic T, Hartree E_H and exchange-correlation $E_{\rm xc}$. In Tab. 7.1 I report the values I computed for these three energy components normalised with respect to the total energy of the system (which is negative).

Table 7.1: Equilibrium interlayer distances and energy contributions.

stacking	d [Å]	$T/E_{\rm tot}$	$E_H/E_{\rm tot}$	$E_{\rm xc}/E_{\rm tot}$
AA	3.64	-0.6861	-0.3371	0.3546
ABA	3.33	-0.6861	-0.2796	0.3548
ABC	3.36	-0.6861	-0.2796	0.3548

The sum $T + E_H + E_{\rm xc} \neq E_{\rm tot}$ because there are other energy contributions (not discussed here) coming from the specific implementation of the KS scheme in the crystal environment (as the Ewald contribution) and from the ionic contribution modelled by the pseudopotential.

Note the relative importance of the kinetic term with respect to the other two, as pointed out in introducing the DFT, at the end of section 3.2.1.

The kinetic and the exchange-correlation contributions do not change in the three considered stackings, indicating that they are not sensitive to the structural differences at long distance. This is in agreement with the fact that in LDA the exchange-correlation potential $V_{\rm xc}(\mathbf{r})$ decays exponentially, so it is well localised on the planes of graphene[39].

On the other hand the Hartree term has a higher ratio in the AA than in the other two structures. The Hartree energy reads $\frac{1}{2}\int \rho(\mathbf{r}')\rho(\mathbf{r})|\mathbf{r}-\mathbf{r}'|^{-1}d\mathbf{r}d\mathbf{r}'$ where ρ is the charge density. In the AA stacking, electronic charges are piled together forming kind of columns of charge, whereas in the other two materials charges are more distributed. Because of this peculiar concentration of charges, the repulsive[40] Hartree term has a higher value.

Band structure

The LDA band structure of the three systems is reported in Fig. 7.6.

[39] This is actually not the correct asymptotic limit; the exact $V_{\rm xc}$ indeed should decay much more slowly.
[40] The negative ratio indicate repulsive interaction.

The valence bands of ABC and ABA are indistinguishable on the in-plane direction $\Gamma - M - K - \Gamma$; differences are noticed when some perpendicular component is explored (section $\Gamma - A - L - H - A$). Similar considerations hold for the first conduction bands (up to ≈ 20 eV).

The AA stacking instead differs also in the plane: for instance along the $\Gamma - M$ line, a higher degeneracy is observed, because of the higher symmetry of this system.

It is also interesting to compare the bands around the Fermi level in the K point (along $M - K - \Gamma$) and around the H point (along $L - H - A$).

In the rhombohedral graphite (ABC, Fig. 7.6a), two almost degenerate bands are found around the K point. One of the two bands splits close to the Fermi energy, avoiding the band crossing between valence and conduction states in K, whereas the other band gives rise to the "Dirac cone" (linearly dispersing bands) slightly off from the K point. Identical scenario is found in the H point.

In the hexagonal graphite (ABA, Fig. 7.6b) a similar dispersion is found at the K point, but the "Dirac cone" is not observed as the bands crossing the Fermi energy have a quadratic dispersion. This aspect is in agreement with other calculations performed in multilayer graphene [141]. At the H point, instead, the difference with the ABC stacking is more pronounced: bands are degenerate in this point because of the higher symmetry of the hexagonal graphite, and an almost linear dispersion is indeed observed.

We come finally to the AA stacking, which displays a peculiar behaviour: in both points bands disperse linearly, but in the K point the tip of the cones is higher than the Fermi energy, while in the H point the bands cross below the Fermi energy, as reported also by other authors [143, 153].

The different structure around K in the three materials can be better appreciated in Fig. 7.7, where the band dispersion near Fermi is reported along the vertical line $K - H$.

In the ABC geometry a "Dirac cone" occurs in a point near K, slightly shifted towards the Γ point. Two doubly degenerate bands are parallel one to the other, without dispersing and without crossing the Fermi level between K and H. The ABA geometry offers a very different scenario: two degenerate bands lay on the Fermi level, along the entire $K - H$ line, while other two bands, which are separated at K by about 1 eV, converge in the H point from above and below the Fermi energy. In the H point all four bands are degenerate. The AA geometry displays a third different band structure, with two degenerate dispersing bands from K to H, which cross the Fermi level in the middle of the $K - H$ line forming one electron pocket in H and a hole pocket in K.

From the band structure alone one can expect spectral functions to be similar, but it is not clear to which extent.

7.3 Electron energy loss spectra

With the electron energy loss spectroscopy one can access the diagonal elements $\epsilon^{-1}_{\mathbf{GG}}(\mathbf{q}, \omega)$ (cfr. equation (2.24)) getting in particular information on the collective excitations of the system such as plasmon resonances. The latter are collective long-range excitations, so they are expected to be sensitive to some extent to the geometry of the stacking. In EEL spectroscopy it is possible to tune the exchanged momentum $\mathbf{q} + \mathbf{G}$ in order to probe excitations along different directions.

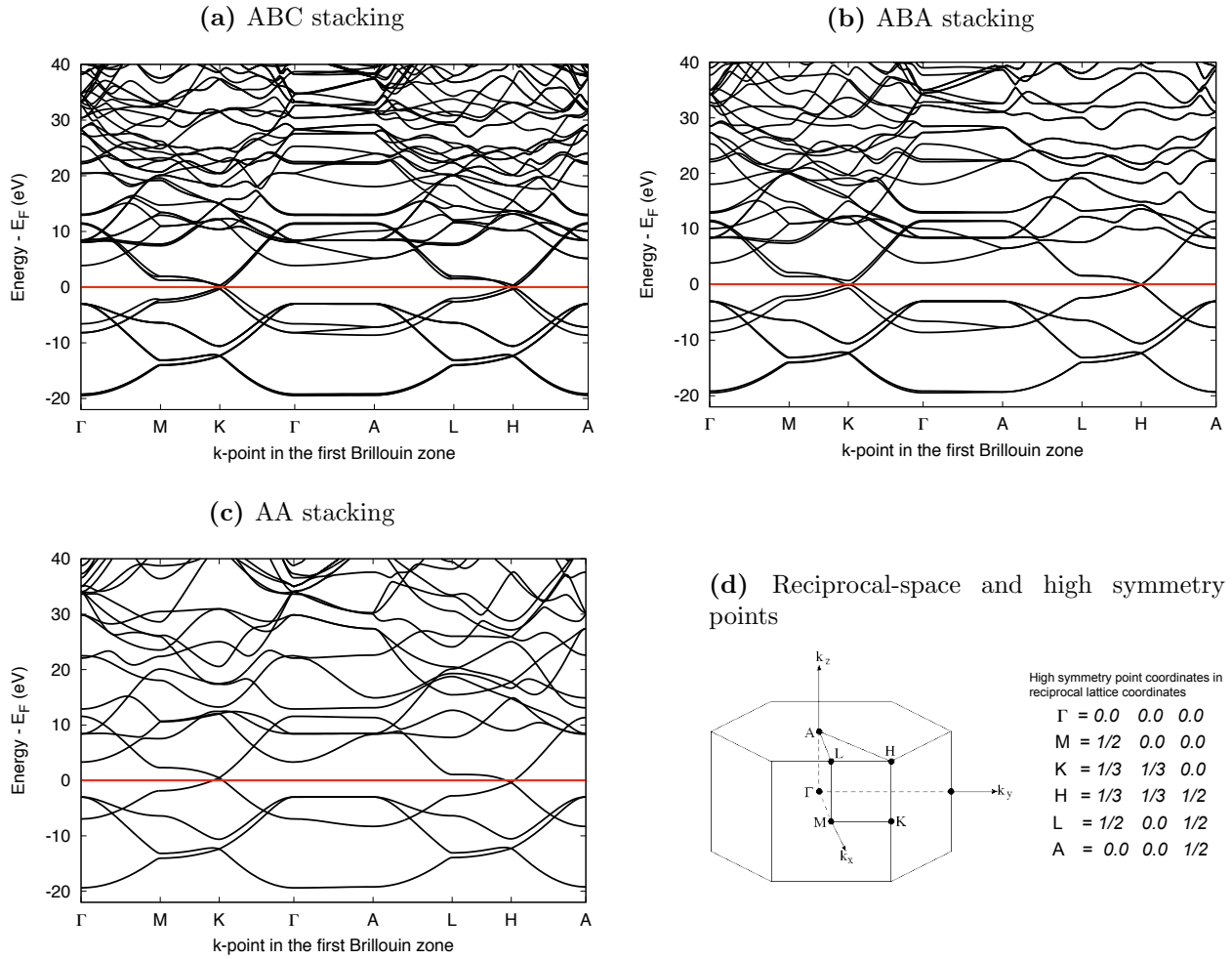

Figure 7.6: Band structure of graphite with different stackings of graphene sheets.

In Figs. 7.8 and 7.9 the EEL spectrum of the three systems at different exchanged momenta is reported. Due to the strong anisotropy of the layered structures I divide the discussion into two sections, one devoted to in-plane momentum transfer, and the second to perpendicular momenta.

Computational details: The EEL spectrum has been computed with the code DP [127]. Ground state KS wave functions and energies, computed with the software ABINIT [124], have been used to construct $\chi^{KS}_{\mathbf{GG'}}$ according to expression (4.10). The RPA expression of ϵ (4.19) has been inverted to get $\epsilon^{-1}_{\mathbf{GG}}(\mathbf{q},\omega)$, accounting in this way for the local fields. The number of plane waves used to reproduce the KS states in the expression of χ^{KS} is 350 for all the three systems, while the number of bands `nbands` included in the calculation and the dimension of the matrix `npwmat` are reported in Table 7.2. The Brillouin zone has been sampled with a mesh $34 \times 34 \times M_z$ centred in Γ where the number M_z of points sampling the k_z direction (also reported in Tab. 7.2) depends on the exchanged momentum.

A broadening of 0.1 eV has been applied.

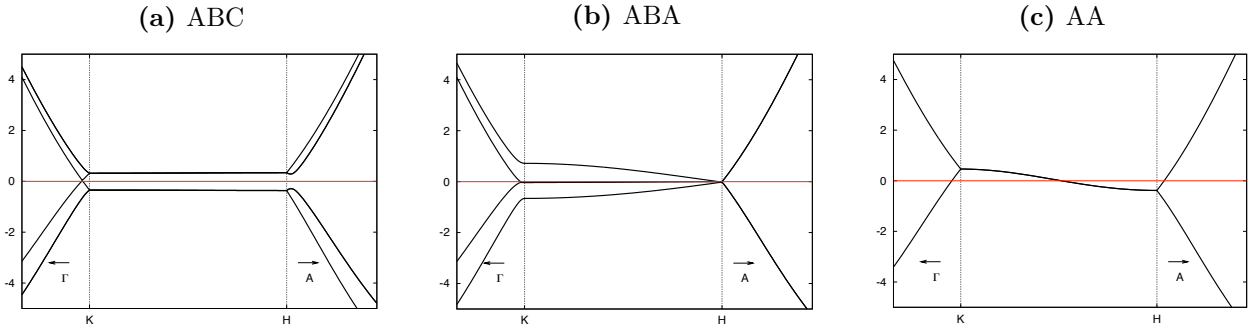

Figure 7.7: The band structure of the three systems along the $K - H$ line of the Brillouin zone.

Table 7.2: Convergence parameters for the caclulation of EEL spectra.

system	`nbands`	`npwmat`	M_z ($q_\parallel$)	M_z ($q_\perp$)
AA	40	50	4	8
ABA	80	100	4	8
ABC	80	100	4	8

Parallel momentum transfer

The EEL spectrum at small parallel momentum is reported in Fig. 7.8a. All systems exhibit two structures, a small peak at around 7 eV, and a second stronger excitation at much higher energy (between 25 and 30 eV depending on the system).

The first structure is ascribed to in-plane collective excitations of the π electrons (π plasmon). The second more intense structure involves the collective vibration of the σ and the π electrons ($\pi + \sigma$ plasmon) [19, 134, 154].

While the π plasmon does not change in the three systems, the $\pi + \sigma$ plasmon displays some modifications. Hexagonal and rhombohedral graphites have essentially the same spectrum: the peak has the same height and it is centred at the same energy of 29.4 eV, while in the AA graphite the $\pi + \sigma$ plasmon is red-shifted by ~ 0.7 eV. I verified that this effect is actually due to the difference in interlayer distance, and it is not induced by the different stacking: the AA graphite, having a lower density per volume because of the higher value of d, has consequently a lower plasmon frequency ($\omega_p^2 \propto \rho$). Indeed, if one uses the same interlayer distance as for the ABA system, both the π and $\pi + \sigma$ plasmons of the AA geometry do not differ any more from the same structures of the other two geometries.

The spectrum reported in Fig. 7.8b refers to large momentum transfer[41] ($q_\parallel \approx 2\,\text{Å}^{-1}$). In this case short distances are probed. At almost the same position as in the previous case we find two structures. Although they resemble the π and $\pi + \sigma$ plasmons, both are actually originated by inter-band transitions, i.e. they reflect the presence of structures in $\Im[\epsilon_M(\omega)]$. At this range of exchanged momentum, $\Re[\epsilon_M]$ is never 0, so they can not be considered plasmonic excitations. Note also their decrease in intensity. Beside these two structures a third peak (labelled (a)) is predicted at $\sim$16 eV also due to inter-band transitions.

The first structure at 7 e V seems not to be modified by the different stacking of the planes and it is essentially identical in the three considered geometries.

The (a) peak located at 16 eV for the three systems is followed by a small shoulder at

[41] Large with respect to the reciprocal lattice vector $4\pi 3^{-1/2} a^{-1}$ with $a = 2.46\,\text{Å}$.

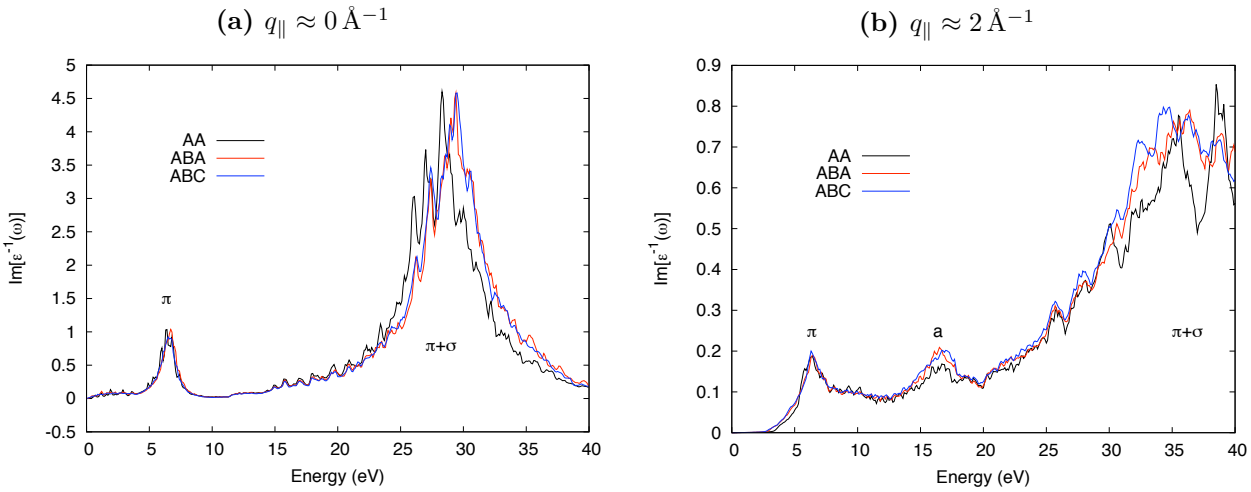

Figure 7.8: Electron energy loss spectra for in-plane momentum transfer at small momentum 7.8a and large momentum 7.8b. The spectra of the three systems are depicted with a black curve (AA), a red curve (ABA) and a blue curve (ABC).

an energy 2 eV higher. Although the excitation energy is the same, in the AA system the weight of the first peaks is lower whereas the shoulder has the same intensity in the three geometries.

The broad and high structure at 35 eV exhibits some interesting differences, in all the three geometries, although the ABA and the ABC systems differ for minor details. More modulations are observed in the AA geometry where the high energy part of the spectrum displays a global height comparable with the other two systems, but with two sharper peaks on top.

At short $q_{\|}$ (that is probing long distances), there is no significant difference in the EEL signals when the same interlayer distance is employed for all structure. On the other hand some major difference is observable at large momentum transfer, that is when short distances are probed, especially in the higher region of the spectrum. This is in agreement with the physical intuition that the electronic density of the three graphites differ more on a microscopic scale description (local inhomogeneities) than on a macroscopic scale. This is particularly true for the AA structure: since all carbon atoms are piled one on top of the other, the inhomogeneities of the charge density are expected to be higher than in the other two systems. As a result, for large parallel momentum transfer, the AA geometry seems to be distinguishable from the other systems, with differences likely within experimental resolution, whereas the other two spectra are too similar to be discerned experimentally.

The theoretical calculations I presented here for the ABA structure are in agreement with recent theoretical calculations on graphite computed by A. G. Marinopulos et al. [134], whereas differences are found in comparing our data to [154] because the latter calculations have been performed without local fields.

Perpendicular exchanged momentum

When perpendicular momentum is exchanged, the family of excitations is much richer, although the intensity is significantly reduced.

Spectra obtained for small perpendicular momentum transfer are reported in Fig. 7.9a.

Structures of interest are labelled with letters (b,c,d,e_1,e_2 and f). As in the previous case, the ABA and the ABC signal are similar to each other, while the AA geometry gives a significantly different spectrum, much more different than what observed in the in-plane case.

The (b) structure is common only to the ABA and ABC spectra, while no excitation is found at the same energy in the AA geometry. These excitations are due to HOMO-LUMO transitions ($\pi-\pi^*$)[154] which are actually forbidden in the AA geometry because of selection rules.

At higher energy, all the three geometries display a first group of structures at 10 eV (c), stemming from structures of the $\Im[\epsilon_M]$, and a strong and narrow peak at 18-19 eV (d) of plasmonic nature ($\Re[\epsilon_M] = 0$). While no significant difference is found in the three systems when looking at the (c) structure, the (d) peak has interesting characteristics in the AA which are not found in the other two geometries. I report a close up on this structure in Fig. 7.10, where EEL spectrum (red lines) is reported together with $\Re[\epsilon_M]$ (blue) and $\Im[\epsilon_M]$ (black). A double peak is displayed (AA) instead of a single structure (ABA and ABC). The first one, around 18 eV, is a plasmon, alike the similar structure in the other two systems; the second, higher than the first and located at 20 eV, is another collective excitation[42]. Moreover the AA version of the (d) peak decreases sharply, whereas in the other two geometries the presence of a shoulder at 22 eV makes the slope more gradual.

Beyond 22 eV two notable inter-band structures are found: a first one labelled (e) and a second labelled (f). The first displays important differences depending on the stacking, appearing as a relatively narrow and high peak (e_1) in the AA stacking or as a much broader and lower structure (e_2) in the other two geometries. Morevoer its position changes: it is centred at 25 eV in the AA graphite, whereas it is at much higher energy ($\sim$ 28 eV) in the other two cases.

Finally the (f) structure, still an inter-band transition, is actually a broad excitation which displays a well defined peak in the AA geometry at 34 eV, whereas no clear feature can be distinguished in the hexagonal and rhombohedral graphite. The latter result is in contrast with the ABA calculation reported in [154], where a strong peak is predicted on top of the (f) structure. The difference has to be ascribed to local field effects, which are more important for perpendicular components.

In the large momentum regime (Fig. 7.9b), similar features can be found. All excitations are of inter-band nature, as $\Re[\epsilon_M]$ never crosses the zero line.

At very low energy, ABA and ABC still display an excitation not so different in shape from the (b) structures originated by the same HOMO-LUMO transitions. Contrary to the small momentum case, also the AA displays a structure (g) which is strongly peaked at very low energy. It comes from the semi-metallic nature of the AA system highlighted in Fig. 7.7c and is actually strongly dependent on the k-point sampling.

After a plateau with no intensity, the signal has a second structure (h) around 10 eV. In the ABA and ABC graphites, the (h) structure has a strong peak at 19 eV which decrease abruptly at higher energies. Instead, the same structure in the AA graphite appears broader and red-shifted by almost 2.5 eV. At its basis, around 22 eV, the ABA and ABC signals have a small structure which has the same origin as the shoulder discussed for the (d) peak.

The (e) and (f) structures are also recognisable, and marked here with (i) and (j) letters. Characteristics of the (i) structure change importantly in passing from the AA to the ABA

[42]Strictly speaking this second peak is not a plasmon, since the $\Re[\epsilon_M]$ does not cross the zero.

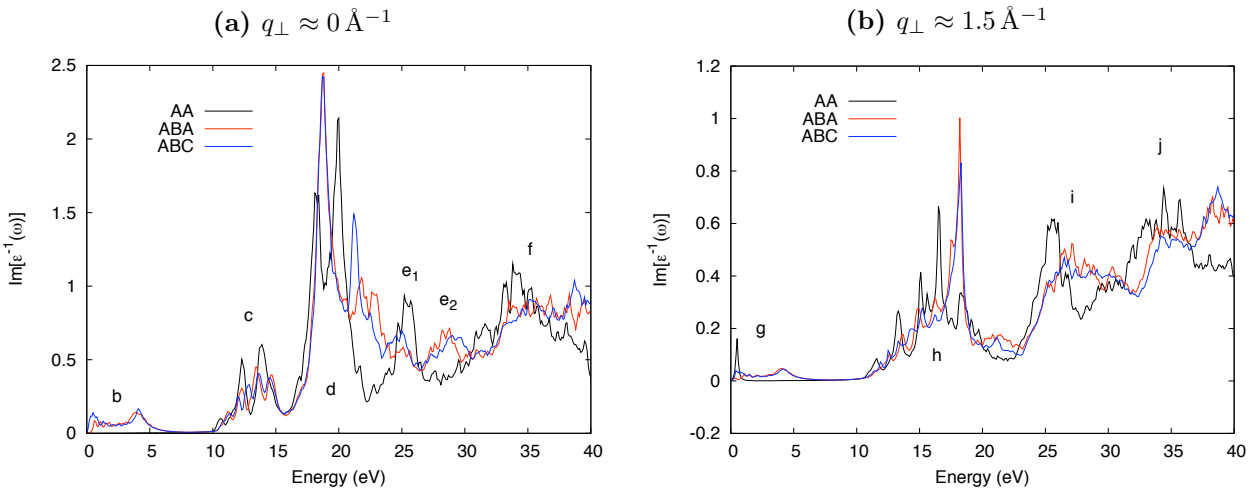

Figure 7.9: Electron energy loss spectra for momentum transfer perpendicular to the graphene sheets at small momentum (7.9a) and large momentum (7.9b). The spectra of the three systems are depicted with a black curve (AA), a red curve (ABA) and a blue curve (ABC).

or ABC geometries, as it was the case for the (e) peaks.

In the case of perpendicular momentum transfer, the number of excitations is much higher than in the in-plane case and the line shape is more modified by the stacking. Also in this case, ABC and ABA graphites seem to have too similar spectra to be experimentally distinguished, whereas the AA graphite differ from them in several regions, thing that may be used to characterise a sample. In particular, major differences can be found in the region between 20 and 30 eV where AA displays sharp peaks (e and i) while the other two geometries present broader blue-shifted structures.

In the perpendicular momentum case, local fields effects significantly change the line shape of the spectra, especially at high energy.

7.4 Spectral functions

Let us now move to the one-particle spectral functions.

When electrons are extracted from the material, the creation of the hole can couple with other excitations of the system. This is accounted for by the dynamical self-energy Σ. The dynamical coupling between the hole and other excitations has moves part of the weight of the primary peak (quasiparticle peak) to other structures. As a result the quasiparticle peak broadens and satellites are observed at higher binding energies.

The self-energy is computed in the GW approximation, where $\Sigma \propto W = \epsilon^{-1} v$. Hence, in order to discuss the dynamical effects of the self-energy, one has to analyse the effects of the matrix $\epsilon^{-1}_{\mathbf{G}\mathbf{G}'}(\omega)$ on the single-particle excitations. That justifies the presented study of the EEL spectrum, but how the elements of $\epsilon^{-1}_{\mathbf{G}\mathbf{G}'}$ enter in Σ is more involved.

Summing together (5.29) and (5.30) to get Σ, and using the Lehmann representation of

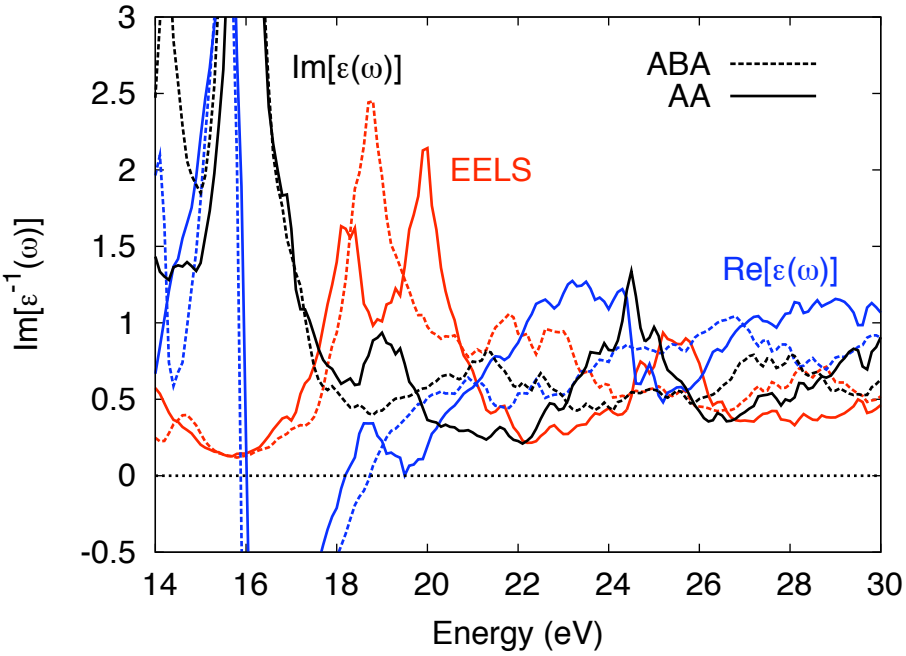

Figure 7.10: Particular of the structure (d) of Fig. 7.9a. EEL spectrum: $\Im[\epsilon^{-1}(\omega)]$ (red), $\Im[\epsilon_M(\omega)]$ (black) and $Re[\epsilon_M(\omega)]$ (blue) are reported for the AA geometry (solid line) and for the ABA geometry (dashed line).

G, the matrix elements of the self-energy read

$$\langle i|\Sigma(\mathbf{r},\mathbf{r}',\omega)|i\rangle = \\ = \frac{i}{(2\pi)^4}\sum_{\mathbf{G}\mathbf{G}'j}\int e^{-i\delta\omega'}\int \frac{\tilde{\rho}^*_{ji}(\mathbf{q}+\mathbf{G})W_{\mathbf{G}\mathbf{G}'}(\mathbf{q},\omega')\tilde{\rho}_{ji}(\mathbf{q}+\mathbf{G}')}{\omega-\omega'-\varepsilon_j+i\,\mathrm{sign}(\varepsilon_j-\mu)}d\mathbf{q}d\omega' \tag{7.1}$$

where $\tilde{\rho}_{ji}$ are defined in (4.11), ε_j are KS energies, and the screened Coulomb interaction W is reported in its Fourier components.

Because of the sum over $\mathbf{G}$ and $\mathbf{G}'$ and the integration in $\mathbf{q}$, all elements of the dielectric function (long range, short range, both parallel and perpendicular) contribute to the self-energy. Thus it is not trivial to predict how the stacking influences this sum. The analysis has to pass through the calculation of the spectral function.

In the previous section I showed that AA graphite can be distinguished from the other two stackings, especially when perpendicular elements of ϵ^{-1} are considered. What is the scenario in the case of spectral functions?

General considerations

Spectral functions of the three graphitic systems have been computed according to expression (5.32), reported below to ease the discussion:

$$\mathcal{A}_i(\omega) = \frac{1}{\pi}\frac{|\mathcal{I}_i(\omega)|}{\mathcal{R}_i^2(\omega)+\mathcal{I}_i^2(\omega)} \tag{7.2}$$

with

$$\mathcal{I}_i(\omega) = \Im[\Sigma_i(\omega)] \qquad \text{and} \qquad \mathcal{R}_i(\omega) = \omega - E_i^H - \Re[\Sigma_i(\omega)]$$

where E_i^H is the Hartree energy of the $|i\rangle$ state (in the case considered here the bottom valence) and $\Sigma_i(\omega) = \langle i|\Sigma(\mathbf{r},\mathbf{r}',\omega)|i\rangle$ is computed according to (7.1). For a discussion of possible structures in the spectral function we refer to section 5.1.5.

Computational details: The screening matrix $\epsilon^{-1}_{\mathbf{GG}'}(\mathbf{q},\omega)$ has dimension 170×170, the KS states needed to construct the oscillator strengths are represented by 715 plane waves and the number of bands included in the sum over states is 150. The $\mathbf{k}$-point grid used to sample the BZ is $10\times10\times2$ centred in Γ. The screening has been computed with the contour deformation method in order to give an accurate description of all the structures of the dielectric matrix. The real energy axis has been sampled up to 55 eV with 270 energies, while 5 imaginary energies have been used.

The self energy has been computed using 200 bands and 715 $\mathbf{G}$ vectors in the exchange part, while the correlation part is dimensioned as ϵ^{-1}. The number of plane waves used to represent the KS states is 715.

Common features

First let us look separately at the three geometries to recognise features common to the three systems. In Fig. 7.11 the spectral function $\mathcal{A}$ and its components ($\mathcal{I}$ and $\mathcal{R}$) are reported for the three materials.

It is possible to recognise three structures in the spectral functions (red lines) of each system.

1. The quasiparticle appears as sharp peak around -20 eV. It is generated by the almost vanishing denominator in expression (7.2). Dynamical effects of the self-energy are responsible for broadening and damping the peak, with the corresponding occurrence of extra structures at higher binding energy (satellites).

2. A secondary peak is found at a binding energy of ≈ -28 eV. At this energy $\mathcal{I}$ has the low π plasmon peak and $\mathcal{R}$ is almost 0. It can be considered to have a strong plasmaronic component although in the ABC and ABA systems the function $\mathcal{R}$ does not cross the zero.

3. At much higher binding energy (≈ -55 eV), the three spectral functions display a very broad and low structure. This is essentially originated by the numerator of expression (7.2), contrary to the other two peaks. Although the corresponding structure of $\mathcal{I}$ is broad, it is strong enough to produce an appreciable plasmon satellite in $\mathcal{A}$.

Note the similarity in all the three systems between the imaginary part of the self-energy $\mathcal{I}(\omega)$ and the EEL spectrum at vanishing $q_\parallel$. In fact, if one measures the energy difference between the quasiparticle peak and the other structures of $\mathcal{A}(\omega)$ (around 7 and 23 eV respectively), one realises that they fall at the same position of the π and the $\pi+\sigma$ plasmons in EELS. For this reason I will refer to these two structures with the name of π and $\pi+\sigma$ plasmons (in $\mathcal{I}$ and $\mathcal{R}$) and plasmon satellites (in $\mathcal{A}$).

Some consideration about the plasmaron

Although the plasmaron is a spurious result of GW (see section 5.1.5), it is often located not far from where some structure should be observed in principle. For example a plasmaron

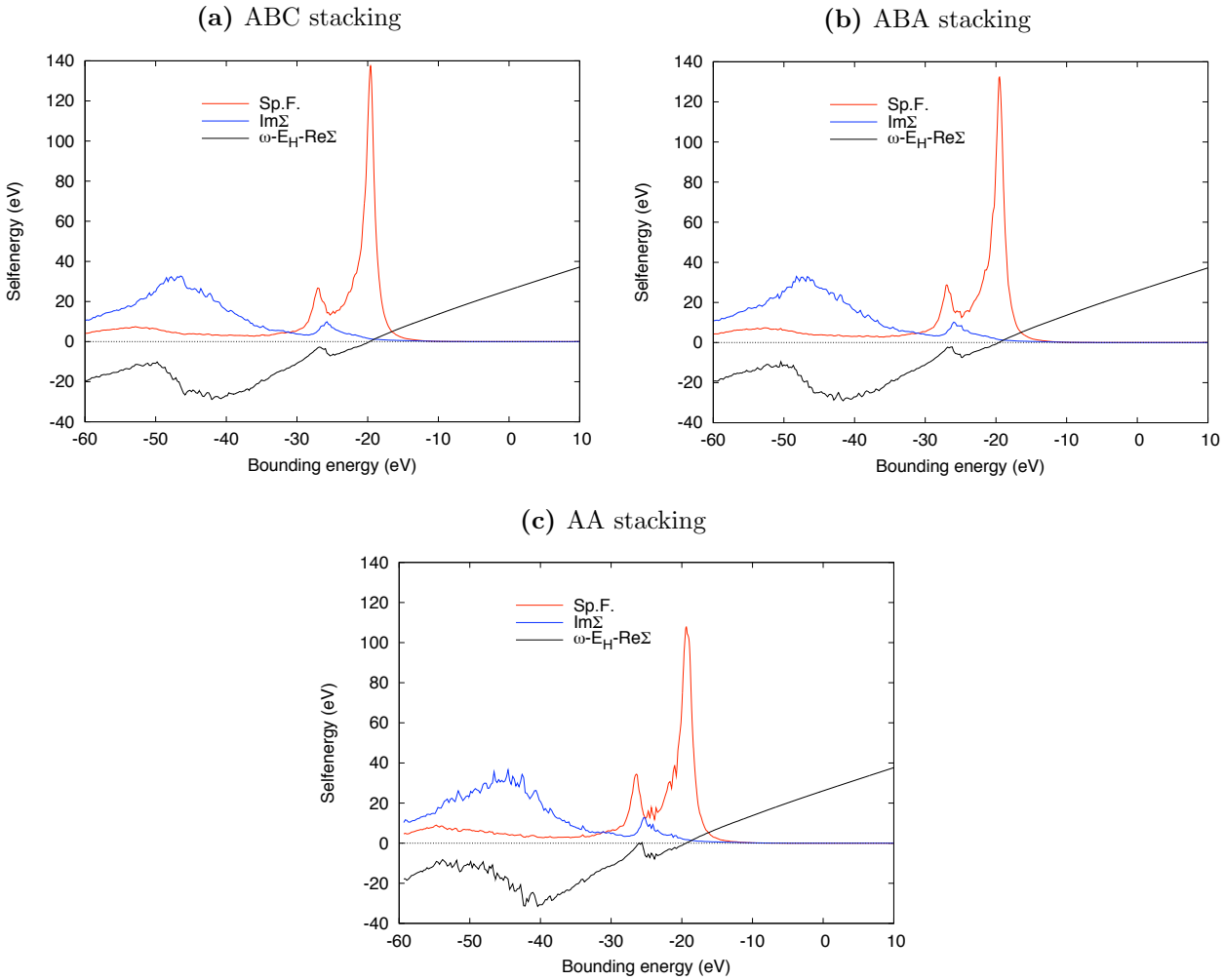

Figure 7.11: Spectral function $\mathcal{A}$ (red), $\mathcal{I}$ (blue) and $\mathcal{R}$ (black) at bottom valence for the ABC, the ABA and the AA graphites. The y axis refers to $\mathcal{I}$ and $\mathcal{R}$, the spectral function being plotted in arbitrary units.

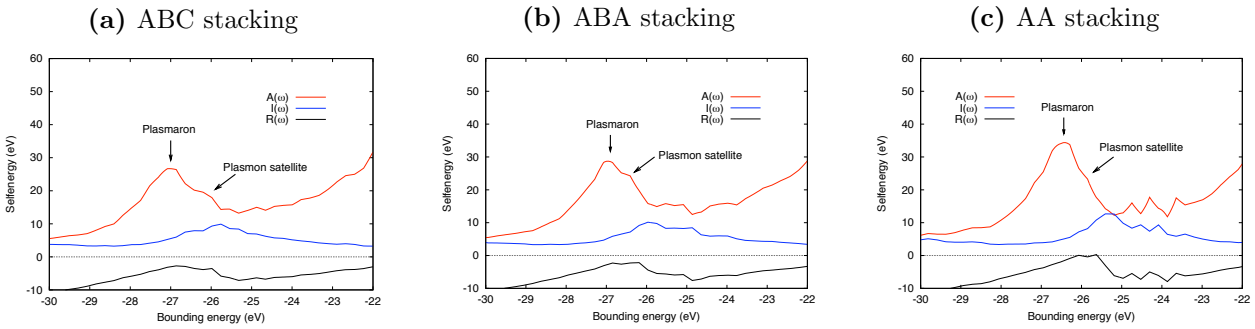

Figure 7.12: Close up on the plasmaron excitation. On the ABC and the ABA systems the π plasmon satellite appears as a shoulder in the stronger plasmaron excitation. In the AA system the plasmaron is so strong ($\omega - E^H - \Re[\Sigma] = 0$) that the plasmon satellite is completely hidden.

can appear when $\mathcal{I}$ has sharp structures relatively close to the QP peak (for instance low energy plasmons, as the π plasmon). In fact, because of the Kramers-Kronig relations, also $\mathcal{R}$ displays a peak which may eventually pass the zero line, so creating a the plasmaron peak, as evident from equation (7.2).

On the other hand, because of the presence of structures in $\mathcal{I}$, a plasmon satellite should indeed be found, but this is in many cases completely overwhelmed by the much stronger (and wrong) plasmaron peak.

In Fig. 7.12 a close up of the three plasmarons is shown. In the case of the ABA and the ABC structures, the π excitation of Σ is not strong enough to make the real part cross the zero. Strictly speaking the corresponding structure is not therefore a plasmaron, nevertheless a strong peak is observed due to the small denominator in (7.2). Nevertheless the correct plasmon satellites can still be recognised as shoulders in both curves.

On the other hand, in the AA geometry, the real part of Σ crosses the zero line, resulting in a sharper plasmaron peak. As a consequence the π satellite that should be seen is barely visible.

Comparison between systems

To compare better the three structures, all spectral features are reported in Figs. 7.13 and 7.14. As it can be seen, the differences between hexagonal and rhobohedral graphites are really small and most likely the two structures can not be distinguished experimentally, neither from the quasiparticle peak, nor from the satellite structures.

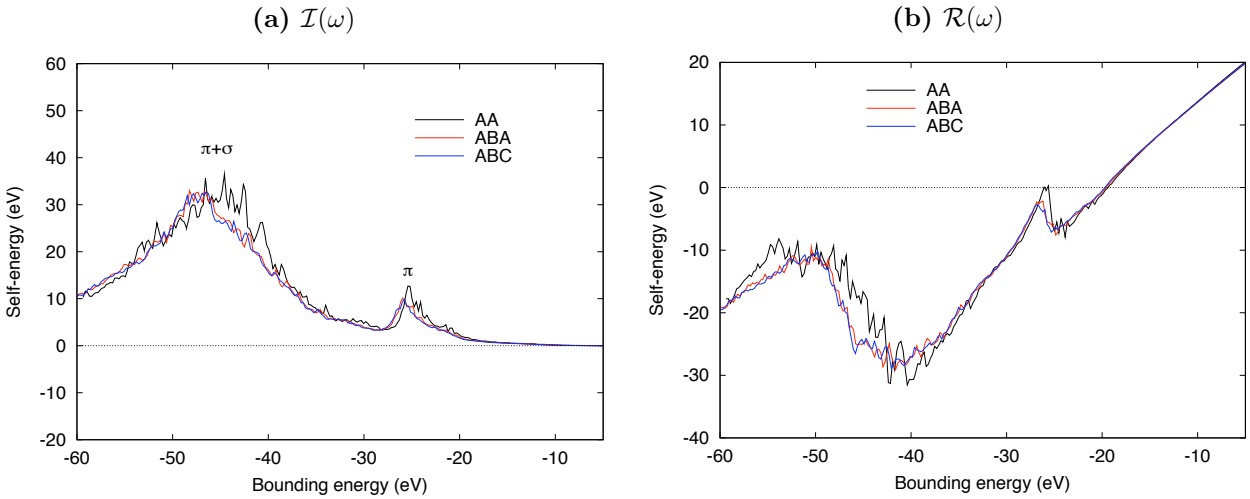

Figure 7.13: Spectral properties at bottom valence for the AA, ABA and ABC graphite. The ABA and ABC system have identical features, while some difference in the structures of the AA system is found with respect to the other two geometries.

On the other hand the AA stacking shows some major difference with respect to the other two systems, essentially because of the plasmonic excitations. In fact the π structure of $\mathcal{I}$ is more intense and it is peaked at a binding energy lower by 1 eV with respect to the same excitation in the other two geometries. Important differences are also observed in the $\pi + \sigma$ structure, which is moved by ~ 5 eV to lower binding energy.

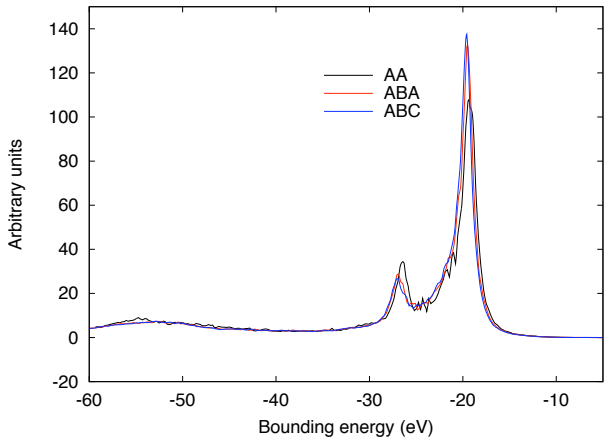

Figure 7.14: Spectral function $\mathcal{A}$ at bottom valence of the three systems. While QP peaks are similar in the three graphites, the satellites of the AA system differ clearly from the ABA and the ABC system.

7.5 Conclusion

LDA band structure

The LDA band structure of the three systems are appreciably different. In particular directions $\Gamma - M$ and $A - H$ may be used to distinguish the three geometries. In fact at Γ and A a band can be found at ≈ -10 eV which disperses as a plane wave through the directions $\Gamma - M$ and $A - H$. The degree of degeneracy of this state can be used to discriminate the system: only one band is observed in both paths for the AA, two non degenerate bands are found in the ABC and two bands along $\Gamma - M$ but only one along $A - H$ characterise the ABA stacking. Major differences in the band structure are found closer to the Fermi level and in the empty states.

EEL spectra

EEL spectra have a very different line shape when parallel or perpendicular momentum transfer are considered. In the first case, few structures are found: one is generally located around 7 eV, (π plasmon at $q_{\|} \approx 0$) and another much more intense is at 30 eV or beyond (the $\pi + \sigma$ plasmon at $q_{\|} \approx 0$). Differences between the AA geometry and the other two systems are found at high energy for large momentum transfer, whereas the ABC and the ABA graphites are almost identical to each other. Differences at small momentum transfer are rather ascribed to the different lattice constant along the z axis.

When the momentum is exchanged perpendicularly, a bigger variety of excitations are predicted for all systems, some of them due to inter-band transitions, such as e.g. the (b),(g),(e) and (i) peaks, others of plasmonic nature, e.g. (c) and (d). Once again the ABA and the ABC spectra look very similar; major differences can be found in the AA spectrum. In particular AA has peculiar characteristics in the range between 20 and 30 eV (structures (e_1) and (i)). At low energies the structure (g) due to transitions along the $K - H$ line of the BZ, is strongly sensitive to the k-point sampling and is ascribed to the semi-metallic character of the bands in the $K - H$ direction.

These conclusions suggest that electron energy loss spectroscopy is indeed sensitive to the stacking of planes, but only up to the first layer. Parallel momentum could be used to

characterise the system only when very short distances are probed, that is at big exchanged momentum. Perpendicular components instead are more sensitive, with no substantial preference for small or big $q_\perp$. In theoretical spectra, local field effects have to be included, especially when high energy structures are of interest and for perpendicular momentum transfer.

Spectral functions

The quasiparticle peaks in the spectral functions seem to be undistinguishable in the three systems. Small differences may be observed between the AA and the other two graphites, but they are probably not strong enough to be resolved experimentally.

Clearer could be the distinction based on satellite structures (especially on the $\pi + \sigma$), but they have to be resolved with enough accuracy. Instead the ABA and ABC signals are almost identical also in this range.

A structure that is almost a plasmaron is observed in the three geometries, close to the quasiparticle peak. It is more intense in the AA stacking and slightly blue-shifted with respect to what seen in the other two graphites. The intensity of this spurious structure is such that in all the cases the plasmon satellite arising from the π peak either appears as a small shoulder (ABA and ABC) or it is barely visible (AA stacking).

Since the plasmaron is an artefact of GW [76], one should not expect the calculated spectra to predict experiment quantitatively. However, the corresponding differences between stakings can be traced back to the imaginary part of Σ (see Fig. 7.13), which means that they would also persist in more elaborate approaches. In particular on ABA graphite, cumulant expansion calculations [5, 79] yield results in good agreement with experiment.

Chapter 8

From bulk graphite to isolated graphene

In this and in the subsequent chapters I will focus on the isolated graphene sheet and on the transition from bulk graphite to isolated graphene. Starting from the AA geometry, the distance between layers is progressively increased in order to study the electronic properties of the system at different inter-layer separations, with a special interest for the band structure, the EEL spectrum and the spectral function.

Dynamical effects of the dielectric function $\epsilon^{-1}_{\mathbf{GG'}}(\omega)$ *are discussed on the basis of the direct calculation of the matrix elements (EEL spectra) and the calculation of the self-energy* $\Sigma = iGv\epsilon^{-1}$*. In fact, as seen in the previous chapters, the real and the imaginary part of* Σ *determine the peaks of the spectral function. The self-energy and the spectral function is computed with* G_0W_0 *and also via a self-consistent update of the poles of the Green's function. Moreover an approximated self-consistent calculation is obtained using a technique introduced by Hedin [2] and presented in section 5.1.4.*

In the context of the graphite-graphene transition, I took part into two experimental sessions in the beamline TEMPO [6] in the synchrotron radiation source Soleil in Saclay (France). We collected data of valence band angle-resolved photoemission spectroscopy from graphite and graphene samples. These measurements have been used to corroborate theoretical studies on the plasmonic structures of the spectral function of graphene and graphite [94]. More details on this can be found in Appendix D.

Introduction: a single graphene sheet

As explained at the beginning of the previous chapter, graphite is made by layers of graphene sheets. The previous chapter was focused on the variations of the electronic properties of bulk graphite due to different stacking of its constituent layers, while this chapter is focused on the properties of the building block itself. Recently it has been possible to produce single monolayers of graphene by exfoliation [156], by heating hexagonal SiC crystals [157, 158] or by chemical synthesis [159, 160].

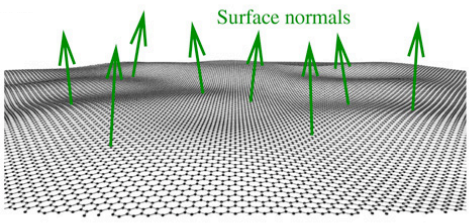

Figure 8.1: Pictorial image of free-standing graphene taken from Ref. [155].

The feasibility of isolating free standing [161] and quasi-free standing [158, 162] graphene

flakes, made it possible to measure electronic properties of bidimensional crystals by means of e.g., EEL spectroscopy [154, 163] and angle-resolved photoemission spectroscopy [138]. Though, theoretical arguments based on thermodynamics predict 2D crystals to be unstable [164, 165]. This apparent contradiction is solved by the occurrence of a long wavelength buckling[43] in free-standing sheets and by van der Waals interactions with the substrate in quasi-free standing graphene.

The elementary cell of graphene is planar. It has two lattice vectors $\mathbf{a}_1$ and $\mathbf{a}_2$ forming an angle of 120° on the xy plane

$$\mathbf{a}_1 = (a\ ;\ 0.0\ ;\ 0.0) \text{ and } \quad \mathbf{a}_2 = \left(-\frac{1}{2}a\ ;\ \frac{\sqrt{3}}{2}a\ ;\ 0.0\right)\ , \quad \text{with } a = 2.46 \text{ Å } [166]. \tag{8.1}$$

Atomic coordinates are

$$\tau_1 = (0.0\ ;\ 0.0\ ;\ 0.0) \qquad \text{and} \qquad \tau_2 = \left(\frac{1}{3}\mathbf{a}_1\ ;\ \frac{2}{3}\mathbf{a}_2\ ;\ 0.0\right) \tag{8.2}$$

that results in a nearest neighbour distance of 1.42 Å .

The reciprocal lattice still has a honeycomb structure, but it is rotated by 90° with respect to the real space one. Reciprocal lattice vectors are

$$\mathbf{b}_1 = \left(\frac{\sqrt{3}}{2}b\ ;\ \frac{1}{2}b\ ;\ 0.0\right) \quad \text{and} \quad \mathbf{b}_2 = (0.0\ ;\ b\ ;\ 0.0)\ , \quad \text{with } b = 4\pi/\sqrt{3}a^{-1}\ . \tag{8.3}$$

Real and reciprocal space elementary cells of graphene are reported in Fig.s 8.2a and 8.2b.

(a) Real space. Carbon atoms as circles, full circles in τ_1 and τ_2.

(b) Reciprocal lattice. First Brillouin zone and reciprocal lattice vectors.

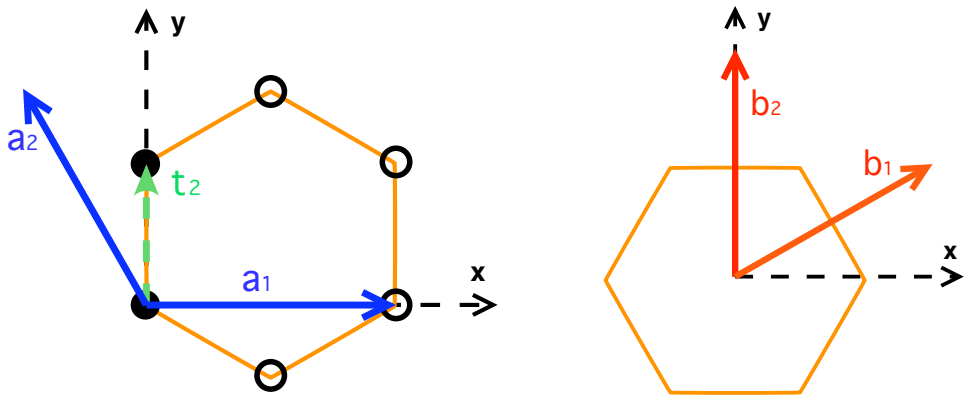

Figure 8.2: Left: real space unit cell and lattice vectors of graphene. Right: first Brillouin zone and reciprocal lattice vectors.

[43]The length of a corrugation in free-standing graphene is of the order of one hundred of Å whereas the nearest neighbour distance is ∼ 1.4 Å. Therefore the isolated graphene sheet can be considered locally a perfect 2D crystal. As a consequence the bucklng will be ignored in following discussions.

8.0.1 The transition from graphite to graphene

Graphene has attracted huge interest for its outstanding electronic and structural properties [167, 168]. Beside interesting properties of the graphene layer itself, an active field of research is the transition from graphite to graphene [133, 135, 141, 154]. The interest is both theoretical and technological, because changes in the number of layers, in their distance or in the stacking geometry, can be used to tune the electronic properties of a sample to a considerable extent. An example of this has been given in the previous chapter, where different stackings of graphene sheets were studied. Here I will investigate the evolution of spectral properties from the bulk graphite to the isolated sheet. The change itself of the electronic properties is a subject of this chapter, but furthermore I want to give an answer to the question "*At what interlayer distance a graphene sheet can be considered isolated? And with respect to which spectral feature?*"

To study this transition, two methods can be followed: the first consists in piling monolayers of graphene one on top of the other until the graphite system is obtained, the second consists in increasing progressively the distance between planes of graphite until the isolated film is found.

Increasing the number of layers

Experimentally, it is possible to grow and characterise graphitic structures with considerable control on the number of graphene layers. In a work by Eberlein and coworkers [154], a series of EEL measurements on graphitic systems with different deposition layers is presented. Spectra have been measured using a scanning transition microscope. They collected spectra from a monolayer of graphene, a bilayer, a trilayer and so on up to more than 10 layers which retrieves the bulk graphite signal. Their experimental curves, taken at vanishing momentum parallel to the planes, are reported in Fig. 8.3. One can recognize the π and the $\pi + \sigma$ plasmon excitations already showed in Fig. 7.8a.

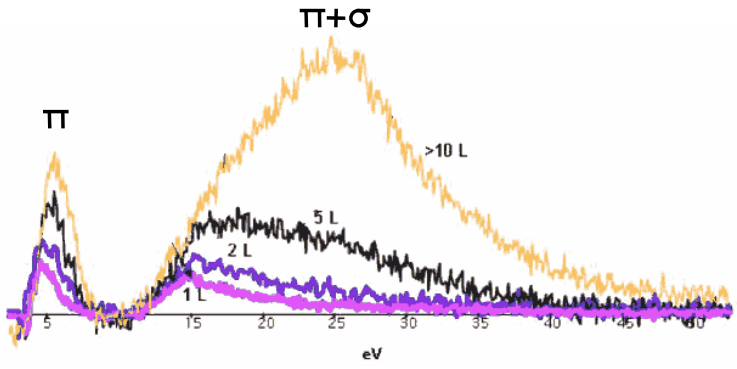

Figure 8.3: EELS at different monolayer deposition for $q_{\parallel} \approx 0$. Image taken from [154].

In going from graphene to graphite, the π plasmon is blue-shifted by $\approx$ 2 eV and its relative intensity with respect to the $\pi + \sigma$ plasmon passes from almost 1 to approximately 0.5. The $\pi + \sigma$ plasmon is much more sensitive to the stacking of graphene layers, its peak moves 10 eV towards higher energy (15 eV in graphene and 27 in graphite). The $\pi + \sigma$ structure extends up to 50 eV in graphite, whereas in graphene the signal is negligible already at 30 eV.

The explanation given by the authors is the progressive fading of the bulk plasmons of graphite (at 7 eV and at 26 eV) with the survival only of the surface modes ($\sim$ 5 eV and $\sim$ 15 eV).

In the same paper are presented also theoretical results obtained by increasing the number of deposited layers (and so mimicking the experiment) and by increasing the interlayer distance. These calculations have been obtained in the RPA neglecting local field effects for both parallel and perpendicular momentum transfer. As noted in the previous chapter (discussing structure (f) in Fig. 7.9a), local fields may play a non negligible role in modifying the line-shape of the spectrum, especially when perpendicular components are considered. In fact, an isolated plane constitutes a strong inhomogeneity along z, so local fields have to be included in theoretical calculations.

Increasing the interlayer distance

A different approach to study the graphite-graphene transition, is by increasing the separation d between the layers of graphene until convergence to the isolated signal. It is important to note that the converged distance may differ if looking at different quantities. Because of this reason, I will speak of isolated system for a given distance d, with respect to a given property. This approach, easy to follow in simulations, can hardly be performed in an experimental situation.

This will be the technique of choice in the present work, so all results showed in this chapter will refer to a transition obtained by an increase in the interlayer distance d.

In this context I took part into an experiment of angle-resolved photoemission from the valence bands of graphene and graphite. The experiment has been performed at the TEMPO beamline [6] in the synchrotron radiation source Soleil on July 2011 and February 2012. We studied the dynamical self-energy effects in graphene and graphite comparing our theoretical results with the experimental data we collected. More details on this work are reported into Appendix D and in reference [78]. The analysis, mainly based on the interpretation of photoemission spectroscopy of M. Guzzo et al. [5], yielded an article we submitted to Physical Review Letters [94].

In order to understand some features of the satellites and in particular of the plasmaron, I simulated two intermediate graphite-like systems (in future called $2d_0$ and $4d_0$) where the separation between graphene sheets was multiplied by a factor of two and four respectively.

The detailed comparison of the electronic properties of these two intermediate systems, of the AA graphite and of isolated graphene is the subject of the present chapter.

The supercell method

To isolate the planes of graphene from their periodic replicas, the distance between successive layers is increased. The simulation box contains the elementary 2D cell of graphene plus some empty space in the z direction, as depicted in Fig. 8.4a. The simulation box is called supercell as it is bigger than the unit cell of the material. The height of the supercell L_z is then a parameter to converge. The corresponding reciprocal cell (Fig.8.4b) has height $b_3 = 2\pi/L_z$, which shrinks to 0 as L_z increases. Note that, even though the system of study is a 2D system, from a computational point of view it is necessarily conceived as a 3D periodic crystal. I will come back to this point later.

Throughout this chapter, I will use the supercell method based on the increase of the interlayer distance d. Since the goal is to describe the isolated graphene, I will work only in the AA stacking, as it has the lowest number of atoms per unit cell. At large d one may reasonably expect that all stackings yield the same result. In this configuration $d = L_z$ because only one layer of graphene enters in the unitary cell. The interlayer distance d will be increased by integer multiples of the ABA graphite distance $d_0 = 3.335$Å; accordingly the corresponding systems will be labelled $1d_0$, $2d_0$, $4d_0$ and $6d_0$ (see Tab. 8.1).

Table 8.1: Table of graphitic systems

system	L_z [Å]
$1d_0$	3.335
$2d_0$	6.71
$4d_0$	13.42
$6d_0$	20.13

d_0 = interlayer distance in the ABA graphite.

8.1 Ground state properties

Here I report and discuss band structure calculations for the four systems of interest. I will discuss the effect of confinement along the z axis looking at the DFT band structure before moving to excited state properties.

In Fig. 8.5, the band plots computed up to 40 eV are reported. The highest occupied state is set to 0 eV for all calculations and it is marked by a red horizontal line.

Computational Details: They do not differ from the parameters used in the previous chapter[44]. The k-point grid employed in the calculation of the density ($17 \times 17 \times 8$) yields converged total energy values for all systems.

Valence bands

For all the structures, the four valence bands have a total bandwidth of 20 eV.

For $L_z > 1d_0$, the states along the perpendicular directions $K - H$ and $A - \Gamma$ do not disperse at all, which is an indication that the system is confined along k_z. From the $2d_0$ system, the KS charge density of occupied states can be considered to be identical to that of the isolated graphene. As a confirmation of this, the valence bands do not change when increasing further the interlayer distance ($4d_0$ and $6d_0$).

On the contrary, in the $1d_0$ graphite, constitutive layers still interact with each other. With respect to the systems reported in Figs. 7.6c and 7.7c, the only difference is in the

[44] Actually the number of planewaves has been converged directly on the $6d_0$ graphene sheet.

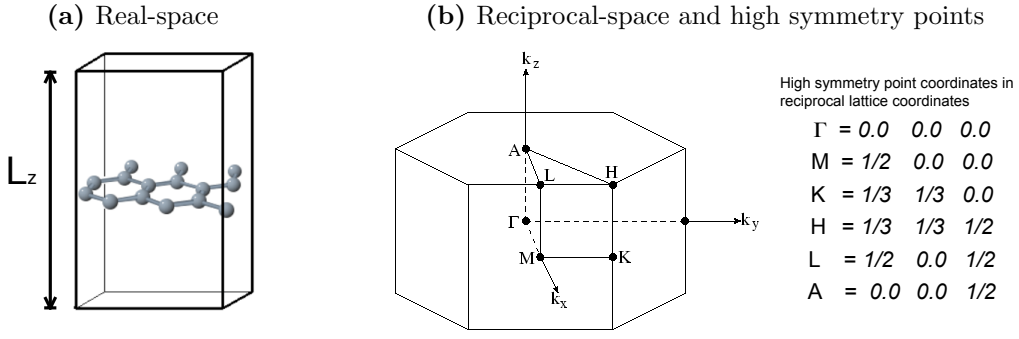

Figure 8.4: Real and reciprocal supercell for theoretical calculations of graphene

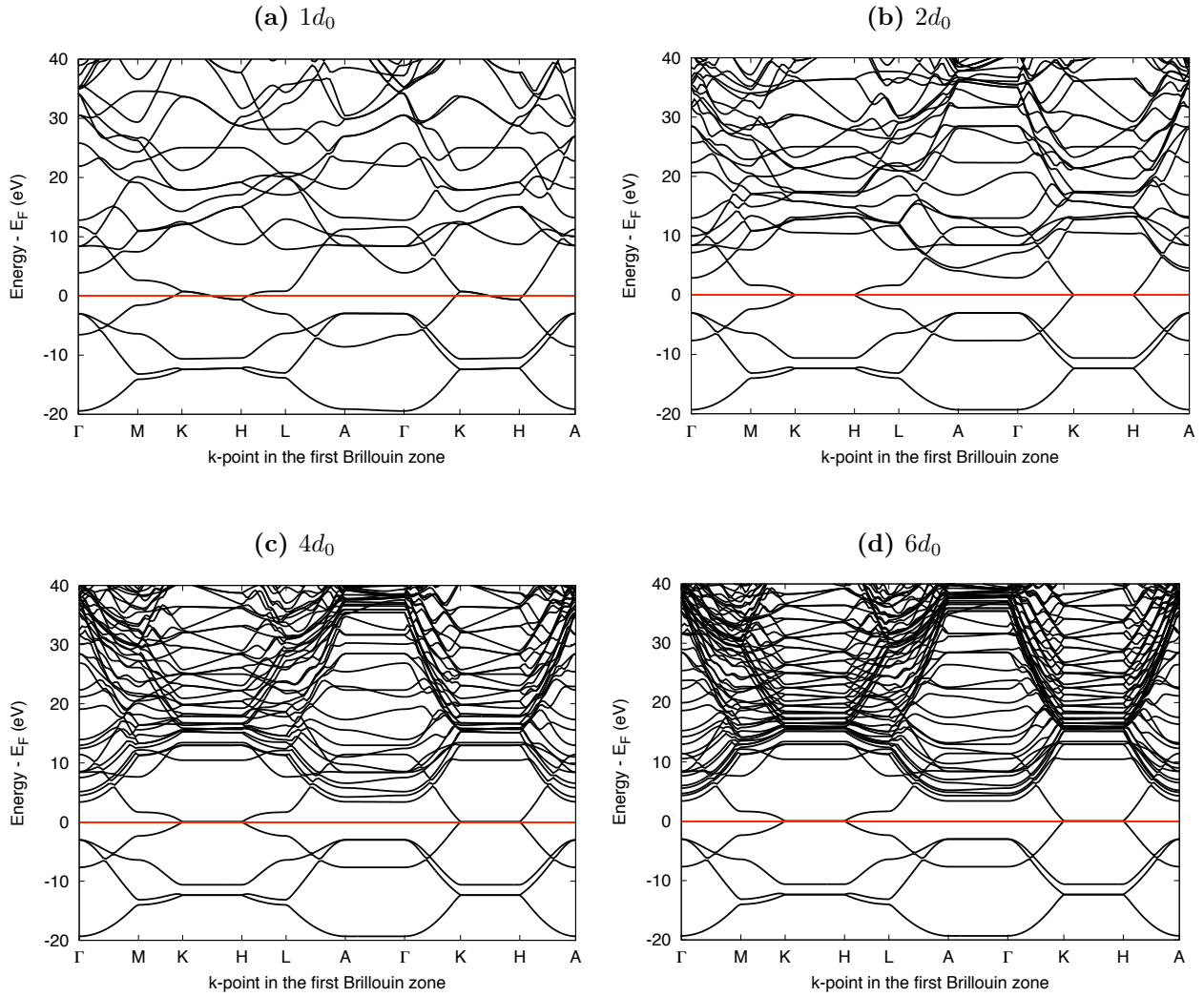

Figure 8.5: Band structure of four graphitic systems. Fermi energy is marked by a red line at $E_F = 0$ eV.

smaller interlayer distance (3.335 instead of 3.64 Å) which has minor effects on the band structure. And in fact the same features are recognised. Valence bands disperse along the $K - H$ and $A - \Gamma$ directions, demonstrating that the carbon layers are not isolated from their replicas. It is also remarkable that the greatest differences are located closer to the Fermi energy, in particular along the $K - H$ line, repeating the same crossing highlighted in Fig. 7.7c Note finally that in the limit of $d \to \infty$, the $\Gamma - A$, $M - L$ and $K - H$ lines collapse to a point. These effects in particular are responsible of the formation of the famous "Dirac cone" in graphene [143].

Conduction bands

Passing to the analysis of conduction states, the most evident effect of the increase in cell height is the close-packing of the conduction bands. This is due to the fact that the smaller the Brillouin zone ($|\mathbf{b}_3| = 2\pi/L_z$) is, the denser the folding of the plane wave-like states become. In the limit $L_z \to \infty$, all discretized conduction bands would give rise to a continuum of states, in agreement with an ideal confinement in two dimensions. As expected, also the conduction states have a reduced dispersion in the vertical directions $K - H$ and $A - \Gamma$, but

still, some dispersing bands can be found in all systems. This peculiar aspect will turn out to be important in determining the BZ sampling when computing EEL spectra.

8.2 Electron energy loss spectra

As seen in the introduction (equation (2.20)), the electron energy loss spectroscopy gives access to the diagonal elements $\epsilon^{-1}_{\mathbf{GG}}(\mathbf{q},\omega)$ of the inverse dielectric matrix which enters in the screened Coulomb interaction $W = \epsilon^{-1}v$. Hence the investigation of EEL spectra can give insight into the dynamical screening. I will examine EEL spectra of the four chosen systems $1d_0$, $2d_0$, $4d_0$ and $6d_0$.

Computational details : The polarizability χ of the four systems has been computed in the Random Phase Approximation using the software DP [127]. Kohn-Sham eigenvalues and eigenfunctions have been computed with ABINIT [124]. Spectra have been computed up to 40 eV, sampling the BZ with $34 \times 34 \times M_z$ k-point grids centred in Γ. The converged values of M_z depend on the system and on the direction of the exchanged momentum $\mathbf{q}$: see Tab. 8.2.

In the same way, the number of bands `nbands` included in the sum over states (4.10), the dimension of the $\chi^{KS}_{\mathbf{GG'}}(\omega,\mathbf{q})$ matrix [`npwmat`×`npwmat`] and the number of plane waves `npwwfn` needed to expand the KS states, all depend on the geometry of the system. The parameters used in the calculations are reported in Tab. 8.2. I have checked that they give converged spectra.

Table 8.2: Converged parameters for EELS

system	`nband`	`npwwfn`	`npwmat`[45]	M_z ($\mathbf{q}_\parallel$)	M_z ($\mathbf{q}_\perp$)
$1d_0$	40	350	50	4	8
$2d_0$	60	450	70	1	6
$4d_0$	80	850	90	1	2
$6d_0$	80	1300	160	1	2

Since χ^{KS} is inversely proportional to the cell volume, what is compared in all figures is $\frac{d}{d_0}S(\mathbf{q}+\mathbf{G},\omega)$ where S is the spectrum, i.e. $-\Im[\epsilon^{-1}_{\mathbf{GG}}(\mathbf{q},\omega)]$ in the case of EELS and $\Im[1/\epsilon^{-1}_{\mathbf{00}}(\mathbf{q},\omega)]$ with $\mathbf{q}\to 0$ in the case of absorption.

Due to the strong anisotropy of the systems, I will divide the results into in-plane momentum and perpendicular momentum, as done in the previous chapter.

8.2.1 Parallel momentum transfer

In Fig. 8.6, I report the EEL spectra for in-plane momentum transfer of amplitude $q_\parallel \approx 0.003$ Å^{-1} (8.6a), $q_\parallel \approx 0.17$ Å^{-1} (8.7) and $q_\parallel \approx 2$ Å^{-1} (8.6b). In all figures the EEL spectrum is reported in red for the $1d_0$ system, in green for the $2d_0$, in blue for the $4d_0$ and in black for

[45] In these anisotropic systems the `npwmat` parameter is difficult to converge. It has indeed a step-wise influence on the spectra due to the specific implementation which groups plane waves in spheres of discrete radius. Minimal changes can still be seen in increasing the `npwmat` parameter. So the converged values reported here are a good compromise between speed and accuracy.

the $6d_0$. For isolated systems, the absorption spectrum and the EELS coincide, as expressed in (4.30), hence I also report the $\Im[1/\epsilon^{-1}(\omega)]$ for the $2d_0$ (cyan line) and for the $6d_0$ systems (violet crosses or line).

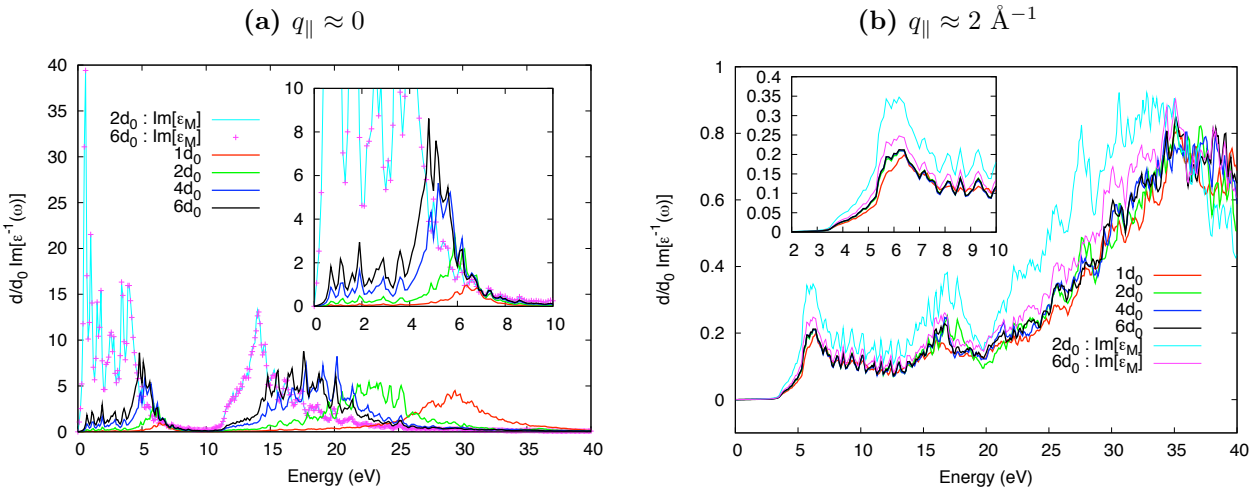

Figure 8.6: In-plane momentum transfer spectra. $-\frac{d}{d_0}\Im[1/\epsilon_M]$ (EELS) is reported for the $1d_0$ (red), $2d_0$ (green), $4d_0$ (blue) and $6d_0$ (black) systems; $\frac{d}{d_0}\Im[\epsilon_M]$ is reported for the $2d_0$ (cyan) and $6d_0$ (violet). For an isolated system $-\Im[\epsilon^{-1}_{\mathbf{GG}}(\mathbf{q})] = \Im[1/\epsilon^{-1}_{\mathbf{GG}}(\mathbf{q})]$ according to equation (4.30). At small $q_\parallel$ (8.6a), the absorption spectrum converges rapidly with respect to the interlayer distance, while the EEL spectrum is much slower. At large momentum (8.6b), the scenario is opposite, displaying a fast convergence for EELS and a slow one for absorption spectra.

The convergence to the isolated spectrum can be discussed on the basis of two different properties: EELS and absorption. A first observation can be done on EEL spectra only: when the EEL spectrum does not change by increasing d, convergence to the isolated graphen is attained, and similarly can be said for the absorption spectrum. However, when EEL and absorption spectra coincide in force of expression (4.30), i.e. when $-\Im[\epsilon^{-1}_{\mathbf{GG'}}(\mathbf{q})] = \Im[1/\epsilon^{-1}_{\mathbf{GG'}}(\mathbf{q})]$, then the system itself, and not only one specific spectral property, is considered isolated.

For vanishing (Fig. 8.6a) and long momentum transfer (Fig. 8.6b) two opposite convergence trends are observed. In the first case absorption spectra converge immediately (cyan line and violet dots are on top of each other) while EEL spectra are still evolving. Accordingly the system is not isolated: only the optical absorption reached convergence to the isolated spectrum.

Opposite is the scenario when large momentum is exchanged. In this case the EEL spectra are superimposed starting from a double interlayer separation, whereas the absorption spectrum is still not at convergence, although evolving in the right direction.

An intermediate case is shown in Fig. 8.7 for $q_\parallel \approx 0.17$Å^{-1}. It can be seen that neither absorption nor EEL spectra are converged to the isolated spectrum that should be found somewhere between the black (EELS $6d_0$) and the violet line (absorption $6d_0$). These convergence aspects have been extensively discussed in the in-plane case by R. Hambach [19] in his Ph.D. thesis on spatially-resolved EELS.

I note finally that in the bulk material (red line) interactions between planes are stronger. Its eigenfunctions and density are significantly different from those of the isolated system so it is not surprising that its spectrum differs from the others in all regimes. Nevertheless at

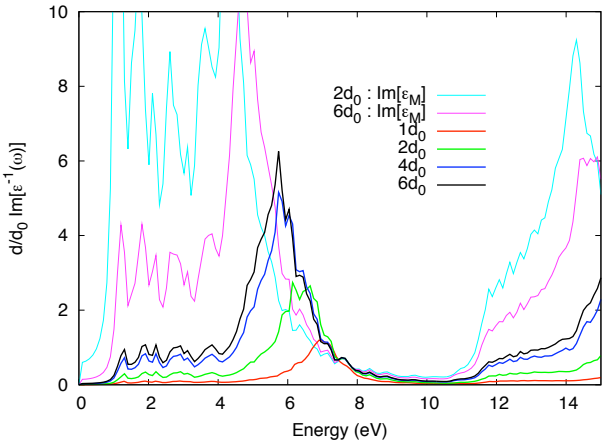

Figure 8.7: $q_{\parallel} \approx 0.17$ Å^{-1}. At an intermediate momentum transfer, none of absorption spectra or EELS are at convergence, indicating that L_z must be increased beyond $6d_0$ to get converged spectra. Note the different energy scale of this plot with respect to the previous two.

large momenta (small wavelengths) the differences are small, which is compatible with the physical intuition that locally, in the plane, isolated and the bulk systems are similar.

8.2.2 Perpendicular momentum transfer

In Fig. 8.8, I report the computed spectra for perpendicular momentum transfer in two different regimes: small momentum (Fig. 8.8a, $q_z \approx 0$) and large momentum[46] (Fig. 8.8b, $q_z \approx 1.41$ Å^{-1}).

(a) $q_{\perp} \approx 0$ **(b)** $q_{\perp} \approx 1.4$ Å^{-1}

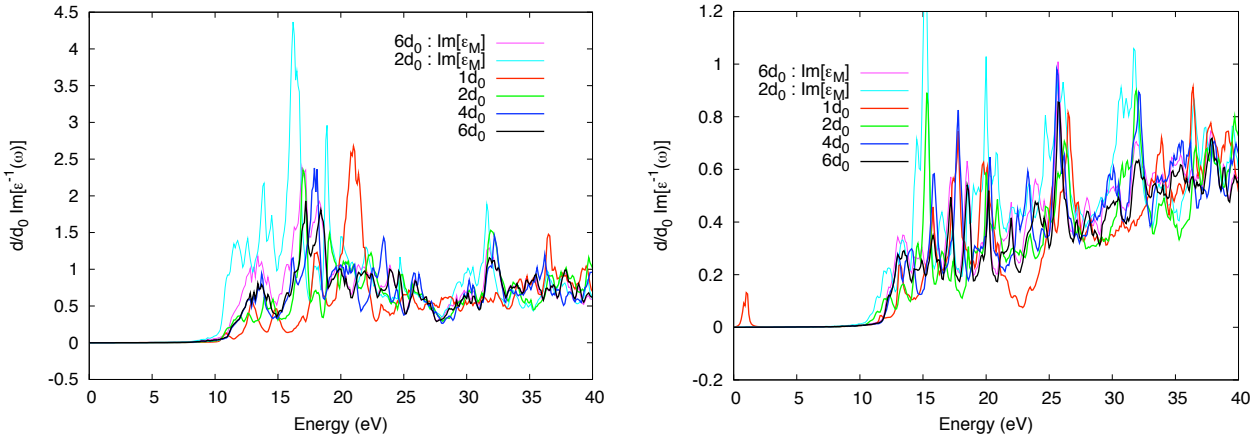

Figure 8.8: Perpendicular momentum transfer spectra. $-\frac{d}{d_0}\Im[1/\epsilon_M]$ (EELS) is reported for the $1d_0$ (red), $2d_0$ (green), $4d_0$ (blue) and $6d_0$ (black) systems. $\frac{d}{d_0}\Im[\epsilon_M]$ is reported for the $2d_0$ (cyan, only in Fig. 8.8a) and $6d_0$ (violet). For an isolated system $\Im[\epsilon_M] = \Im[1/\epsilon_M]$ according to equation (4.30). Convergence to the isolated EEL spectrum is attained at the level of $4d_0$ in both small and large momentum regimes.

The convergence to the isolated system has a different trend than in the in-plane case. Comparing Figs. 8.8a and 8.8b, one can verify that there is no particular difference in the

[46] The exchanged momentum is "large" with respect to the reciprocal lattice vector off-plane of the $1d_0$ system: $2\pi/d_0 \approx 1.88$Å^{-1}.

convergence behaviour between the small and the large momentum regimes, contrary to what observed in the in-plane case. In the small momentum case (Fig. 8.8a) the $6d_0$ EEL spectrum and the $4d_0$ spectrum are almost coincident, while minor differences can be found at larger momentum (Fig. 8.8b). Anyway differences are small enough to be considered at convergence even in the large momentum regime. Moreover principal features are already caught with a separation of $2d_0$.

Absorption spectra are slower to converge, especially at small momentum, displaying an opposite trend with respect to the in-plane case.

In both cases ($q_\perp \approx 0$ and $q_\perp \approx 1.4$) the differences between absorption and EEL spectra at $6d_0$ interlayer distance are small. One can consider that a distance $d = 6d_0$ is a good approximation of an isolated system (spectra do not coincide, but they are very similar).

In any case, the interlayer separation d determines the convergence also in another way: in fact the number of k-point sampling the k_z axis converges much more slowly than for in-plane momentum, as reported in Tab. 8.2. This is due to the dispersing conduction states found in all systems. For in-plane transitions, the correct description of these bands was not crucial so a smaller number of k-points was enough to converge the spectra (4 points in the $1d_0$, 1 point in the other systems), but when perpendicular momenta are considered, a finer description of the dispersion along z is necessary even at $6d_0$ of interlayer distance.

The interaction between the layers in the $1d_0$ geometry is such that the bulk spectrum differs significantly from that of the isolated sheet also at large momentum, even though differences are smaller than in the $q_\perp \approx 0$ case. Interesting is the low energy peak around 1 eV, found also in the previous chapter and highlighted by letter (g) in Fig. 7.9b. As explained in that context, this structure comes from transitions near the semi-metallic band in the $K - H$ line and it is strongly dependent on the k-point sampling.

8.2.3 Conclusions on the EEL spectra

For in-plane momentum transfer a clear dependence of the convergence on the amplitude of the momentum is observed for both EELS and absorption. At higher momentum $q_\parallel$, smaller lengths are probed and consequently the EEL spectrum is not so sensitive to the presence of other layers. The convergence is therefore faster. Instead when small momentum is exchanged, macroscopic differences in the electronic density are probed and one has to go way beyond $d = 6d_0$ to get a converged EEL spectrum. On the contrary absorption spectrum displays an inverse behaviour, converging faster for smaller momenta. The result is that the spectral properties of the system can be considered at convergence for $6d_0$ only at large momenta when in-plane components are considered.

If one is interested only in one spectrum (EELS or absorption) one can decide to converge either of the two depending on the regime of interest, as pointed out by Hambach [19]. The reason of this behaviour must be searched in the very difference between EELS and absorption, that is in the macroscopic Coulomb component $v_{\mathbf{0}}$. The macroscopic divergent component $v_{\mathbf{0}}$, which is absent in absorption spectra, spoils the convergence of EELS when small momentum is measured, whereas it has a reduced weight at large momentum. This observation is general, so a similar trend is expected in other simulations of isolated systems.

Although useful, this fact will be not exploited in the following of this thesis. Iso-

lated spectra will be obtained in next chapter using a different technique involving the modification of the very interaction between layers.

For perpendicular components the scenario is simpler. A small dependence on the modulus of the exchanged momentum is observed. Anyway in both small and large momentum transfer the convergence to the isolated system seems to be reached with an interlayer separation of $6d_0$. In this regime, particular attention must be paid to the **k**-point sampling along k_z which has to be much denser than in the in-plane case.

8.3 Spectral functions

In this section, I will make use of formula (7.2) to compute the spectral function $\mathcal{A}_i(\omega)$ for the state i=bottom valence and top conduction in the $1d_0$, $2d_0$, $4d_0$ and $6d_0$ systems. The functions $\mathcal{I}_i(\omega) = \Im[\Sigma_i(\omega)]$ and $\mathcal{R}_i(\omega) = \omega - E_i^H - \Re[\Sigma_i(\omega)]$ are the imaginary part of the self-energy and its shifted real part respectively. Since $\mathcal{A}$ is expressed in terms of the self-energy (7.1), it involves an integral of the dynamical screened Coulomb potential $W_{\mathbf{GG'}}(\mathbf{q},\omega) = \epsilon^{-1}_{\mathbf{GG'}}(\mathbf{q},\omega)v_{\mathbf{G'}}(\mathbf{q})$ and can therefore be related to the EEL spectra reported above. In the previous section, devoted to EEL spectra, it has been possible to observe different trends in the transition graphite-graphene; the question I want to address now is "*How does the spectral function converge to the isolated system?*"

First I will discuss G_0W_0 results, then I will analyse the effect of energy-only self-consistent GW_text0, and finally I will present results obtained with Hedin's approximation to self-consistency (cfr. Chapter 5.1.4).

Computational Details: The k-point grid used is $10 \times 10 \times 2$ for the $1d_0$ and $2d_0$ systems and a $10 \times 10 \times 1$ for the $4d_0$ and the $6d_0$ system.

The self-energy has been computed with the contour deformation method. The real axis has been sampled using 270 energies up to 54 eV and imaginary axis with 5 energies. In computing the self-energy, KS states have been included up to 200 bands and represented on a basis of 715 plane waves. The number of **G** vectors included in the exchange part is 715, while the correlation part needs only 169 **G** vectors. The screening matrix has been computed in RPA including 150 bands in the sum over states of $\chi^{KS}_{\mathbf{GG'}}$. The polarizability matrix is dimensioned as Σ_C.

Spectral functions are computed at the Γ point for the bottom valence and the top valence. Note that the K point of the BZ is not sampled in the k-point grid used here. In real graphene, the Fermi surface consists in the six K points, where the peculiar "Dirac cone" is formed by the shrinking of the vertical length of the BZ and the corresponding coincidence of the K and H points. With the Brillouin zone sampling employed in this work, the K point is not included, so the material results a semiconductor with top valence state at the point P=0.3 , 0.3 , 0.0. I will refer to this point when speaking of Fermi level or top valence. This peculiar sampling is justified because I am interested in higher energy features and not in the Dirac cone.

All calculations have been performed using the ABINIT [124] simulation code.

G_0W_0 spectra

I first analyse the $\pi + \sigma$ plasmon in $\mathcal{I}(\omega)$ (Fig. 8.9b). The $1d_0$ has a more intense peak at a binding energy, higher by ~ 5 eV with respect to the other systems. The $2d_0$, $4d_0$ and the $6d_0$ systems display the structure at the same intensity and position. In the same manner, the π plasmon appears red-shifted to larger binding energies, but its intensity in the $1d_0$ is comparable to that in the other systems. The shifted real part $\mathcal{R}(\omega)$ reflects the same structures of $\mathcal{I}$ because of the Kramers-Kronig relations. Note the plasmaron predicted for all geometries in correspondence with the π plasmon.

In the spectral function $\mathcal{A}(\omega)$ reported in Fig. 8.9a, these features constitute small differences between the $1d_0$ and the other systems. The QP peak in the $1d_0$ system is at slightly larger binding energy because of the different energy where $\mathcal{R}(\omega)$ crosses the zero line. This red-shift of the peak is of the order of 1 eV, comparable to the red-shift of the plasmaron peak. At much larger binding energy the $\pi + \sigma$ plasmon satellite is found as a much broader and weaker structure centred at around 50 eV. The $1d_0$ spectral functions displays major differences in correspondence with this satellite, in agreement with the related structure in $\mathcal{I}$. The $\pi + \sigma$ satellite is peaked at -55 eV, at an energy almost 5 eV larger than in the other three systems and it has also a higher intensity.

At the top valence, the matrix elements of Σ (Figs. 8.9d) differ more than in the previous case. Namely the $\mathcal{I}$ of the the $1d_0$ is clearly not converged to the isolated (black) curve, and similarly the $2d_0$ system presents structures not found in the isolated spectrum. Convergence of the matrix elements of Σ is reached at $d = 4d_0$.

In spite of these important differences in $\mathcal{I}$ and $\mathcal{R}$, the structures are hardly visible in the spectral function because of their exceedingly low intensity. Indeed, at the top valence, the spectral function is essentially a featureless delta-function.

Self-consistent calculations

G_0W_0 spectral functions are intrinsically inconsistent because the self-energy is computed on a LDA energy scale (with an LDA Fermi energy), while the Green's function has poles on the quasiparticle energy scale (with a G_0W_0 Fermi energy). This problem can affect the position and shape of the spectral function and, moreover, it can compromise the description of satellites. In fact these may be located in a wrong position, typically too close to the QP peak, which may give rise to too strong plasmarons (cfr. section 7.4).

A converged self-consistent calculation is unaffected by this problem, even though one should pay attention to other aspects, as discussed in Chapter 5.1.4. In this section I will present results obtained in the self-consistent scheme of S. V. Faleev, M. van Schilfgaarde and T. Kotani [70] performed in the energy-only GW_0 scheme.

Results for bottom valence and Fermi level are reported in Figs. 8.10. In Fig. 8.11 I report the comparison between self-consistent and G_0W_0 calculations at bottom valence for the $1d_0$ and the $6d_0$ systems.

From the comparison of the self-consistent results with the G_0W_0 spectra, it is clear that the bottom valence is indeed modified by the self-consistent cycle.

In the graphene sheet (Fig. 8.11b) the effect of self-consistency is essentially described by a shift to larger binding energies of both the QP and the plasmaron peak. The shift depends on the energy, and it amounts to ~ 0.5 eV for the QP, and to almost 1 eV for the plasmaron,

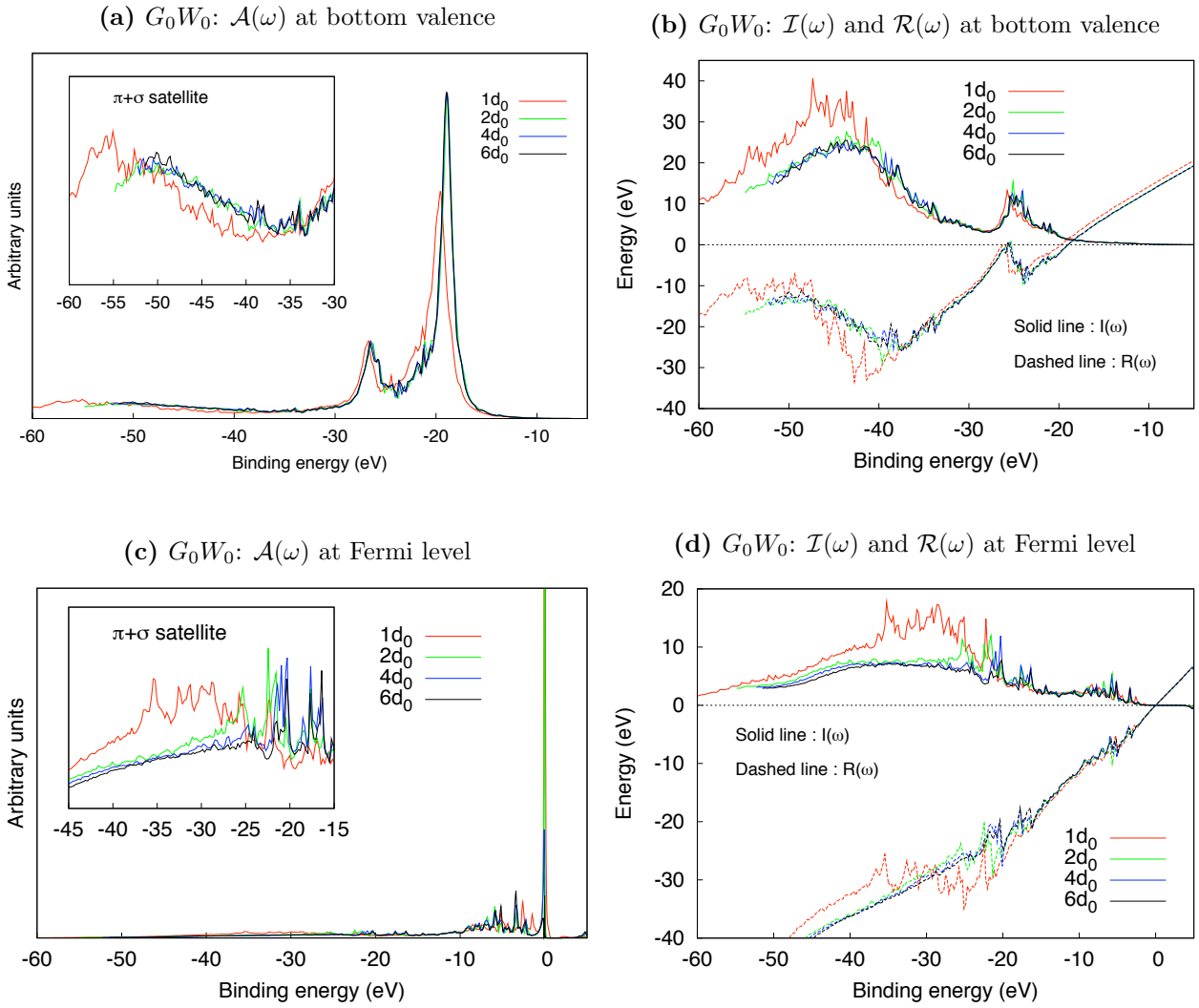

Figure 8.9: Spectral function $\mathcal{A}(\omega)$, imaginary part of Sigma $\mathcal{I}(\omega)$ and shifted real part $\mathcal{R}(\omega) = \omega - E_H - \Re[\Sigma(\omega)]$ computed at the bottom valence and at the Fermi level in the G_0W_0 scheme. In the insets, close-up of the $\pi + \sigma$ plasmon satellite are reported.

occurring together with a damping of the intensity in the latter case. The $\pi + \sigma$ plasmon satellite is too broad to appreciate modifications due to self-consistency.

Of bigger entity are the effects on the bulk material (Fig. 8.11a). The QP peak is moved by almost 1 eV to larger binding energies, and gains one fourth in intensity becoming much sharper. As expected, both satellites are moved accordingly: in the case of the -25 eV satellite, the effect is well visible (it is pushed 2 eV farther), while the $\pi + \sigma$ structure is too weak to quantify correctly the entity of the shift. The effect on the first satellite is of major interest: the π structure of $\mathcal{I}(\omega)$ is moved farther from the QP peak. This effect is strong enough to prevent the shifted real part $\mathcal{R}(\omega)$ to cross the zero before the QP peak, as a result the plasmaron is considerably weakened. The loss of spectral weight of the plasmaron is a consequence of the enhancement of the QP intensity. Within GW, in order to a have better quality description of satellites, it is preferable to employ a partially self-consistent scheme.

Similar behaviour is found at the Fermi level, but, alike the G_0W_0 case, the satellites are so weak that modifications of the spectral function are not sizable.

(a) GW_0: $\mathcal{A}(\omega)$ at bottom valence

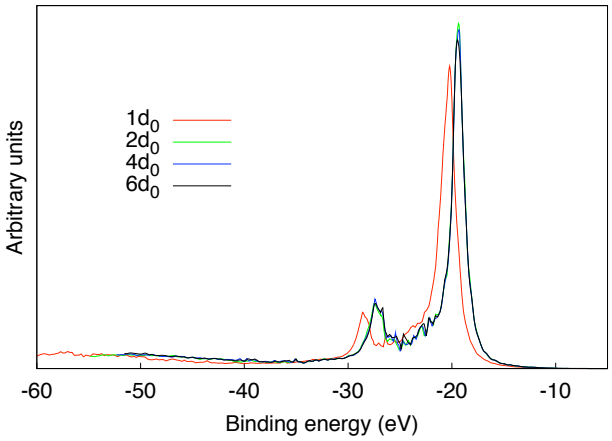

(b) GW_0: $\mathcal{I}(\omega)$ and $\mathcal{R}(\omega)$ at bottom valence

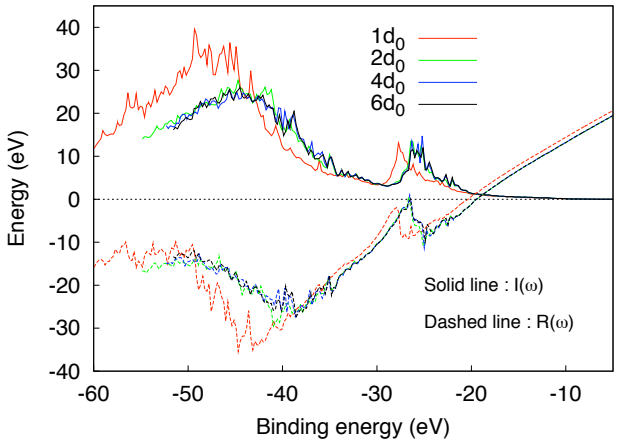

(c) GW_0: $\mathcal{A}(\omega)$ at Fermi level

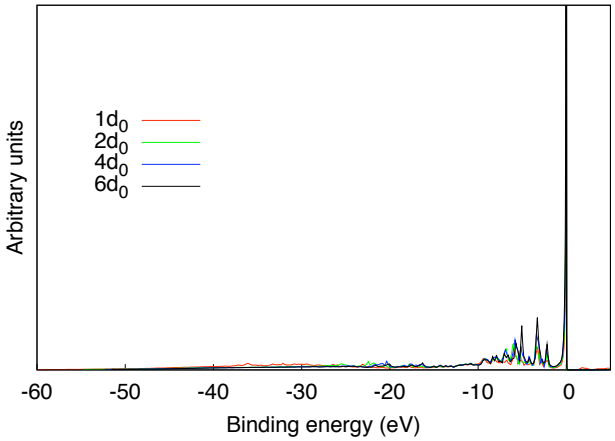

(d) GW_0: $\mathcal{I}(\omega)$ and $\mathcal{R}(\omega)$ at Fermi level

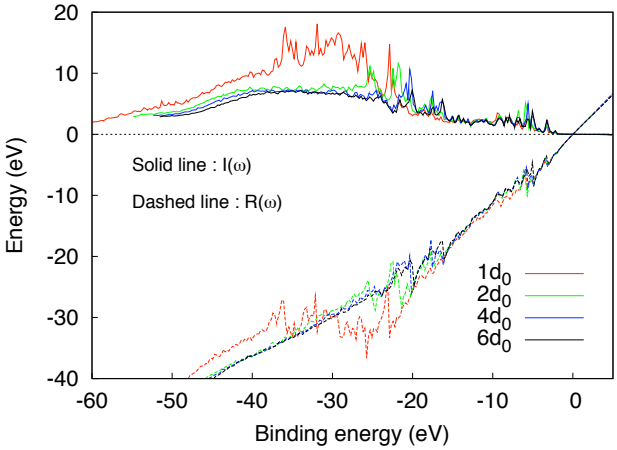

Figure 8.10: Spectral function $\mathcal{A}(\omega)$, imaginary part of Sigma $\mathcal{I}(\omega)$ and shifted real $\mathcal{R}(\omega) = \omega - E_H - \Re[\Sigma(\omega)]$ at bottom valence and Fermi levelcomputed in the energy-only GW_0 scheme within the QPscGW framework [70].

(a) $1d_0$

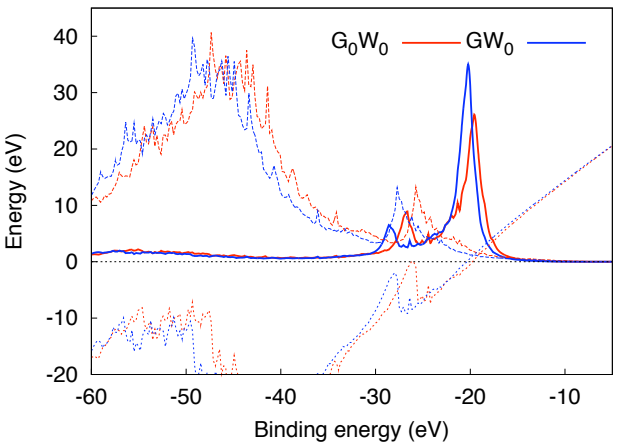

(b) $6d_0$

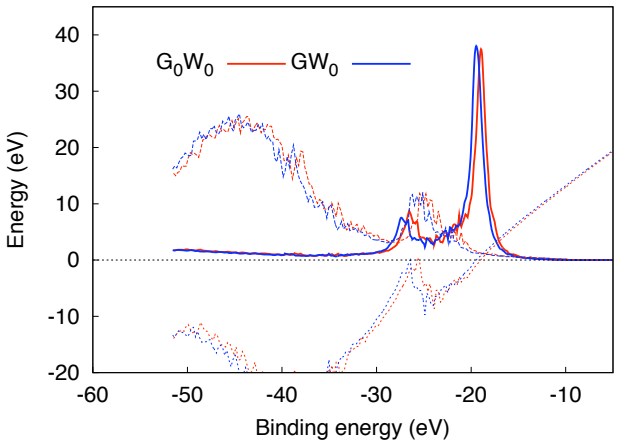

Figure 8.11: Comparison between the QPscGW and the G_0W_0 spectra in bulk AA graphite (8.11a) and isolated graphene (8.11b).

Hedin's approximation to self-consistency

Obviously self-consistent calculations are much more time consuming than G_0W_0 ones. They are also computationally more demanding because every self-consistent step has to be computed for all k-points of the mesh, even when spectral function in only one point are needed, as it is the case in this work. For all these reasons, one would like to resort to other methods, which are good compromises between computational time, memory and quantitative precision.

Hedin's approximation to self-consistency presented in 5.1.4 perfectly fits these requirements consisting in a simple post-processing to be applied on top of a G_0W_0 calculation. In Figure 8.12 I report the spectral function of the $1d_0$ and the $2d_0$ system for both bottom valence and Fermi level.

In the $1d_0$ system (Fig. 8.12a), Hedin's method improves over the G_0W_0 spectrum. In the bottom valence spectrum the plasmaron is moved in the good direction and the weight is reduced, in agreement with the self-consistent calculation. In the same way, the quasiparticle peak is moved to higher binding energy, and the intensity is increased. On the other hand, in the $2d_0$ system (Fig. 8.12c), Hedin's trick has no effect on the spectral function which almost coincides with the G_0W_0 calculation.

The reason for this is clear when comparing the Fermi level of the self-consistent spectra with G_0W_0 ones. In Hedin's approximation, one fixes the shift Δ according to (5.38) in order to assure self-consistency at Fermi. In the $1d_0$ case (Fig. 8.12b), the self-consistent and the G_0W_0 calculations are sizably different at Fermi, so Hedin's Δ has a non-negligible value (namely $\Delta_{1d_0} = -0.861$ eV). Consequently modifications of the spectral function of all states are significant. Instead, in the $2d_0$ system (Fig. 8.12d), the G_0W_0 Fermi level is already so close to the self-consistent level that $\Delta_{2d_0} = 0.102$. This small is such that the spectral function is not affected by Hedin's shift method.

This approximate method is a useful tool since it is fast to implement and it recovers almost half of the self-consistent correction. However, if the Fermi level is too close to the self-consistent result, its effect on the spectral function of all states will be of minor entity.

8.3.1 Comparison with EEL spectra

Both electron energy loss spectra and $\Im[\Sigma]$ stem from to the dynamical screening. In the case of EELS, what is measured (or calculated) is indeed the matrix element $\epsilon^{-1}_{\mathbf{GG}}(\mathbf{q},\omega)$. When looking at $\Im[\Sigma]$, what is observed is more cumbersome since it involves a sum over all elements of $W_{\mathbf{GG'}}(\mathbf{q},\omega)$ as reported in equation (7.1). So the link between the spectral function and $\epsilon^{-1}_{\mathbf{GG}}(\mathbf{q},\omega)$ is more involved.

In section 8.2 devoted to EEL spectra, I concluded that the convergence to the isolated graphene sheet merits to be discussed in two distinct cases, for in-plane momentum transfer $\mathbf{k} = \mathbf{k}_\parallel$ and for off-plane momentum $\mathbf{k} = \mathbf{k}_z$. In the former case, convergence of the spectrum is much faster for large momenta than for small ones. In the latter case, almost no dependence on the modulus of the momentum is observed and the spectrum converges reasonably fast (interlayer distance $6d_0$) in both large- and short-momentum regimes, but one has to consider the much higher number of k-points needed to sample the k_z axis.

As the self-energy involves an integral over all momenta $\mathbf{q}$ and a sum over all $\mathbf{G}$ and $\mathbf{G'}$, the trend towards the graphene signal is driven by a sort of average tendency of the whole matrix $\epsilon^{-1}_{\mathbf{GG'}}(\mathbf{q})$. The result is that the convergence towards the isolated system of $\mathcal{A}$ and of

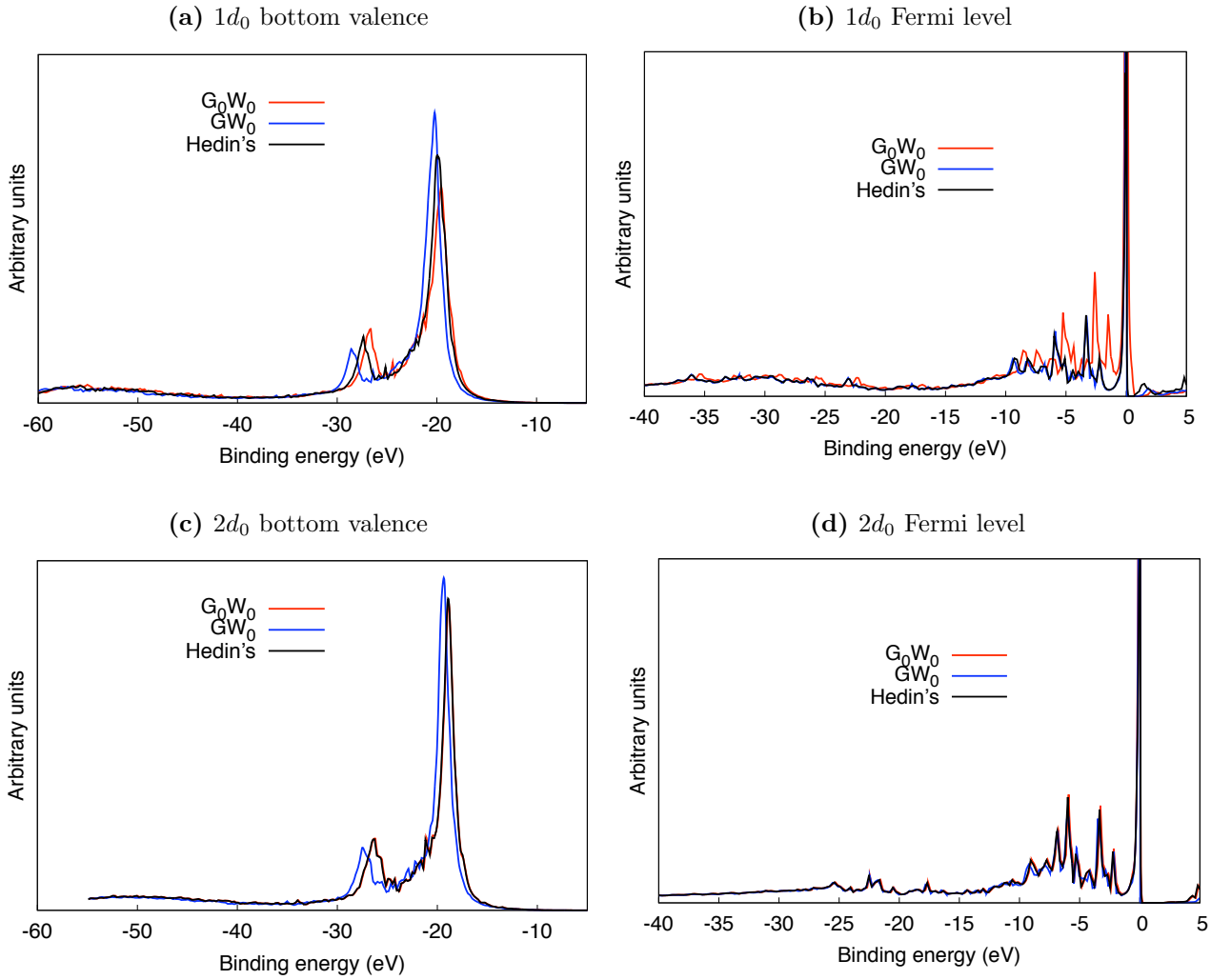

Figure 8.12: Spectral functions computed using Hedin's approximation to self-consistency compared with G_0W_0, and with self-consistent calculations.

the matrix elements of Σ is not dominated by small momentum contributions. This is proven by the fact that the self-energy is pretty close to that of graphene even for small interlayer distances (d=$2d_0$).

This study demonstrates that it is important to pay attention when discussing features of the spectral function only on the basis of EELS at $\mathbf{q} \to 0$, and/or when designing approximations.

8.3.2 Conclusions on the spectral functions

The comparative study of convergence of EELS and spectral functions show that matrix elements of Σ converge rapidly to the isolated graphene because of the contributions of relatively large exchanged momentum terms of $\epsilon^{-1}_{\mathbf{GG'}}(\mathbf{q})$.

This was already suggested by the analysis of spectral functions at different stacking which concluded the previous chapter. In fact the self-energy was not modified seriously by the stacking, indicating a dominance of short-range contributions.

For what concerns self-consistency, I found that updating of the poles of $G(\omega)$ actually

moves to higher binding energies quasi-particle peaks and satellites. The shift grows with the energy, so satellite structures are shifted more than QP peaks. I also noticed that this effect is sizable only for deep QP peaks, where the redistribution of spectral weight enhances satellite structures. Moreover this effect is stronger for smaller interlayer distances. All these elements suggest that whenever interested in satellites, self-consistency is preferable, in particular for bulk materials. Instead no important modification is expected in the case of graphene.

If it were possible, of course one would prefer to save time using approximations instead of doing self-consistent calculations. In the case of the bulk material ($d = 1d_0$), Hedin's method (cfr. Chapter 5.1.4) retrieves almost half of the peak shift and part of the weight redistribution yielded by self-consistency. In the other cases the effect of self-consistency is not so big, especially at Fermi, as a consequence Hedin's method does not affect the spectra. Therefore, whenever the effects of self-consistency are sizable, Hedin's shift method is a useful and fast tool to recover part of the self-consitent corrections.

Part III

Developments

Chapter 9

Isolated 2D-systems: Coulomb cutoff

In this chapter I will answer once again to the question "At what distance the graphene sheet can be considered as isolated?" but using a different way to isolate replicas. Instead of augmenting the interlayer distance to prevent the interaction between graphene layers, the Coulomb potential itself has been modified. This allows for a much more efficient calculation of isolated spectra even at relatively small interlayer distances.

The Coulomb cutoff method consists in setting the Coulomb potential to 0 beyond a distance z_0 from the sheet. I have implemented the resulting formulae of the cutoff-interaction in the code DP [127] which has been also modified to compute the full matrix $\epsilon^{-1}_{\mathbf{GG'}}(\mathbf{q},\omega)$ and to record it in an output file. The compatibility with ABINIT [124] has also been ensured, so that I could compute spectral functions of graphene obtained with the Coulomb-cutoff.

Here I present the theory of this method, together with some solutions to its analytical and numerical complexities. Results for the EEL spectra and spectral functions for the $1d_0$, $2d_0$, $4d_0$ and $6d_0$ geometries are presented and discussed.

9.1 Modifying the interaction

In the previous chapter, I discussed the transition from graphene to graphite through an analysis of EEL spectra and spectral functions. I started the previous chapter looking for the minimum distance d for the graphene sheet to be considered isolated from its replicas. Although an answer has been found concerning spectral functions, an isolated system has not been found in the case of EELS, especially when in-plane momentum components are considered. Moreover, also in the case of $\mathcal{A}(\omega)$ one wishes to keep the supercell as small as possible. Of course, a possible strategy would be that of a further increase of the interlayer distance, but simulations would become more and more demanding and eventually infeasible. In fact, because of the compaction of the G_z space, the dimension of both the plane wave basis and the the $\chi_{\mathbf{GG'}}$ matrix increase with the dimension of the supercell. Moreover the close-packing of conduction states appreciable in Fig. 8.5 causes an increase also in the number of bands. This dependence on the dimension of the cell is evident in Tab. 8.2.

Another way to prevent the interaction between replicas is to artificially impose a cutoff to the long-range Coulomb interaction. The Coulomb-cutoff (CC) method consists in working with a modified Coulomb interaction $\check{v}(\mathbf{r}) = v(\mathbf{r}) f_C(\mathbf{r};\{\mathbf{r}_0\})$ where the cutoff function f_C is specified by means of parameters $\{\mathbf{r}_0\}$ which are defined in order to respect the geometry of the system.

In plane wave codes, the use of periodic boundary conditions can not be avoided, though the simulation of isolated objects requires the Coulomb to vanish between two replicas. The cutoff function f_C has the task to mimic this behaviour.

The advantage of such a procedure is that the simulation cell can be kept at reasonably low volume so that calculations of isolated systems are computationally affordable. This idea has been applied already in the 1997 to molecules and clusters by M. R. Jarvis and coworkers [169].

Point-wise geometry: To study molecules or isolated clusters, one can enclose the system inside a sphere of radius r_0.The cutoff function in real space and the Fourier components of the CC interaction read respectively

$$f_C(\mathbf{r}; r_0) = \theta(r_0 - |\mathbf{r}|) \quad \text{and} \quad \check{v}(k) = \frac{4\pi}{k^2}\left[1 - \cos(kr_0)\right]$$

where $k = |\mathbf{k}|$.

Linear geometry: Unidimensional chains [170, 171], nanotubes or polymers can be isolated from their replicas by enclosing their axis with a cylinder of radius R and infinite height, and by requiring $\check{v}(\mathbf{r}) = 0$ outside this region. Aligning the z to the axis of the material, the cutoff function and the CC interaction read respectively

$$\begin{aligned} &f_C(r_\parallel; R) = \theta(R - r_\parallel) \quad \text{and} \\ &\check{v}(\mathbf{k}) = \frac{4\pi}{k^2}\left[1 + k_\parallel R J_1(k_\parallel R) K_0(|k_z|R) - |k_z| R J_0(k_\parallel R) K_1(|k_z|R)\right] , \end{aligned}$$

with J and K ordinary and modified cylindrical Bessel functions, $r_\parallel = \sqrt{r_x^2 + r_y^2}$ and similar definition for $k_\parallel$.

Planar geometry: To study 2D systems as graphene sheets, the Coulomb interaction has to vanish beyond a distance z_0 from the layer, assumed to lay on the xy plane [170, 171]. The cutoff function $f_C(r_z; z_0)$ and the Fourier components of the CC interaction read

$$f_C(r_z; z_0) = \theta(z_0 - |r_z|) \quad \text{and} \tag{9.1}$$

$$\check{v}(\mathbf{k}) = \frac{4\pi}{k^2}\left[1 + e^{-k_\parallel z_0}\left(\frac{k_z}{k_\parallel}\sin(k_z z_0) - \cos(k_z z_0)\right)\right] , \tag{9.2}$$

with $k = |\mathbf{k}| = (k_x^2 + k_y^2 + k_z^2)^{1/2} = (k_\parallel^2 + k_z^2)^{1/2}$. Since the planar geometry is the topic of this chapter, it is worthwhile to analyse in closer detail the CC interaction in 2D.

9.1.1 The cutoff Coulomb interaction in 2D

What is an isolated 2D system?
For our purpose, an isolated 2D system is defined as a bidimensional crystal enclosed in a supercell of height L_z. The resulting 3D system is periodic in the xy plane with the same periodicity as the 2D crystal, and has period L_z along z. Inside the 3D cell, the Coulomb interaction has the shape of equation (9.2).

In the limit of $L_z \to \infty$, the system is isolated from the replicas above and below and the z-periodicity is lost. Correspondingly, the height of the BZ collapses to 0. As the vertical

distance between two consecutive reciprocal lattice vectors $b_3 = 2\pi L_z^{-1} \to 0$, they form a continuous along k_z. Hence, the vertical components G_z of the reciprocal lattice vectors vary continuously.

Moreover, as L_z goes to infinity, also the cutoff distance z_0 have to taken at infinite distance from the xy plane. It is immediately verified that in this limit, the expression (9.2) reduces to the untruncated Coulomb potential $4\pi/k^2$.

I stress here that taking $L_z \to \infty$ and $z_0 \to \infty$ are two different operations. The first changes the dimensions of the direct and the reciprocal cells, but what is the effect of the second?

Domain of definition, limits and divergences

To answer to the question "*what is the effect of taking* $z_0 \to \infty$*?*", the CC interaction $\check{v}$ must be studied with care. I start analysing the domain of definition of the function, then I will focus on some notable limits. The non analytic behaviour of the cutoff function will finally be discussed.

The **k**-Fourier component of the CC interaction in the planar geometry is reported in expression (9.2). The function $\check{v}(\mathbf{k})$ is well defined almost everywhere in the reciprocal space. Actually it is not defined in the entire $k_\parallel = 0$ space, that is along k_z, except for all those points $\tilde{k}_z^n$ satisfying $\sin(\tilde{k}_z^n z_0) = 0$.

Thus the domain of definition of the CC interaction is the whole space $k_\parallel \neq 0$, where it has the shape of equation (9.2), plus a family of discrete $\tilde{k}_z^n = n\pi z_0^{-1}$ points laying on k_z. As a consequence, when taking limits or performing integrations involving points on the k_z axis, careful attention must be paid for the CC interaction may be not defined.

Two limits are of interest: the limit for $k_z \to 0$, and the limit for $k_\parallel \to 0$. They correspond to the off-plane and in-plane long range contributions of the CC interaction.

One can freely take $k_z = 0$ in equation (9.2) . The in-plane components of CC read

$$\check{v}(\mathbf{k} = \mathbf{k}_\parallel + 0) = \frac{4\pi}{k_\parallel^2}\left[1 - e^{-k_\parallel z_0}\right] \ . \tag{9.3}$$

There is no difference in taking k_z strictly equal to 0 or in evaluating the limit of (9.2) for vanishing k_z. That is, the limit $k_z = 0$ is well defined as long as $k_\parallel \neq 0$.

What does it happen if we take the limit $k_\parallel = 0$? Let's consider three cases: for $k_z = 0$, for a generic k_z and for $k_z = \tilde{k}_z^n$.

In-plane: We first evaluate the long range components for in-plane momentum by expanding the exponential of (9.3) up to the second order in $k_\parallel$:

$$\check{v}(\mathbf{k} = \mathbf{k}_\parallel + 0)\big|_{k_\parallel \to 0^+} \sim \frac{4\pi z_0}{k_\parallel} - 2\pi z_0^2 \tag{9.4}$$

Two contributions can be identified, a first term $\sim k_\parallel^{-1}$ which is integrable in two dimensions, and a second contribution which does not depend on $k_\parallel$ and is finite.

Generic point: The second case is the in-plane long range limit for finite k_z. I now expand the exponential of the general expression (9.2) up to the first order in $\mathbf{k}_\parallel$, getting

$$\check{v}(\mathbf{k} = \mathbf{k}_\parallel + \mathbf{k}_z)\big|_{k_\parallel \to 0} \sim \frac{4\pi}{k_z k_\parallel}\sin(k_z z_0) + \frac{4\pi}{k_z^2}\left[1 - \cos(k_z z_0) - k_z z_0 \sin(k_z z_0)\right] \ . \tag{9.5}$$

Two contributions are obtained also in this case. The first contribution diverges as $k_\parallel \to 0$ in the same way as the in-plane case, although it does not diverge for vanishing k_z. The second contribution depends only on k_z and it is still finite for $k_z \to 0$.

The expression above has been obtained for $k_\parallel$ small, that is for points $\mathbf{k}$ close to, but not laying on, the k_z axis. Since we are not strictly on the k_z axis, we can take the limit for $k_z \to 0$, obtaining

$$\lim_{\mathbf{k}_z \to 0} \left[\check{v}(\mathbf{k} = \mathbf{k}_\parallel + \mathbf{k}_z)\big|_{k_\parallel \to 0^+} \right] \sim \frac{4\pi z_0}{k_\parallel} - 2\pi z_0^2 \tag{9.6}$$

which reproduces the in-plane limit (9.4). That shows that the order of the limits can be interchanged:

$$\lim_{\mathbf{k}_z \to 0} \left[\check{v}(\mathbf{k} = \mathbf{k}_\parallel + \mathbf{k}_z)\big|_{k_\parallel \to 0^+} \right] = \lim_{k_\parallel \to 0} \check{v}(\mathbf{k} = \mathbf{k}_\parallel + 0) \ .$$

Special points $\tilde{k}_z^n = n\pi z_0^{-1}$: If the point $\mathbf{k} = \mathbf{k}_\parallel + \tilde{k}_z^n$ with $n \neq 0$[47], then, by taking the limit of vanishing $k_\parallel$, one reaches one of the discrete points along k_z where the CC is defined.

For $n \neq 0$ the CC interaction reads

$$\check{v}(\mathbf{k} = \mathbf{k}_\parallel + \tilde{k}_z^n) = \frac{4\pi}{k_\parallel^2 + (\tilde{k}_z^n)^2} \left[1 + (-1)^{n+1} e^{-k_\parallel z_0} \right]$$

which is indeed finite for $k_\parallel \to 0$

$$\lim_{k_\parallel \to 0^+} \check{v}(\mathbf{k} = \mathbf{k}_\parallel + \tilde{k}_z^n) = \frac{4\pi}{(\tilde{k}_z^n)^2} \left[1 - (-1)^n \right] = \begin{cases} 0 & \text{for } n = \text{ even and } n \neq 0 \\ \frac{8 z_0^2}{n^2 \pi} & \text{for } n = \text{ odd} \end{cases} \tag{9.7}$$

It is remarkable to notice that for n even, the cutoff function vanishes exactly and so does the CC interaction.

In a 2D isolated system, we expect the macroscopic component of the CC interaction not to diverge along the k_z axis because the cutoff function sets the interaction to 0 at long distance. This is indeed the case, as shown by expression (9.3).

On the contrary, the infinite periodicity along the xy plane makes the CC interaction diverge for $k_\parallel = 0$ in the whole k_z axis, with the exception of the special points $\tilde{k}_z^n = n\pi z_0^{-1}$ with $n \in \mathbb{Z} \setminus \{0\}$, where the CC is finite. In these points the limit for $k_\parallel \to 0$ is given by expression (9.7), while in all other points of the k_z axis the CC interaction is composed by two terms (cfr. expressions (9.4) and (9.6)). One term is regular and does not depend on $k_\parallel$ and a second term diverges as $k_\parallel^{-1}$.

This peculiar structure of the domain of f_C implies some difficulty in practical calculations where the k-point space is necessarily discretized. One would like to use a k-point mesh including as few divergence points as possible. Moreover, as already anticipated, in performing limits or integrals the presence of divergent points must be treated with care. Both problems will be addressed in the next section.

[47] The case $n = 0$ corresponds in taking the origin, that is on the plane, so its limit is accounted by (9.4).

9.1.2 Practical implementation and approximations

In the path from χ^{KS} to W, the Coulomb interaction v enters in three steps[48]:
(a) in the (RPA)-Dyson equation $\chi = \chi^{KS} + \chi^{KS} v \chi$,
(b) in the (test-particle) expression $\epsilon^{-1} = 1 + v\chi$ and finally
(c) in the definition of $W = \epsilon^{-1} v$.
It is not trivial to understand whether the CC has to be used in all steps at the place of the untruncated Coulomb interaction. This subject is addressed in the first part of this section, devoted to the treatment of the external perturbation correction (EPC).

Because of the non analyticity of the CC, it is not trivial to implement the cutoff method in simulation codes. In the second part of this section, I will address some problems found in this context, and in particular I will discuss the choice of the cutoff distance z_0 and the evaluation of matrix elements of $W_{\mathbf{GG'}}(\mathbf{q}, \omega)$ around divergences.

The external perturbation correction

In an isolated system, G_z form a continuum and correspondingly the BZ has vanishing extension along k_z. As stated, this is compatible with sticking on a 3D crystal picture if one assumes infinite periodicity in the z direction ($L_z \to \infty$) and a vanishing v between replicas (imposed by means of the cutoff).

When using the CC, the cutoff function f_C takes into account the close packing of the G_z space in an implicit way. Let G_z be the discrete variable of the periodic framework and let $\mathcal{X} = \sum_{G_z} X_{G_z}$ be the quantity to compute in the periodic framework. In the isolated system the same quantity would read $\check{\mathcal{X}} = \int X(g_z) dg_z$ where g_z is a continuous variable.The cutoff function f_C allows us to compute the isolated $\check{\mathcal{X}}$ by working in the discrete framework, according to a scheme schematically represented by

$$\sum_{G_z} \int_{G_z} X(g_z) dg_z = \check{\mathcal{X}} = \sum_{G_z} \check{X}_{G_z} = \sum_{G_z} X_{G_z} f_C(G_z)$$

and depicted in Fig. 9.1.

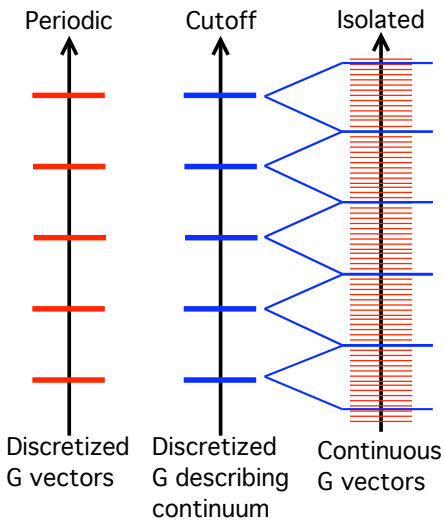

Figure 9.1: Illustration of the effect of the cutoff function in the G_z space.

This argument suggests that whenever integrals over $\mathbf{k}$ (i.e. sums over $\mathbf{G}$) are performed, or whenever matrix multiplications are involved, one has to rely on f_C in order to take into account correctly the compaction of the $\mathbf{G}$ space. One first conclusion is that the CC will substitute the standard v in the Dyson equation (a).where the interaction is integrated.

More delicate is the (b) case, that is equation $\epsilon^{-1} = 1 + v\chi$. The inverse dielectric function is used to compute electron energy loss spectra and to compute W (e.g., in the correlation self-energy). In the first case the matrix describes the response of the system to an external classical field modelled with a plane wave of momentum $\mathbf{q} + \mathbf{G}$. In the second case ϵ^{-1} is

[48] Formulas are schematically reported. They refer to the expressions (4.12), (4.16) and to the definition $W_{\mathbf{GG'}}(\mathbf{q}, \omega) = \epsilon^{-1}_{\mathbf{GG'}}(\mathbf{q}, \omega) v_{\mathbf{G'}}(\mathbf{q})$.

the response to a perturbing field caused by some electrons of the system itself. Their wave functions contains all momentum components, that are therefore integrated over.

In EEL spectroscopy one measures the response to only one specific transferred momentum $\mathbf{q}+\mathbf{G}$ (plane wave-like perturbation), so no integration over $\mathbf{q}$ or sum over $\mathbf{G}$ is done. Because of this reason, the Coulomb interaction appearing in (c) has to be computed according to

$$\check{\epsilon}^{-1}_{\mathbf{G}\mathbf{G}'}(\mathbf{q}) = \delta_{\mathbf{G}\mathbf{G}'} + v_{\mathbf{G}}(\mathbf{q})\check{\chi}_{\mathbf{G}\mathbf{G}'}(\mathbf{q}) \tag{9.8}$$

where v is the Coulomb interaction without the cutoff, whereas the polarizability $\check{\chi}$ comes from the CC-Dyson equation in force of the arguments above and is the polarizability of the isolated system. In this expression and in the following frequency will be neglected if not necessary.

The expression (9.8) is the external-perturbation corrected (EPC) screening because it takes into account the fact that the perturbing field is a plane wave external to the system and hence it must not be screened. The practical implementation of the EPC formula in RPA is actually different from this expression. In fact in RPA calculations, the polarizability is never computed, so one does not have access to $\check{\chi}$. What is usually done, is to compute the dielectric matrix according to formula (4.19) and to invert the result. This actually leads to a full-cutoff (FC) screening

$$\check{\tilde{\epsilon}}^{-1}_{\mathbf{G}\mathbf{G}'}(\mathbf{q}) = [\mathbf{1} - \check{v}\chi^{KS}(\mathbf{q})]^{-1}_{\mathbf{G}\mathbf{G}'} = \delta_{\mathbf{G}\mathbf{G}'} + \check{v}_{\mathbf{G}}(\mathbf{q})\check{\chi}_{\mathbf{G}\mathbf{G}'}(\mathbf{q}) \tag{9.9}$$

which gives bad results for EELS. To recover the EPC-screening expression (9.8) from the latter, a correction is applied according to the formula [19]

$$\check{\epsilon}^{-1}_{\mathbf{G}\mathbf{G}'}(\mathbf{q}) = \begin{cases} \delta_{\mathbf{G}\mathbf{G}'} + \left(\check{\tilde{\epsilon}}^{-1}_{\mathbf{G}\mathbf{G}'}(\mathbf{q},\omega) - \delta_{\mathbf{G}\mathbf{G}'}\right)/f_C(\mathbf{q},\mathbf{G}) & \text{if} \quad f_C^{\mathbf{G}}(\mathbf{q}) \neq 0 \\ \delta_{\mathbf{G}\mathbf{G}'} + v_{\mathbf{G}}(\mathbf{q})\chi^{KS}_{\mathbf{G}\mathbf{G}'}(\mathbf{q}) & \text{if} \quad f_C^{\mathbf{G}}(\mathbf{q}) = 0\,. \end{cases} \tag{9.10}$$

where the second expression accounts for the fact that $\check{\chi} = \chi^{KS}$ whenever $f_C = 0$.

In GW and BSE the matrix elements of the screened Coulomb interaction are needed. The screened Coulomb interaction $W(\mathbf{r},\mathbf{r}')$ in reciprocal space reads

$$W_{\mathbf{G}\mathbf{G}'}(\mathbf{q}) = \epsilon^{-1}_{\mathbf{G}\mathbf{G}'}(\mathbf{q})v_{\mathbf{G}'}(\mathbf{q}) = \delta_{\mathbf{G}\mathbf{G}'}v_{\mathbf{G}'}(\mathbf{q}) + v_{\mathbf{G}'}\chi_{\mathbf{G}\mathbf{G}'}(\mathbf{q})v_{\mathbf{G}'}(\mathbf{q})\,, \tag{9.11}$$

and in particular its matrix elements $\langle ij|W|mn\rangle$ are

$$W^{ij}_{mn}(\omega) = \frac{1}{(2\pi)^3}\sum_{\mathbf{G}\mathbf{G}'}\int_{\mathcal{V}_{\mathrm{BZ}}} \tilde{\rho}^*_{ij}(\mathbf{q}+\mathbf{G})\epsilon^{-1}_{\mathbf{G}\mathbf{G}'}(\mathbf{q},\omega)v_{\mathbf{G}'}(\mathbf{q})\tilde{\rho}_{mn}(\mathbf{q}+\mathbf{G}')d\mathbf{q}\,. \tag{9.12}$$

They enter in the expressions of the correlation self-energy (7.1) and in the BSE kernel (5.52). Following the argument explained above, because of the sum over $\mathbf{G}'$, it is clear that the Coulomb interaction $v_{\mathbf{G}'}$ has indeed to be multiplied by the cutoff function $f_C(\mathbf{q},\mathbf{G}')$. To understand how to handle the $\mathbf{G}$ vectors, it is possible to rely on the symmetry

$$W_{\mathbf{G}\mathbf{G}'}(\mathbf{q},\omega) = W^*_{\mathbf{G}'\mathbf{G}}(\mathbf{q},-\omega)\,, \tag{9.13}$$

which is satisfied only if the cutoff is applied to $v_{\mathbf{G}}$ as well. Then, the resulting screened CC to be employed in the correlation self-energy and in the BSE kernel is

$$\check{W}_{\mathbf{G}\mathbf{G}'}(\mathbf{q},\omega) = \check{\tilde{\epsilon}}^{-1}_{\mathbf{G}\mathbf{G}'}(\mathbf{q},\omega)\check{v}_{\mathbf{G}'}(\mathbf{q}) = \delta_{\mathbf{G}\mathbf{G}'}\check{v}_{\mathbf{G}'} + \check{v}_{\mathbf{G}}\check{\chi}_{\mathbf{G}\mathbf{G}'}(\mathbf{q},\omega)\check{v}_{\mathbf{G}'}(\mathbf{q})\,, \tag{9.14}$$

where the CC interaction as well as the FC screening (9.9) are used.

Summarising, using the CC interaction, formulae (a), (b) and (c) are modified in the following way:

$$\text{(a)} \qquad \check{\chi}_{\mathbf{G}\mathbf{G}'}(\mathbf{q}) = \chi^{KS}_{\mathbf{G}\mathbf{G}'}(\mathbf{q}) + \chi^{KS}_{\mathbf{G}\mathbf{G}''}(\mathbf{q})\check{v}_{\mathbf{G}''}\check{\chi}_{\mathbf{G}''\mathbf{G}'}(\mathbf{q}) \,, \tag{9.15}$$

$$(\text{b}_1) \qquad \check{\epsilon}^{-1}_{\mathbf{G}\mathbf{G}'}(\mathbf{q}) = \delta_{\mathbf{G}\mathbf{G}'} + v_{\mathbf{G}}(\mathbf{q})\check{\chi}_{\mathbf{G}\mathbf{G}'}(\mathbf{q}) \tag{9.16}$$

$$(\text{b}_2) \qquad \check{\tilde{\epsilon}}^{-1}_{\mathbf{G}\mathbf{G}'}(\mathbf{q}) = \delta_{\mathbf{G}\mathbf{G}'} + \check{v}_{\mathbf{G}}(\mathbf{q})\check{\chi}_{\mathbf{G}\mathbf{G}'}(\mathbf{q}) \tag{9.17}$$

$$\text{(c)} \qquad \check{W}_{\mathbf{G}\mathbf{G}'}(\mathbf{q}) = \check{\tilde{\epsilon}}^{-1}_{\mathbf{G}\mathbf{G}'}(\mathbf{q})\check{v}_{\mathbf{G}'}(\mathbf{q}) \tag{9.18}$$

where $\check{v}_{\mathbf{G}}(\mathbf{q}) = v_{\mathbf{G}}(\mathbf{q}) f_C(\mathbf{q}+\mathbf{G})$, (b_1) is the EPC expression of the screening and (b_2) is the FC screening.

How to fix the cutoff distance

For physical reasons, it is reasonable to set $z_0 = L_z/2$, that means cutting the Coulomb interaction at halfway between two graphene layers. This has the advantage that minimizes the empty volume in the supercell. Besides this argument, another argument related to the non-analyticity of the CC leads to the same conclusion.

We are always working in a periodic arrangement of (isolated) replicas of the simulation cell. In this framework the k_z axis is naturally split into $\mathbf{q}$ points which are continuous inside the first Brillouin zone and discrete reciprocal lattice vectors $\mathbf{G}$. The cutoff distance z_0 can be fixed by requiring the n-th reciprocal lattice vector $2n\pi/L_z$ to coincide with the n-th special point $\tilde{k}^n_z = n\pi z_0^{-1}$, by setting

$$\frac{n\pi}{z_0} = n\frac{2\pi}{L_z} \quad \Longleftrightarrow \quad z_0 = \frac{L_z}{2} \,. \tag{9.19}$$

This argument (introduced by Beigi et al. [171]) goes with the prescription of sampling the BZ only in one plane (for example the xy plane), so that the only perpendicular component of the exchanged momentum $\mathbf{k} - \mathbf{k}' + \mathbf{G}$ is G_z.

$$\text{If the BZ is sampled on one plane, then} \quad (\mathbf{k} - \mathbf{k}' + \mathbf{G})_\perp = G_z$$

The advantage is twofold. First, the only points along k_z included in the simulation grid are special points k^n_z where the CC does not diverge, consequently the only divergent term of the CC interaction is in the origin. Second, the generic point of the simulation grid is of the form $\mathbf{k} = \mathbf{k}_\parallel + 2n\pi/L_z$ so the CC interaction reads

$$\check{v}(\mathbf{k}) = \frac{4\pi}{k^2_\parallel + (2n\pi/L_z)^2}\left[1 - e^{k_\parallel L_z/2}\cos(n\pi)\right] \,. \tag{9.20}$$

The prescription of working only with in-plane k-point grids, which at first sight could seem a limitation, turns actually out to be another strong point of the CC technique, as it will be clearer in the following.

Integration around $\mathbf{k} = 0$

The matrix elements $W^{ij}_{mn}(\omega)$ computed as in (9.12) are needed for the correlation self-energy Σ_c and the Coulomb term of the BSE kernel. The calculation of the 2D isolated system relies on this expression since it has been defined as a 3D system subject to the CC interaction. It

involves an integral in the whole BZ is required, including the k_z axis where the CC is not defined. Although the set is of vanishing measure, the CC diverges in all the points of the set, so the integral of the CC interaction should be treated with care.

In order to carefully treat the divergent terms, I put in evidence parallel and perpendicular components of the $\mathbf{k} = \mathbf{q} + \mathbf{G}$ vectors in expression (9.12), getting

$$W^{ij}_{mn} = \frac{1}{(2\pi)^3} \sum_{\mathbf{G}_\parallel G_z} \sum_{\mathbf{G}'_\parallel G'_z} \int_{-\pi/L_z}^{+\pi/L_z} dq_z \int_{\mathbb{A}_{\mathrm{BZ}}} d\mathbf{q}_\parallel \times$$
$$\times \tilde{\rho}^*_{ij}(\mathbf{q}_\parallel + q_z + \mathbf{G}_\parallel + G_z) \frac{4\pi \epsilon^{-1}_{\mathbf{G}_\parallel G_z \mathbf{G}'_\parallel G'_z}(\mathbf{q}_\parallel, q_z)}{|\mathbf{q}_\parallel + q_z + \mathbf{G}'_\parallel + G'_z|^2} \tilde{\rho}_{mn}(\mathbf{q}_\parallel + q_z + \mathbf{G}'_\parallel + G'_z) \ ,$$

where $\mathbb{A}_{\mathrm{BZ}}$ is the area of the basis of the Brilloin zone.

In order to compute the self-energy and the BSE kernel within the CC framework, the screening and the Coulomb interaction have to be substituted by truncated quantities. The screening (9.9) is analytic everywhere, while the CC interaction presents singularities as explained at the beginning of the chapter. In the following I assume $v = 4\pi/|\mathbf{q} + \mathbf{G}'|$ and ϵ^{-1} to be substituted with $\check{v}$ and $\check{\epsilon}^{-1}$.

In evaluating the expression above, attention must be paid with vectors $\mathbf{k}'$ such that $\mathbf{q}_\parallel + \mathbf{G}'_\parallel = 0$. The $\mathbf{q} + \mathbf{G}$ vectors instead do not pose any problem since $\check{v}$ does not depend on them. For this reason I split the above expression into a sum over $\mathbf{G}$ and a sum over $\mathbf{G}'$. At the same time, I introduce a contracted notation for sake of simplicity, calling the integrand function

$$y^{ij}_{mn}(\mathbf{q}_\parallel, q_z, \mathbf{G}, G'_\parallel, G_z) :=$$
$$:= \tilde{\rho}^*_{ij}(\mathbf{q}_\parallel + q_z + \mathbf{G}) \check{\epsilon}^{-1}_{\mathbf{G}_\parallel G_z \mathbf{G}'_\parallel G'_z}(\mathbf{q}_\parallel, q_z) \check{v}_{\mathbf{G}'_\parallel G'_z}(\mathbf{q}_\parallel + q_z) \tilde{\rho}_{mn}(\mathbf{q}_\parallel + q_z + \mathbf{G}'_\parallel + G'_z) \ .$$

With this definition the matrix element of W reads

$$W^{ij}_{mn} = \frac{1}{(2\pi)^3} \sum_{\mathbf{G}} Y^{ij}_{mn}(\mathbf{G}) \qquad \text{with}$$
$$Y^{ij}_{mn}(\mathbf{G}) := \sum_{\mathbf{G}'_\parallel G'_z} \int_{-\pi/L_z}^{+\pi/L_z} dq_z \int_{\mathbb{A}_{\mathrm{BZ}}} d\mathbf{q}_\parallel \, y^{ij}_{mn}(\mathbf{q}_\parallel, q_z, \mathbf{G}, G'_\parallel, G'_z) \ .$$

What has been done up to now is nothing but rearranging terms. No approximation has been assumed and I haven't exploited the isolated system geometry. The only aspect used from the very beginning is that the expression is written in a 3D periodic arrangement. In other words, the expression above is still valid even if untruncated quantities (v and ϵ^{-1}) are used.

Now let us work out the elements of Y, remembering that whenever $\mathbf{q} + \mathbf{G}$ has a parallel contribution, even small, the integrand function y is well defined and smooth. I put in evidence the $\mathbf{G}_\parallel = 0$ component

$$Y^{ij}_{mn}(\mathbf{G}) = \sum_{G'_z} \int_{-\pi/L_z}^{+\pi/L_z} dq_z \int_{\mathbb{A}_{\mathrm{BZ}}} d\mathbf{q}_\parallel \, y^{ij}_{mn}(\mathbf{q}_\parallel, q_z, \mathbf{G}, 0, G'_z) + \tag{9.21}$$
$$+ \sum_{\mathbf{G}'_\parallel \neq 0} \sum_{G'_z} \int_{-\pi/L_z}^{+\pi/L_z} dq_z \int_{\mathbb{A}_{\mathrm{BZ}}} d\mathbf{q}_\parallel \, y^{ij}_{mn}(\mathbf{q}_\parallel, q_z, \mathbf{G}, G'_\parallel, G'_z) \ . \tag{9.22}$$

Since every $\mathbf{G}'_\parallel$ appearing in the second term is finite, all its elements are well defined. For each element, the integrals in $\mathbf{q}_\parallel$ and q_z can be approximated[49] by appropriate averages of the function y

$$\int_{-\pi/L_z}^{+\pi/L_z} dq_z \int_{\mathbb{A}_{\mathrm{BZ}}} d\mathbf{q}_\parallel \, y^{ij}_{mn}(\mathbf{q}_\parallel, q_z, \mathbf{G}, G'_\parallel, G'_z) \;\approx\; \frac{(2\pi)^3}{\mathcal{V}} \sum_{\mathbf{q}_i} y^{ij}_{mn}(\mathbf{q}^i_\parallel, q^i_z, \mathbf{G}\mathbf{G}'_\parallel, G'_z) \tag{9.23}$$

implying a proper choice of the points $\mathbf{q}^i$ inside the BZ. The crystal volume $\mathcal{V} = \mathcal{V}_{\mathrm{cell}} N_{\mathbf{k}}$ is the volume of a unit cell times the number of $\mathbf{k}$ points.

We are left wit the first term (9.21) which contains points of non-analyticity. In particular, when $\mathbf{q}_\parallel = 0$ the integral is performed on the k_z axis, where y is not defined[50]. The integral $\int_{\mathbb{A}_{\mathrm{BZ}}} d\mathbf{q}_\parallel = \sum_i \int_{\mathbb{A}^i} d\mathbf{q}_\parallel$ can be split into smaller integrals centred on points $\mathbf{q}^i_\parallel$. The approximation used in (9.23) can now be used once again for all $\mathbb{A}^i$, except for the integral $\int_{\mathbb{A}^0} d\mathbf{q}_\parallel$ which encloses the origin. Therefore in the expression (9.21) one can introduce the following approximation

$$\begin{aligned}
&\int_{-\pi/L_z}^{+\pi/L_z} dq_z \int_{\mathbb{A}_{\mathrm{BZ}}} d\mathbf{q}_\parallel \, y^{ij}_{mn}(\mathbf{q}_\parallel, q_z, \mathbf{G}, 0, G'_z) \approx \\
&\approx \int_{-\pi/L_z}^{+\pi/L_z} \int_{\mathbb{A}_0} y^{ij}_{mn}(\mathbf{q}_\parallel, q_z, \mathbf{G}, 0, G'_z) d\mathbf{q}_\parallel dq_z + \frac{(2\pi)^3}{\mathcal{V}} \sum_{q^i_\parallel \neq 0} y^{ij}_{mn}(\mathbf{q}^i_\parallel, q^i_z, \mathbf{G}, 0, G'_z) \; .
\end{aligned} \tag{9.24}$$

The last expression is summed over all G'_z vectors (cfr. (9.21)). The first term of (9.24) still have to be handled with care for it is an integral enclosing the k_z axis. I remember that the integrand function is divergent in all the k_z axis except for some special point. A possible way out is to integrate numerically all these terms [172].

But one can reason in a different way: since we are working with an isolated object, the BZ is planar and the G_z vectors are infinitely close. Moreover if one follows Beigi's prescription (9.19), then G_z points happen to coincide with the special points $\tilde{k}^n_z$ where the CC is defined. Then in the limit of an isolated system the following substitution can be justified

$$\sum_{G'_z} \int_{-\pi/L_z}^{+\pi/L_z} y(q_z, G'_z) dq_z \xrightarrow[z_0 = L_z/2]{L_z \to \infty} \int_{-\infty}^{+\infty} y(0, G'_z) dG'_z \approx \sum_{G'_z} \frac{2\pi}{L_z} y(0, G'_z)$$

which inserted into (9.24), leads to

$$\begin{aligned}
&\sum_{G'_z} \int_{-\pi/L_z}^{+\pi/L_z} \int_{\mathbb{A}_0} y^{ij}_{mn}(\mathbf{q}_\parallel, q_z, \mathbf{G}, 0, G'_z) d\mathbf{q}_\parallel dq_z \approx \\
&\approx \frac{2\pi}{L_z} \int_{\mathbb{A}_0} y^{ij}_{mn}(\mathbf{q}_\parallel, 0, \mathbf{G}, 0, 0) d\mathbf{q}_\parallel + \frac{(2\pi)^3}{\mathcal{V}} \sum_{G'_z \neq 0} y^{ij}_{mn}(0, 0, \mathbf{G}, 0, G'_z) \; ,
\end{aligned} \tag{9.25}$$

[49] For the generic function $g(\mathbf{k})$ integrated in the volume $\mathcal{D} = \sum_i \mathcal{D}_i$, with $\mathcal{D}_i$ non-overlapping volumes, the equality $\int_{\mathcal{D}} g(\mathbf{k}) d\mathbf{k} = \sum_i \int_{\mathcal{D}_i} g(\mathbf{k}) d\mathbf{k} = \sum_i g(\mathbf{k}_i) \mathcal{D}_i$ is exact if every $\mathbf{k}_i$ is contained in the volume $\mathcal{D}_i$ and is such that $g(\mathbf{k}_i) = \frac{1}{\mathcal{D}_i} \int_{\mathcal{D}_i} g(\mathbf{k}) d\mathbf{k}$, i.e. $g(\mathbf{k}_i)$ is the average value of the integral in the volume $\mathcal{D}_i$.

[50] Sampling only the xy plane, y is not defined in any point of k_z axis inside the BZ.

where the same approximation used in (9.23) and (9.24) has been made for all the integrations around the points of analyticity. The last approximation is justified by the fact that we are working with isolated 2D systems, which have planar BZ (**q**-points only in-plane).

Collecting all terms together, the final expression of the matrix element $\langle ij|\check{W}|mn\rangle$ is

$$\begin{aligned}\check{W}^{ij}_{mn} = &\frac{1}{\mathcal{V}}\sum_{\mathbf{G}}\sum_{\mathbf{G}'_\parallel\neq 0}\sum_{\mathbf{q}_i,G'_z} y^{ij}_{mn}(\mathbf{q}^i_\parallel, q^i_z, \mathbf{G}, \mathbf{G}'_\parallel, G'_z) + \\ &+\frac{1}{\mathcal{V}}\sum_{\mathbf{G}}\sum_{\mathbf{G}'_z}\sum_{\mathbf{q}^i_\parallel\neq 0} y^{ij}_{mn}(\mathbf{q}^i_\parallel, q^i_z, \mathbf{G}, 0, G'_z) + \\ &+\frac{1}{\mathcal{V}}\sum_{\mathbf{G}}\sum_{G'_z\neq 0} y^{ij}_{mn}(0,0,\mathbf{G},0,G'_z) + \\ &+\frac{1}{(2\pi)^3}\sum_{\mathbf{G}}\frac{2\pi}{L_z}\int_{\mathcal{A}_0} y^{ij}_{mn}(\mathbf{q}_\parallel,0,\mathbf{G},0,0)d\mathbf{q}_\parallel\ . \end{aligned} \tag{9.26}$$

The use of Beigi's prescription allows one to reduce considerably the number of points where the integral has to be treated by hand. In the end, only the case $\mathbf{q}+\mathbf{G}=0$ needs a special treatment, exactly as for standard calculations.

9.2 EELS of graphite and graphene using the CC

In this section I present the EELS computed for the four systems $1d_0$, $2d_0$, $4d_0$ and $6d_0$, using the CC interaction. Since Beigi's prescription (9.19) has been used, the **q** points have null perpendicular components in all geometries. The resulting implemented expression for the CC is

$$\check{v}_{\mathbf{G}}(\mathbf{q}_\parallel) = \frac{4\pi}{|\mathbf{q}_\parallel+\mathbf{G}_\parallel|^2+G_z^2}\left[1-e^{-(\mathbf{q}_\parallel+\mathbf{G}_\parallel)z_0}\cos(G_z\,z_0)\right] \quad \text{having fixed} \quad z_0=\frac{L_z}{2}\ . \tag{9.27}$$

To differentiate these calculations with those of the previous chapter, the notation $1d_0+CC$ (and similarly for the other systems) will be adopted.

Computational details: The EEL spectra have been computed in the RPA. The EPC has been applied to all calculations according to formula (9.10). KS equations formulated with using the standard Coulomb interaction have been solved using ABINIT [124] .

The CC interaction has been implemented in the form (9.27) in the simulation codes DP [127] and EXC [86]. In all gemoetries, the KS polarizability χ^{KS} has been computed over a grid of $34\times34\times1$ **k**-points centred in Γ. The number of bands used, the number of plane waves and the dimension of the matrix are the same as in the previous chapter[51], listed in Tab. 8.2 and here repeated for clarity.

Comparison between the systems is done by plotting scaled spectra $-d/d_0\Im[1/\epsilon_M]$ for EELS and $d/d_0\Im[\epsilon_M]$ for absorption.

[51]The cutoff function $\theta(|z|-z_0)$ is abruptly varying in space, so one may expect that a higher number of plane waves is needed to converge the matrix dimension. I tested that in the systems considered here, the same parameters of the untruncated simulations gives converged results even when employing the cutoff.

Table 9.1: Converged parameters for EELS with the CC interaction

system	nband	npwwfn	npwmat
$1d_0 + CC$	40	350	50
$2d_0 + CC$	60	450	70
$4d_0 + CC$	80	850	90
$6d_0 + CC$	80	1300	160

9.2.1 Parallel momentum transfer

In Fig. 9.2 the EEL spectra of the $1d_0+CC$, $2d_0+CC$ and $6d_0+CC$ calculations are reported for vanishing in-plane momentum transfer (Fig. 9.2a) and for larger momentum (Fig. 9.2b). For both plots, also the corresponding $6d_0$ calculation without cutoff has been reported as a dotted black line in the case of EELS and as a violet line in the case of the absorption spectrum.

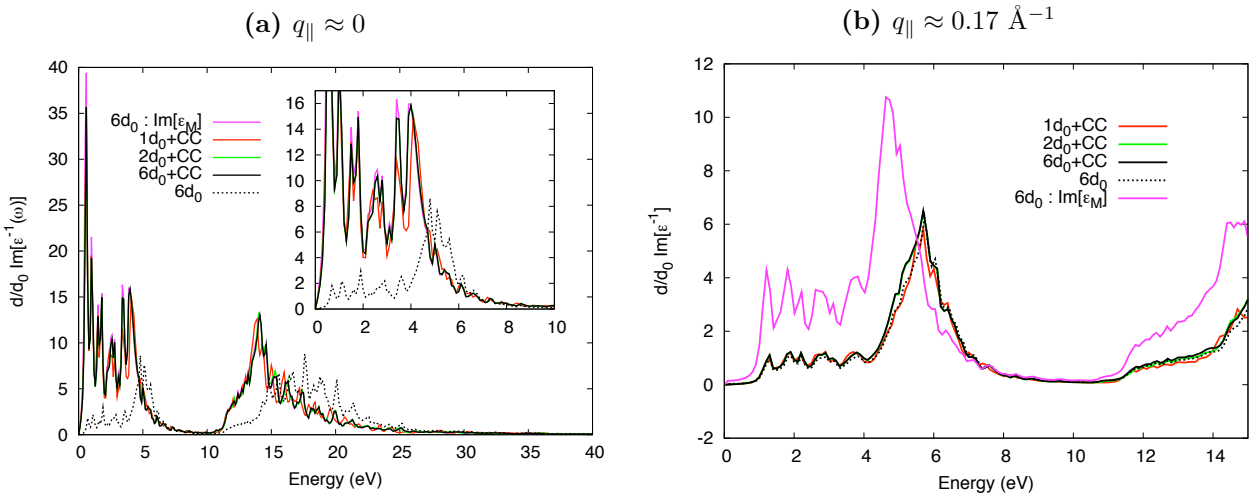

Figure 9.2: EEL spectra for in-plane momentum transfer. In solid red, green and black lines the $1d_0 + CC$, $2d_0 + CC$, and $6d_0 + CC$ spectra respectively. Dotted line is the corresponding untruncated $6d_0$ calculation (Fig. 8.6a). Violet crosses draw the absorption spectrum $\Im[\epsilon_M(\omega)]$ of the $6d_0$ system.

The effect of the CC is striking, especially for small momenta. Already the $1d_0$ system, is extremely close to the converged result despite the interaction still occurring between planes (cfr. Fig. 8.5). No difference with respect to the converged result is found when the CC is applied to the $2d_0$ system or for higher interlayer distances.

The use of CC has much more effect for small momenta. This can be easily understood by looking at the CC expression (9.27): the exponential factor is such that $\lim_{k\to\infty} f_C(\mathbf{k}) = 1$, so for high transferred momenta the untruncated- and the cutoff-Coulomb interactions tend to coincide, as already underlined by R. Hambach [19].

Before passing to the perpendicular momentum transfer, I underline that, in force of Beigi's prescription, the **k**-point grid used has only in-plane ($k_z = 0$) points, even for the $1d_0$ and $2d_0$ systems, contrary to what has been necessary for the untruncated Coulomb calculations. What seemed to be a limitation of the CC method, turns out to be an advantage since, not only convergence in the distance d is faster, but also it is reached with a coarser **k**-point grid.

The reason for this is that off-plane k-points correspond to Fourier components propagating along the k_z direction, which are negligible in the isolated system [19]. In other words, by sampling only the plane, we look at those electrons which are confined in the 2D layer. So, from one side, the CC method allows us to include in the calculation only those electrons that are meaningful for the description of the isolated system (Beigi's prescription to sample only in-plane) and, on the other side, it forces them to move as they were isolated by means of the cutoff function.

9.2.2 Perpendicular momentum transfer

With the **k**-point grid used, the off-plane momentum can be only of the kind $G_z^n = 2n\pi/L_z$ (with $n \neq 0$). In this case, the expression of $\check{v}_{G_z^n}(\mathbf{q}_\parallel = 0)$ reduces to (9.7). Correspondingly, the imaginary part of the EPC-screening (9.8) is either proportional to χ^{KS} (n even) or to $\check{\chi}$ (n odd). Depending on the value of n, two different relations can be verified,

$$n \neq 0 \text{ even} \Rightarrow -\Im[\check{\epsilon}^{-1}] = -\Im[v\chi^{KS}] = \Im[\epsilon^{\text{NLF}}] \tag{9.28}$$

$$n \text{ odd} \Rightarrow -\Im[\check{\epsilon}^{-1}] \xrightarrow{L_z\to\infty} \Im\left[1/\check{\epsilon}^{-1}\right] \ . \tag{9.29}$$

The second expression have been demonstrated in equation (4.30).

In Fig. 9.3, I report an example of the $d = 2d_0$, $4d_0$ and $6d_0$ spectra with off-plane momentum transfer. In order to compare G_z components of same size, the integer n has to be changed for the different values of d; it is $n = 1$ in the $2d_0$, $n = 2$ in the $4d_0$ and $n = 3$ in the $6d_0$.

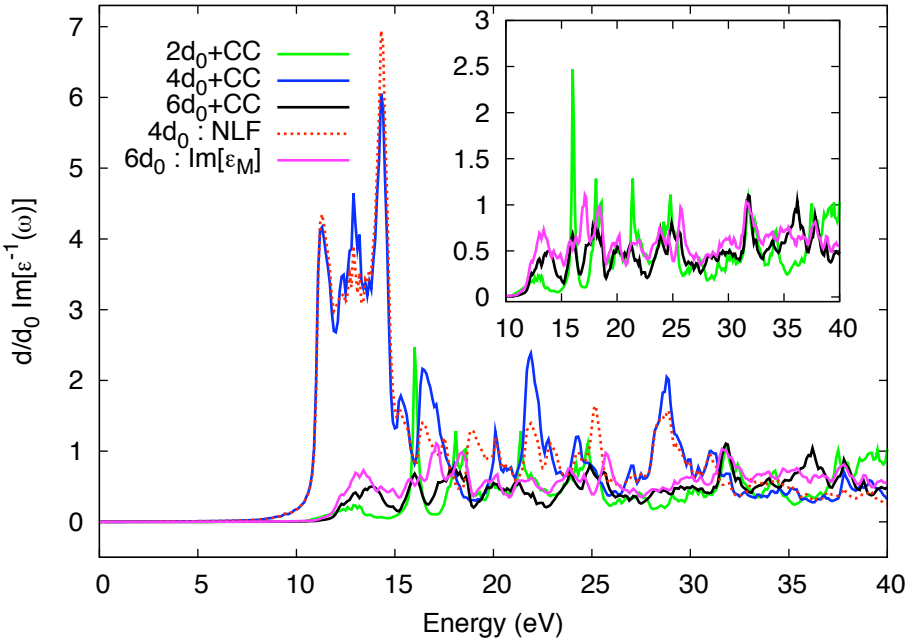

Figure 9.3: Perpendicular momentum transfer with CC for $G_z \approx 0.94$ Å^{-1}. Green and black solid lines corresponds to $2d_0 + CC$ and $6d_0 + CC$ calculations for which G_z is an odd multiple of $2\pi/L_z$ ($n = 1$ and $n = 3$ respectively). They both converge to the $\Im[\epsilon_M]$ spectrum of the $6d_0$ (violet line). Red dotted and blue solid line correspond to the $4d_0$ $\Im[\epsilon_M^{\text{NLF}}]$ and $4d_0 + CC$ EELS respectively. For this system G_z is an even multiple of $2\pi/L_z$ ($n = 2$).

The conclusion is that for off-plane momenta the convergence to the isolated system is much as fast as for the in-plane momenta. In fact in half of the cases (n odd) the $2d_0 + CC$

is very close to the converged spectrum, as it can be seen in the inset of Fig. 9.3. In the other half (n even), the EEL spectrum corresponds to the NLF absorption spectrum, which is proportional to χ^{KS}. As demonstrated by R. Hambach [19], the KS polarizability is strongly localised in the plane, so it is almost blind to the the presence of other layers near the graphene sheet. As a consequence it converges to the long-range absorption spectrum very rapidly and so does the $\check{\epsilon}^{-1}$.

In the case of perpendicular exchanged momenta, the effect of the CC is that of counting all $G_z^{\text{even}} = 2\pi(2n)/L_z$ as the $G_z = 0$ term.

It is important to underline that also in this case only $k_z = 0$ points have been used to sample the BZ, similarly to what done for the in-plane study.

9.3 Spectral functions of isolated graphene

I now pass to the discussion of spectral functions, computed using the CC method. The interlayer distance considered are again $d = 1d_0$, $2d_0$, $4d_0$ and $6d_0$.

Computational details: The parameters of the calculations of Σ and of the screening are the same as in the previous chapter, except for the **k**-point grid which is in all cases a $10 \times 10 \times 1$ because of Beigi's prescription. The screening has been computed using the FC-screening formula (9.9), as I implemented it in the code DP [127]. Matrix elements of W entering in the calculation of the correlation self-energy have been computed as summarised in formula (9.26) where the integral enclosing the origin has been evaluated through an analytical integration of the long-range parallel components of CC, as detailed in Appendix D.

Computational development

To make ABINIT compute spectral functions via the CC interaction, I had to modify in several aspects the codes ABINIT and DP.

Up to now, DP was designed to compute absorption or EEL spectra at specific $\mathbf{q}$ vectors. So it has been necessary to make DP write the full matrix $\epsilon^{-1}_{\mathbf{GG'}}(\mathbf{q},\omega)$ and record it in a ".SCR" outpu file. To do so I have included the sequence of subroutines computing $\epsilon^{-1}_{\mathbf{GG'}}(\mathbf{q},\omega)$ inside a loop over all possible $\mathbf{q}$ points compatible with the chosen k-point grid. In this way it has been possible to store in an output file ".SCR" the full matrix $\epsilon^{-1}_{\mathbf{GG'}}(\mathbf{q},\omega)$. Moreover I added the calculation of the cutoff function, which means, beside the simple implementation of expression (9.20), the implementation of the EPC formula (9.10).

Once the cutoff-dielectric matrix is computed and recorded in ".SCR" by DP, it can be used in ABINIT to compute the self-energy. Two main problems are found at this stage. One is the fact that ABINIT uses a symmetrised form of the Coulomb interaction ($\tilde{\epsilon}^{-1}$), leading to a screened Coulomb interaction

$$W_{\mathbf{GG'}}(\mathbf{q}) = \tilde{\epsilon}^{-1}_{\mathbf{GG''}}(\mathbf{q}) \cdot \tilde{v}_{\mathbf{G''G'}}(\mathbf{q})$$

where $\cdot$ is a matrix multiplication and

$$\tilde{v}_{\mathbf{G''G'}}(\mathbf{q}) = \frac{4\pi}{|\mathbf{q}+\mathbf{G''}||\mathbf{q}+\mathbf{G'}|}$$

is the symmetrized Coulomb interaction. The second is that the ".SCR" file is used only in the calculation of Σ_c, while the cutoff function $f_C(\mathbf{q}+\mathbf{G})$ is also needed to compute Σ_x (cfr. (9.14)).

I solved the problems of the inclusion of f_C in Σ_c and the necessity of symmterizing ϵ^{-1} by devising a generalised symmetrization formula

$$\tilde{\epsilon}^{-1}_{\mathbf{GG'}}(\mathbf{q}) = \epsilon^{-1}_{\mathbf{GG'}}(\mathbf{q}) \times \left\{ \frac{|\mathbf{q}+\mathbf{G}|}{|\mathbf{q}+\mathbf{G'}|} f_C(\mathbf{q}+\mathbf{G'}) + \delta_{\mathbf{GG'}} \left[\frac{1}{\epsilon^{-1}_{\mathbf{GG}}(\mathbf{q})} - \frac{f_C(\mathbf{q}+\mathbf{G})}{\epsilon^{-1}_{\mathbf{GG}}(\mathbf{q})} \right] \right\} \tag{9.30}$$

which allows to simultaneously include the cutoff-function and to symmetrize the screening.

The second problem, that is how to include f_C in the exchange self-energy, has been solved by means of a second output file written by DP and read by ABINIT. In the file ".CTF", the function $f_C(\mathbf{q}+\mathbf{G})$ is recorded at all $\mathbf{G}$ and all $\mathbf{q}$.

To summarise, to write the full cutoff dielectric matrix in the ".SCR" output file, the CC interaction has been implemented in DP, together with the possibility of enabling the EPC formula. Both computations have been inserted into a cycle over the $\mathbf{q}$ points compatible with the sampling of the BZ. The CC spectral functions are then computed with ABINIT in two steps:
Σ_x is computed by reading a file ".CTF" where the only cutoff function is recorded to all $\mathbf{q}$ and all $\mathbf{G}$,
Σ_c is computed by reading the ".SCR" file, written with a specific symmetrization formula which allows for the inclusion of the f_C in the expression $\epsilon^{-1} f_C\ v$.

The general structure of this procedure is such that further manipulations of W to add in future GW calculations (e.g., vertex corrections) can be taken into account more easily by changing the DP code.

The Hartree potential, the XC potential and the nuclei

The exact V_{xc} is proportional to Q/r, where Q is the charge on a finite system and r the distance from it. Therefore it has a long-range tail similar to the Hartree potential. Instead, in LDA, it decays exponentially with the distance from the plane, so at small interlayer separations, the matrix elements $\langle V_{xc} \rangle$ are at convergence with the isolated system. This was already evident in Chapter 7, where ground state energy contributions were discussed.

On the other hand, ionic and Hartree contributions both have the correct long-range behaviour Q/r, but with opposite sign, so they cancel mutually. Indeed it has been demonstrated by Rozzi et al. [170] that the inclusion of the CC interaction in both potentials give essentially the untruncated result.

Because of these arguments the cutoff interaction has been included only in the self-energy and not in the KS calculation.

9.3.1 G_0W_0 spectra

In Fig. 9.4, I report the spectral function obtained using the CC for the four systems.

Let us first look at the self-energy, decomposed in its imaginary part $\mathcal{I}(\omega)$ and its shifted real part $\mathcal{R}(\omega)$, both reported in Fig. 9.4b. This figure has to be compared with the same calculations made with standard Coulomb interaction of Fig. 8.9. The extremely good performance of the CC calculation even at the level of the $1d_0$ geometry is remarkable when

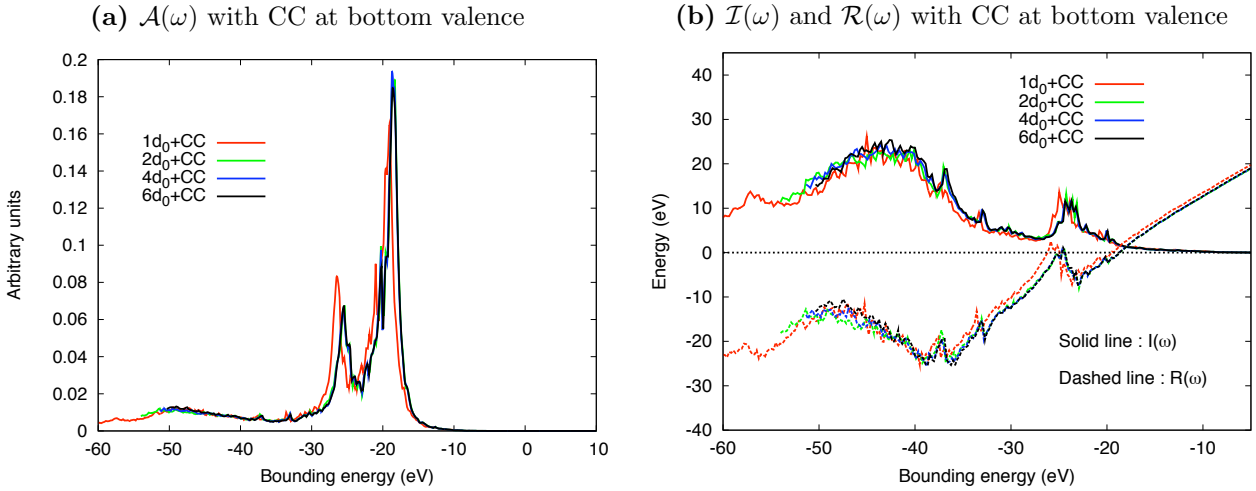

Figure 9.4: Spectral function $\mathcal{A}(\omega)$, imaginary part of Σ $\mathcal{I}(\omega)$ and real shifted part of Σ $\mathcal{R}(\omega)$ calculated with Coulomb cutoff within G_0W_0, at the bottom valence in the $1d_0$ (red lines), $2d_0$ (green lines), $4d_0$ (blue lines) and $6d_0$ (black lines) systems.

comparing the high energy peak around -50 eV (π plasmon) in the two calculations (Fig. 9.4b with cutoff and Fig. 8.9b without cutoff). Although the *pi* plasmon and the global line shape is essentially at convergence already in the $1d_0 + CC$ calculation, some features are not well reproduced. This is the case, for instance, of the peak at ~ -60 eV, predicted by the $1d_0+CC$ calculation, but absent in the other systems. It may be ascribed to a bad evaluation of the matrix elements of W. Indeed, the amplitudes $\tilde{\rho}_{ij} = \int \phi_i^*(\mathbf{r})\phi_j(\mathbf{r})d\mathbf{r}$ entering in (9.26) are computed from KS states of the bulk material, where planes are still interacting. Since they are not modified by the presence of the cutoff, they correspond to the $\tilde{\rho}$s computed in the bulk, and this may lead to some error in the matrix elements of Σ. The CC seems to be less efficient also with respect to the π plasmon, at ~ -25 eV, which is actually enhanced with respect to the untruncated case.

Passing to the the spectral function $\mathcal{A}(\omega)$ reported in Fig. 9.4a, one draws similar conclusions, noticing that the quasiparticle peak is much closer to the converged energy and weight, but the π plasmaron is stronger. On the other hand the $\pi + \sigma$ plasmon, that was significantly far from convergence in the untruncated case, reproduces now the converged satellite, in agreement with what observed in $\mathcal{I}(\omega)$.

Selecting the relevant physics

In order to reduce the size of the system used to simulate isolated graphene, one needs to use the CC formula with its complicated domain of definition. Beigi's recipe to cope with this problem is simple: $(z_0 = L_z/2)$ + (only $k_z = 0$ sampling). However, in Chapter 8, I stressed that only one point along the k_z axis is not sufficient to calculate accurately the EEL spectrum, and even calculations in the $2d_0$ geometry need at least 2 points along k_z. The question which arises naturally is "*How does Beigi's prescription influence the CC calculation of spectral functions?*" or differently stated "*Is the constraint of having only in-plane k-points a drawback of this method?*"

In Fig. 9.5 I report the $\mathcal{I}(\omega)$ of the $1d_0$ system computed for a number of **k**-point sampling the k_z axis $M_z = 1$ and $M_z = 2$ (solid and dashed blue curves respectively) together with the $1d_0 + CC$ calculation (solid red), the $6d_0 + CC$ and $6d_0$ calculations (solid and dashed

black). The grids are centred in Γ, so that only points laying on the xy plane are included in the $M_z = 1$ case, whereas in the $M_z = 2$, the points are outside the plane.

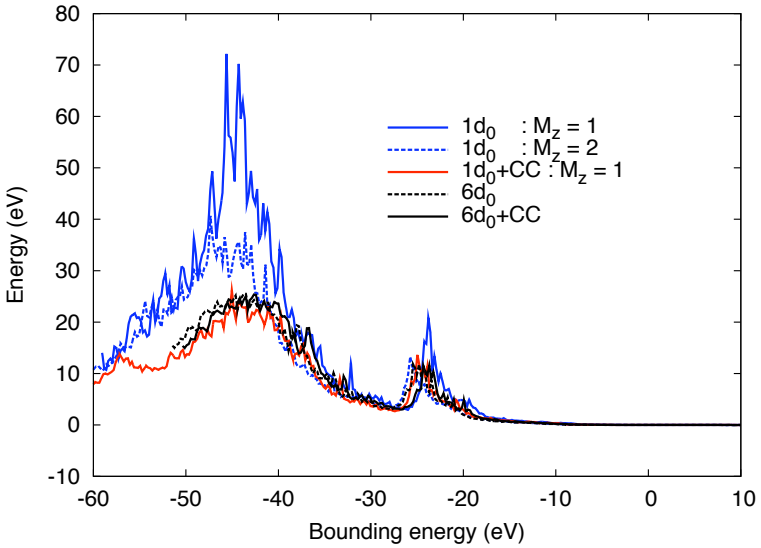

Figure 9.5: $\mathcal{I}(\omega)$ in the $1d_0$. Calculations without the cutoff are performed by sampling the k_z axis with $M_z = 1$ or $M_z = 2$ points ($M_z = 1$ in solid blue and $M_z = 2$ in dashed blue). The $1d_0 + CC$ calculation performed within Beigi's prescription ($M_z = 1$) is reported in red. For comparison the converged $6d_0$ and $6d_0 + CC$ calculations are also plotted (dashed and solid black).

The $\mathcal{I}(\omega)$ of bulk graphite $1d_0$ computed with only in-plane points (solid blue), is substantially different from the isolated curves ($6d_0$ and $6d_0 + CC$), even though the same grid gives remarkably good results when the CC is added (red curve). The same strong point of Beigi's prescription underlined at the end of section 9.2.1 is retrieved in this context. The inclusion in the grid of the only $q_z = 0$ points actually allows for a selection of the physics of interest. In fact this choice corresponds in taking only those Fourier components (plane waves) that are propagating in the plane and in discarding the others. But this is not enough, otherwise the solid blue curve would coincide with the isolated graphene. This selection is efficient only if these components are made blind to the other planes, which is the task accomplished by the cutoff function.

This last result validates completely Beigi's recipe (in-plane only k-point sampling)+CC, which is indeed a very efficient way to compute the spectral function of isolated graphene, and most likely of many other 2D crystals.

9.3.2 Conclusions

To conclude, I observe that the use of the CC interactions does not affect importantly the quasiparticle peak and the first satellite, while the higher energy $\pi + \sigma$ plasmon satellite converges much faster to the graphene shape with respect to the untruncated calculation. Although the CC interaction brings the $1d_0 + CC$ self-energy much closer to the graphene one, a high energy structure and a small shift in the π plasmon energy are found. These features may be ascribed to the fact that the inter-layer separation is not high enough at the DFT level so the Bloch integrals $\tilde{\rho}$ are not correctly calculated. Using KS states computed for the $d = 2d_0$ instead gives converged graphene results, with half of the k_z points needed in the untruncated calculation.

Nevertheless the striking effect of the CC on the $1d_0$ spectrum, made possible to understand what is the very advantage in using the recipe (in-plane sampling + CC). Only the relevant Fourier components are selected by the choosing only in-plane k-points, and they are made isolated by the effect of the cutoff function. So, what at the beginning may have seemed a limitation of the CC method, namely the use of in-plane only k-points, turns out to be actually another strong point of this method.

The convergence trend observed in EELS calculations can explain why spectral functions converge faster. As concluded in the previous chapter, the convergence of spectral functions is driven by short-wavelength components of the $\epsilon^{-1}_{\mathbf{GG'}}(\mathbf{q})$ matrix. As observed before, in EELS + CC the in-plane components of $\check{v}$ tend rapidly to the untruncated Coulomb. For off-plane elements, the convergence to the isolated case is also fast (half of them coincide with the NLF absorption spectrum). Therefore, in computing the sums in expression (9.26), many terms are close to the standard Coulomb ones and the convergence to the isolated system is as fast as in the untruncated case.

To calculate EELS and spectral functions, the CC interaction has been implemented in the code DP, together with the capability of recording the full matrix $\epsilon^{-1}_{\mathbf{GG'}}(\mathbf{q},\omega)$ in a file that can be read by the codes ABINIT and EXC. These features are tested and easy to use, so they can be employed in future by other users, for example to study other 2D materials (such as h-BN), or to develop further improvements which may take advantage of this implementation, such as the CC at the BSE level[52].

[52]Some preliminary development in this sense has been done already during this work.

Chapter 10

A different(ial) approach to the dynamics of absorption

In the previous chapters I have discussed dynamical effects in the one particle spectral function. However, the final aim of this thesis is the inclusion of the dynamical e-h interaction in the description of the optical properties.

The description of dynamical correlation effects in photoemission has been the main subject of the the works of G. Lani [55] and especially of M. Guzzo [5, 78, 94]. The approach followed in these works is based on the solution of the equation of motion of G in the form of the integro-differential equation (5.8)*. It is therefore a self-energy free approach which does not rely on the solution of the Dyson equation.*

Amongst the advantages, there is the fact that the interaction is not hidden in the effective field represented by the self-energy. Higher order interactions are not embodied into a demanding and very hard to approximate 3-point vertex. Of course, the integro-differential equation is not simpler to solve than the Dyson equation, so other approximations have to be assumed (cfr. especially [55]). However in this approach, the dynamical structure of the screening is preserved and dynamical effects as satellite replicas can be correctly described [5], contrary to what achieved with state-of-the-art self-energy based approaches.

With the aim of inserting dynamical effects into the description of light absorption, I followed the same strategy and I eventually derived a differential equation for the two particle correlation function L. Within some approximations I have been able to solve the equation. The solution contains dynamical effects of the electron, of the hole and of the electron-hole interaction, accounting for mutual partial cancellations.

Some clarification on the notation

Due to the complexity of the equations reported in this chapter, some simplified notation has to be clarified from the beginning.
1) Integration over repeated variables and summation over repeated matrix indexes have always to be assumed, even if $\int$ or $\sum$ symbols are not written explicitly. When the extrema of several integrals coincide, if the integration symbol is used, only one $\int$ will appear for all integrations.
2) Compact variables $1 = \mathbf{r}_1, t_1, \sigma_1$ are used throughout the chapter; no comma will be put between variables so that $G(\mathbf{r}_1, \mathbf{r}_2, t_1, t_2, \sigma_1, \sigma_2) = G(12)$. Similarly, when only time or space variables are listed, a cumulative index will be used so that $\mathbf{r}_{12} = \mathbf{r}_1, \mathbf{r}_2$ and analogously for

integration variables $d\mathbf{r}_{12} = d\mathbf{r}_1 d\mathbf{r}_2$.
3) Some quantity has been generalised to a 4-point formalism to be closer to the matrix notation. Therefore the following definitions have to be assumed:

$$\begin{aligned}
\Gamma(1234) &= -\frac{\delta G^{-1}(12)}{\delta U(34)} \\
v(1234) &= v(\mathbf{r}_{13})\delta(\mathbf{r}_{12})\delta(\mathbf{r}_{34})\delta(t_{12})\delta(t_{34})\delta(t_{13}) \\
V_H(12) &= -iv(1234)G(34) \qquad (10.1) \\
\epsilon^{-1}(1234) &= \frac{\delta V_{\text{tot}}(12)}{\delta U(34)} = \delta(13)\delta(24) - iv(1256)\frac{\delta G(56)}{\delta U(34)} \\
W(1234) &= \epsilon^{-1}(1256)v(5634) \\
\Sigma(12) &= iv(1345)\frac{\delta G(36)}{\delta U(45)}G^{-1}(62) \qquad (10.2)
\end{aligned}$$

where $V_{\text{tot}} = V_H + U$.

10.1 The linear integro-differential functional equation

The two-particle correlation function is defined by Schwinger's equation (5.7)

$$L(1234) := L^0(1234) + iG_2(1234) = -i\frac{\delta G(12)}{\delta U(34)}$$

where $L^0(1234) = -iG(13)G(42)$ has been introduced in (5.44). For our aim, the operator $\delta G/\delta U$ must not be taken at vanishing U, contrary to what is done in deriving the BSE.

The differential equation for L is obtained by differentiating the last equality with respect to U, but first I get rid of the self-energy by substituting it with its definition (5.9) into the Dyson equation (5.10), getting

$$G_H^{-1}(1'2')G(2'2) = \delta(1'2) + \Sigma(1'2')G(2'2) = \delta(1'2) + iv(1'2'3'4')\frac{\delta G(2'2)}{\delta U(3'4')} \,. \qquad (10.3)$$

Then I take the differentiation with respect to the external field U obtaining

$$\frac{\delta G_H^{-1}(1'2')}{\delta U(34)}G(2'2) + G_H^{-1}(1'2')\frac{\delta G(2'2)}{\delta U(34)} = iv(1'2'3'4')\frac{\delta^2 G(2'2)}{\delta U(3'4')\delta U(34)} \,.$$

Noticing that $G_H^{-1}(12) = H_0(1)\delta(12) - U(12) - V_H(12)$, using the definition of the 2-point Hartree potential $V_H(12) := -iv(1234)G(34)$, and inverting the order of the two derivatives in the right hand side of the equation, one finally gets

$$\begin{aligned}
L(1234) = &-iG_H(13)G(42)+ \\
&- iG_H(15)G(62)v(5678)L(7834)+ \\
&+ iG_H(15)v(5678)\frac{\delta L(6234)}{\delta U(78)} \qquad (10.4)
\end{aligned}$$

where all quantities are functionals of U. Moreover we suppose that $G[U]$ is a known functional of U.

This equation represents the starting point of the present approach and the solution of this equation will be the subject of the entire chapter. It is a linear integro-differential functional equation for the two-particle correlation function L.

It is characterised by three terms:

- an "independent particle" term

$$L^H(1234) := -iG^H(13)G(42) \tag{10.5}$$

  which describes the propagation of two particles inside the medium. These particles do not interact with each other (that is why it is called "independent-particle"), but both are interacting with the rest of the system. The peculiar thing is that the interaction with the system is not described in a symmetric way: one particle is polarizing the medium through a simple Hartree interaction ($G^H(13)$), the other interacts via a full many-body interaction ($G(42)$). This asymmetry is restored at the end of the calculation. Because of this asymmetry, if one wants to describe the two particles on the same footing the screened Coulomb interaction has to be handled carefully.

- a bare Coulomb term

$$+L^H(1256)v(5678)L(7834)$$

  which describes the self-consistent interaction between the two particles and the rest of the system in terms of a classical Hartree interaction. It describes the polarization induced in the rest of the system because of the propagation of the particle pair, exactly as the RPA term in BSE.

- a differential term

$$iG^H(15)v(5678)\frac{\delta L(6234)}{\delta U(78)}$$

  which accomplishes two tasks: it accounts for the electron-hole interaction including dynamical effects and it restores the "asymmetry" discussed above, as it will be clearer at the end of the chapter. Indeed it comes from the differentiation of the self-energy so it can be compared with the kernel Ξ of the BSE.

With these notations, equation (10.4) reads

$$\begin{aligned} L(1234) = L^H(1234)+ \\ + L^H(1256)v(5678)L(7834)+ \\ + iG_H(15)v(5678)\frac{\delta L(6234)}{\delta U(78)} \end{aligned} \tag{10.6}$$

Both the standard BSE and this equation are derived from the same Dyson equation for G, hence it is possible to cast a parallel to get a deeper understanding of the derived equation and of some aspects of the BSE.

10.1.1 Mutual cancellations in the Bethe-Salpeter Equation

In order to trace a parallel between (10.6) and the BSE (5.44), it turns out to be useful to re-derive the BSE by differentiating the equality $G^{-1}(13)G(32) = \delta(12)$.

Using

$$G^{-1}(12) = H_0(1)\delta(12) - U(12) - V_H(12) - \Sigma(12) = G_H^{-1}(12) - \Sigma(12) \ ,$$

where the 2-point Hartree potential (10.1) has been used, one gets

$$\begin{aligned}
&\frac{\delta G^{-1}(15)}{\delta U(34)}G(52) + G^{-1}(15)\frac{\delta G(52)}{\delta U(34)} = \\
&= -\frac{\delta U(15)}{\delta U(34)}G(52) - \frac{\delta V_H(15)}{\delta U(34)}G(52) - \frac{\delta \Sigma(15)}{\delta U(34)}G(52) + G_H^{-1}(15)\frac{\delta G(52)}{\delta U(34)} - \Sigma(15)\frac{\delta G(52)}{\delta U(34)} = 0 \ .
\end{aligned} \tag{10.7}$$

This formulation of the BSE puts in evidence the mutual cancellation between (dynamical) terms containing the self-energy. In fact, using definition (10.2), and the exact relation $\frac{\delta G^{-1}(15)}{\delta U(34)}G(52) = -G^{-1}(15)\frac{\delta G(52)}{\delta U(34)}$, the following equality can be verified:

$$\frac{\delta \Sigma(15)}{\delta U(34)}G(52) = iv\frac{\delta^2 G(52)}{\delta U(34)\delta U(67)} - \Sigma(15)\frac{\delta G(52)}{\delta U(34)} \tag{10.8}$$

which, inserted into (10.7), leads to the following equation

$$\begin{aligned}
-\frac{\delta U(15)}{\delta U(34)}G(52) - \frac{\delta V_H(15)}{\delta U(34)}G(52) - iv\frac{\delta^2 G(52)}{\delta U(34)\delta U(67)} + \Sigma(15)\frac{\delta G(52)}{\delta U(34)} = \\
= -G_H^{-1}(15)\frac{\delta G(52)}{\delta U(34)} + \Sigma(15)\frac{\delta G(52)}{\delta U(34)}.
\end{aligned} \tag{10.9}$$

On each side of the equality, appears a term proportional to Σ. That on the left hand side comes from the $\frac{\delta G^{-1}}{\delta U}G$ contribution of the left hand side of (10.7), the second, on the right hand side, comes from the term $G^{-1}\frac{\delta G}{\delta U}$. After the cancellation of these two terms, what is left is the novel differential equation (10.6).

One can follow the same procedure without exploiting $G^{-1} = G_H^{-1} - \Sigma$ at the very beginning (equation (10.7)); in this case, the right hand side of equation (10.9) sums to $G^{-1}(15)\frac{\delta G(52)}{\delta U(34)}$, so the mutual cancellation is consequently hidden. In this case, what one gets by rearranging the terms, is the standard BSE

$$-\frac{\delta U(15)}{\delta U(34)}G(52) - \frac{\delta V_H(15)}{\delta U(34)}G(52) - \frac{\delta \Sigma(15)}{\delta U(34)}G(52) + G^{-1}(15)\frac{\delta G(52)}{\delta U(34)} = 0 \ .$$

This derivation shows that in the BSE the use of $-iGG = L^0$ introduces terms that must be partially cancelled by the kernel. The novel equation (10.6) is equivalent to BSE, but has the advantage that these mutual cancellations are accounted for from the beginning. The consequence of this cancellation is the introduction of the "asymmetric" independent-particle term $L^H = -iG_H G$.

Equation (10.8) suggests also an alternative formulation of the differential equation derived in the previous section. Using the chain rule in equality (10.8) and making use of the definitions of $\Xi(1234) = i\frac{\delta\Sigma(12)}{\delta G(34)}$ and $L(1234) = -i\frac{\delta G(12)}{\delta U(34)}$, one gets the relation

$$v(5678)\frac{\delta L(6234)}{\delta U(78)} = -G(62)\Xi(5678)L(7834) - i\Sigma(57)L(7234) \ .$$

Inserting now $\delta(82) = G^{-1}(86)G(62)$ into the last term, one can write the differential term of (10.6) as

$$iG^H(15)v(5678)\frac{\delta L(6234)}{\delta U(78)} = L^H(1256)\left[\Xi(5678) + i\Sigma(57)G^{-1}(86)\right]L(7834)$$

where the definition of $L^H(1234) = -iG^H(13)G(42)$ has been used.

The last relation defines a kernel

$$\Xi_I(5678) := \Xi(5678) + i\Sigma(57)G^{-1}(86) \tag{10.10}$$

which allows me to write the differential equation (10.6) in the form of a Dyson equation

$$L(1234) = L^H(1234) + L^H(1256)\left[v(5678) + \Xi_I(5678)\right]L(7834)\ . \tag{10.11}$$

The extra term $i\Sigma G^{-1}$ obtained in this approach corrects the "asymmetry" of L^H and restores the BSE.

These two derivations show that dynamical effects entering in $L^0 = -iGG$ are partially cancelled by dynamical effects entering in Ξ. This confirms what was observed by R. Del Sole and R. Girlanda [83] and F. Bechstedt and coworkers [90]. Moreover I showed that the novel differential accounts for these cancellations from the beginning, offering a natural framework to treat dynamical contributions on the same footing.

Finally, the last equation (10.11) allows for the definition of a dynamical kernel Ξ_I stemming from Σ, so the same approximations can in principle be done for the calculation of G and L. Though, I will not follow this strategy.

10.2 Solving the differential equation

Matrix form of the equation

Instead of working in the space domain, I switch to a transition-basis, as done in section 5.2.2 to solve the BSE . Being $\{\phi_i(\mathbf{r})\}$ a complete set of orthonormal functions (e.g. plane waves), we define an element of the transition-space basis as

$$\Phi_{ij}(\mathbf{r}_1, \mathbf{r}_2) := \phi_i(\mathbf{r}_1)\phi_j^*(\mathbf{r}_2) = |i_1, j_2\rangle\ .$$

On this basis, the following expansions are made

$$\begin{aligned} G^{(H)}(12) &= \textstyle\sum_{ab} G^{(H)}_{ab}(t_{12})\Phi_{ab}(\mathbf{r}_{12}) \\ L^{(H)}(1234) &= \textstyle\sum_{abcd} \Phi_{ab}(\mathbf{r}_{12})L^{(H)\,ab}_{\quad cd}(t_{1234})\Phi^*_{cd}(\mathbf{r}_{34}) \\ \frac{\delta}{\delta U(12)} &= \textstyle\sum_{ab} \frac{\delta}{\delta U_{ab}(t_{12})}\Phi^*_{ab}(\mathbf{r}_{12}) \end{aligned}$$

having defined

$$\begin{aligned} G^{(H)}_{ab}(t_{12}) &:= \textstyle\int G^{(H)}(12)\Phi^*_{ab}(\mathbf{r}_{12})d\mathbf{r}_{12} \\ L^{(H)\,ab}_{\quad cd}(t_{1234}) &:= \textstyle\int \Phi^*_{ab}(\mathbf{r}_{12})L^{(H)}(1234)\Phi_{cd}(\mathbf{r}_{34})d\mathbf{r}_{1234} \\ \frac{\delta}{\delta U_{ab}(t_{12})} &:= \textstyle\int \frac{\delta}{\delta U(12)}\Phi_{ab}(\mathbf{r}_{12})d\mathbf{r}_{12}\ . \end{aligned}$$

The Coulomb interaction $v(1234)$ follows the same expansion as $L(1234)$, as already pointed out in (5.51).

Consequently the differential equation (10.6) reads

$$\begin{aligned} L^{ab}_{cd}(t_{1234}) &= L^{H\,ab}_{\quad cd}(t_{1234}) + \\ &+ \int L^{H\,ab}_{\quad ef}(t_{1256}) v^{ef}_{gh}(t_{5678}) L^{gh}_{cd}(t_{7834}) dt_{5678} + \\ &+ i \int G^{H}_{ae}(t_{15}) v^{ef}_{hg}(t_{5678}) \frac{\delta L^{fb}_{cd}(t_{6234})}{\delta U_{gh}(t_{78})} dt_{5678} \end{aligned} \tag{10.12}$$

where equalities

$$\Phi^{*}_{gh}(\mathbf{r}_{34}) = \Phi_{hg}(\mathbf{r}_{43}) \quad \text{and} \quad v(\mathbf{r}_{1234}) = v(\mathbf{r}_{1243})$$

have been used in writing the differential term.

Approximations

To evaluate L^H, the best approximation to $G[U]$ has to be taken. To this aim, the exponential form of G introduced in [78] and used in [5] will be adopted because of the similarity of the approach followed by the authors and in force of the good results [5, 78] obtained with their method. To be consistent with this choice a decoupling approximation between states is assumed at the one-particle level, that is both G^H and G are assumed to be diagonal on the $\{\phi_i(\mathbf{r})\}_i$ basis. As a consequence also the matrix L^H is diagonal on the basis of the Φs.

Moreover I extend the **decoupling approximation to the two-particle correlation function** assuming that

$$L^{ab}_{cd}(t_{1234}) = L^{ab}_{ab}(t_{1234}) \delta_{ac} \delta_{db} \tag{10.13}$$

on the Φ-basis.

N.B. The experience we have from standard BSE tells us that the coupling between IP-transitions is crucial in the description of the excitonic effect, especially in solids, where the first order correction to the transition energies vanishes or, in other words, the contribution of diagonal elements is negligible. This is a sign of the many-body nature of the electron-hole interaction and it can not be neglected. From these considerations one need eventually to introduce approximations in order to relax this hypothesis, making the theory reliable for applications to real systems. For the moment we assume the decoupling between transitions in order to solve the equation for diagonal elements only. This will tell us much about the structure of the solution and the nature of cancellations.

With the decoupling approximation at the G and at the L level, the problem of solving a matrix equation (10.12) becomes that of solving one scalar equation for each independent-particle transition.

The exponential form of the Green's function, derived in [55] for the state l, reads

$$G_{ll}(t_{12}) = -i\theta(t_1 - t_2)\mathcal{G}^{e}_{ll}(t_{12}) + i\theta(t_2 - t_1)\mathcal{G}^{h}_{ll}(t_{12}) \tag{10.14}$$

where $\mathcal{G}^e$ is the electron Green's function, for which the state l is an empty conduction state, and $\mathcal{G}^h$ is the hole Green's function, with l labelling a valence state. In both cases[53]

$$\mathcal{G}^{e,h}_{ll}(t_1, t_2) = e^{i\varepsilon^{H}_{l}(t_2 - t_1)} e^{-i\frac{1}{2}\int_{t_1}^{t_2}\int_{t_1}^{t_2} W^{ll}_{ll}(tt')dxt'dt} e^{i\int_{t_1}^{t_2}\tilde{U}_{ll}(t)dt} \tag{10.15}$$

[53]Strictly speaking, when the external potential is time dependent, one should use non-equilibrium Green's

where ε_l^H is the Hartree energy of the state ϕ_l, W_{ll}^{ll} is the diagonal matrix element of the screened Coulomb interaction (5.52) and $\tilde{U} = \epsilon^{-1}U$ is the screened external potential [78].

The term $L^H = -iG^HG$ is therefore the sum of four terms corresponding to different orderings of the four time variables t_1, t_2, t_3 and t_4. Since we are interested in light absorption, i.e. only in *e-h* pairs, we neglect the particle-particle and hole-hole contributions, considering only the resonant and antiresonant components

$$L^H_{ab}(t_{1234}) = -i\theta(t_3 - t_1)\theta(t_4 - t_2)\mathcal{L}^{HR}_{ab}(t_{1234}) - i\theta(t_1 - t_3)\theta(t_2 - t_4)\mathcal{L}^{HA}_{ab}(t_{1234}) \,. \tag{10.16}$$

Because of the theta functions, only one term at once can be different from zero. If the non-vanishing term is the resonant term, then a is always a valence and b always a conduction state. If the antiresonant term is non-vanishing, then valence and conduction states are inverted with respect to the resonance case. To emphasize this difference I will use the letter v to label occupied states, and c for the empty states. The two independent particle terms read

$$\begin{aligned}
\mathcal{L}^{HR}_{vc}(t_{1234}) &= \mathcal{G}^H_{vv}(t_{13})\mathcal{G}_{cc}(t_{42}) && (10.17)\\
&= e^{-i\left[\varepsilon^H_c(t_4-t_2)-\varepsilon^H_v(t_3-t_1)\right]}e^{-i\left[\int_{t_2}^{t_4}\tilde{U}_{cc}(t)dt-\int_{t_1}^{t_3}\tilde{U}_{vv}(t)dt\right]}e^{-\frac{i}{2}\int_{t_2}^{t_4}W^{cc}_{cc}(t-t')dtdt'} \text{ and}\\
\mathcal{L}^{HA}_{cv}(t_{1234}) &= \mathcal{G}^H_{cc}(t_{13})\mathcal{G}_{vv}(t_{42}) && (10.18)\\
&= e^{i\left[\varepsilon^H_c(t_3-t_1)-\varepsilon^H_v(t_4-t_2)\right]}e^{i\left[\int_{t_1}^{t_3}\tilde{U}_{cc}(t)dt-\int_{t_2}^{t_4}\tilde{U}_{vv}(t)dt\right]}e^{-\frac{i}{2}\int_{t_4}^{t_2}W^{vv}_{vv}(t-t')dtdt'} \,.
\end{aligned}$$

The differential equation in principle couples the two terms, but we further assume the **decoupling between resonant and antiresonant contributions**. The two decoupled differential equations are then

$$\begin{aligned}
\mathcal{L}^R_{vc}(t_{1234}) &= \mathcal{L}^{HR}_{vc}(t_{1234}) + \\
&\quad - i\int_{\max\{t_1,t_2\}}^{\min\{t_3,t_4\}} \mathcal{L}^{HR}_{vc}(t_{1255})v^{vc}_{vc}\mathcal{L}^R_{vc}(t_{5534})dt_5 + \\
&\quad - \int_{t_1}^{t_3}\sum_{gh}\mathcal{G}^H_{vv}(t_{15})v^{vv}_{hg}\frac{\delta\mathcal{L}^R_{vc}(t_{5234})}{\delta U_{gh}(t_{55})}dt_5 && (10.19)\\
\mathcal{L}^A_{cv}(t_{1234}) &= \mathcal{L}^{HA}_{cv}(t_{1234}) + \\
&\quad - i\int_{\max\{t_3,t_4\}}^{\min\{t_1,t_2\}} \mathcal{L}^{HA}_{cv}(t_{1255})v^{vc}_{vc}\mathcal{L}^A_{cv}(t_{5534})dt_5 + \\
&\quad + \int_{t_3}^{t_1}\sum_{gh}\mathcal{G}^H_{cc}(t_{15})v^{cc}_{hg}\frac{\delta\mathcal{L}^A_{cv}(t_{5234})}{\delta U_{gh}(t_{55})}dt_5 && (10.20)
\end{aligned}$$

where we used the fact that $v(t_{1234}) = v\delta(t_1 - t_2)\delta(t_3 - t_4)\delta(t_1 - t_3)$. Both expressions are multiplied by the respective couple of θ-functions as in (10.16), so for a given time ordering only one of the two terms can be different from zero, as stated for the independent-particle term.

functions. All time integrals should then been interpreted as contour integrals. The structure of the equations is however unchanged, and since we are only interested in the $U \to 0$ result at the end, we do not specify this further. Moreover we omit to specify infinitesimal time differences, such as $U(t_{55^+})$ instead of $U(t_{55})$ in equation (10.17).

N.B. For the rest of the chapter, unless explicitly specified, I will discuss only the resonant equation (10.19). The argument used for its solution are in fact valid also in the antiresonant case.

10.3 The bare Coulomb equation (BCE)

To get a first understanding of the physics described by this equation and to gain insight into the different dynamical contributions carried by the single-particle propagations and the *e-h* interaction, I initially drop the differential term. Consequently the only dynamical screening appearing in the equation (10.19) is the contribution carried by the Green's function $\mathcal{G}_{cc}(t_{42})$ defining $\mathcal{L}_{vc}^{HR}(t_{1234})$.

Since I will work only with the resonant contribution for the *vc* transition, the superscript R and the subscript vc will be dropped for sake of simplicity.

Immediately one observes that it is possible to contract the time variables, taking $t_4 = t_3$ and $t_1 = t_2$. This reduces the equation to a 2-point problem whose solution is the (resonant) polarizability $\chi^R(t_{13}) = \mathcal{L}(t_{1133})$. The equation to solve reads

$$\mathcal{L}(t_{1133}) = \mathcal{L}^H(t_{1133}) - iv \int_{t_1}^{t_3} \mathcal{L}^H(t_{1155})\mathcal{L}(t_{5533})dt_5 \tag{10.21}$$

called bare Coulomb equation (BCE).

Moreover the limit $U \to 0$ can be already taken, so the equation is expressed at equilibrium. Because of the limit $U \to 0$, a single time-variable $\tau = t_3 - t_1$ can be introduced.

This would allow for an immediate reformulation of the equation in the frequency domain. The formulation of (10.21) in the frequency domain would be much simpler because the convolution becomes a simple product. However, I prefer to stay in the time domain in order to ease the comparison with the next results, where the transformation will be possible only at the end of the calculation.

10.3.1 Solution of the bare Coulomb equation

To solve equation (10.21), I first introduce the ansatz $\mathcal{L}(t_{1133}) = \mathcal{L}^H(t_{1133})y(t_{13})$. The resulting equation

$$y(t_{13}) = 1 - iv \int_{t_1}^{t_3} e^{i\mathcal{T}_c(t_5;t_{13})}y(t_{53})dt_5 \tag{10.22}$$

verifies the ansatz and constitutes an integral equation for y.

The integrated exponential of $i\mathcal{T}_c(t_5;t_{13})$, called from now on "wing term", is defined according to $\mathcal{T}_c(t_5;t_{13}) := \int_{t_3}^{t_5}\int_{t_5}^{t_1} W_{cc}^{cc}(t-t')dtdt'$ and it is depicted schematically in Figure 10.1. Its origin may be ascribed to the split of the full equation, suggesting that it is an artefact, but I do not have clear indications in this sense. In any case its presence does not alter the physical insight we will gain from solving the BCE[54].

Two methods have been devised to solve equation (10.22), one by differentiation and another by iteration. The former is presented in the following, the latter is the subject of Appendix A.

[54]Moreover, one can assume that its contribution is small and approximate consequently $e^{i\mathcal{T}} \approx 1$

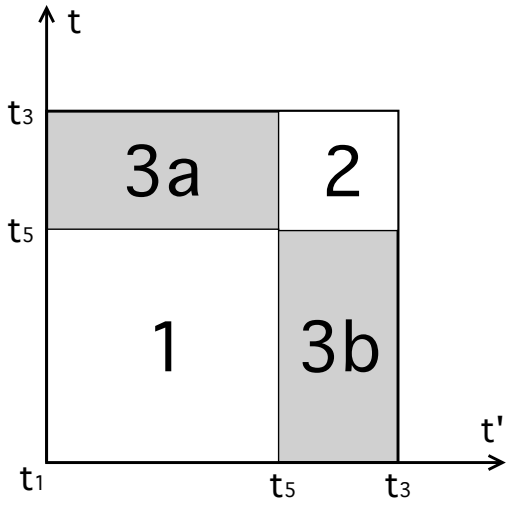

Figure 10.1: The difference $\int_{t_1}^{t_3}\int_{t_1}^{t_3} - \int_{t_1}^{t_5}\int_{t_1}^{t_5}$ is represented by the full square minus the area 1. Areas are labeled: $1 = \int_{t_1}^{t_5}\int_{t_1}^{t_5}$; $2 = \int_{t_5}^{t_3}\int_{t_5}^{t_3}$; $3a = \int_{t_1}^{t_5}\int_{t_5}^{t_3} dtdt'$ and $3b = \int_{t_5}^{t_3}\int_{t_1}^{t_5} dtdt'$. The integrals $3a$ and $3b$ are equal because of the symmetries of W. The grey area $3a + 3b = 2\mathcal{T}$ is the wing-term.

The differentiation of (10.22) with respect to t_1, is formally identical to the problem

$$\frac{df(t_3)}{dt_1} = \frac{d}{dt_1}\left[1 - iv\int_{t_1}^{t_3} f(t)h(t)dt\right] \quad \Longleftrightarrow \quad \frac{d\log[f(t_3)]}{dt_1} = ivh(t_1)$$

which is solved by the family of functions

$$f_C(t_3) = C\exp\left\{-iv\int_{t_1}^{t_3} h(t)dt\right\}$$

differing in the value of the constant C which can be fixed by specifying the the boundary conditions. The fact that $y(t_{11}) = 1 = f(t_1)$ fixes $C = 1$, leading to the solution

$$y(t_{13}) = \exp\left\{-iv\int_{t_1}^{t_3} e^{i\mathcal{T}_c(t;t_{13})}dt\right\} \ . \tag{10.23}$$

Another proof of the solution can be found in Appendix B.

Similar arguments can be followed also for the antiresonant equation (10.20) leading to a similar exponential form.

The total equilibrium solution is the sum of the resonant and antiresonant parts. The equilibrium ($U = 0$) polarizability depends on the only time difference $\tau = t_3 - t_1$ and is given by

$$\begin{aligned}\chi_{vc}(\tau) &= -i\theta(\tau)\chi^R_{vc}(\tau) - i\theta(-\tau)\chi^A_{cv}(\tau) = \\ &= -i\theta(\tau)e^{-i\Delta\varepsilon^H_{vc}\tau}e^{-\frac{i}{2}\int_0^\tau\int_0^\tau W^{cc}_{cc}(t-t')dtdt'}e^{-iv^{vc}_{vc}\int_0^\tau e^{i\mathcal{T}_c(t;\tau)}dt} + \\ &\quad - i\theta(-\tau)e^{i\Delta\varepsilon^H_{vc}\tau}e^{-\frac{i}{2}\int_0^\tau\int_0^\tau W^{vv}_{vv}(t-t')dtdt'}e^{iv^{vc}_{vc}\int_0^\tau e^{i\mathcal{T}_v(t;\tau)}dt}\end{aligned} \tag{10.24}$$

where the symmetry of the Coulomb potential $v^{vc}_{vc} = v^{cv}_{cv}$ has been used and the Hartree transition energy $\Delta\varepsilon^H_{vc} = \varepsilon^H_c - \varepsilon^H_v$ has been introduced.

10.3.2 Spectrum of the bare Coulomb solution

For each components (resonant and antiresonant) of the solution (10.24) one identifies three contributions.

IP-transitions : The independent-transition term $e^{\pm i\Delta\varepsilon^H_{vc}\tau}$ corresponds to the elementary transition from empty to occupied Hartree states.

Self-energy contribution : A single-particle screening term $\exp\{-i/2\int\int W^{jj}_{jj}(t-t')dtdt'\}$ with $j=v,c$ depending on the case, is carried by the fully interacting Green's function G in the definition of L^H. It is by construction the same exponential contribution as that obtained by M.Guzzo in [5, 78]. The physics embodied by this term is the full many-body interaction (with the restriction of the linear screening and the decoupling approximation) of the propagating particle within the medium. So it includes the quasiparticle correction, its broadening due to dynamical self-energy effects and the coupling with the other excitations of the system (e.g., plasmon satellites).

Electron-hole interaction : The third component is the electron-hole Hartree interaction v^{vc}_{vc}, also called *e-h* exchange term in the exciton language, which is modified by a phase factor (the wing term) The phase term depends on the quasiparticle propagation.

A clearer insight into the meaning of the BCE result is reached once the Fourier transform of the equilibrium solution is taken

$$\chi_{vc}(\tau)=\frac{1}{2\pi}\int\chi_{vc}(\omega)e^{-i\omega\tau}d\omega \quad \text{with} \quad \chi_{vc}(\omega):=F_\tau[\chi_{vc}](\omega)=\int\chi_{vc}(\tau)e^{i\omega\tau}d\tau \qquad (10.25)$$

The true Random Phase Approximation: W=0

The analysis of the spectral properties of the solution of the BCE starts from the approximation $W=0$. Neglecting the screened Coulomb interaction, implies a Hartree description in the propagation of both particles ($L^H\approx -iG^HG^H$) and the vanishing of the wing term. As a consequence the *e-h* pair interacts only through the classical Hartree interaction. The expression of the polarizability in this case corresponds to the RPA; it reads

$$\begin{aligned}\chi_{vc}(\tau)&=-i\theta(\tau)e^{-i\left(\Delta\varepsilon^H_{vc}+v^{vc}_{vc}\right)\tau}-i\theta(-\tau)e^{i\left(\Delta\varepsilon^H_{vc}+v^{vc}_{vc}\right)\tau}\\ \chi_{vc}(\omega)&=\left\{\frac{1}{\omega-(\Delta\varepsilon^H_{vc}+v^{vc}_{vc})+i\eta}-\frac{1}{\omega+(\Delta\varepsilon^H_{vc}+v^{vc}_{vc})-i\eta}\right\},\end{aligned}$$

where the infinitesimal positive quantity η assures convergence of the transformation.

The resonant part has a pole for the positive energy $E_R=\Delta\varepsilon^H_{vc}+v^{vc}_{vc}$ while the antiresonant has a negative-energy pole at $E_A=-(\Delta\varepsilon^H_{vc}+v^{vc}_{vc})$.

This term is for example responsible for the blue-shift of spectra due to the LFE or to he fact that EEL spectra have dominant structures at higher energies than absorption, as we have seen in the previous chapters.

Static screening approximation

The self-energy contribution $W^{ii}_{ii}(t-t')\approx 2W^s_i\delta(t-t')$ is approximated with an instantaneous response of intensity $2W^s_i$. The integrals of W in the resonant and antiresonant parts are

evaluated remembering that $\int_a^b f(x)\delta(x)dx = -f(0)$ if $a > b$. The wing term vanishes in both cases.

In the static approximation the polarizability in frequency domain reads

$$\chi_{vc}(\omega) = \left\{ \frac{1}{\omega - (\Delta\varepsilon^H_{vc} + v^{vc}_{vc} + W^s_c) + i\eta} - \frac{1}{\omega + (\Delta\varepsilon^H_{vc} + v^{vc}_{vc} + W^s_v) - i\eta} \right\} .$$

The RPA energies are shifted by a state-dependent quantity which is a many-body correction to the electron (resonant) or the hole (antiresonant) state. This static contribution corrects the Hartree energy ε^H_i adding static self-energy corrections which leads to a further blue-shift of the spectrum.

At this stage W is static inside Σ. Therefore no renormalization of the quasiparticle peak is included. Indeed the shift of the IP energies does not create extra excitations (i.e. no satellites), so no redistribution of the spectral weight occurs. The parallel with the GW+RPA approach discussed in section 5.2.1 is here evident: real (static) quaiparticle energies E^{QP} are substituted to independent-particle states (usually KS, in this case Hartree) and a simple RPA polarizability is computed to get the absorption spectrum.

Plasmon pole approximation

To perform analytically the integrals beyond the static approximation, I use a plasmon pole model for W in the self-energy contribution, while the wing term will be disregarded. In real time the plasmon pole model (PPM) reads

$$W^{ii}_{ii}(t-t') := -i\lambda_i \left[\theta(t-t')e^{-i\omega_i(t-t')} + \theta(t'-t)e^{i\omega_i(t-t')} \right] , \tag{10.26}$$

it has the advantage of keeping all time symmetries of the screening and to be analytically integrable. Hence, it is here introduced as a good approximation of W, in order to gain a qualitative understanding of the physics of the dynamical correlation.

Through the PPM, the self-energy contribution reads

$$\int_0^\tau \int_0^\tau W^{ii}_{ii}(t-t')dt'dt = 2i\frac{\lambda_i}{\omega_i^2} \times \begin{cases} (e^{-i\omega_i\tau} + i\omega_i\tau - 1) & \text{Resonant: } i = c \\ (e^{i\omega_i\tau} - i\omega_i\tau - 1) & \text{Anitresonant: } i = v \end{cases}$$

and the real time polarizability becomes

$$\begin{aligned} \chi_{vc}(\tau) = &-i\theta(\tau)e^{-\frac{\lambda_c}{\omega_c^2}} e^{-i(\Delta\varepsilon^H_{vc} + v^{vc}_{vc} - \lambda_c/\omega_c)\tau} e^{\lambda_c/\omega_c^2 e^{-i\omega_c\tau}} + \\ &- i\theta(-\tau)e^{-\frac{\lambda_v}{\omega_v^2}} e^{i(\Delta\varepsilon^H_{vc} + v^{vc}_{vc} - \lambda_v/\omega_v)\tau} e^{\lambda_v/\omega_v^2 e^{i\omega_v\tau}} . \end{aligned} \tag{10.27}$$

In the latter expression one recognises three different dynamical contributions.

Let us analyse for instance the resonant term.

1) A first real exponential of $-\lambda_c/\omega_c^2$ accounts for the quasiparticle renormalization and the shift of spectral weight to higher energy excitations.

2) The static contribution correcting the RPA transition energies with the quasiparticle corrections to the Hartree level is still present with the form $W^s_c = -\lambda_c/\omega_c$.

3) The third contribution, i.e. the double exponential, is responsible for the series of plasmon satellites shown in [5]. In the polarizability χ, it generates extra poles beyond the elementary excitation $E_c = \Delta\varepsilon^H_{vc} + v^{vc}_{vc} - \lambda_c/\omega_c$, as can be seen clearly by expanding the outer exponential in powers of λ.

For the resonant part one gets[55]

$$-i\theta(\tau)\chi^R_{vc}(\tau) = -i\theta(\tau)e^{-\frac{\lambda_c}{\omega_c^2}}e^{-i(\Delta\varepsilon^H_{vc}+v^{vc}_{vc}-\lambda_c/\omega_c)\tau}\left[1+\frac{\lambda_c}{\omega_c^2}e^{-i\omega_c\tau}+\frac{\lambda_c^2}{2\omega_c^4}e^{-i2\omega_c\tau}+O(3)\right]$$

$$\chi^R_{vc}(\omega) = e^{-\frac{\lambda_c}{\omega_c^2}}\left[\frac{1}{\omega-E_c+i\eta}+\right.$$
$$+\frac{\lambda_c}{\omega_c^2}\frac{1}{\omega-(E_c+\omega_c)+i\eta}+$$
$$\left.+\frac{\lambda_c^2}{2\omega_c^4}\frac{1}{\omega-(E_c+2\omega_c)+i\eta}+O(3)\right]\ . \tag{10.28}$$

The creation of an electron-hole pair costs an energy E_c if no additional excitation takes place. Instead, it costs $E_c+n\,\omega_c$ if n plasmon satellites are created together with the exciton. The important thing to stress here is that these extra excitations are not due to the creation of the electron-hole pair itself, but they are caused only by the propagation of the hole. In fact, in the resonant (antriesonant) term, L^H introduces dynamical correlation effects due uniquely to the hole (electron). In order to account in both terms for the the contributions due to the other particle and to the particle-pair, i.e. to account for a complete description of the dynamical effects induced by the exciton, the differential equation has to be solved.

Similarly, the renormalization term in front of expression (10.28) takes into account only the renormalization of the quasihole (or of the quasielectron in the antiresonant case).

The dynamical effects of the expression above stem entirely from the dynamical effects of the one-particle Green's function. In photoemission, the dynamical effects such that the renormalization, the quasiparticle corrections and the occurrence of satellites are all well described by the cumulant expansion of G. This result reflects the same physics in absorption and indeed the Green's function used here comes from the work of M. Guzzo who generalised the cumulant expansion proposing a new derivation.

The step further is to include these effects at the level of the e-h interaction, that is the topic of next section.

10.4 The Differential equation

Let us now pass to the dynamical part of equation (10.19). I neglect the Hartree term to focus on the differential contribution. Contrary to what done in the BCE, the contraction $t_1 = t_2$ can not be taken, although the other two times can be contracted $t_3 = t_4$ so that the number of variables is reduced to three. For the resonant part of the differential equation the equation to solve is

$$\mathcal{L}_{vc}(t_{1233}) = \mathcal{L}^H_{vc}(t_{1233}) - \int_{t_1}^{t_3}\sum_{gh}\mathcal{G}^H_{vv}(t_{15})v^{vv}_{hg}\frac{\delta\mathcal{L}_{vc}(t_{5233})}{\delta U_{gh}(t_{55})}dt_5\ . \tag{10.29}$$

[55]Note that the following definitions are used: $\chi(\tau) = -i\theta(\tau)\chi^R(\tau) - i\theta(-\tau)\chi^A(\tau)$ as introduced in (10.24) and $\chi(\omega) = \chi^R(\omega) + \chi^A(\omega)$.

10.4.1 From the differential operator to the dynamical screening

An iterative argument can be used to evaluate the differential operator. The 0-th iteration is taken for $\mathcal{L} = \mathcal{L}^H$, so the first order is obtained inserting $\mathcal{L}^H$ into the differential term.

I remind that the one-particle Green's function (10.15) is a known functional of the screened $\tilde{U}$, where $\tilde{U}_{ab}(t_{12}) := \int \epsilon^{-1\,ab}_{\ \ cd}(t_{1234}) U_{cd}(t_{34}) dt_{34}$, and that the equality $W^{ab}_{cd} = v^{ef}_{cd}\epsilon^{-1\,ab}_{\ \ ef} \equiv v^{cd}_{fe}\epsilon^{-1\,ab}_{\ \ ef}$ is verified in force of the symmetries of the Coulomb interaction. With this in mind, (10.29) becomes

$$\mathcal{L}_{vc}(t_{1233}) = \mathcal{L}^H_{vc}(t_{1233}) - \sum_{ij}\int_{t_1}^{t_3}\int \mathcal{G}^H_{vv}(t_{15}) W^{ij}_{vv}(t_{6655}) \frac{\delta \mathcal{L}_{vc}(t_{5233})}{\delta \tilde{U}_{ij}(t_{66})} dt_6 dt_5 \ .$$

To first order in W, this reads

$$\mathcal{L}^{(1)}_{vc}(t_{1233}) = \mathcal{L}^H_{vc}(t_{1233}) - \sum_{ij}\int_{t_1}^{t_3}\int \mathcal{G}^H_{vv}(t_{15}) W^{ij}_{vv}(t_{6655}) \frac{\delta \mathcal{L}^H_{vc}(t_{5233})}{\delta \tilde{U}_{ij}(t_{66})} dt_6 dt_5 \ .$$

The differential of $\mathcal{L}^H = \mathcal{G}^H\mathcal{G}$ is evaluated using the exponential Green's function (10.15). It is verified that

$$\frac{\delta \mathcal{L}^H_{vc}(t_{5233})}{\delta \tilde{U}_{ij}(t_{66})} = i\mathcal{L}^H_{vc}(t_{5233}) \left[\delta_{vi}\delta_{vj}\theta(t_5 - t_6)\theta(t_6 - t_1) - \delta_{ci}\delta_{cj}\theta(t_3 - t_6)\theta(t_6 - t_2)\right]$$

which leads to the following expression for the first iteration

$$\begin{aligned}
&\mathcal{L}^{(1)}_{vc}(t_{1233}) = \mathcal{L}^H_{vc}(t_{1233}) + \\
&- i\int_{t_1}^{t_3} \mathcal{G}^H_{vv}(t_{15})\mathcal{G}^H_{vv}(t_{53})\mathcal{G}_{cc}(t_{32}) \left[\int_{t_1}^{t_5} W^{vv}_{vv}(t_{6655}) dt_6 - \int_{t_2}^{t_3} W^{cc}_{vv}(t_{6655}) dt_6\right] dt_5 \ ,
\end{aligned}$$

where the substitution $\mathcal{L}^H = \mathcal{G}^H\mathcal{G}$ has been used in the last passage.

Using

$$\mathcal{G}^H_{aa}(t,t')\mathcal{G}^H_{aa}(t',t'') = \mathcal{G}^H_{aa}(t,t'') \ ,$$

a term $\mathcal{L}^H_{vc}(t_{1233})$ can be factored out from the integral, leading to a result of the kind $\mathcal{L}^{(1)} = \mathcal{L}^H(1 - i\int W + i\int W)$.

The screened Coulomb interaction W is taken at vanishing U, thus it does not depend on the external field and a formulation $\mathcal{L}^{(1)}_{vc}(t_{1233}) = \mathcal{L}^H_{vc}[U](t_{1233})\mathcal{F}^{(1)}_{vc}(t_{1233})$ is possible. Only the $\mathcal{L}^H[U]$ term depends on the external field U. It is clear that at any successive iteration, the differential operator will act on the first term only. Therefore a similar splitting

$$\mathcal{L}^{(N)}_{vc}(t_{1233}) = \mathcal{L}^H_{vc}[U](t_{1233})\mathcal{F}^{(N)}_{vc}(t_{1233}) \tag{10.30}$$

is possible at any order N.

10.4.2 Solution of the Dynamical equation

In force of conclusion (10.30) I make the following ansatz

$$\mathcal{L}_{vc}(t_{1233}) = \mathcal{G}^H_{vv}[U](t_{13})\mathcal{G}_{cc}[U](t_{32})\mathcal{F}_{vc}(t_{1233}) \ . \tag{10.31}$$

Inserting this ansatz into the differential equation (10.29) and following the same procedure as before, one gets to the equation

$$\mathcal{L}^H_{vc}(1233)\mathcal{F}_{vc}(t_{1233}) = \mathcal{L}^H_{vc}(1233)\left\{1 - i\int_{t_1}^{t_3} \mathcal{S}_{vc}(t_5;t_{123})\mathcal{F}_{vc}(t_{5233})dt_5\right\} \tag{10.32}$$

$$\text{having defined} \quad \mathcal{S}_{vc}(t_5;t_{123}) := \left[\int_{t_1}^{t_5} W^{vv}_{vv}(t_{6655})dt_6 - \int_{t_2}^{t_3} W^{cc}_{vv}(t_{6655})dt_6\right] . \tag{10.33}$$

Equation (10.32) satisfies the ansatz (10.31) and defines an integral equation for the dynamical contribution $\mathcal{F}$.

By differentiating both sides of equation (10.32) with respect to t_1 and by fixing the boundary conditions as done in the previous section, that is observing that equation (10.32) implies $\mathcal{F}(t_{1211}) = 1$, the dynamical equation can be solved. The resulting expression of the function $\mathcal{F}$ is

$$\mathcal{F}_{vc}(t_{1233}) = \exp\left\{-i\int_{t_1}^{t_3} \mathcal{S}_{vc}(t_5;t_{123})dt_5\right\} \quad \text{which gives}$$

$$\mathcal{F}_{vc}(t_{1233}) = \exp\left\{-i\int_{t_1}^{t_3}\int_{t_1}^{t_5} W^{vv}_{vv}(t_{6655})dt_6dt_5 + i\int_{t_1}^{t_3}\int_{t_2}^{t_3} W^{cc}_{vv}(t_{6655})dt_6dt_6\right\}$$

and similarly for the antiresonant component.

The solution to the dynamical equation is then $\mathcal{L} = \mathcal{L}^H\mathcal{F}$. At the end of the calculation the equilibrium solution can be taken in the limit $U \to 0$. Exploiting the time symmetries of W, one can substitute $\int_{t_1}^{t_3}\int_{t_1}^{t_5} W(t_{6655})dt_6dt_5 = \frac{1}{2}\int_{t_!}^{t_3}\int_{t_1}^{t_3} W(t_{6655})dt_6dt_5$ and the resonant part of the 2-particle correlation function finally reads

$$\begin{aligned}\mathcal{L}^{vc}_{vc}(t_{1233}) &= e^{-i\left[\varepsilon^H_c(t_3-t_1)-\varepsilon^H_v(t_3-t_1)\right]}e^{-\frac{i}{2}\int_{t_2}^{t_3}\int_{t_2}^{t_3} W^{cc}_{cc} - \frac{i}{2}\int_{t_1}^{t_3}\int_{t_1}^{t_3} W^{vv}_{vv} + i\int_{t_1}^{t_3}\int_{t_2}^{t_3} W^{cc}_{vv}} \\ &= \mathcal{G}_{vv}(t_{13})\mathcal{G}_{cc}(t_{32})e^{i\int_{t_1}^{t_3}\int_{t_2}^{t_3} W^{cc}_{vv}}\end{aligned} \tag{10.34}$$

where variables of integrations have been dropped to simplify the notation.

In the equilibrium limit ($U \to 0$), the contraction $t_1 = t_2$ can finally be done; the resulting polarizability is found to depend only on the time difference $\tau = t_3 - t_1$, as expected:

$$\begin{aligned}\chi_{vc}(\tau) = &-i\theta(\tau)e^{-i\Delta\varepsilon^H_{vc}\tau}e^{-\frac{i}{2}\int_0^\tau\int_0^\tau W^{cc}_{cc}(t-t')dtdt' - \frac{i}{2}\int_0^\tau\int_0^\tau W^{vv}_{vv}(t-t')dtdt'}\times \\ &\times e^{+i\int_0^\tau\int_0^\tau W^{cc}_{vv}(t-t')dtdt'} \quad + \\ &- i\theta(-\tau)e^{i\Delta\varepsilon^H_{vc}\tau}e^{-\frac{i}{2}\int_0^\tau\int_0^\tau W^{cc}_{cc}(t-t')dtdt' - \frac{i}{2}\int_0^\tau\int_0^\tau W^{vv}_{vv}(t-t')dtdt'}\times \\ &\times e^{+i\int_0^\tau\int_0^\tau W^{cc}_{vv}(t-t')dtdt'} .\end{aligned} \tag{10.35}$$

10.4.3 Discussion of the dynamical contributions

Let us look more in detail at the dynamical screened contributions

$$\mathcal{S}_{vc}(t_5;t_{123}) := \left[\int_{t_1}^{t_5} W^{vv}_{vv}(t_{6655})dt_6 - \int_{t_2}^{t_3} W^{cc}_{vv}(t_{6655})dt_6\right] \tag{10.36}$$

introduced above. As before, I take as example the resonant part.

The term W_{vv}^{vv} is the quasiparticle correction to the Hartree energy of the hole. This restores the electron-hole symmetry lost at the beginning with the introduction of $\mathcal{L}_{vc}^{H} = \mathcal{G}_{v}^{H}\mathcal{G}_{c}$. In fact a similar term W_{cc}^{cc} is carried by the $\mathcal{G}_c$ appearing in the definition of $\mathcal{L}^H$. I stress that these two contributions are one-particle terms: W_{vv}^{vv} (W_{cc}^{cc}) corresponds to the coupling of the creation of the hole (electron) with all neutral excitations of the system.

But the electron-hole pair, being of neutral charge, is expected to lower the effect of the two separated particles. The additional *e-h* term, that is the interference term between the electron and the hole, is described by the interaction contribution W_{vv}^{cc}. The opposite sign with respect to the quasiparticle contributions reminds to the partial cancellations of the dynamical effects already discussed in [83, 90] and reformulated in this thesis in section 10.1.1.

As done in discussing the solution of the BCE, the static and the plasmon pole approximations of W to the screening are now introduced.

Static screening approximation

Inserting the static screening $W_{ij}^{s}(t-t') = 2W_{jj}^{ii}\delta(t-t')$ into (10.35), the polarizability becomes

$$\begin{aligned}\chi_{vc}(\tau) &= -i\theta(\tau)e^{-i(\Delta\varepsilon_{vc}^{H}+W_{cc}^{s}+W_{vv}^{s}-2W_{cv}^{s})\tau} - i\theta(-\tau)e^{i(\Delta\varepsilon_{vc}^{H}+W_{cc}^{s}+W_{vv}^{s}-2W_{cv}^{s})\tau} \\ \chi_{vc}(\omega) &= \left\{\frac{1}{\omega - E_{vc} + i\eta} - \frac{1}{\omega + E_{vc} - i\eta}\right\}\end{aligned} \tag{10.37}$$

with elementary excitation energy

$$E_{vc} = (\varepsilon_{c}^{H} + W_{cc}^{s}) - (\varepsilon_{v}^{H} - W_{vv}^{s}) - 2W_{cv}^{s} \tag{10.38}$$

where one recognizes the independent particle (Hartree) energies, their state dependent correction due to quasiparticle effects, and the electron-hole contribution.

This result is the perfect analogue to what usually computed in the static BSE approach. G_0W_0 energies are used instead of Kohn-Sham eigenvalues, so the group $(\varepsilon_i^H + W_{ii}^s)$ is usually substituted by $(\varepsilon_i^{KS} + E_i^{G_0W_0})$, but the physics described here is exactly the same. The static electron-hole interaction appearing here W_{cv}^s is the same kind of matrix element W_{vv}^{cc} used in the static BSE calculations.

Plasmon pole approximation

Similarly to what done for the BCE, I now discuss the effect of dynamical correlation assuming the plasmon pole model (10.26) for each matrix element $W_{jj}^{ii}(t-t')$.

Once inserted into the time-dependent expression, the resonant part reads[56]

$$-i\theta(\tau)\chi_{vc}^{R}(\tau) = -i\theta(\tau)e^{-R_{vc}}e^{-iE_{vc}\tau}\exp\left\{\frac{\lambda_{cc}}{\omega_{cc}^2}e^{-i\omega_{cc}\tau} + \frac{\lambda_{vv}}{\omega_{vv}^2}e^{-i\omega_{vv}\tau} - 2\frac{\lambda_{vc}}{\omega_{vc}^2}e^{-i\omega_{vc}\tau}\right\} \tag{10.39}$$

[56] There is no difficulty in computing the antiresonant contribution, but formulae are then too cumbersome.

where the renormalization term R_{vc} and the elementary excitation energy E_{vc} are defined respectively

$$R_{vc} := \frac{\lambda_{cc}}{\omega_{cc}^2} + \frac{\lambda_{vv}}{\omega_{vv}^2} - 2\frac{\lambda_{vc}}{\omega_{vc}^2} \tag{10.40}$$

$$E_{vc} := \left(\varepsilon_c^H - \frac{\lambda_{cc}}{\omega_{cc}}\right) - \left(\varepsilon_v^H + \frac{\lambda_{vv}}{\omega_{vv}}\right) + 2\frac{\lambda_{vc}}{\omega_{vc}} \tag{10.41}$$

In the solution of the BCE, where only self-energy contributions of one particle (the hole in resonant case) were accounted for, the renormalization term had only one term. In contrast, when all dynamical contributions are included, the other particle gives symmetric contributions and, more important, interference effects appear in the form of a third term of inverse sign.

Similar considerations are valid for the extra poles and the quasi-static corrections to the Hartree level. In particular the structure of the extra poles is much more complex: already at the first order in W three extra poles are created. At higher orders mixed terms arise[57].

Order 0 (Resonant):

$$\chi_{vc}^{(0)}(\omega) = e^{-R_{vc}} \frac{1}{\omega - E_{vc} + i\eta}$$

Order 1 (Resonant):

$$\chi_{vc}^{(1)}(\omega) = e^{-R_{vc}} \left[-2\frac{\lambda_{vc}/\omega_{vc}^2}{\omega - (E_{vc} + \omega_{vc}) + i\eta} + \right.$$
$$\left. + \frac{\lambda_{cc}/\omega_{cc}^2}{\omega - (E_{vc} + \omega_{cc}) + i\eta} + \frac{\lambda_{vv}/\omega_{vv}^2}{\omega - (E_{vc} + \omega_{vv}) + i\eta} \right]$$

Order 2 (Resonant):

$$\chi_{vc}^{(2)}(\omega) = e^{-R_{vc}} \left[\frac{2\lambda_{vc}^2}{\omega_{vc}^4} \frac{1}{\omega - (E_{vc} + 2\omega_{vc}) + i\eta} + \right.$$
$$+ \frac{\lambda_{cc}^2}{2\omega_{cc}^4} \frac{1}{\omega - (E_{vc} + 2\omega_{cc}) + i\eta} + \frac{\lambda_{vv}^2}{2\omega_{vv}^4} \frac{1}{\omega - (E_{vc} + 2\omega_{vv}) + i\eta} +$$
$$+ \frac{\lambda_{cc}\lambda_{vv}}{\omega_{cc}^2\omega_{vv}^2} \frac{1}{\omega - (E_{vc} + \omega_{cc} + \omega_{vv}) + i\eta} +$$
$$\left. - \frac{2\lambda_{cc}\lambda_{vc}}{\omega_{cc}^2\omega_{vc}^2} \frac{1}{\omega - (E_{vc} + \omega_{cc} + \omega_{vc}) + i\eta} - \frac{2\lambda_{vv}\lambda_{vc}}{\omega_{vv}^2\omega_{vc}^2} \frac{1}{\omega - (E_{vc} + \omega_{vv} + \omega_{vc}) + i\eta} \right] \tag{10.42}$$

If all the poles are similar $\omega_{ij} \approx \tilde{\omega}$, then the term of order N has a pole at the energy $E_{vc} + N\tilde{\omega}$ and the weight of the corresponding structure is

$$e^{-\frac{(\lambda_{cc}+\lambda_{vv}-2\lambda_{vc})}{\tilde{\omega}^2}} \frac{(\lambda_{cc} + \lambda_{vv} - 2\lambda_{vc})^N}{\tilde{\omega}^{2N}} .$$

[57]Note that there may be cases where $\Im[\chi] < 0$; for instance if $(\omega_{vc} \neq \omega_{vv} \neq \omega_{cc})$, then $\Im[\chi^{(1)}] < 0$ in $\omega = E_{vc} + \omega_{vc}$. Most likely this problem disappears going beyond the plasmon pole approximation for W and once the decoupling approximation on transitions is relaxed (see 10.5).

10.4.4 Where dynamical effects are important?

From these results one can immediately see where dynamical effects will be important. Let us concentrate on the effect of the weights λ, differences in $\tilde{\omega}$ being a less pertinent quantity in the thermodynamic limit. Of course, effects are large when the λs are large, most importantly, however, is the fact that

$$\lambda_{cc} + \lambda_{vv} - 2\lambda_{vc}$$

is dominated by the difference of matrix elements of W involving different states: valence only (proportional to the Σ contribution to the valence states), conduction only (proportional to the Σ contribution to the conduction states), and the valence-conduction pairs (that governs e-h interaction matrix elements in the standard BSE). When these matrix elements are very similar there is perfect cancellation. Instead, when they are different, the main absorption peak will be damped and satellites will appear. One case that one may imagine is when valence and conduction states are localised in different spatial regions (e.g., in charge-transfer excitations). In this case, W^{cc}_{cc} and W^{vv}_{vv} should be significantly larger than W^{cc}_{vv}. This leads to self-energy effects that are relatively large compared to the electro-hole interaction effects. This can be of particular importance in nanostructures whose shape can be tailored to host and optimize specific processes.

10.5 Conclusions and perspectives

I have presented here a theoretical approach to include dynamical effects in the e-h interaction at the level of the two-particle correlation function L. The starting point is the differentiation of the Dyson equation of G with respect to an external field $U(1,2)$. The resulting differential term is not substituted by a kernel, but is kept in a differential form, leading to the linear integro-differential functional equation

$$\begin{aligned} L(1234) = &-iG_H(13)G(42)+ \\ &- iG_H(15)G(62)v(5678)L(7834)+ \\ &+ iG_H(15)v(5678)\frac{\delta L(6234)}{\delta U(78)} \,, \end{aligned} \tag{10.6}$$

where $\mathcal{G}^H$ and $\mathcal{G}$ are functionals of U.

The differential equation (10.6) can be cast in the form of a Dyson equation (10.9) where the kernel Ξ_I is defined in terms of the kernel of the BSE and the self-energy Σ. This way of writing allowed me to point out in a clean form (cfr. section 10.1.1) the occurrence of mutual cancellations between the dynamical BSE kernel and the self-energy. This result confirms what was already observed by other authors [83, 90, 91], and shows that the differential approach (10.6) is less affected by this issue thanks to the introduction of the "independent-particle" term $L^H = iG^HG$.

To solve the differential equation, two approximations have been introduced. The first is the exponential diagonal G (10.14) obtained by G. Lani [82] and M. Guzzo [78]. It relies on a diagonal G over the single-state basis. This has been proven to give excellent results in describing one-particle dynamical effects beyond the GW approximation, with no additional computational effort (see Ref.s [5, 78, 94] and Appendix D). The second approximation is

the decoupling approximation at the L level, which assumes L diagonal on the transition basis.

Within these approximations, I divided the problem of solving the equation (10.6), in solving a bare Coulomb equation (10.21), and a differential equation (10.29).

The solution of the bare Coulomb equation is carried out in section 10.3. It leads to a polarizability for the vc transition (10.24) where the dynamical effects are only of the one-particle kind. They include a renormalization of the spectral weight, a shift of the IP transition energies and the occurrence of additional peaks at higher energy due to the coupling with other excitations. This is clear when a plasmon pole model is inserted in the result (10.24), leading to the expression (10.28).

The differential equation (10.29), obtained from (10.6) by neglecting the bare Coulomb term, reads

$$\mathcal{L}_{vc}(t_{1233}) = \mathcal{L}^H_{vc}(t_{1233}) - \int_{t_1}^{t_3} \sum_{gh} \mathcal{G}^H_{vv}(t_{15}) v^{vv}_{hg} \frac{\delta \mathcal{L}_{vc}(t_{5233})}{\delta U_{gh}(t_{55})} dt_5 \ . \tag{10.29}$$

Following an iterative argument, I introduced and verified an ansatz for $\mathcal{L}$, exploiting the screened external potential appearing in the exponential G (10.14), I was finally able to solve the equation. The resulting polarizability reads

$$\chi_{vc}(\tau) = -i\theta(\tau) e^{-i\Delta\varepsilon^H_{vc}\tau} e^{-\frac{i}{2}\int_0^\tau\int_0^\tau W^{cc}_{cc}(t-t')dtdt' - \frac{i}{2}\int_0^\tau\int_0^\tau W^{vv}_{vv}(t-t')dtdt' + i\int_0^\tau\int_0^\tau W^{cc}_{vv}(t-t')dtdt'} \tag{10.35}$$

here reported for the resonant component only. This is the new result of the chapter and one of the main results of this thesis.

In obtaining the result above, dynamical contributions in the one-particle G and in the e-h interaction have been treated on the same footing and are summed to all perturbative orders in the screened Coulomb interaction W. These dynamical effects give rise to three terms

$$-\frac{i}{2}\int_0^\tau\int_0^\tau W^{cc}_{cc}(t-t')dtdt' - \frac{i}{2}\int_0^\tau\int_0^\tau W^{vv}_{vv}(t-t')dtdt' + i\int_0^\tau\int_0^\tau W^{cc}_{vv}(t-t')dtdt' \tag{10.43}$$

where the W^{ii}_{ii} are the one-particle contributions. The interference term W^{ii}_{jj} with $j \neq i$ arises uniquely from the dynamical contribution in the e-h interaction, it has opposite sign with respect to the other two terms and it has twice their weight. As a consequence, if there is no big difference between the three terms, dynamical effects in absorption would be negligible even when important at the G level.

This result is consistent with what published by F. Bechstedt et al. [90] who found to first order in W a similar interference term (5.62) looking at the dynamical correction to the spectral renormalization.

However, the result I obtained is more general because it includes dynamical effects at all orders in W, describing at the same time the renormalization of the absorption peaks, their shift (exciton binding) and the multiple excitations arising at higher energies. Moreover it does not repose on the GW approximation for the self-energy which may give a bad description of one-particle dynamical effects [5, 78].

On the other hand, as already pointed out, the decoupling approximation at the L level constitutes a big issue. Although it is a good starting point for the design of approximate methods, this approximation is not justified in solids because of one major problem: each

single matrix element W_{jj}^{ii} tends to 0 because of a factor $1/N_{\mathbf{k}}$ (see expression (5.52)). Hence formulae have to be reinterpreted in terms of "effective matrix elements". Otherwise, and to be really predictive, one has to go beyond this approximation in order to apply this approach to calculations in real systems.

Some possible way out to this problem has been explored in this thesis. What is finally needed to compute optical spectra is

$$L_{\mathbf{G}=0\mathbf{G}'=0}(\mathbf{q},\omega) = \sum_{ijkl} \tilde{\rho}_{ij}(\mathbf{q})\tilde{\rho}^{*}_{kl}(\mathbf{q})L^{ij}_{kl}(\omega) \ .$$

The sum over all transitions, that is proportional to $N_{\mathbf{k}}^2$, cures the $1/N_{\mathbf{k}}$ problem. To use this fact, one has to derive an expression for off-diagonal elements of L, and $\delta L/\delta U$. The decoupling approximation at the single-particle level is inherited by the $\delta L/\delta U$ term, which has the effect of making diagonal the whole equation.

When the decoupling approximation at the G level is not applied to the differential term, approximations inspired on the RPA ($L = -iG^H G^H$) lead to an expression that includes dynamical off-diagonal effects evaluated on the basis of quantities one is able to compute with nowadays simulation software.

It seems therefore possible to generalise my results in order to include off-diagonal elements and to allow for quantitative calculations in real materials. The work I made is therefore a promising approach to give quantitative predictions of multiple exciton generation and other dynamical effects interesting for fundamental questions and for technological applications such as the production of solar energy.

Chapter 11

Conclusions

This work has been developed as part of a project whose goal is the enhancement of the efficiency of solar cell devices. To this aim two joint aspects can be tackled:
1) taking benefit from the new and tunable properties of nanostructures, and
2) increasing the efficiency of light absorption through the generation of several *e-h* pairs from a single absorbed photon (multiple exciton generation: MEG).

My thesis is a fundamental work which addresses these two aspects in the framework of *ab-initio* theories, and more specifically within the formalism of the many-body perturbation theory (MBPT). At a theoretical level, the description of MEG necessarily requires the inclusion of dynamical effects in the *e-h* interaction. In the MBPT they are in principle accounted for by the dynamical kernel $\delta\Sigma(1,2)/\delta G(3,4)$ (see (5.45)) of the Bethe-Salpeter equation (BSE), but in practical implementations dynamical effects are most often neglected and it is very difficult to include them properly. It is therefore worthwhile to look for an alternative to the dynamical BSE.

Moreover most of the calculations of optical spectra are performed with the codes DP [127] and EXC [86], both developed in the framework of the ETSF [173]. These codes make use of plane-waves basis set, which are extremely efficient for bulk systems. One of the challenges is to devise methods allowing to keep this efficiency in the description of isolated systems. In fact, the calculation of electronic properties of isolated systems with plane-wave codes is cumbersome because, in order to isolate the replicas of the simulation cell, one needs to increase the size of the cell through the addition of empty space. This method has the drawback that many convergence parameters (dimension of the basis, bands, matrix dimension) increase accordingly, until a point where calculations are not feasible any more even though replicas are still interacting (that is the case of Fig. 8.7). One question I addressed in my work is:
"*Is it possible to devise and set up a method to isolate the repeated replicas within reasonable convergence parameters? And if so, how does it affect the dynamical contributions determining the spectrum?*"

The dynamical BSE has been the subject of several works (see section 5.2.3), but in most of these approaches, the dynamical *e-h* interaction has been included only to limited order in the screened Coulomb interaction W (most often only to the first order). Moreover each work focuses on specific spectral features (multiple excitations, renormalization of the intensity), whereas the spectrum must be known over a wide range of energies if one aims to application in solar energy production. So, the second question I addressed in this work is:

"Can we devise a method to predict the optical spectrum in a wide range of energies, allowing for the dynamical coupling of electron-hole pairs with the other excitations of the system?"

From graphite to graphene

Graphene is an almost 2D crystal of carbon atoms arranged on a honeycomb lattice. It can be rolled to build nanotubes or manipulated to obtain nanostructures of various shapes. It is therefore a versatile building block for many possible technological applications. For instance carbon nanotubes [12], graphene layers [174] or carbon nanotowires [175] have been used to assemble solar cells of promising performances. The closest bulk system to graphene is graphite.

I studied the transition from graphite to graphene of the EEL spectra and the spectral function by increasing the empty space between different layers. The system is considered at convergence to the isolated graphene where the condition EELS = absorption is met, that is

$$v_{\mathbf{00}}\bar{\chi}_{\mathbf{00}} = \frac{\chi_{\mathbf{00}}v_{\mathbf{00}}}{1+v_{\mathbf{00}}\chi_{\mathbf{00}}} \approx v_{\mathbf{00}}\chi_{\mathbf{00}} \ . \tag{4.30}$$

Looking at perpendicular components (Fig. 8.8), the convergence to the isolated system is reached with a moderate interlayer distance ($d \approx 6d_0$). The dimension of the system is anyway high because of the great number of k-points that are needed to sample the BZ along the k_z direction (see Tab. 8.2). Instead, for parallel components (Figs. 8.6 and 8.7), condition (4.30) is met only for large momenta (see also [19]). In particular, EELS converges extremely slowly for small parallel momentum because of the divergent Coulomb term in $\epsilon^{-1} = 1 + v\chi$.

I demonstrated that small-momentum components of $\epsilon^{-1}_{\mathbf{GG'}}(\mathbf{q})$ do not dominate the convergence of the spectral function. This is because all the matrix elements of $W_{\mathbf{GG'}}(\mathbf{q}) = \epsilon^{-1}_{\mathbf{GG'}}(\mathbf{q})v_{\mathbf{G'}}(\mathbf{q})$ mix in the self-energy

$$\begin{aligned}&\langle i|\Sigma(\mathbf{r},\mathbf{r}',\omega)|i\rangle = \\ &\quad = \frac{i}{(2\pi)^4}\sum_{\mathbf{GG'}j}\int e^{-i\delta\omega'}\int \frac{\tilde{\rho}^*_{ji}(\mathbf{q}+\mathbf{G})W_{\mathbf{GG'}}(\mathbf{q},\omega')\tilde{\rho}_{ji}(\mathbf{q}+\mathbf{G'})}{\omega-\omega'-E_j+i\,\mathrm{sign}(E_j-\mu)}d\mathbf{q}d\omega' \ ,\end{aligned} \tag{7.1}$$

hence also large-momentum and perpendicular components, which converge faster, contribute.

For this reason, in computing spectral functions, a system with interlayer distance $d = 2d_0$ fulfils the criteria.

In the context of this work, I took part in two experimental sessions at the beamline TEMPO [6] in the synchrotron light source Soleil, to collect photoemission data from the valence bands of graphite and graphene samples. (see Appendix D).

Isolating nanostructures

To prevent the interaction between repeated replicas in a more efficient way, I set up the Coulomb cutoff method.

I demonstrated that this method allows for efficient calculations of EELS and spectral functions of the isolated system with a reduced computational effort.

Condition (4.30) is met at all exchanged momenta (small- and large-) and in both the parallel (Fig. 9.2) and the perpendicular (Fig. 9.3) configurations, for a system which is only $d = 2d_0 + CC$ and whose the Brillouin zone has been sampled only with $k_z = 0$ points. I showed that the Coulomb cutoff method in an improvement on supercell calculations also for spectral functions (Fig. 9.4). The $2d_0 + CC$ computed with only in-plane points ($k_z = 0$) gives perfectly converged spectra. The use of the Coulomb cutoff method also improves on the $d = 1d_0$ system (see Fig. 9.5). The requirement of working with ($z_0 = L_z/2$) + ($k_z = 0$ plane), is not only a technical aspect: my results on the spectral function of the $1d_0$ and the $1d_0 + CC$ fully validate this prescription, offering physical arguments to justify the limitation to the in-plane sampling of the BZ. By taking only Fourier components in the plane, one actually selects only the electrons propagating parallel to the plane, and describes their properties by means of the cutoff function to isolate them from the other replicas.

I implemented important modifications in the codes DP and EXC. These simulation codes are daily used by many researchers. Amongst the added features, the most important are:

- the implementation of the Coulomb cutoff expression (9.20) in the calculation of the RPA dielectric matrix $\epsilon^{-1}_{\mathbf{GG'}}(\mathbf{q}, \omega)$, together with the implementation of the external perturbation correction (EPC) (equation 9.10) which can be enabled at will by the user,

- the inclusion of the whole calculation from χ^{KS} to ϵ^{-1} inside a loop over all possible $\mathbf{q}$ points compatible with the k-point grid,

- the production of files of format ".SCR" and ".CFT" containing the dielectric matrix and the cutoff function. The first of the two can be read by ABINIT vers.6 with no supplementary modification required to the user. The second file to be used requires minor modification on ABINIT.

Moreover I implemented some tests to ensure the stability of these modifications, for example by means of internal checks to prevent contradiction between input variables.

The limits of standard approximations...

I have conducted a detailed study of the absorption spectrum of $SrTiO_3$ using state of the art techniques in the frameworks of the time-dependent density functional theory and the many-body perturbation theory. I compared my results with experimental data [109, 120]. Structures of interest are found in the range 0-15 eV (direct experimental gap = 3.75 eV), where the RPA calculation reproduces the experiment within the limits of this theory (cfr. Fig. 6.7). I included the *e-h* interaction by solving the BSE in the standard implementation, that implies a static and diagonal approximation for the screened Coulomb interaction

$$W_{\mathbf{GG'}}(t - t') \approx W_{\mathbf{GG}}\delta_{\mathbf{GG'}}\delta(t - t') \; . \tag{11.1}$$

The absorption onset is very well reproduced, demonstrating the presence of important excitonic effects in the system. At higher energy excitonic effects predicted by BSE are overestimated (cfr. Fig. 6.9). This overestimation is striking in two structures: a strong and narrow peak at 6.4 eV, corresponding to a step-like bump at ~ 7 eV in experimental spectra,

and a broader group of excitations located around 8 eV which are red-shifted in the BSE spectrum by about 1 eV with respect to the experiments (structures B_b and C_b in Fig. 6.11a).

The analysis I conducted of the BSE spectra allowed me to identify the IP transitions concurring in the creation of the sharp peak, and to point out the different role played in the optical transitions by Ti $3t_{2g}$, Ti $3e_g$ and Sr $4d$ electrons in relation with their localised (or not) character. The remaining discrepancies allowed me to put into evidence the necessity to go beyond standard approximations to get a reliable spectrum. This result has been obtained by partially relaxing the diagonal-$W_{\mathbf{GG}'}$ approximation (11.1), and by using instead a (static) matrix $W_{\mathbf{GG}'}\delta(t-t')$ which better takes into account the inhomogeneities of the electronic response. To improve further the agreement with experiments, most likely one also has to go beyond the static approximation, but a feasible dynamical theory of absorption is needed first.

...and developments towards a dynamical theory

I derived the equation of motion for the two-particle correlation function L

$$\begin{aligned} L(1234) = & -iG_H(13)G(42)+ \\ & - iG_H(15)G(62)v(5678)L(7834)+ \\ & + iG_H(15)v(5678)\frac{\delta L(6234)}{\delta U(78)} \ . \end{aligned} \tag{10.6}$$

It accounts for dynamical effects at the single-particle and at the two-particle level through a differential operator. The strategy has been inspired by the recent works by G. Lani [55, 82] and M. Guzzo [5, 78, 94] conducted in the LSI theoretical spectroscopy group. The underlying philosophy is to get rid of the self-energy operator and to substitute it with its definition instead. This is a functional operator formulated in terms of the Coulomb interaction v and the differential of G with respect to an external field U.

The resulting equation (10.6) is equivalent to the general BSE (5.44). This is shown by casting (10.6) in the form of a Dyson equation

$$L(1234) = L^H(1234) + L^H(1256)\left[v(5678) + \Xi_I(5678)\right] L(7834) \tag{10.11}$$

where the kernel

$$\Xi_I(5678) := \Xi(5678) + i\Sigma(57)G^{-1}(86) \tag{10.10}$$

can be expressed in terms of the self-energy Σ and the dynamical BSE kernel Ξ. This allowed me to point out some mutual cancellations between dynamical effects in Σ and Ξ [83, 90, 91] and to show that in the differential equation (10.6) these cancellations are partially taken into account from the very beginning by the introduction of the "asymmetric" independent particle term $L^H = -iG^HG$.

I solved (10.6) by employing an exponential form of G [78, 82] and by assuming the decoupling between optical transitions.

In equation (10.35)

$$\begin{aligned} \chi_{vc}(\tau) = & -i\theta(\tau)e^{-i\Delta\varepsilon^H_{vc}\tau}e^{-\frac{i}{2}\int_0^\tau\int_0^\tau W^{cc}_{cc}(t-t')dtdt' - \frac{i}{2}\int_0^\tau\int_0^\tau W^{vv}_{vv}(t-t')dtdt'}\times \\ & \times e^{+i\int_0^\tau\int_0^\tau W^{cc}_{vv}(t-t')dtdt'} \quad + \\ & - i\theta(-\tau)e^{i\Delta\varepsilon^H_{vc}\tau}e^{-\frac{i}{2}\int_0^\tau\int_0^\tau W^{cc}_{cc}(t-t')dtdt' - \frac{i}{2}\int_0^\tau\int_0^\tau W^{vv}_{vv}(t-t')dtdt'}\times \\ & \times e^{+i\int_0^\tau\int_0^\tau W^{cc}_{vv}(t-t')dtdt'} \end{aligned} \tag{10.35}$$

I report the resulting polarizability for the $v \to c$ transition. In this expression three dynamical contributions are recognized: two one-particle terms W_{cc}^{cc} and W_{vv}^{vv}, depicting the propagation of the two particles in the many-body environment, and a third contribution W_{vv}^{cc} describing the interference arising from the dynamical *e-h* interaction.

In this result, dynamical effects are summed to all orders in W. I showed that partial mutual cancellation between one-particle and two-particle dynamical effects are accounted from the beginning in the equation (10.6). The two contributions are treated on the same footing throughout the entire derivation, which is necessary not to spoil the account for these cancellations. The resulting polarizability includes at once the renormalization of the peaks, the excitonic correction to the QP energies and the occurrence of extra structures in the optical spectrum, as depicted in the formulae at page 160.

The final result can suggest where dynamical effects should be strong and when their cancellation would enable to neglect them instead. This gives precious hint for materials design, for example in the domain of photovoltaics where multiple exciton generation (MEG) is desirable. In order to become a true *ab-initio* theory, however, one has to overcome the approximation of decoupled transitions, since single matrix elements tend to zero in the thermodynamic limit. We have explored this issue, and we are currently working on a promising expression that goes beyond the decoupling approximation.

Appendix A

Solution by iteration of the bare Coulomb equation

It is easy to verify that the N-th iteration of equation (10.22) reads

$$y^{(N)}(t_0, T) = \sum_{j=0}^{N} (-iv)^j I_j(t_0, T) \tag{A.1}$$

where the integral I_j is a series of j chained integrals of the kind

$$I_j(t_0, T) := \underbrace{\int_{t_0}^{T} f(t_1) \left[\int_{t_1}^{T} f(t_2) \left[\dots \left[\int_{t_{j-1}}^{T} f(t_j) dt_j \right] \dots \right] dt_2 \right] dt_1}_{j \text{ chained integrals}}$$

The 0-th order imposes the definition $I_0 = 1$.

One can demonstrate by induction that

$$I_j(t_0, T) = \frac{1}{j!} \left[\int_{t_0}^{T} f(t) dt \right]^j \tag{A.2}$$

assuming the integrability of function f between the limits t_0 and T.

The primitive of f reads

$$F(t) = \int_{t}^{T} f(t') dt' + C(T)$$

where C is a constant value which is fixed by the boundary conditions.

In the case $j = 1$ the equality (A.2) is obviously satisfied, so we need to demonstrate its

validity for the $j+1$ order, assuming it valid for the j-the order:

$$\begin{aligned}
&\int_{t_0}^{T} f(t_1)\left[\dots\left[\int_{t_j}^{T} f(t_{j+1})dt_{j+1}\right]\dots\right]dt_1 = \\
&= \frac{1}{j!}\int_{t_0}^{T} f(t_1)[F(T)-F(t_1)]^j dt_1 \\
&= \frac{1}{j!}\sum_{k=0}^{j}(-1)^k\binom{j}{k}F(T)^k\int_{t_0}^{T} f(t_1)F(t_1)^{j-k}dt_1 \\
&= \frac{1}{(j+1)!}\left\{[F(T)-F(t_0)]^{j+1} - F(t_0)^{j+1}\sum_{k=0}^{j+1}(-1)^k\binom{j+1}{k}\right\}
\end{aligned}$$

By observing that

$$0 = 0^{j+1} = (1-1)^{j+1} = \sum_{k=0}^{j+1}(-1)^k\binom{j+1}{k}, \tag{A.3}$$

the demonstration is concluded.

Inserting equality (A.2) into the expression (A.1), the solution to the bare Coulomb equation is finally found by taking the limit for $N \to \infty$

$$y(t_{t_0,T}) = \sum_{j=0}^{\infty}\frac{1}{j!}\left[-iv\int_{t_0}^{T} e^{i\mathcal{T}_c(t;t_{24})}dt\right]^j = \exp\left\{-iv\int_{t_0}^{T} e^{i\mathcal{T}_c(t;t_0,T)}dt\right\} \tag{A.4}$$

which is equal to the solution (10.23).

Appendix B

Proof of the solution

In this Appendix I prove that $L = L^H y$ with y given by (10.17) and (10.18) is indeed solution of the bare Coulomb equation. I substitute the solution $L = L^H y$ into the bare Coulomb equation and I get

$$L^H(t_{1234})e^{-i\hat{v}(t_{1234})} = L^H(t_{1234}) - iv\int L^H(t_{1255})L^H(t_{5534})e^{-i\hat{v}(t_{5534})}dt_5 \tag{B.1}$$

where

$$\hat{v}^{vc}_{vc}(t_{1234}) = \begin{cases} v^{vc}_{vc}\int_{\max\{t_1,t_2\}}^{\min\{t_3,t_4\}} e^{i\mathcal{T}_c(t;t_{24})}dt & \text{for resonant} \\ v^{vc}_{vc}\int_{\max\{t_3,t_4\}}^{\min\{t_1,t_2\}} e^{i\mathcal{T}_v(t;t_{24})}dt & \text{for antiresonant} \end{cases} . \tag{B.2}$$

Resonant and antiresonant part are decoupled because of the assumption of the Tamm-Dancoff approximation. I will give the prove for the resonant part only, since the same arguments are valid also for the antiresonant part.

The equality (B.1) is satisfied it is satisfied at every order of an expansion in powers of v. By expanding $\exp\{\hat{v}\}$, the equation (B.1) for the resonant part reads:

$$\begin{aligned} &\mathcal{L}^H(t_{1234})\left\{\sum_N \frac{[-i\hat{v}(t_{1234})]^N}{N!}\right\} = \\ &= \mathcal{L}^H(t_{1234}) - iv\int_{\max\{t_1,t_2\}}^{\min\{t_3,t_4\}} \mathcal{L}^H(t_{1255})\mathcal{L}^H(t_{5534})\left\{\sum_N \frac{[-i\hat{v}(t_{5534})]^N}{N!}\right\}dt_5 , \end{aligned} \tag{B.3}$$

having in mind that all the equation is multiplied by a time-ordering term $\theta(t_3-t_1)\theta(t_4-t_2)$.

In the integrand of the right hand side a term $\mathcal{L}^H(t_{1234})$ can be put in evidence by exploiting the fact that

$$\mathcal{L}^H(t_{1255})\mathcal{L}^H(t_{5534}) = \mathcal{L}^H(t_{1234})e^{i\mathcal{T}_c(t_5;t_{24})} . \tag{B.4}$$

I recall the definition of $\mathcal{T}_k(t;t_{12}) = \int_{t_2}^{t}\int_{t}^{t_1} W_k(\tau,\tau')d\tau' d\tau$. Consequently the bare Coulomb equation now reads

$$\sum_N \frac{[-i\hat{v}(t_{1234})]^N}{N!} = 1 - iv\int_{\max\{t_1,t_2\}}^{\min\{t_3,t_4\}} e^{i\mathcal{T}_c(t_5;t_{24})}\left\{\sum_N \frac{[-i\hat{v}(t_{5534})]^N}{N!}\right\}dt_5 , \tag{B.5}$$

having factorised a term $\mathcal{L}^H(t_{1234})$ from both sides of the equation.

The N-th term of the expansion in the right hand side depends on the (N+1)th power of v, so the equation is verified if

$$\frac{[-i\hat{v}(t_{1234})]^{N+1}}{(N+1)!} = -iv \int_{\max\{t_1,t_2\}}^{\min\{t_3,t_4\}} e^{i\mathcal{T}_c(t_5;t_{24})} \left\{ \frac{[-i\hat{v}(t_{5534})]^N}{N!} \right\} dt_5 \tag{B.6}$$

is true for all N.

By introducing the notation:

$$t_0 = \max\{t_1, t_2\} \tag{B.7}$$
$$B = \min\{t_3, t_4\} \tag{B.8}$$
$$f(t) = e^{i\mathcal{T}_c(t;t_{24})} \tag{B.9}$$
$$F(t) = \text{Primitive of } f(t)\ , \tag{B.10}$$

the previous problem can be written as

$$\frac{(-iv)^{N+1}}{(N+1)!} \left[\int_{t_0}^{B} f(t)dt \right]^{N+1} = \frac{(-iv)^{N+1}}{N!} \int_{t_0}^{B} f(t) \left(\int_{t}^{B} f(t')dt' \right)^N dt\ , \tag{B.11}$$

or, that is equivalent,

$$\frac{1}{N+1} \left[\int_{B}^{t_0} f(t)dt \right]^{N+1} = \int_{B}^{t_0} f(t) \left(\int_{B}^{t} f(t')dt' \right)^N dt\ . \tag{B.12}$$

In Appendix B, in force of (A.3), I demonstrated that

$$I_{N+1}(t_0, B) = \frac{1}{(N+1)!} \left[\int_{B}^{t_0} f(t)dt \right]^{N+1} \tag{B.13}$$

where $I_{N+1} = \int_B^{t_0} f(t_1) \left[\ldots \left[\int_B^{t_N} f(t_{N+1})dt_{N+1} \right] \ldots \right] dt_1$. By inserting this equality into the equation (B.12), the latter is proven at any order N which concludes the demonstration.

Appendix C

Singularity at the origin of the Coulomb cutoff matrix elements of W

For the calculation of self-energy matrix elements and for the BSE kernel, one needs the matrix elements of W (9.12). To get to this expression integrals in $\mathbf{q}$ and sums over $\mathbf{G}$ and $\mathbf{G}'$ have been split into different terms. Except for the integral enclosing the origin, all terms have been approximated as in (9.23), taking them equal to a constant value times the integrated volume (cfr. also footnote 49). This procedure is standard for points with non-null parallel components, whereas for points on the k_z axis, this is justified by the employ of the Beigi's prescription. At the end of the manipulation the only term to be treated by hand is

$$I_{sz} = \int_{-\pi/L_z}^{\pi/L_z} dq_z \int_{\mathcal{A}_0} d\mathbf{q}_\parallel y(\mathbf{q}_\parallel, q_z, 0, 0)$$

which encloses the origin (cfr. equation (9.24)). In order to perform the integration in q_z, I used the fact that in isolated systems the height of the BZ shrinks to 0, justifying the expression

$$I_{sz} \approx \frac{2\pi}{L_z} \int_{\mathcal{A}_0} d\mathbf{q}_\parallel y(\mathbf{q}_\parallel, 0, 0, 0) = \frac{2\pi}{L_z} I_{\text{sz}}^{\parallel}$$

which is the term appearing in equation (9.26) concluding section 9.1.2.

In this appendix I treat the problem of how to compute the planar integral

$$I_{\text{sz}}^{\parallel} = \int_{\mathcal{A}_0} d\mathbf{q}_\parallel y(\mathbf{q}_\parallel, 0, 0, 0) \ . \tag{C.1}$$

This problem has not be addressed in chapter 9.

Analytic integral at vanishing $\mathbf{q}_\parallel$

The problem in evaluating (C.1) comes from the divergence of the CC interaction. In fact, the FC inverse dielectric function $\check{\tilde{\epsilon}}^{-1}$, and the Bloch integrals $\tilde{\rho}$ are well behaved also at the origin. We can extract them from the integration following similar arguments to those used for (9.23):

$$I_{\text{sz}}^{\parallel} \approx \tilde{\rho}_{ij}^{*}(0) \check{\tilde{\epsilon}}_{\mathbf{00}}^{-1}(0,\omega) \tilde{\rho}_{mn}(0) \ 4\pi \int_{\mathcal{A}_0} \frac{f_C(\mathbf{q}_\parallel)}{q_\parallel^2} dq_x dq_y = \tilde{\rho}_{ij}^{*}(0) \check{\tilde{\epsilon}}_{\mathbf{00}}^{-1}(0,\omega) \tilde{\rho}_{mn}(0) I_0 \ . \tag{C.2}$$

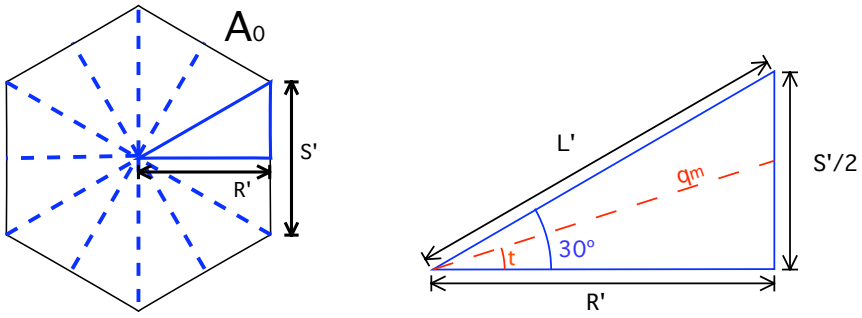

(a) $\mathcal{A}_0$ **(b)** Small triangle inside $\mathcal{A}_0$

Figure C.1: Geometry of the analytic integral of long-range CC on the $\mathcal{A}_0$ area which is centred on the origin.

The area $\mathcal{A}_{\text{BZ}}$ of the BZ is an hexagon of side $S = b/\sqrt{3}$ where b is the length of the unitary vector $b = 4\pi a^{-1}/\sqrt{3}$ and a is the parameter of the unitary cell. The radius of the inscribed circle $R = b/2$.

If a $M_{xy} \times M_{xy} \times 1$ grid is used to sample the BZ, the area $\mathcal{A}_0$ is an hexagon of side $S' = S/M_{xy}$ and radius of the inscribed circle $R' = R/M_{xy}$. The geometry is reported in Fig. C.1a.

At convergence with the $\mathbf{k}_\parallel$-point sampling, the longest value of $q_\parallel = L'$ can be considered small enough for the CC interaction to be substituted with its long-range limit (9.4). Accordingly the integral to evaluate reads

$$I_0 \approx \int_{\mathcal{A}_0} \frac{4\pi z_0}{q_\parallel} dq_x dq_y = 48\pi z_0 \int_0^{\pi/6} \int_0^{\frac{R'}{\cos(\theta)}} dq_\parallel d\theta = 24\pi R' z_0 \log(3) \ , \tag{C.3}$$

where I used the symmetry of the integrand function to rewrite the integral inside the hexagon as twelve times the integral in the smaller triangle of Fig. C.1b.

The approximation I implemented in all calculations for the evaluation of the I_{sz} integral is

$$\begin{aligned} I_{\text{sz}} &= \frac{2\pi}{L_z} \times \tilde{\rho}^*_{ij}(0) \check{\tilde{\epsilon}}^{-1}_{\mathbf{00}}(0,\omega) \tilde{\rho}_{mn}(0) \times 24\pi R' z_0 \log(3) \\ &= \tilde{\rho}^*_{ij}(0) \check{\tilde{\epsilon}}^{-1}_{\mathbf{00}}(0,\omega) \tilde{\rho}_{mn}(0) 12\pi^2 \log(3) \ b \ M_{xy}^{-1} \ , \end{aligned}$$

having used $z_0 = L_z/2$.

Appendix D

Dynamical effects in the Green's function of real materials

This work is inscribed into a much wider research project on the dynamical contribution to electronic correlation. The dynamical effects in the one-particle G have been object of study of the Ph.D. tesis of G. Lani [82] and M. Guzzo [78].

The latter work M. Guzzo used the exponential form of G (10.14) (derived together with G. Lani [55, 82]) to correct theoretical GW spectra by means of a post-processing procedure. This correction to dynamical effects improves over the GW approximation and gives a realistic description of satellite structures. Moreover, other measurable effects usually

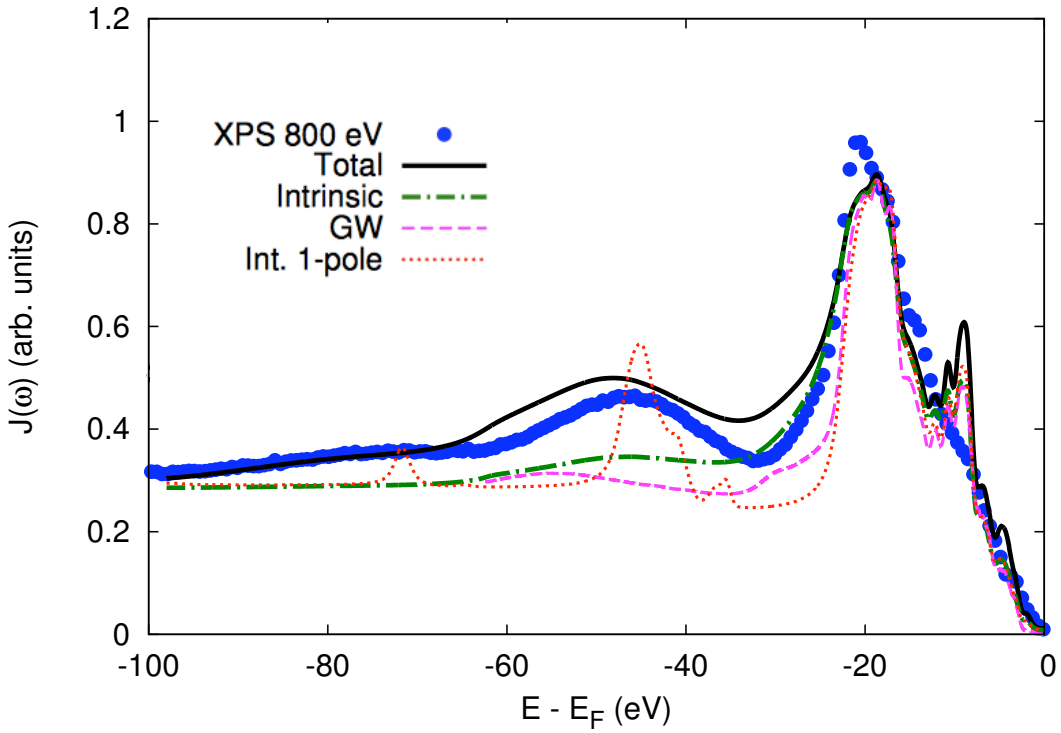

Figure D.1: Experimental data (blue dots) from valence photoemission of graphite at photon energy $h\nu$ =800 eV. GW calculation (violet dashed) and GW+C* with single and multiple plasmon pole models (dotted red and dashed-dotted green). Multi-pole GW+C* including extrinsic effects (black line). Secondary electrons have been added to all calculations. Image taken from [94].

neglected have been added to the calculation, such as background electrons, extrinsic and interference effects [5]. The first application of this method (GW+C*) gave extremely good results in the description of the spectrum of Si [5]. In this application some approximations were used, in particular the plasmon pole approximation for the screening W.

With the aim to validate this approach in more general cases, it was necessary to study materials with a more complex plasmonic structure. Graphite and graphene, with their double peak in the EEL spectrum were excellent candidates for this study.

First of all, to study the satellite structures in photoemission spectra from valence states, good experimental data were needed. Actually only recently the attention is moving from quasiparticles to satellites, so in literature it is hard to find well resolved data in the wide energy range necessary for this analysis. This made necessary the acquisition of new experimental data.

I participated in the measurement of angle-resolved photoemission spectra (ARPES) from graphene and graphite samples. Measurements have been collected on July 2011 and on February 2012 at the TEMPO [6] beamline in the Soleil synchrotron radiation source.

A photon energy of 800 eV has been employed in order to have good signal to noise ratio from the satellites; experimental data from the ABA graphite appear as blue dots in Fig. D.1. At this energy, the electron mean free path is long enough for the experimentalists to be sensitive essentially to the bulk, which does not constitute a problem in studying graphite but imposes strong geometry constraints to the measurements on graphene. For this reason we analysed electrons photoemitted with a grazing angle of 12° with respect to the surface of the sample.

The analysis conducted on graphite data, reported in Fig.D.1, shows clearly that the GW approximation (violet dashed line) reproduces only qualitatively the measured satellites, whereas the full GW+C* method (black solid line) perfectly reproduces the experiment. This analysis and the derivation of a model to predict the level of accuracy one has to expect from GW in describing satellites yielded a work that has been recently submitted to Physical Review B [94]. My calculations, shown in Chapter 8, on the $2d_0$ and the $4d_0$ geometries have been of precious help in understanding the flaws of the GW approximation beyond the quasiparticle region.

The analysis of graphene data is on the way.

Bibliography

[1] M. Gatti, Ph.D. thesis, École Polytechnique (2007).

[2] L. Hedin, J. Phys: Condens. Matter **11**, R489 (1999).

[3] C. N. Berglund and W. E. Spicer, Phys. Rev. **136**, A1030 (1964).

[4] G. D. Mahan, Phys. Rev. B **2**, 4334 (1970).

[5] M. Guzzo, G. Lani, F. Sottile, P. Romaniello, M. Gati, J. J. Kas, J. J. Rehr, M. G. Silly, F. Sirotti, and L. Reining, Phys. Rev. Lett. **107**, 166401 (2011).

[6] F. Polack, M. Silly, C. Chauvet, B. Lagarde, N. Bergeard, M. Izquierdo, O. Chubar, D. Krizmancic, M. Ribbens, J.-P. Duval, et al., AIP Conf. Proc. **1234**, 185 (2009).

[7] R. D. Schaller and V. I. Klimov, Phys. Rev. Lett. **92**, 18661 (2004).

[8] M. C. Beard, K. P. Knutsen, P. Yu, J. M. Luther, Q. Song, W. K. Metzger, R. J. Ellingson, and A. J. Nozik, Nano Letters **7**, 2506 (2007).

[9] A. J. Nozik, Chem. Phys. Lett. **457**, 3 (2008).

[10] M. Govoni, I. Marri, and S. Ossicini, Nature Photonics **6**, 672 (2012).

[11] A. J. Nozik, Physica E **14**, 115 (2002).

[12] *Carbon nanotubes could make efficient solar cells*, URL `http://www.news.cornell.edu/stories/2009/09/carbon-nanotubes-could-make-efficient-solar-cells`.

[13] S. Konabe and S. Okada, Phys. Rev. Lett. **108**, 227401 (2012).

[14] P. Würfel, *Physics of Solar Cells: From Basic Principles to Advanced concepts* (Wiley-VCH Verlag, Weinheim, Germany, 2009).

[15] P. Schattshneider, *Fundamentals of Inelastic Electron Scattering* (Springer, Wien, 1986).

[16] H. Kohl and H. Rose, *Theory of Image Formation by Inelastically Scattered Electrons in the Electron Microscope* (Academic Press, 1985).

[17] L. van Hove, Phys. Rev. **95**, 249 (1954).

[18] R.Kubo, Reports of Progress in Physics **29**, 255 (1966).

[19] R. Hambach, Ph.D. thesis, École Polytechnique (2010).

[20] P. Hohenberg and W. Kohn, Phys. Rev. **136**, B864 (1964).

[21] W. Kohn and L. J. Sham, Phys. Rev. **140**, A1133 (1965).

[22] R. M. Martin, *Electronic Structure: Basic Theory and Practical Methods* (Cambridge University Press, 2004).

[23] L. H. Thomas, Proc. Cambridge Phil. Society **23**, 542 (1927).

[24] E. Fermi, Rend. Lincei **6**, 602 (1927).

[25] P. A. M. Dirac, Proc. Cambridge Phil. Society **26**, 376 (1930).

[26] R. van Leeuwen, Adv. Quant. Chem. **43**, 25 (2003).

[27] D. M. Ceperley and B. J. Alder, Phys. Rev. Lett. **45**, 566 (1980).

[28] C.-O. Almbladh and U. von Barth, Phys. Rev. B **31**, 3231 (1985).

[29] A. V. Kosobutsky, S. Y. Sarkisov, and V. N. Brudnyi, Journal of Physics and Chemistry of Solids **74**, 1240 (2013).

[30] N. W. Ashcroft and N. D. Mermin, *Solid State physics* (Thomson Learning, London WC1 V7AA, United Kingdom, 1976).

[31] E. Runge and E. K. U. Gross, Physical Review Letters **52**, 997 (1984).

[32] T. Ando, Z. Phys. B **26**, 263 (1977).

[33] T. Ando, Solid State Commun. **21**, 133 (1977).

[34] V. Peuckert, J. Phys. C **11**, 4945 (1978).

[35] A. Zangwill and P. Soven, Phys. Rev. A **21**, 1561 (1980).

[36] A. Zangwill and P. Soven, Phys. Rev. Lett. **45**, 204 (1980).

[37] N. T. Maitra and K. Burke, Phys. Rev. A **63**, 042501 (2001).

[38] N. T. Maitra and K. Burke, Phys. Rev. A **64**, 039901(E) (2001).

[39] N. T. Maitra, T. N. Todorov, C. Wodward, and K. Burke, Phys. Rev. A **81**, 042525 (2010).

[40] S. L. Adler, Phys. Rev. **126**, 413 (1962).

[41] R. van Leeuwen, Phys. Rev. Lett. **80**, 1280 (1998).

[42] N. Wiser, Phys. Rev. **129**, 62 (1963).

[43] I. Timrov, Ph.D. thesis, École Polytechnique (2013).

[44] L. Reining, V. Olevano, A. Rubio, and G. Onida, Phys. Rev. Lett. **88**, 066404 (2002).

[45] S. Botti, F. Sottile, N. Vast, V. Olevano, L. Reining, H.-C. Weissker, A. Rubio, G. Onida, R. D. Sole, and R. W. Godby, Phys. Rev. B **69**, 155112 (2004).

[46] S. Botti, A. Fourreau, F. Nguyen, Y.-O. Renault, F. Sottile, and L. Reining, Phys. Rev. B **72**, 125203 (2005).

[47] S. Sharma, J. K. Dewhurst, A. Sanna, and E. K. U. Gross, Phys. Rev. Lett. **107**, 186401 (2011).

[48] S. Sharma, J. K. Dewhurst, A. Sanna, A. Rubio, and E. K. U. Gross, New J. Phys. **14**, 053052 (2012).

[49] P. E. Trevisanutto, A. Terentjevs, L. A. Constantin, V. Olevano, and F. D. Sala, Phys. Rev. B **87**, 205143 (2013).

[50] V. U. Nazarov and S. Kais, p. Arxiv:1308.3013v1 (2013).

[51] V. M. Galidskii and A. B. Migdal, Sov. Phys. JETP-USSR **7**, 96 (1958).

[52] H. Lehmann, Il Nuovo Cimento **11**, 342 (1954).

[53] G. Strinati, Rivista del Nuovo Cimento **11**, 1 (1988).

[54] J. Schwinger, Proceedings of the National Accademy of Science **37**, 452 (1951).

[55] G. Lani, P. Romaniello, and L. Reining, New J. Phys. **14**, 013056 (2012).

[56] F. J. Dyson, Phys. Rev. **75**, 486 (1949).

[57] F. J. Dyson, Phys. Rev. **75**, 1736 (1949).

[58] G. Baym and L. P. Kadanoff, Phys. Rev. **124**, 287 (1961).

[59] L. Hedin, Phys. Rev. **139**, A796 (1965).

[60] F. Caruso, P. Rinke, X. Ren, A. Rubio, and M. Scheffler, arXiv:1304.4039 (2012).

[61] M. van Schilfgaarde, T. Kotani, and S. Faleev, Phys. Rev. Lett. **96**, 226402 (2006).

[62] P. García-González and G. Kresse, Phys. Rev. B **63**, 075112 (2001).

[63] A. Schindlmayr, P. García-González, and R. W. Godby, Phys. Rev. B **64**, 235106 (2001).

[64] B. Holm and U. von Barth, Phys. Rev. B **57**, 2108 (1998).

[65] A. Schindlmayr, T. J. Pollehn, and R. W. Godby, Phys. Rev. B **58**, 12684 (1998).

[66] R. T. M. Ummels, P. A. Bobbert, and W. van Haeringen, Phys. Rev. B **57**, 11962 (1998).

[67] E. L. Shirley, Phys. Rev. B **54**, 7758 (1996).

[68] U. von Barth and B. Holm, Phys. Rev. B **54**, 8411 (1996).

[69] F. Bruneval, N. Vast, and L. Reining, Phys. Rev. B **74**, 045102 (2006).

[70] S. V. Faleev, M. van Schilfgaarde, and T. Kotani, Phys. Rev. Lett. **93**, 126406 (2004).

[71] R. W. Godby and R. J. Needs, Phys. Rev. Lett. **62**, 1169 (1989).

[72] M. S. Hybersten and S. J. Needs, Phys. Rev. B **34**, 5390 (1986).

[73] W. von der Linden and P. Horsch, Phys. Rev. B **37**, 8351 (1988).

[74] P. E. Trevisanutto, C. Giorgetti, L. Reining, M. Ladisa, and V. Olevano, Phys. Rev. Lett. **101**, 226405 (2008).

[75] L. Hedin, B. I. Lundqvist, and S. Lundqvist, Solid State Communications **5**, 237 (1967).

[76] B. Bergersen, F. W. Kus, and C. Blomerg, Canadian Journal of Physics **51**, 102 (1973).

[77] D. C. Langreth, Phys. Rev. B **1**, 471 (1970).

[78] M. Guzzo, Ph.D. thesis, École Polytechnique (2012).

[79] F. Aryasetiawan, L. Hedin, and K. Karlsson, Phys. Rev. Lett. **77**, 2268 (1996).

[80] O. Gunnarsson, V. Meden, and K. Schönhammer, Phys. Rev. B **50**, 10462 (1994).

[81] C.-O. Almbadh and L. Hedin, *Handbook of Synchrotron Radiation* (North-Holland, Amsterdam, 1983).

[82] G. Lani, Ph.D. thesis, École Polytechnique (2011).

[83] R. D. Sole and R. Girlanda, Physical Review B **54**, 14376 (1996).

[84] P. Romaniello, D. Sangalli, J. A. Berger, F. Sottile, and L. G. M. *et al.*, Journal of Chemical Physics **130**, 044108 (2009).

[85] D. Sangalli, P. Romaniello, G. Onida, and A. Marini, Journal of Chemical Physics **134**, 034115 (2011).

[86] *Exc simulation code*, URL `http://theory.polytechnique.fr/codes/exc/`.

[87] F. Sottile, Ph.D. thesis, École Polytechnique (2003).

[88] K. Shindo, J. Phys. Soc. Japan **29**, 287 (1970).

[89] K. Sturm and A. Gusarov, Phys. Rev. B. **62**, 116474 (2000).

[90] F. Bechstedt, K. Tenelsen, B. Adolph, and R. D. Sole, Physical Review Letters **78**, 1528 (1997).

[91] A. Marini and R. D. Sole, Phys. Rev. Lett. **91**, 176402 (2003).

[92] V. Olevano and L. Reining, Phys. Rev. Lett. **86**, 5962 (2000).

[93] M. Zimmermann, Z. Zhang, and C. B. Musgrave, Nature Chemistry **10**, 1038 (2010).

[94] M. Guzzo, J. J. Kas, L. Sponza, C. Giorgetti, F. Sottile, D. Pierucci, M. G. Silly, F. Sirotti, J. J. Rehr, and L. Reining, submitted to Phys. Rev. Lett. (2012).

[95] L. Sponza, V. Véniard, F. Sottile, C. Giorgetti, and L. Reining, Phys. Rev. B **87**, 235102 (2012).

[96] M. S. Kim and C. H. Park, J. Kor. Phys. Soc **1**, 490 (2010).

[97] C. E. Ekuma, M. Jarrel, J. Moreno, and D. Bagayoko, AIP Advances **2**, 012189 (2012).

[98] M. Betzinger, C. Friedrich, A. Görling, and S. Blügel, Phys. Rev. B **85**, 245124 (2012).

[99] M. Jourdan, N. Blümer, and H. Adrian, Eur. Phys. J. B **33**, 25 (2003).

[100] A. Otomo and H. Y. Hwang, Nature **427**, 423 (2004).

[101] J. G. Bednorz and K. A. Müller, Phys. Rev. Lett. **52**, 2289 (1984).

[102] F. Bottin and F. Finocchi, Phys. Rev. B **76**, 165427 (2007).

[103] R. Evarestov, E. Blokhin, D. Gryaznov, E. Kotomin, R. Merkle, and J. Maier, Phys. Rev. B **85**, 174303 (2012).

[104] R. Loetzsch, A. Lübcke, I. Uschmann, E. Förster, V. Große, M. Thuerk, T. Koettig, F. Schmidl, and P. Seidel, Appl. Phys. Lett. **96**, 07901 (2010).

[105] J. Inaba and T. Katsufuji, Phys. Rev. B **72**, 052408 (2005).

[106] M. cardona, Phys. Rev. **140**, A651 (1965).

[107] D. Bäuerle, W. Braun, V. Saile, G. Sprüssel, and E. Koch, Z. Phys. B **29**, 179 (1978).

[108] J. L. Servoin, Y. Luspin, and F. Gervais, Phys. Rev. B **22**, 5501 (1980).

[109] K. van Benthem, C. Elsässer, and R. French, J. Appl. Phys. **90**, 6156 (2001).

[110] J. E. J. Jr., L. A. Boatner, D. H. Lowndes, R. A. McKee, and M. Godbole, Appl. Opt. **33**, 6053 (1994).

[111] D. J. Lee, Y. K. Seo, Y. S. Lee, and H.-J. Noh, Solid State Commun. **150**, 301 (2010).

[112] A. H. Kahn and A. J. Leyendecker, Phys. Rev. **135**, A1321 (1964).

[113] L. F. Mattheiss, Phys. Rev. B **6**, 4718 (1972).

[114] R. Ahuja, O. Eriksson, and B. Johansson, J. Appl. Phys. **90**, 1845 (2001).

[115] Y. X. Wang, W. L. Zhong, C. L. Wang, and P. L. Zhang, Solid State Comm. **120**, 133 (2001).

[116] M. Arai, S. Kohiki, H. Yoshikawa, S. Fukushima, Y. Waseda, and M. Oku, Phys. Rev. B **65**, 085101 (2002).

[117] M.-Q. Cai, Z. Yin, and M.-S. Zhang, Chem. Phys. Lett. **388**, 223 (2004).

[118] G. Gupta, T. Nautiyal, and S. Auluk, Phys. Rev. B **69**, 052101 (2004).

[119] C. B. Samantaray, H. Sim, and H. Hwang, Microelec. J. **36**, 725 (2005).

[120] E. D. Palik, *Handbook of Optical Constants of Solids II* (Academic, San Diego CA, 1991).

[121] R. W. G. Wycoff, *Crystall Structures II* (Interscience, New York, 1964).

[122] R. G. Burns, *Mineralogical Applications of Crystal Field Theory, second edition* (Cambridge University Press, London, UK, 1993).

[123] L. van Heeringen, Ph.D. thesis, Radboud University Nijmegen (2012).

[124] *Abinit simulation package*, URL `http://www.abinit.org`.

[125] M. Rohlfing, P. Krüger, and J. Pollmann, Phys. Rev. Lett. **75**, 3489 (1995).

[126] A. Fleszar and W. Hanke, Phys. Rev. B **56**, 10228 (1997).

[127] *Dp simulation code*, URL `http://dp-code.org`.

[128] L. Yang, J. Deslippe, C.-H. Park, M. L. Cohen, and S. G. Louie, Phys. Rev. Lett. **103**, 186802 (2009).

[129] J. T. Devreese, S. N. Klimin, J. L. M. van Mechelen, and D. van der Marel, Phys. Rev. B **81**, 125119 (2010).

[130] W. S. Choi, H. Ohta, S. J. Moon, Y. S. Lee, and T. W. Noh, Phys. Rev. B **82**, 024301 (2010).

[131] C. Z. Bi, J. Y. Ma, J. Yan, X. Fang, B. R. Zhao, D. Z. Yao, and X. G. Qiu, J. Phys: Cond. Matt. **18**, 2553 (2006).

[132] R. Ahuja, S. Auluck, J. M. Willis, M. Alouani, B. Johansson, and O. Eriksson, Phys. Rev. B **55**, 4999 (1997).

[133] M. Klittenberg, S. Lebègue, C. Ortiz, B. Sanyval, J. Fransson, and O. Eriksson, J. Phys.: Condens. Matter **21**, 335502 (2009).

[134] A. G. Marinopoulos, L. Reining, A. Rubio, and V. Olevano, Phys. Rev. B **69**, 245419 (2004).

[135] P. E. Trevisanutto, M. Holzmann, M. Côté, and V. Olevano, Phys. Rev. B **81**, 121405(R) (2010).

[136] L. Papagno and L. S. Caputi, Surface Science **125**, 530 (1983).

[137] M. Vos, A. S. Kheifets, E. Weigold, and F. Aryasetiawan, Phys. Rev. B **63**, 033108 (2001).

[138] A. Grüneis, C. Attaccalite, T. Pichler, V. Zabolotnyy, H. Shiozawa, S. L. Molodtsov, D. Inosov, A. Koitzsch, M. Knupfer, J. Schiessling, et al., Phys. Rev. Lett. **100**, 037601 (2008).

[139] A. Grüneis, C. Attaccalite, L. Wirtz, H. Shiozawa, R. Saito, T. Pichler, and A. Rubio, Phys. Rev. B **78**, 205425 (2008).

[140] C. S. Leem, C. Kim, S. R. Park, M.-K. Kim, H. J. Choi, C. Kim, B. J. Kim, S. Johnston, T. Devereaux, T. Ohta, et al., Phys. Rev. B **79**, 125438 (2009).

[141] B. Partoens and F. M. Peeters, Phys. Rev. B **74**, 075404 (2006).

[142] V. N. Strocov, A. Charrier, J.-M. Themlin, M. Rohlfing, R. Claessen, N. Barrett, J. Avila, J. Sanchez, and M.-C. Asensio, Phys. Rev. B **64**, 075105 (2001).

[143] I. Lobato and B. Partoens, Phys. Rev. B **83**, 165429 (2011).

[144] S. B. Trickey, F. Müller-Plathe, and G. H. F. Dierksen, Phys. Rev. B **45**, 4460 (1992).

[145] J.-K. Lee, S.-C. Lee, J.-P. Ahn, S.-C. Kim, J. I. Wilson, and P. John, Journal of Chemical Physics **129**, 234709 (2008).

[146] S. Horiuchi, T. Gotou, M. Fujiwara, R. Sotoaka, M. Hirata, K. Kimoto, T. Asaka, T. Yokosawa, Y. Matsui, K. Watanabe, et al., Jpn. J. Appl. Phys. **42**, L1073 (2003).

[147] B.-R. W. J.-H. Wong and M.-F. Lin, Computer Physics Communications **182**, 77 (2011).

[148] B. Kwiecińska and H. I. Petersen, International Journal of Coal and Geology **57**, 99 (2004).

[149] Y. Baskin and L. Meyer, Phys. Rev. **100**, 544 (1955).

[150] H. A. Wilhelm, B. Croset, and G. Medjahdi, Carbon **45**, 2356 (2007).

[151] W. Kohs, H. J. Santner, F. Hofer, H. Schröttner, J. Doninger, I. Barsukov, H. Buqa, J. H. Albering, K.-C. Möller, J. O. Besenhard, et al., Journal of Power Sources **119**, 528 (2003).

[152] J.-C. Charlier, J.-P. Michenaud, and P. Lambin, Phys. Rev. B **46**, 4540 (1992).

[153] C. W. Chiu, S. H. Lee, S. C. Chen, F. L. Shyu, and M. F. Lin, New Journal of Physics **12**, 083060 (2010).

[154] T. Eberlein, U. Bangert, R. R. Nair, R. Jones, M. Gass, A. L. Bleloch, K. S. Novoselov, A. Geim, and P. R. Briddon, Phys. Rev. B **77**, 233406 (2008).

[155] J. C. Meyer, A. K. Geim, M. I. Katsnelson, K. S. Novoselov, D. Obergfell, S. Roth, C. Girit, and A. Zettl, Solid State Comm. **143**, 101 (2007).

[156] K. S. Novoselov, A. K. Geim, S. V. Morozov, D. Jiang, Y. Zhang, S. V. Dubonos, I. V. Grigorieva, and A. A. Firsov, Science **306**, 666 (2004).

[157] C. Berger, Z. Song, T. Li, X. Li, A. Y. Ogbazghi, R. Feng, Z. Dai, A. N. Marchenkov, E. H. Conrad, P. N. First, et al., J. Phys. Chem. B **108**, 19912 (2004).

[158] C. Riedl, C. Coletti, and U. Starke, J. Phys. D: Appl. Phys. **43**, 374009 (2010).

[159] C. Gómez-Navarro, M. Burghard, and K. Kern, Nano Lett. **8**, 2045 (2008).

[160] S. Park and R. S. Ruoff, Nature Nanotechnology **4**, 217 (2009).

[161] J. C. Meyer, A. K. Geim, M. I. Katsenelson, K. S. Novoselov, T. J. Booth, and S. Roth, Nature **446**, 60 (2007).

[162] C. Riedl, C. Coletti, T. Iwasaki, A. A. Zakharov, and U. Starke, Phys. Rev. Lett. **103**, 246804 (2009).

[163] M. H. Gass, U. Bangert, A. L. Bleloch, P. Wang, R. R. Nair, and A. K. Geim, Nature Nanotechnology **3**, 676 (2008).

[164] R. E. Peierls, Ann. I. H. Poincaré **5**, 177 (1935).

[165] L. D. Landau, Phys. Z. Sowjetunion **11**, 26 (1937).

[166] J.-C. Charlier, X. Gonze, and J.-P. Michenaud, Physical Review B **43**, 4579 (1991).

[167] K. S. Novoselov, A. K. Geim, S. V. Morozov, D. Jiang, M. I. Katsnelson, I. Grigorieva, S. V. Dubonos, and A. A. Firsov, Nature **438**, 197 (2005).

[168] Y. Zhang, Y.-W. Tan, H. L. Stromer, and P. Kim, Nature **438**, 201 (2005).

[169] M. R. Jarvis, I. D. White, R. W. Godby, and M. C. Payne, Phys. Rev. B **56**, 14972 (1997).

[170] C. A. Rozzi, D. Varsano, A. Marini, E. K. U. Gross, and A. Rubio, Phys. Rev. B **73**, 205119 (2006).

[171] S. Ismail-Beigi, Phys. Rev. B **73**, 233103 (2006).

[172] C. D. Spataru, S. Ismail-Beigi, L. X. Benedict, and S. G. Louie, Appl. Phys. A **78**, 1129 (2004).

[173] *European theoretical spectroscopy facility*, URL `http://www.etsf.eu/`.

[174] *Nanotube solar cells improve efficiency 10 times*, URL `http://www.greenoptimistic.com/2008/06/19/nanotube-solar-cells-improve-efficiency-10-times/`.

[175] *Georgia tech cadmium coated carbon nanotube micron-scale "towers" boost solar power production by 300%*, URL `http://nanopatentsandinnovations.blogspot.fr/2009/12/georgia-tech-cadmium-coated-carbon.html`.